UNIVERSITY OF COPENHAGEN
DEPARTMENT OF CHEMISTRY

PhD Thesis
Yang Wang

Exploring Long-Lived Luminescence in Supramolecular Constructs

Copenhagen
2024

UNIVERSITY OF COPENHAGEN

DEPARTMENT OF CHEMISTRY

Exploring Long-Lived Luminescence in Supramolecular Constructs

PhD Thesis

Yang Wang

Supervisor: Prof. Bo Wegge Laursen

Copenhagen 2024

Title: Exploring Long-Lived Luminescence in Supramolecular Constructs

The thesis has been submitted to the Faculty of Science, University of Copenhagen, as part of the fulfillment for obtaining a Doctor of Philosophy (Ph.D.) degree. The work presented in this thesis was conducted at the University of Copenhagen from January 2021 to March 2024.

PhD Candidate: Yang Wang (yw@chem.ku.dk)
Nano-Science Center & Department of Chemistry
University of Copenhagen
Universitetparken 5
DK-2100 København Ø
Denmark

Academic Supervisor: Prof. Bo Wegge Laursen (bwl@nano.ku.dk)
Nano-Science Center & Department of Chemistry
University of Copenhagen
Universitetparken 5
DK-2100 København Ø
Denmark

Printed in Denmark 2024

ISBN:

Preface

This thesis was submitted to obtain a Ph.D. degree in Nanoscience from the University of Copenhagen. Commenced as a TALENT Doctoral Fellowship Programme (HORIZON 2020, No 801199), the work of this thesis has been conducted at the Department of Chemistry at the University of Copenhagen, within the period from 15th January 2021 to 31st March 2024.

The project has been financially supported by both Marie Skłodowska-Curie Grant and the University of Copenhagen. The project implementer and beneficiary person (Yang Wang) shows the greatest appreciation for the funding from both organizations and also the supervision from his academic supervisor Prof. Bo Wegge Laursen.

HORIZON 2020
This project has received funding from the European Union's Horizon 2020 research and innovation programme under the Marie Skłodowska-Curie grant agreement No 801199.

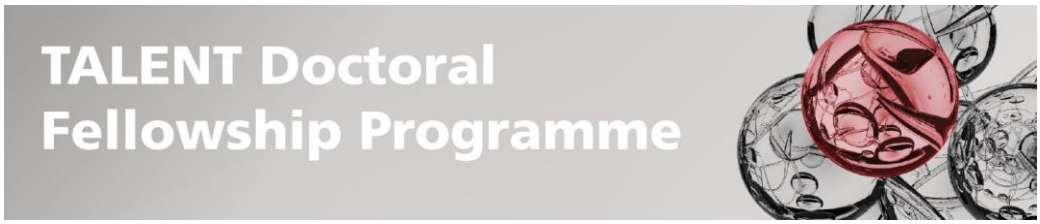

Abstract

This thesis investigates sustaining long-lived luminescence in a supramolecular construct, which is Small-Molecule Ionic Isolation Lattices (SMILES), through two key strategies. Firstly, exploring the reinstatement of triplet emission from phosphorescent dyes when embedded in SMILES. Secondly, exploring the generation of electronic donor-acceptor systems within SMILES by energetically activating Cyanostar (CS), the macromolecule unit constructing SMILES, and result in charge-transfer emission with prolonged lifetimes.

In Part I, fundamental investigations were performed to focus on the bimolecular interactions between cyanostar (CS) and mono-cationic phosphorescent dyes, particularly PtTA complexes. Stern-Volmer experiments elucidate the triplet energy transfer between PtTA complexes and CS, indicating methods to prevent efficient triplet energy transfer to CS for phosphorescent chromophores. The performances of three PtTA complexes in SMILES solid emitters align with the triplet energy matching criterion, leading to the successful generation of Pt3-SMILES crystals and nanoparticles with enhanced emission and prolonged lifetime. Investigations on the enhanced phosphorescence in Pt3-SMILES suggest the effectively circumvented non-radiative deactivation pathways, hereby the phosphorescent SMILES strategy has been fundamentally established.

Part II extends the exploration to multi-cationic metalloporphyrin dyes, specifically Por4, aiming to amplify phosphorescence within SMILES structures. The efficiency of SMILES in boosting Por4 phosphorescence is demonstrated, with Por4-SMILES crystals and nanoparticles emitting red phosphorescence with millisecond-range lifetimes. These findings highlight the potential of SMILES as an alternative to cryogenic conditions for achieving strong phosphorescence in metalloporphyrin dyes, by sufficiently suppressing the non-radiative pathways.

Part III shifts focus to exciplex formation in SMILES solids, as a method to extend fluorescence lifetimes within SMILES. By measuring solid samples with varying molar ratios of CS and fluorophore (TPT), the long-lived excited state arising from the charge-transfer mechanism is validated. This approach offers a promising method for fluorophores to prolong luminescence lifetimes in SMILES-based structures.

In summary, this thesis offers a comprehensive exploration of strategies to achieve long-lived luminescence in SMILES-based supramolecular structures. By elucidating fundamental bimolecular interactions, enhancing phosphorescence from phosphorescent dyes, and leveraging the formation of charge-transfer transition, significant achievements have been made towards extending luminescence lifetimes in SMILES materials, laying the groundwork for diverse applications in luminescent materials and beyond.

Resumé (DK)

Denne afhandling undersøger opretholdelsen af langvarig luminescens i en supramolekylær struktur, kendt som Small-Molecule Ionic Isolation Lattices (SMILES), gennem to nøglestrategier. For det første undersøges genetableringen af triplet emission fra fosforescerende farvestoffer, når de indlejres i SMILES. For det andet udforskes genereringen af elektroniske donor-acceptorsystemer inden for SMILES ved energisk at aktivering af Cyanostar (CS), den makromolekylære enhed der opbygger SMILES, og resulterer i ladningsoverførselsemission med forlængede levetider.

I Del I blev der udført grundlæggende undersøgelser for at fokusere på bimolekylære interaktioner mellem cyanostar (CS) og mono-kationiske fosforescerende farvestoffer, især PtTA-komplekser. Stern-Volmer-eksperimenter klarlægger triplet energioverførslen mellem PtTA-komplekser og CS, hvilket indikerer metoder til at forhindre effektiv triplet energioverførsel til CS for fosforescerende kromoforer. Ydelserne af de tre PtTA-komplekser i SMILES fast stof emittere stemmer overens med kriteriet for triplet energimatching, hvilket fører til den vellykkede dannelse af Pt3-SMILES krystaller og nanopartikler med forbedret emission og forlænget levetid. Undersøgelser af den forbedrede fosforescens i Pt3-SMILES antyder de effektivt omgåede ikke-radiative deaktiveringsveje, hvilket etablerer den fosforescerende SMILES-strategi fundamentalt.

Del II udvider uddersøgelsen til multi-kationiske metalloporfyrin-farvestoffer, specifikt Por4, med det sigte at forstærke fosforescensen inden for SMILES-strukturer. Effektiviteten af SMILES i at øge Por4-fosforescensen demonstreres, med Por4-SMILES krystaller og nanopartikler, der udsender rød fosforescens med millisekundområde levetider. Disse fund fremhæver potentialet for SMILES som et alternativ til kryogene betingelser for at opnå stærk fosforescens i metalloporfyrin-farvestoffer, ved tilstrækkeligt at undertrykke de ikke-radiative veje.

Del III skifter fokus til exciplex-dannelse i SMILES fast stof, som en metode til at forlænge fluorescenslevetider inden for SMILES. Ved at måle faste prøver med varierende molforhold af CS og fluorofor (TPT), valideres den langvarige excitations-state, der opstår fra ladningsoverførselsmekanismen. Denne tilgang tilbyder en lovende metode til fluoroforer for at forlænge luminescenslevetider i SMILES-baserede strukturer.

Sammenfattet tilbyder denne afhandling en omfattende udforskning af strategier til opnåelse af langvarig luminescens i SMILES-baserede supramolekylære strukturer. Ved at klarlægge grundlæggende bimolekylære interaktioner, forbedre fosforescensen fra fosforescerende farvestoffer og udnytte dannelsen af ladningsoverførselsovergang, er der opnået betydelige fremskridt med hensyn til at forlænge luminescenslevetider i SMILES-materialer, hvilket danner grundlaget for adskillige anvendelser inden for luminescerende materialer med videre.

概述 (CN)

该论文旨在通过两种关键策略探索 "小分子离子隔离晶格"Small-Molecule Ionic Isolation Lattices (SMILES) 结构中的长寿命发光。首先，探索再现和增强嵌入 SMILES 中的磷光染料分子的三重态发光。其次，通过激活 SMILES 结构的核心大分子 Cyanostar (CS)，在 SMILES 内生成电子给体-受体体系，从而促进了电荷转移（charge-transfer）机制的形成并诱导产生具有延长寿命的发光。

在第一部分，基础研究聚焦于 CS 与一系列单一价态阳离子磷光染料之间的双分子相互作用，尤其是 CS 与三种 PtTA 分子的相互作用。 Stern-Volmer 实验阐明了 PtTA 和 CS 之间的三重态能量转换，并建立了避免三重态能量转移至 CS 的磷光染料分子筛选机制。通过在溶液中研究这些相互作用，确立了三重态能量匹配准则，从而成功制备了 Pt3-SMILES 晶体和纳米颗粒，其具有增强的磷光发光和延长的寿命，这是因为 SMILES 有效地抑制了非辐射性失活途径，继而我们基本确立磷光 SMILES 的策略。

第二部分将探索多价态阳离子卟啉染料 (Por4) 在 SMILES 中的应用，旨在拓宽磷光 SMILES 的寿命范围。实验证明了 SMILES 可有效提高 Por4 的磷光发射。Por4-SMILES 晶体和纳米颗粒发出红色磷光，且具有毫秒级的寿命。这些发现证明 SMILES 通过有效抑制非辐射性途径来提升磷光染料分子的磷光发射，突显了 SMILES 的优越性。

第三部分将研究焦点转向激基复合物（exciplex）的形成，以及探索 SMILES 结构内的电荷转移（charge-transfer）机制延长荧光发光寿命的现象。通过测量 CS 和荧光分子 (TPT) 不同摩尔比的固体样品，实验验证了来自电荷转移机制的长寿命激发态。这种方法为在基于 SMILES 的结构中延长荧光发光寿命提供了一个有前景的途径，扩展了 SMILES 在固态发光材料中的实用性。

总之，该论文对实现 SMILES 超分子结构中的长寿命发光的策略进行了全面的探索。通过阐明基本主客体相互作用、磷光染料分子发光的增强机制以及利用电荷转移过程，实现延长发光寿命的相关论证，为超分子主客体材料的长寿命发光研究奠定了基础。

Contents

Glossary of Acronyms

ε	absorption coefficient
λ	wavelength
τ	photoluminescence lifetime
Φ	quantum yields
k_{ISC}	intersystem crossing rate constant
k_{TET}	triplet energy transfer rate constant
k_{diff}	difussion limited rate constant
k_{nr}	non-radiative rate constant
k_q	quenching rate constant
k_r	radiative rate constant
ACQ	aggregation caused quenching
CA[n]	calix[n]arenes
CB[n]	cucurbit[n]urils
CD	cyclodextrin
COD	coefficient of determination
CS	cyanostar, pentacyanopentabenzo [25]annulene
DCM	dichloromethane
DLS	dynamic light scattering
DNA	deoxyribonucleic acid
em	emission
ET	energy transfer
ex	excitation
Fc/Fc$^+$	ferrocene/ferrocenium
FL	fluorescence
FRET	Föster resonance energy transfer
HOMO	highest occupied molecular orbital
IRF	instrument response function
ISC	intersystem crossing
LP	long-pass filter
LUMO	lowest unoccupied molecular orbital
MeCN	acetonitrile (methyl cyanide)
MO	molecular orbitals
MOF	metal-organic frameworks
NIR	near-infrared (spectral region)
NMR	nuclear magnetic resonance
NPs	nanoparticles
PA[n]	pillar[n]arenes
PEG	polyethyleneglycol
Phos	phosphorescence
PL	photoluminescence
Por4	*Palladium(III)–5,10,15,20–(tetra-N-methyl-4-pyridyl) porphyrin complex*
PS	polystyrene
Pt1	*Platinum(II) terpyridyl hydroxylacetylide complex*
Pt2	*Platinum(II) terpyridyl phenylacetylide complex*
Pt3	*Platinum(II) terpyridyl naphthylacetylide complex*
PtTA	*Platinum(II) terpyridyl acetylide complexes*
QY	quantum yields
S_1	first singlet excited state
SMILES	small-molecule ionic isolation lattices
T_1	first triplet excited state
TA	transient absorption
TBA	tetrabutylammonium cations
TCSPC	time-correlated single photon counting
TET	triplet energy transfer
TG	time gating
THF	tetrahydrofuran
TOTA	trioxatriangulenium
TPT	*2,4,6-Triphenylpyrylium tetrafluoroborate*
UV	ultraviolet
XRD	X-ray diffraction

INTRODUCTION

Chapter 1

Background Introduction

This thesis delves into the exploration of long-lived luminescence in solid emitters, constructed via self-assembly systems involving chromogenic cationic dyes paired with anions within macromolecular hosts, categorized as host-guest systems. Specifically, the supramolecular structures are constructed using the Small-Molecule Ionic Isolation Lattices (SMILES) strategy,[1] developed in 2020 following the introduction of the core macromolecule cyanostar (CS).[2] The main themes of the projects in this thesis revolve around supramolecular self-assembly (SMILES), long-lived luminescence, and solid emitters, with detailed theories, experiments, and analyses presented in subsequent chapters.

Utilizing the self-assembly of chromophores is a novel and efficient strategy to create materials with optical properties without extensive modifications and synthetic procedures. For most investigations, most insights have focused on exploring the predictive materials design and programmable optical performances of the hierarchical structures.[3] The understanding of the coevolution of the structures and properties allows the exploitation of constructing self-assembled systems exclusively stemming from noncovalent forces, including hydrogen bonds, and π-π interactions, such as the success in H-/J- aggregations.[4-6]

Apart from the creations based on mono-component systems and neutral chromophores, embedding two or even more components has not been common in the past decade, though it has

gradually attracted more and more attention, as combining the complementary properties from different components into an assembled system fosters chances to generate optical materials or devices possessing multi-functionalities.[7-9]

However, in the meantime, there exist challenges of avoiding component phase separation and predictably co-assembling different components. Recently, the usage of charged chromophores turned out to be an effective solution to such challenges, as the stronger Coulombic forces among charged chromophores will enforce predictable stoichiometry based on a charge balance, which facilitates the synthesis of self-assembly materials. Among them, the cation-anion-receptor approach has the potential to even simplify the synthesizing and engineering parts by just mixing the building blocks. Cationic chromophores attracted by anions captured inside macromolecular receptor-cyanostar (CS) and then form into charge-by-charge stacked *Small-Molecule Ionic Isolation Lattices (SMILES)* has been proven as a useful strategy,[1, 2] which allows generating photoluminescent solid emitters with optical properties retaining single molecular level high fidelities.[10-12]

Before we step into the experimental explorations on long-lived luminescence in the novel supramolecular organization (SMILES), it is important to obtain a fundamental understanding of the terminologies and technologies to be utilized. Therefore, the first introductory chapter, functioning as the guider, is encompassed by three aspects:

(1) The basic definitions of chromophoric absorption and emission, which include the photoexcitation processes, luminescences stemmed from electrons involving different spin multiplicities – singlet and triplet, and therein refer to fluorescence and phosphorescence, respectively.

(2) The methodologies used to facilitate the challenging spectroscopic measurements on solid emitters, which pave a preliminary pathway for our understanding and unveiling of the intrinsic photophysical properties of solid emitters.

(3) Strategies developed in the past several decades focusing on generating luminescent host-guest assembly materials based on utilizing supramolecules. Also previous research on the important strategies contributing to prolonging the exciton's fate, which brings out long-lived luminescence in solid emitters.

1.1 Chromophoric Absorption and Emission

1.1.1 Photoexcitation Processes

The ability of organic chromophores to absorb visible light is attributed to their π-extended conjugated systems, giving rise to distinct occupied and unoccupied molecular orbitals. Figure 1.1 illustrates this phenomenon.[13] Typically, absorption of photons occurs when an electron transitions from the highest occupied molecular orbital (HOMO), usually the ground state, to the lowest unoccupied molecular orbital (LUMO). Such a transition requires a photon whose energy matches the gap between these orbitals. Additionally, the photon's electric field must align with the electric dipole moment associated with the transition. The direction of the transition dipole moment, a complex vector, determines the polarization of the incoming light most likely to be absorbed.[14, 15] Understanding the origins, arrangements, and interactions of these transitions is critical as they can impact the observable photophysical properties of chromophores.

When a monochromatic ray of visible light traverses a medium, its intensity diminishes based on the number of absorbers present and their capacity to absorb light at that particular wavelength. This attenuation of incident radiation is governed by the Lambert-Beer law, expressed as:

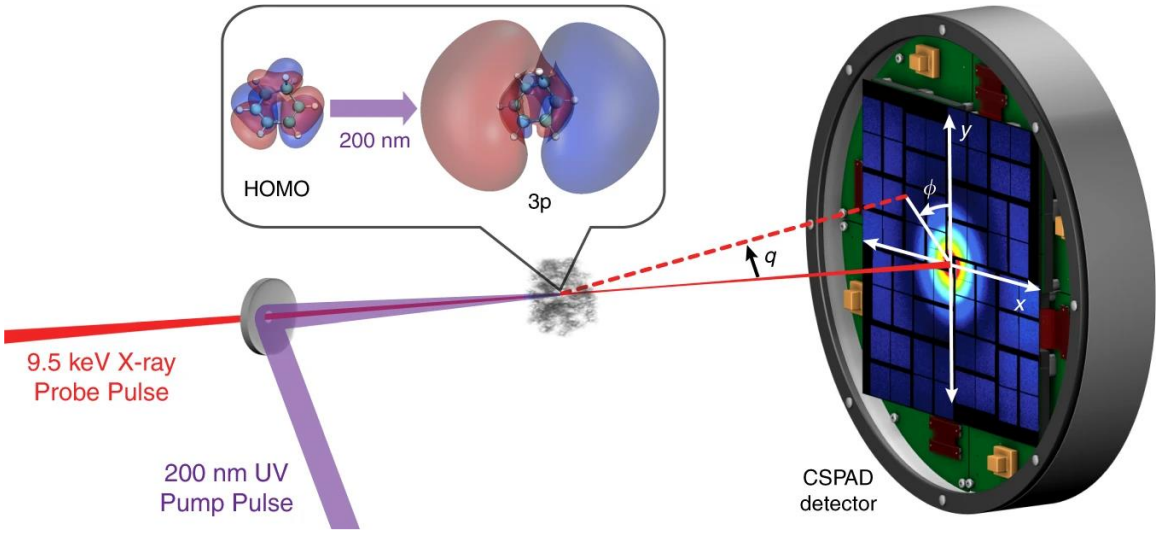

Figure 1.1. Photoexcitation processes. The 1,3-cyclohexadiene (CHD) molecules are excited by a 200 nm UV pump pulse and the molecules are probed by X-ray pulses with a variable time delay. The insert shows the highest occupied molecular orbital (HOMO), which has π character, and the excited 3p molecular orbital. Reproduced with permission.[13] Copyright 2020, Nature.

$$A = log\frac{I_0}{I} = lc\varepsilon_\lambda \quad (1\text{-}1)$$

Here, ***A*** represents absorbance, I_0 denotes the intensity of the incident light, I is the intensity of the transmitted light, c stands for the concentration of the absorbing sample, l represents the path length, and ε_λ represents the molar absorption coefficient at the wavelength λ. The molar absorption coefficient (ε) indicates the molecule's propensity to absorb light and has been shown, both theoretically and experimentally, to exhibit significant wavelength dependence. This implies that photons of different energies do not have uniform probabilities of being absorbed. This phenomenon underscores the intricate relationship between the molecular structure of absorbers and their interaction with incident light, which is a crucial aspect to consider in understanding absorption processes.

1.1.2 Fate of the Molecule in the Excited State

In the excited state, a molecule's fate is governed by a plethora of potential pathways.[14] These include emitting light through fluorescence or phosphorescence, undergoing internal conversion or intersystem crossing processes, participating in energy transfer with neighboring molecules, engaging in charge transfer reactions or photochemical reactions, or returning to the ground state through relaxation mechanisms such as vibrational or thermal relaxation. The specific outcome depends on various factors including molecular structure, electronic configuration, and environmental conditions, and understanding these pathways is crucial for numerous applications in fields ranging from materials science to biological imaging.[16-18]

Singlet or Triplet - Fluorescence or Phosphorescence

Following initial absorption, electrons being excited to upper vibrational states undergo radiationless decay, releasing energy to the surroundings. Subsequently, a transition occurs from the vibrational ground state of the upper electronic state to the lower electronic state, which follows Kasha's Rule,[19, 20] defining the organic chromogenic molecules' electrons at the excited state normally undergo internal conversion to the lowest excited state (S_1), and then leads to characteristic features in emission spectra.

In fluorescence, the lower electronic state's structure is observed, displaying a mirror image of the absorption spectrum but shifting to lower frequencies. Phosphorescence involves a distinct sequence of steps, notably intersystem crossing, facilitated by spin-orbit coupling, which switches the molecule from a singlet state to a triplet state.[21] The triplet state, being spin-forbidden to return to the ground state, acts as a slowly radiating reservoir. Moreover, the triplet state typically occupies at a lower energy level than singlets, resulting in red-shifted emission and longer lifetimes compared to fluorescence.

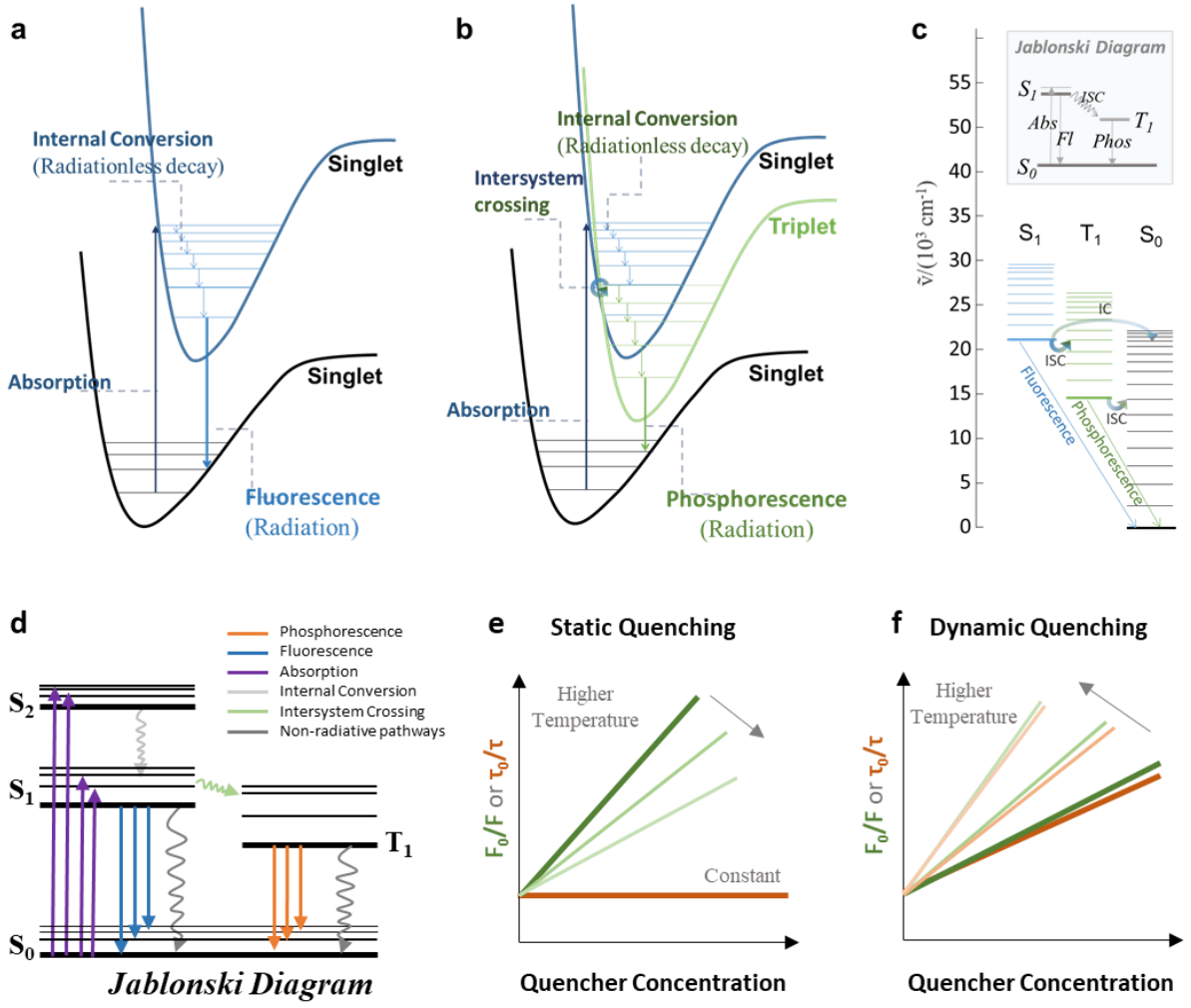

Figure 1.2. Illustrations suggesting the sequence of steps leading to (a) fluorescence and (b) phosphorescence. (c) Diagram indicating the relative positions of the electronic energy levels of a molecule. Vibrational levels of an electronic state lie above each other. (d) Jablonski diagram of a typical electronic transitions and deactivation pathways for the molecule in the excited state. (e,f) Stern-Volmer plots for: (e) Static quenching, where lifetime plot is constant, and emission intensity plot becomes less steep as temperature increases. (f) Dynamic quenching, where both lifetime plot and intensity plot simultaneously become steeper as temperature increases.

For practical issues of applications, fluorescence has been widely utilized in fields including biomolecule labeling, cellular imaging, and diagnostic assays.[9, 18, 22] Phosphorescence, which involves radiative transitions between electronic states of different spin multiplicities,[23] has diverse applications but is hindered by sensitivity to factors like molecular quenchers and temperature.[24] Studies are often limited to cryogenic or air-proof environments. The most used phosphorescent organic chromophores are organometallic complexes containing heavy transitional metal elements, which facilitate singlet-triplet transitions.[24] However, phosphorescence is often quenched by vibrational relaxation upon molecular collision, resulting in low quantum yield emission under ambient conditions. Despite efforts to embed phosphors into solid media at cryogenic temperatures, restoring intrinsic molecular phosphorescence in room temperature remains challenging due to the distortion of optical properties caused by efficient sensitization and energy transfer.

TCSPC and Average Radiative Lifetime

TCSPC stands for Time-Correlated Single Photon Counting, a technique used in fluorescence spectroscopy and microscopy to measure the lifetimes of fluorescent or phosphorescent emissions from samples. In TCSPC, individual photons emitted from the sample are detected and their arrival times are recorded with high precision. By analyzing the distribution of arrival times, researchers can determine the lifetimes of the emitted photons, providing valuable information about the molecular environment and dynamics of the sample.

In practical applications like bioimaging, fluorescent labels often display multi-exponential decay, deviating from the ideal mono-exponential decay expected of a good chromophore. This deviation arises from environmental heterogeneities, indicating the presence of distinct chromophore populations. To approximate luminescence decay characteristics and predict parameters like radiative lifetime, quenching, or energy transfer efficiency, the average radiative lifetime $\langle\tau\rangle$ is commonly used. Two primary methods are employed to express both average: intensity-weighted and amplitude-weighted average luminescence lifetimes, $\langle\tau\rangle_{\text{int}}$ and $\langle\tau\rangle_{\text{amp}}$.[15] These methods provide valuable insights into the dynamic behavior of fluorophores in complexed environments, enhancing understanding of luminescence phenomena in practical applications.

$$\langle\tau\rangle_{int} = \frac{\sum_{i=1}^{n} \alpha_i \tau_i^2}{\sum_{i=1}^{n} \alpha_i \tau_i} \tag{1-2}$$

$$\langle \tau \rangle_{amp} = \sum_{i=1}^{n} \alpha_i \tau_i \quad (1\text{-}3)$$

The intensity-weighted average fluorescence lifetime $\langle \tau \rangle_{int}$ considers each lifetime component (τ_i) weighted by the intensity ($\alpha_i \tau_i$) it produces. While reflecting the actual average time between excitation and observed emission, it is primarily useful for determining practical observation duration. On the other hand, the amplitude-weighted average fluorescence lifetime $\langle \tau \rangle_{amp}$ accounts for the fraction of emitters with specific lifetime components. In cases where all emissive sub-populations have identical intrinsic decay rates (such as with partial dynamic quenching), the amplitude-weighted average fluorescence lifetime $\langle \tau \rangle_{amp}$ directly represents the abundance of these sub-populations. This measure proves particularly useful for describing phenomena like energy transfer, average quantum yield, or quenching efficiency, as it quantifies the fractions of emitters rather than just their contribution to overall emission intensity.

Quenching Mechanisms

Quenching of luminescence involves mechanisms like energy transfer, complex formation, and excited state reactions that reduce luminescence intensity. Quenching mechanisms are categorized as static or dynamic.[15] Static quenching occurs in the ground state, hindering photon emission until complex dissociation. However, dynamic quenching occurs in the excited state, which is more efficient at higher temperatures due to increased diffusion.

The Stern-Volmer equation quantifies quenching mechanisns, revealing luminescence intensity and lifetime decrease with quencher concentration.[25]

$$\frac{I_0}{I} = \frac{\tau_0}{\tau} = 1 + k_q \tau_0 [Q] \quad (1\text{-}4)$$

where I_0 and I refer to the luminescence intensity of chromophore without and with the presence of quencher, τ_0 and τ refer to the luminescence intensity of chromophore without and with the presence of quencher, k_q is the bimolecular quenching constant, [Q] is the concentration of quencher. Based on the bimolecular quenching constant, further interpretations can be made in terms of collisional frequency between freely diffusing chromophores and quenchers.

1.2 From Single Molecules to Molecular Solids

1.2.1 Preparation and Measurements for Luminescent Solids

Photoluminescence (PL) measurements present several challenges, including the need to correct for detection unit wavelength sensitivity and lamp source excitation, as well as compensating for artificial spectral broadening in scattering samples.[26] Additionally, misinterpretations of second-order peaks and solvent Raman peaks must be addressed,[27] along with inner filter effects in PL excitation spectra.[28] Measurements on aggregated samples pose even greater challenges, with variable preparation methods and characterization setups impacting the measured photophysical properties, as the sample size and morphology significantly impact the scattering of illuminated photons.[26] In Figure 1.3, for a typical PL measurement on solid samples attached to glass slides, the alignment angle of the solid sample's position to the orientation of the illumination beam impacts both measured emission intensity and spectra shape.

Small objects or polycrystalline samples tend to exhibit PL quenching dominated by trapping, leading to non-exponential lifetimes. In such cases, the intensity-weighted average lifetime $\langle\tau\rangle_{int}$ serves as a useful parameter for comparison of radiative and non-radiative pathways. The most effective method to suppress trapping in PL measurements is to use larger monolithic objects, such as single crystals.[17, 29, 30] However, the drawback of larger objects is their size, which is typically much larger than the wavelength of visible light, leading to spectral deformations and intrinsic light scattering during absorption, which showcase apparent inner filter effects.

Inner filter effects,[28] commonly known as self-absorption, become more pronounced for chromophores with reduced Stokes shifts between absorption and emission. Self-absorption can be mitigated by reducing the size of measured objectives, although it still remains considerably. For nanoparticle (NP) suspensions, cuvettes with small path lengths can circumvent self-absorption to obtain accurate optical properties. Therefore, in general, even if there exists risks of quenching, nanoparticle (NP) suspensions offer advantages in reducing light scattering and facilitating PL quantum yield determination. For certain cases, the suspension of small-size powders evenly distributed in viscous matrices also improves the high-fidelity reproduction of the intrinsic photophysical properties, as shown in Figure 1.3-d,e,f,g.

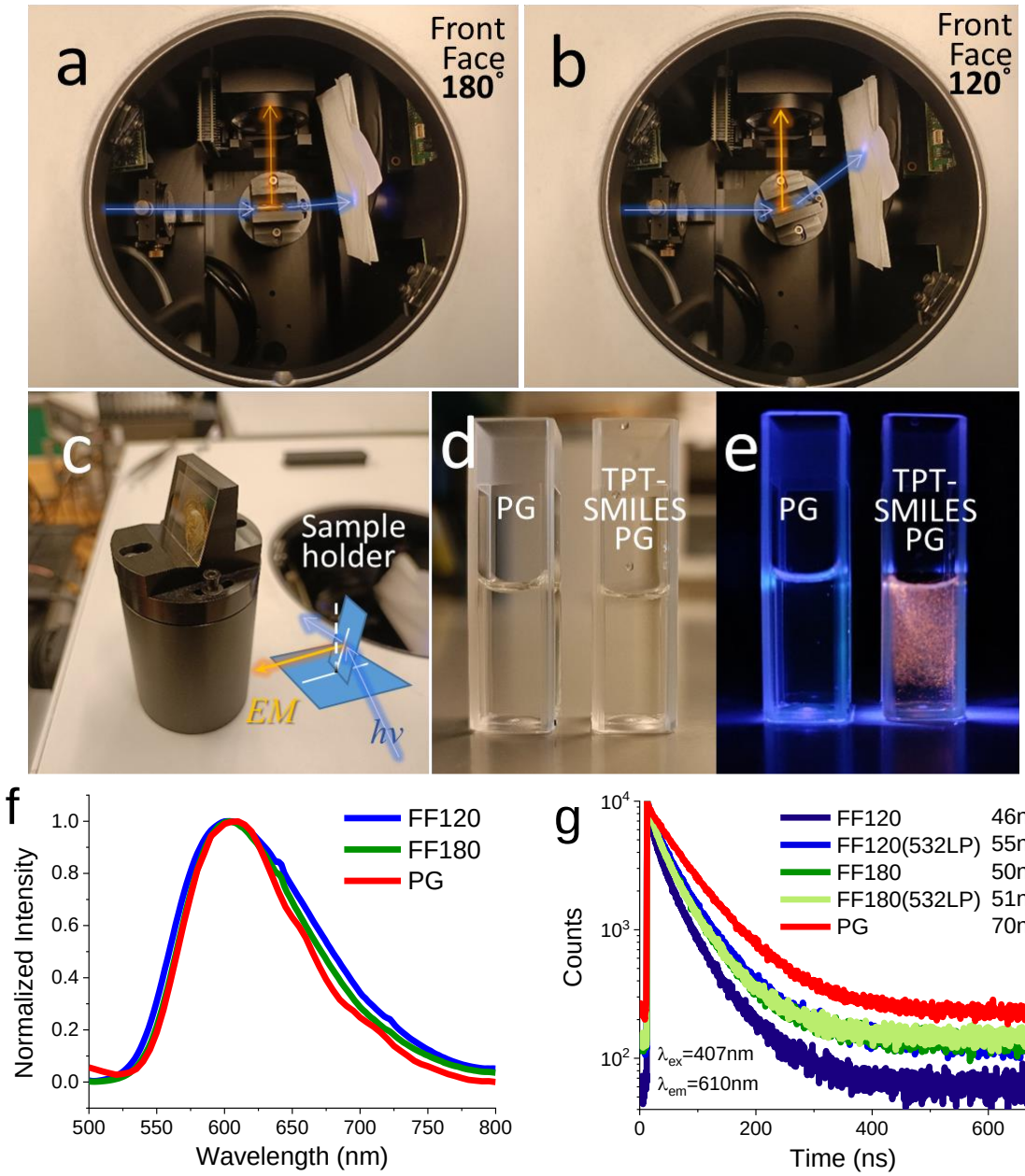

Figure 1.3. Experimental setup for the measurements of solid samples (**TPT**-SMILES) on glass slides or in viscous solvent (PG, propylene glycol). (a,b,c) Typical operations of front-face (FF) measurements on solid samples and the angle mentioned is the alignment angle between the incited illumination beam and scattered beam, the collection pathway of the sample's emission is always perpendicular to the incited illumination. (d,e) Solid powder samples were suspended into viscous PG, (d) under white light and (e) illuminated by ultraviolet light λ_{em}= 365 nm. (f) Emission spectra and (g) decay curves of the same solid sample measured by different experimental setups. The excitation resource was laser λ_{ex}= 407 nm, for decay curves, detector was set at λ_{em}= 610 nm, 532LP refers to a long-pass filter that selectively permits the transmission of light with wavelengths greater than 532 nm.

1.2.2 Luminescence in Molecular Solids

Spectroscopic measurements on solid sample are challenging due to distortion in absorption and emission spectra, lifetimes, and brightness, which are heavily influenced by their aggregated structures with varied molecular arrangements.[26] Molecular dimers are often used as models to study photoexcited electron's excited states in aggregated structures.

Exploration of molecular dimers began with the puzzling phenomenon of quenched emission in chromophore aggregation, where increasing the number of fluorophores per volume did not yield a brighter emitter as expected. Instead, attempts to develop solid-state fluorophores resulted in relatively low brightness, distorted absorption and emission spectra, unpredictable lifetimes, and low quantum yields. This phenomenon, observed across various fluorophores, indicates the critical role of short-range intermolecular interactions.[31]

At very short distances between fluorophores, strong Coulombic interactions between chemical groups become significant, leading to distorted energy landscapes of excited states according to the molecular exciton model proposed by Michael Kasha.[32] Consequently, such aggregates exhibit distinct differences in absorption spectra compared to free, well-solvated fluorophores.

When the molecules forming into dimers are simplified as planar models, and the bimolecular interactions are cofacially occurring, for which the angle between two molecular planes is 0˚. Then the exciton splitting energy ($\Delta\varepsilon$) is given by:

$$\Delta\varepsilon = \frac{2|\boldsymbol{M}|^2}{r^3}(1 - 3cos^2\theta) \tag{1-5}$$

where *M* is the transition moment for singlet-singlet transition in the monomer, r is the bimolecular distance between molecules, and θ is the angle between the polarization axes and the line of molecular centers.

According to the exciton theory, the interaction and coupling between two dipoles at proximity lead to the splitting of an excited state and induces both chromophores transiting to two distinct energy levels. This results in two main types of aggregate formation: head-to-tail assembly (J-aggregates) and face-to-face stacking (H-aggregates), as displayed in Figure 1.4-a.[4, 33]

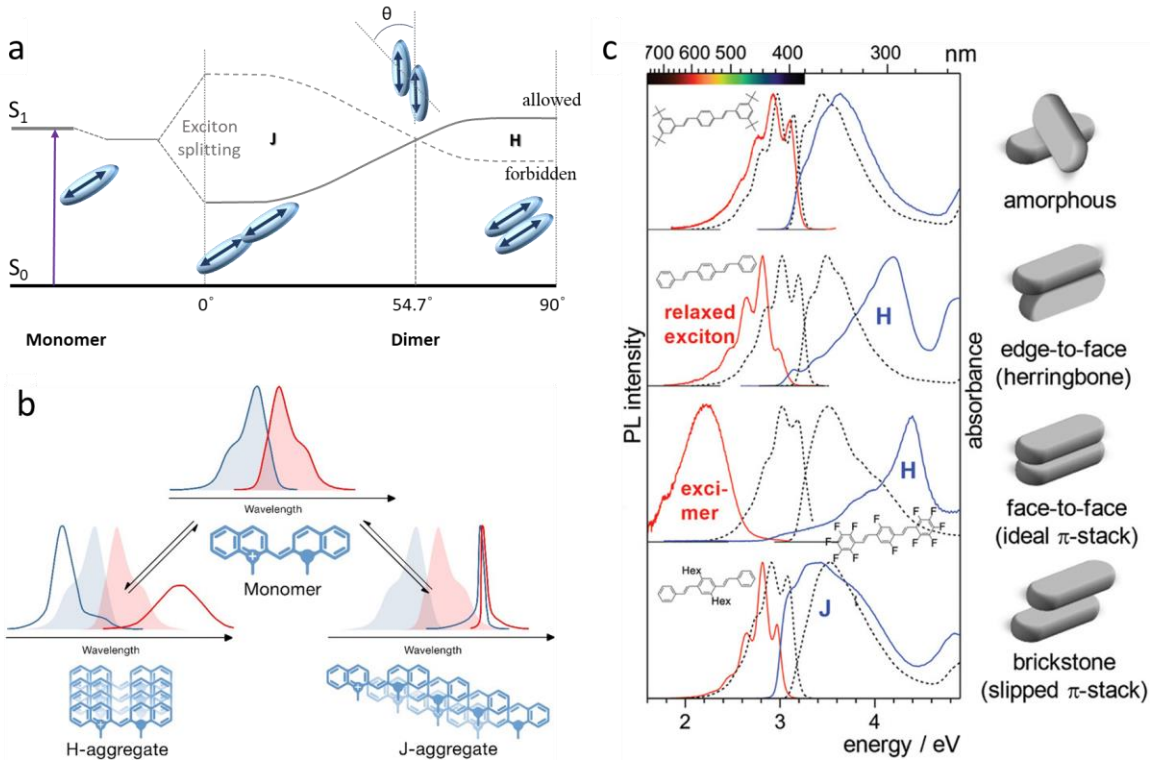

Figure 1.4. Dimer models. (a) Energy diagram showcasing transition from monomer to aggregated dimers with coplanar inclined transition dipoles in photoexcitation processes. Definition of J-aggregation and H-aggregation is based on the slip angle θ. For θ < 54.7˚, the lower energy state is allowed, leading to red-shifted J-band in absorption. For θ > 54.7˚, the higher energy state is allowed, leading to blue-shifted H-band in absorption. (b) A scheme displaying the optical property variations for a typical cyanine dye in the monomer, H-aggregate and J-aggregate conditions. Reproduced with permission.[33] Copyright 2018, IOP. (c) Comparisons for nanoparticle suspensions of chromophore DSB in different aggregated modes, absorption (right) and emission (left) features the excimer emission and J/H-aggregation absorption bandshapes. Reproduced with permission.[35] Copyright 2013, Royal Society of Chemistry.

In H-aggregates, characterized by parallel dipole arrangement, electrostatic repulsion between in-phase transition dipoles leads to a higher-lying excited state and stronger overall oscillator strength. This arrangement typically exhibits intense blue-shifted absorption relative to well-solvated molecules, a large Stokes shift, and often negligible fluorescence due to deactivation via non-radiative relaxation through vibrational levels (Figure 1.4-b).[33]

Conversely, in J-aggregates, characterized by anti-parallel dipole assembly, the overall energy of the excited state is lower, resulting in significantly red-shifted absorption and relatively high

fluorescence quantum yield with a small Stokes shift, as radiative decay from a lower-lying state is favored (Figure 1.4-a,b).[4, 6]

In practice, however, these arrangements are rarely observed individually, as fluorophores tend to pack into more complex intermediate structures,[34] resulting in band splitting and a combination of photophysical properties, depending on the bimolecular distances and the angle between the molecules, which can be observed in Figure 1.4-c.[26, 35]

1.3 Luminescence in Supramolecular Organizations

As the formation of chromophores aggregation normally induces quenching and distortion of molecular optical properties, many strategies have been implemented to circumvent forming into aggregations. Among them, the host-guest assembly strategy has gained popularity over the past decade.[3, 7, 36-39] Luminescent molecular materials formed by using such a strategy are primarily based on non-covalent forces, which ensure easy synthesis and adaptable conformation variability. Furthermore, supramolecular assemblies composed of macromolecule-dye systems are increasingly attracting attention.[8, 9, 40, 41] Such host-guest assemblies facilitate feasibly fabricating luminescent materials, particularly for emitters in aggregated states, which originally required precise control over intermolecular interactions to achieve desirable optical properties.

Interpreting molecular interactions between macromolecules and guest dyes is crucial for understanding and reliably controlling supramolecular self-assembled structures. Organic molecules' luminescence is sensitive to surrounding microenvironments, with relocation from solvent to macromolecular vicinity altering polarity and non-covalent interactions, thereby affecting radiative and non-radiative pathways. Energy or electronic transfer often occurs during transient collisions between macromolecules and organic dyes, as indicated by changes in luminescence.[9, 42, 43] This interaction dynamics elucidation is facilitated by observing luminescence changes between macromolecule and luminescent dyes.

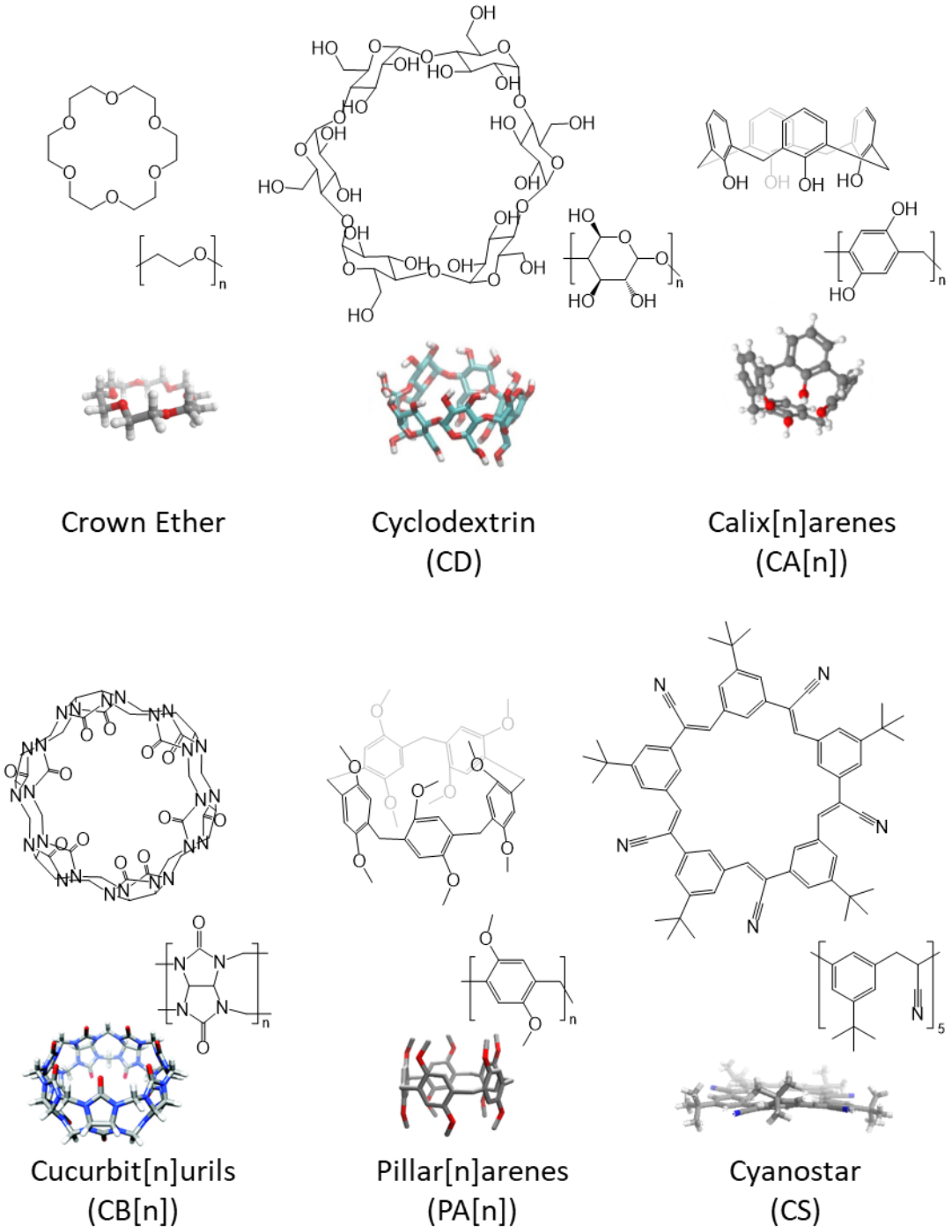

Figure 1.5. Illustration of typical macromolecules used for constructing host-guest self assemblies, the chemical structures, structure units, and 3D illustrations from side view.

1.3.1 Supramolecular Host-Guest Assembly

Recent research has delved into the dye-tuning capabilities of macromolecules using the strategy of host-guest self-assembly. It has been observed that the confined, low-polarity environment offered by the macromolecular hosts results in several advantageous outcomes. These include enhanced brightness, increased photostability, prolonged fluorescence lifetimes.[8, 40, 44]

Based on the differences of macromolecule species, we can simply classify the supramolecular host-guest systems into the following types, with the host of: Crown ether, Cyclodextrin (CD), Cucurbituril (CB), Calixarene (CA), Pillararene (PA) and Cyanostar (CS), as in Figure 1.5.

Crown Ether

Since Pedersen's discovery and synthesis of crown ether compounds in the 1960s,[45] these molecules have been utilized as host molecules for selectively binding alkali metals. Crown ethers typically contain heteroatoms such as oxygen, aza, thia, selenium, and silicon. These heteroatoms endow crown ethers with a strong coordination ability, allowing them to interact effectively with electropositive groups or metal ions. As a result of their unique properties, crown ethers have become increasingly utilized as effective design tools in fabricating various topological structures with precise functions.[46] These structures include rotaxanes and supramolecular polymers. Consequently, crown ethers play a crucial role in facilitating the formation of intricate and functional molecular architectures, as exemplified in Figure 1.6-a.[47]

Cyclodextrin and Cucurbituril

The unique structural features of cyclodextrin (CD)[48] and cucurbituril (CB)[49-51] determine their hydrophilic outer surface and hydrophobic inner cavity. This feature renders both compounds highly soluble in water, making them ideal candidates for constructing aqueous luminescent assembly systems.

In Figure 1.6-b and c, explorations suggest that within these assembly systems, various types of CD[n] and CB[n] complexes can be utilized to incorporate luminescent guest molecules either partially or entirely through host-guest interactions.[52-54] This interaction enhances the luminescent properties of the complexes, making them favorable for applications that demand precise control over luminescence.

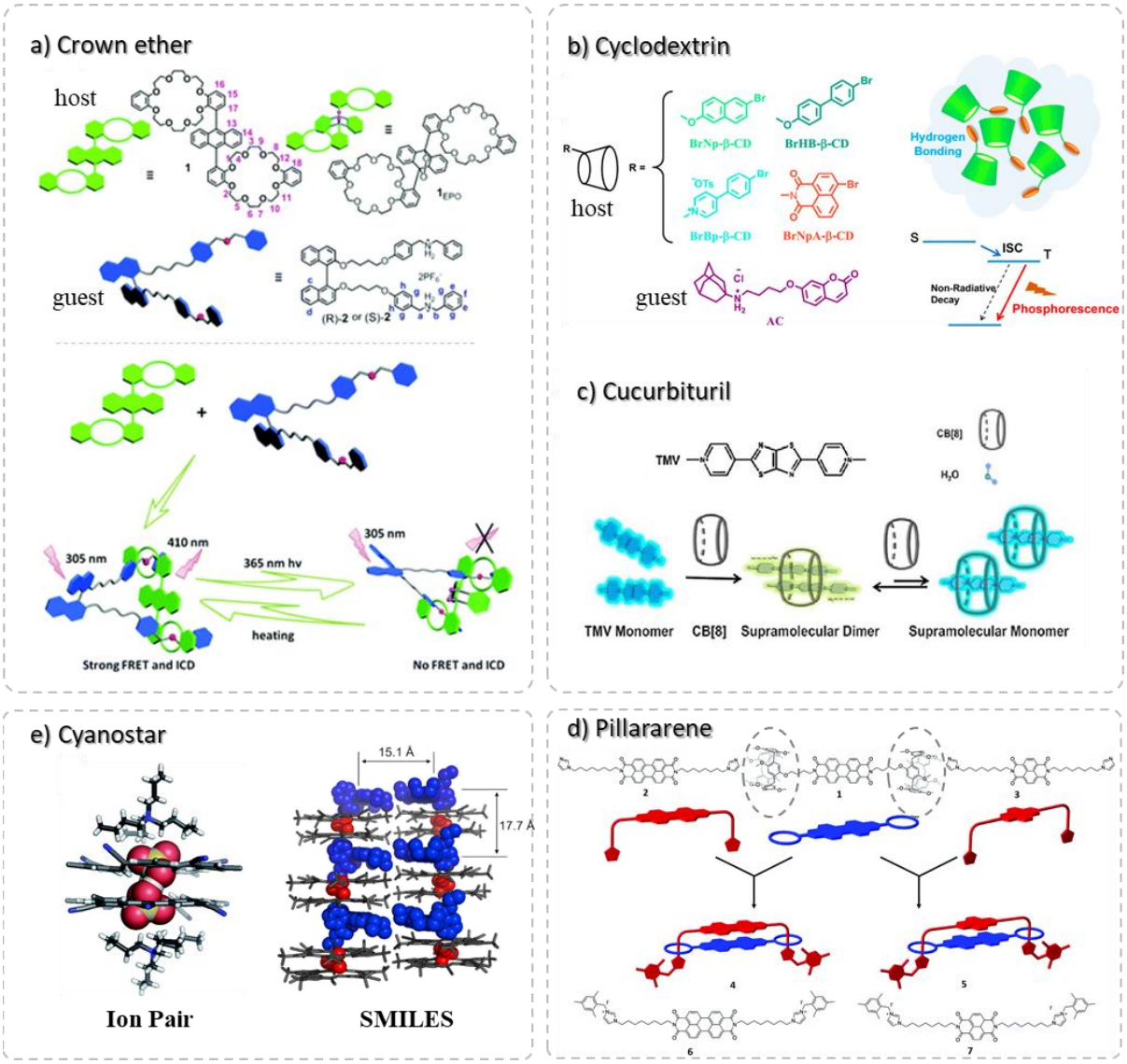

Figure 1.6. Methods of supramolecular host-guest strategies by using different macromolecules: (a) crown ether,[47] (b) cyclodextrin,[54] (c) cucurbituril,[53] (d) pillararene[58] and (e) cyanostar.[1, 59]

Calixarene and Pillararene

Different from cyclodextrin and cucurbituril, the constructing unit for calixarene (CA)[55] and pillararene (PA)[56-58] involves aromatic components, therein apparently strengthen the hydrophobic microenvironment within the cavity. Although calixarene and pillararene differ in their connection sites during the ring formation process, they share similar constituent units and

frameworks. These composition characteristics equip the two macromolecular hosts with similar properties:

(1) Adjustable cavity structure size: Both calixarenes and pillararenes belong to a class of synthetic oligomers, allowing for artificial adjustment of the size of the cavity structure. This adjustability enables tailoring of the host's cavity size to accommodate specific guest molecules.

(2) Easy to modify: Both the upper and lower edges of the benzene ring in calixarenes and pillararenes can undergo derivatization reactions, allowing for the introduction of functional groups. This ability to introduce functional groups enhances the host's selectivity and facilitates molecular recognition capabilities, making them valuable tools in various applications.

Cyanostar (SMILES)

Since 2013, Flood and colleagues discovered cyanostar: a C5-symmetric cyanostilbene macrocycle.[2] It has represented a significant breakthrough in macromolecule and rotaxane research, due to its feasible and high-yield synthetic method and its high binding affinity to large ions like BF_4^-, ClO_4^-, and PF_6^-.[59] Notably, cyanostar's electropositive central cavity stabilizes anions via CH hydrogen-bonding units.[60, 61] This feature presents notable potential for isolating cationic dyes upon transformation into solids, thereby initiating explorations for ultra-bright solid emitters using SMILES (*Small-Molecule Ionic Isolation Lattices*).[1, 10, 12]

The strategy SMILES is an effective approach to reinstating chromophores' photophysical characteristics into solid emitters. This innovative method involves incorporating the anion-binding macromolecule cyanostar (CS) with cationic fluorophores. Consequently, the counter-ions become encapsulated within sizable disc-shaped 2:1 CS/anion ion pair complexes ($CS_2•X^-$), fostering a pattern of alternating charge-by-charge stacked structures with the cationic dyes. It was revealed that the transfer of optical properties from solution to solid arises from the decoupling of dyes at increased dye-dye distances, a phenomenon observed only when the frontier molecular orbitals of the dyes align with those of the cyanostar-anion complex. Notably, a typical 2:1 cyanostar-ClO_4^- complex defines a wide 3.45 V window with reduction and oxidation processes at -1.94 V and +1.5 V versus ferrocene (Figure 1.7-a), further emphasizing the importance of this orbital alignment in decoupling the dyes from the $CS_2•X^-$ ion pair complex.[1]

This strategic arrangement effectively segregates cationic dyes within SMILES materials, thereby reducing pronounced dye-dye interactions, mitigating aggregation-caused quenching (ACQ), and reproducing solution state optical properties into solid emitters. Consequently, SMILES materials restore fluorescence properties reminiscent of those observed in solution, various classes of fluorophores have been successfully integrated into fluorescent SMILES, which have been realized in diverse forms such as crystals, powders and thin films (Figure 1.7-b).[11, 62]

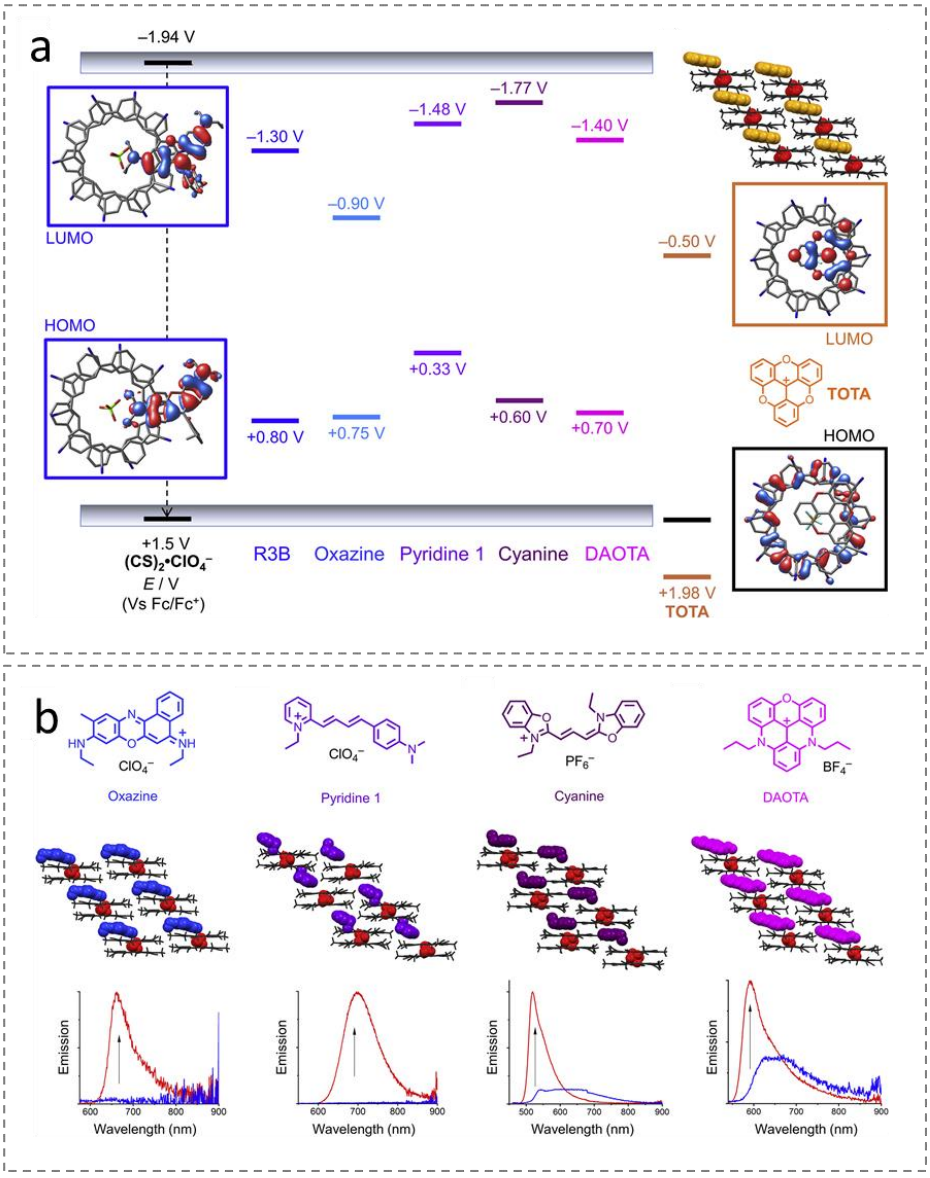

Figure 1.7. (a) Energy level diagram showing positions of frontier orbitals mapped using electrochemistry. (b) SMILES based on fluorophores (Oxazine, Pyridine 1, Cyanine, DAOTA), turn-on emission in SMILES films relative to dye alone. Reproduced with permission.[1] Copyright 2020, Elsevier.

1.3.2 Long-Lived Luminescence in Host-Guest Materials

To obtain long-lived luminescence in chromophoric systems, researchers in the realm of molecular design are generally aiming at attaining desirable phosphorescence in molecular chromophores, and three primary objectives emerge[63]: (1) Facilitating an efficient intersystem crossing process. (2) Ensuring a prolonged lifetime of the triplet excited state. (3) Achieving a high absorption molar coefficient within the visible light range. These objectives primarily focus on intramolecular aspects, whereas strategies for achieving long-lived luminescence in host-guest materials revolve around intermolecular forces, which can be categorized as follows[40, 64]:

Suppressing Non-radiative Pathways

Utilizing a rigid matrix for incorporating organic chromophores is a widely employed strategy in designing long-lived luminescent host-guest materials. Within such systems, efficient intermolecular interactions serve to stabilize triplet excitons, effectively shielding guest molecules from external contact to quenchers and minimizing their vibration/rotation. The selection of an appropriate rigid matrix is of great importance, necessitating considerations such as compatibility, processing capability, and the ability to engage in efficient interactions with guests. Furthermore, achieving efficient long-lived luminescence requires a rigid matrix with a high triplet energy level to avoid inducing triplet energy transfer to the matrix.

While numerous options exist for rigid matrices,[65] macrocyclic molecules like cyclodextrin and cucurbituril, along with different polymers,[66] amines,[67] and acid derivatives,[68] are commonly favored. This preference possibly arises from their possession of multiple interaction sites, which facilitate the formation of robust and stable intermolecular interactions.

Mediating Exciton's Fate

In addition to strategies aimed at protecting chromophores' emission by minimizing non-radiative pathways, it's important to note that for chromophores with inherently short excited state lifetimes, these approaches may not lead to desired long-lived luminescence. Instead, mediating the fate of excitons to extend their excited state duration can effectively yield a much longer emissive state, which is often achieved via the introduction of donor or acceptor components.[10] When donor-acceptor interactions involve charge or electron migration and recombination

processes, the formation of exciplexes occurs. Conversely, another method primarily entails interactions of dipole-dipole resonance-induced energy transfer.[36] Employing the energy transfer process stands out as a promising strategy for combining the long-lived luminescence from phosphorescent emitters and high brightness of fluorephores. The energy transfer processes depend on significant spectral overlap between the emission spectrum of the energy donor and the absorption spectrum of the luminescent emitter (acceptor). This approach significantly promote the modulations on phosphorescent materials, offering tunable emission colors, high brightness, and long luminescence lifetime.

Exciplexes, comprising donors and acceptors, offer potential advantages in charge carrier transportation, and charge recombination processes help with stabilize the excited state. Notably, exciplexes efficiently transfer charges from the highest occupied molecular orbital (HOMO) of the donor to the lowest unoccupied molecular orbital (LUMO) of the acceptor.[19, 69] This feature provides a favorable platform for generating charge-separated states upon photoexcitation. Through careful selection of donors and acceptors, exciplex systems can facilitate the formation of radical cations and radical anions. Subsequently, upon cessation of the excitation source, the gradual recombination of electrons and holes originating from stable anion and cation radicals can lead to a typical exciplex emission, accompanied with prolonged luminescence lifetime.

1.4 Inspirations and Outline

In addition to the growing interest in supramolecular host-guest assembly for creating luminescent materials, SMILES has emerged as a highly effective method to restore solution state emission in densely packed solids. Significant progress has been made in modulating the fluorescence of SMILES to achieve variable wavelengths and desired brightness. However, for bio-imaging applications where the luminescent lifetime serves as a signal, a broader range of luminescent lifetimes is preferred. Thus, this thesis aims to explore the reinstatement of long-lived luminescence in SMILES-based structures. Specifically, the thesis focuses on two main aspects: Firstly, protecting the triplet emission of phosphorescent dyes in SMILES by suppressing non-radiative pathways. Secondly, the electronic donor-acceptor systems were created in SMILES to facilitate forming exciplexes, which involve charge-transfer transitions between fluorophores and CS, and eventually generate charge-transfer emission with prolonged luminescence lifetime.

Part I delves into fundamental investigations of bimolecular interactions between CS and a series of mono-cationic phosphorescent dyes (PtTA). These dyes, with varying energy levels of triplet excited states, were used to determine the triplet energy transfer to CS through Stern-Volmer experiments. Consequently, a benchmark was established for selecting dyes that prevent efficient triplet energy transfer to CS, laying the groundwork for achieving phosphorescent SMILES solid emitters, and eventually inspires the generation of phosphorescent Pt3-SMILES nanoparticles.

In Part II, a multi-cationic metalloporphyrin dye (Por4) was employed to explore phosphorescent SMILES with longer lifetimes. SMILES was proved as highly effective in enhancing the phosphorescence of Por4, similar to the effect achieved with cryogenic conditions. Consequently, weak phosphorescence of Por4 in solution, accompanied by fluorescence, is significantly improved in SMILES. And Por4-SMILES nanoparticles were synthesized, emitting red phosphorescence with millisecond-range lifetimes.

Contrary to previous sections focusing on monitoring chromophores' triplet emission, Part III focuses on utilizing exciplex formation to prolong fluorophores' luminescence lifetimes. This charge-transfer transition was tracked by measuring solid samples with various molar ratios of CS and fluorophore (TPT), ultimately confirmed the long-lived excited state originating from the charge-transfer mechanism.

PART I

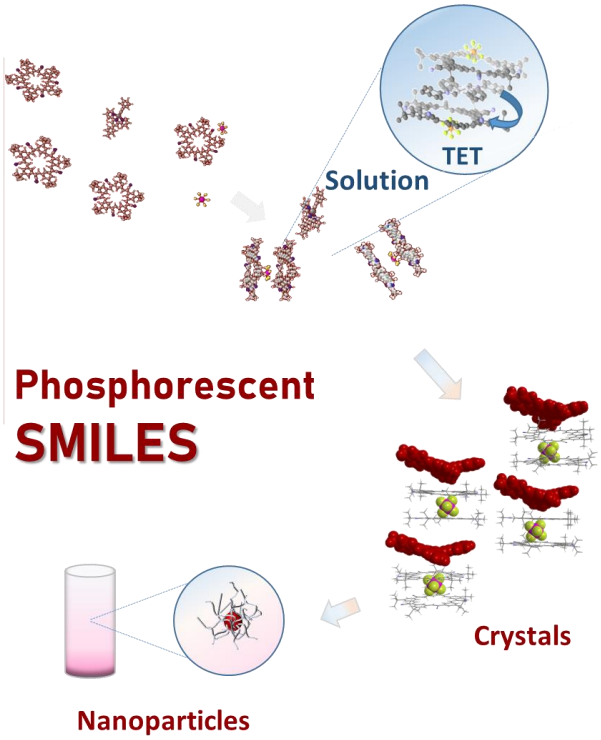
TET
Solution
Phosphorescent
SMILES
Crystals
Nanoparticles

Chapter 2

Exploring Triplet Energy Transfer in Cyanostar-Based Systems

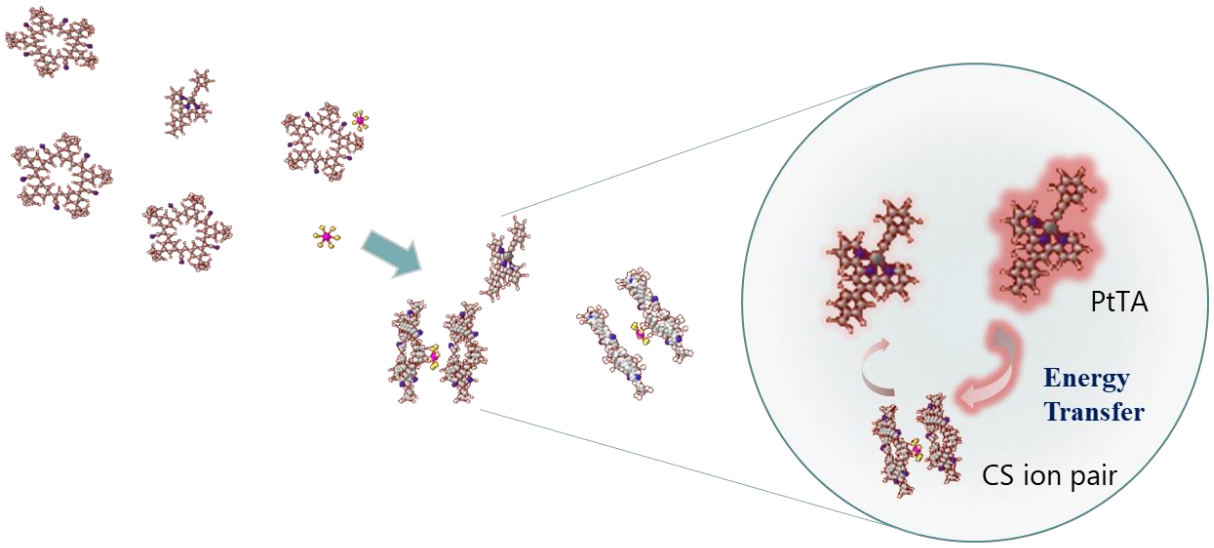

Chapter Acknowledgement

The Pt1 and Pt2 complexes were synthesized by Dr. Niels Bisballe, the Pt3 complex was synthesized by Marko H. Nowack in Prof. Bo W. Laursen group (University of Copenhagen). The cyanostar was synthezied in Prof. Amar H. Flood group (Indiana University). All Stern-Volmer titration experiments, spectroscopic measurements, and data analysis were conducted by Yang Wang at the University of Copenhagen. This chapter partially contributes to the publication *Triplet States of Cyanostar and Its Anion Complexes (DOI: 10.1021/acs.jpca.3c02701)*

2.1 Background and Motivation

The recent discovery of *small-molecule ionic isolation lattices* (SMILES) presents a promising strategy to mitigate the coupling of fluorescent dyes in close contact,[1] this breakthrough has enabled the creation of fluorescent materials with significantly enhanced fluorescence brightness. While dense packing of chromophores often induces exciton coupling, leading to deterioration in the properties of singlet (S) states, it typically doesn't alter chromophores' triplet states. Therefore to generate phosphorescent SMILES materials, an in-depth understanding of triplet state energies of SMILES before and after being transformed into high-density solids is highly required.

To address this issue, Frederik and his colleagues conducted fundamental investigations into the T_1 energy of cyanostar (CS), a crucial component in the SMILES approach.[70] They employed experimental and theoretical methods, utilizing a series of phosphorescent dyes as triplet energy donors to facilitate a dynamic triplet energy transfer (TET) process to the energy acceptor, cyanostar.[71, 72] The efficiency of this energy transfer, represented by the rate constant k_{TET}, was found to be strongly influenced by the energy difference between the triplet excited state of the donor ($E_{T\text{-}D}$) and the acceptor-cyanostar ($E_{T\text{-}A}$). If $E_{T\text{-}D} > E_{T\text{-}A}$, a large k_{TET} approaches the diffusion limit rate k_{diff}, signifying highly efficient triplet energy transfer and consequent quenching of the triplet energy donor's emission. Conversely, if $E_{T\text{-}A} > E_{T\text{-}D}$, k_{TET} decreases exponentially, resulting in less quenching of the donor's emission. These findings underscore the significance of the T_1 energy of cyanostar (2.0 eV) as a crucial guideline for designing SMILES materials, when aimed at sustaining phosphorescence emission in SMILES.

Following this preliminary research, this chapter validates the energy-matching principle derived from the T_1 energy of cyanostar (2.0 eV). To this end, a series of phosphorescent dyes, *Platinum(II) terpyridyl acetylide* (PtTA) complexes were selected, which possess triplet energies spanning the expected triplet state energy of cyanostar (Scheme 2.1). Through Stern-Volmer experiments, the chapter examines the triplet energy transfer process. These chosen dyes are mono-cationic and possess planar structures, indicating their potential to form the characteristic charge-by-charge stacking structure of SMILES. Thus, in addition to investigating bimolecular interactions, this chapter establishes fundamental guidelines for subsequent chapters focusing on phosphorescent SMILES solid emitters.

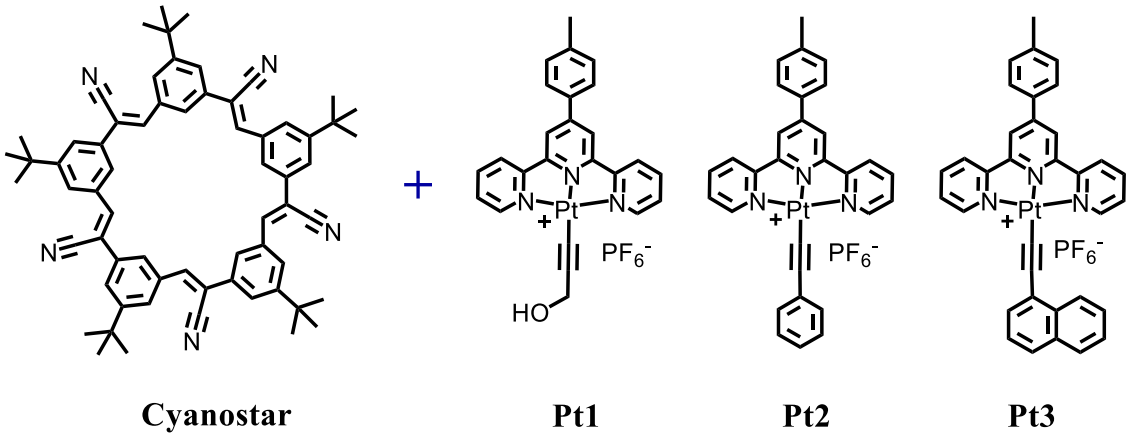

Cyanostar **Pt1** **Pt2** **Pt3**

Scheme 2.1. Chemical structure of CS and three PtTA complexes: Pt1, Pt2, and Pt3

2.2 Photophysical Properties of PtTA Complexes

Prior to delving into the bimolecular interactions between cyanostar and PtTA complexes, it is important to conduct fundamental investigations into the excited state emission of PtTA complexes. These investigations encompass a study of basic photophysical properties and comparisons of excited states, detailed in the subsequent sections.

2.2.1 Basic Photophysical Properties

The hydroxylacetylide complex (**Pt1**), phenylacetylide complex (**Pt2**), and naphthylacetylide complex (**Pt3**) were synthesized according to the method described in Appendix §1.4.[73, 74] Spectroscopic characterizations revealed significant medium effects on the photophysical properties of PtTA complexes. Factors such as chromophore solubility, quenching, and solvatochromism phenomena were observed to readily distort the steady-state and time-resolved photophysical properties of each PtTA complex.[75-77] Therefore, the first step is to choose the best medium for investigating the PtTA complexes. Overlay spectra of steady-state measurements and time-resolved decay curves for each PtTA complex in different organic solvents are presented in Figure 2.1.

In general, the most accurate reproduction of photophysical properties for all PtTA complexes is observed in dichloromethane (DCM). In DCM, the absorption, emission, and excitation spectra are clearly showcased, with the lowest absorption band and excitation curve overlapping, indicating a mono-chromophoric system.

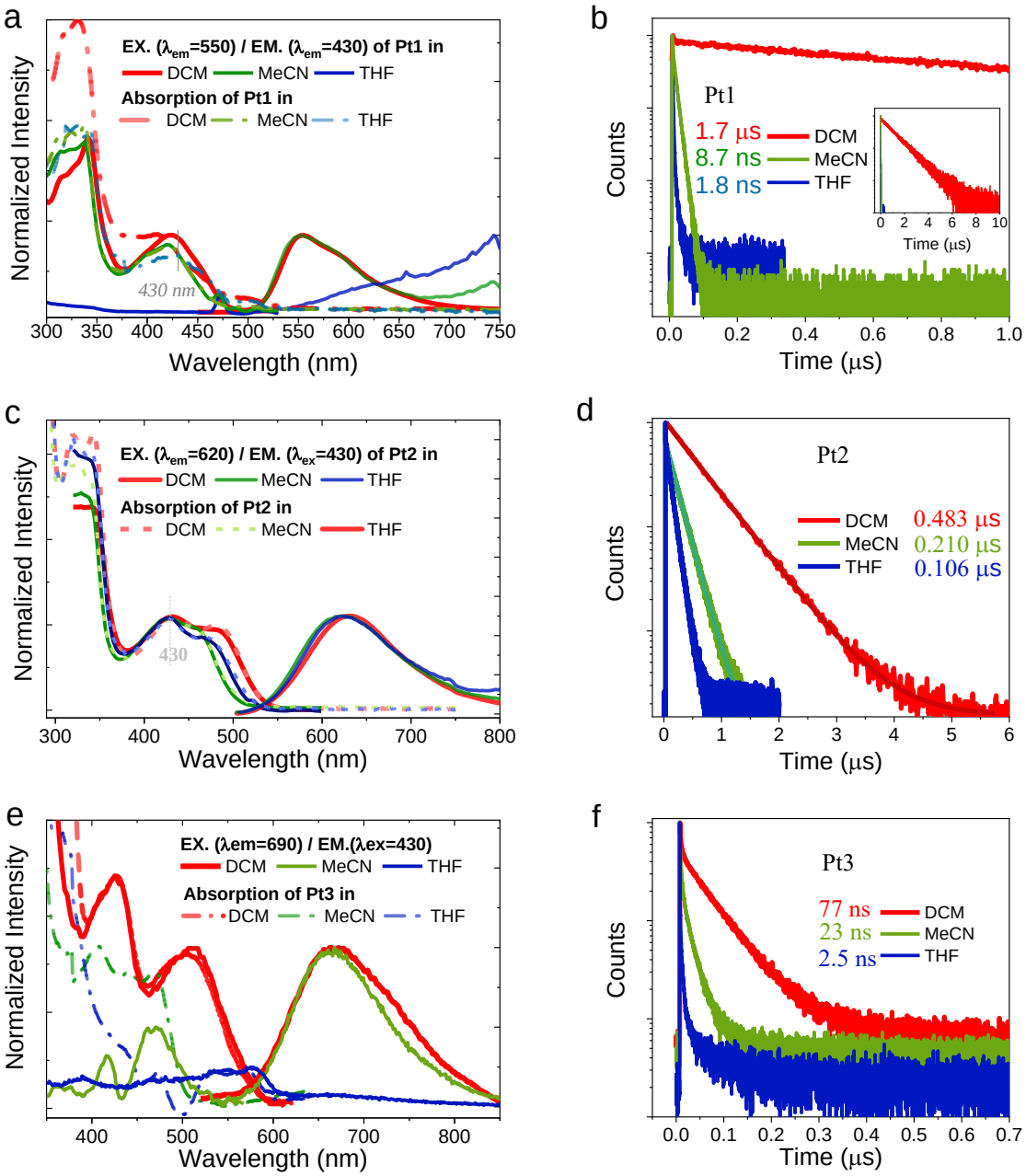

Figure 2.1. (a, c ,e) Steady state photophysical properties (absorption, emission and excitation) of Pt1, Pt2 and Pt3 in DCM, MeCN and THF (10 μM), respectively. Emission spectra were obtained at λ_{ex}=430 nm, excitation spectra were obtained at λ_{ex}=550 nm, 620 nm and 690 nm, respectively. (b, d, f) Time resolved decay curves of Pt1, Pt2 and Pt3 in different optically diluted organic solutions (DCM, MeCN and THF, 10 μM), excitation was λ_{ex}=450 nm, detector was set at λ_{em}=550 nm (Pt1), 620 nm (Pt2) and 690 nm (Pt3), respectively

However, this phenomenon is only observed in DCM for all three PtTA complexes. In acetonitrile (MeCN), although the solubility of PtTA complexes is acceptable, the absorption and excitation spectra are distorted, and accompanied with quenched decay lifetimes compared to the DCM solutions. Additionally, tetrahydrofuran (THF) proves to be a poor solvent for all three PtTA complexes, resulting in weak emission and ineffective reproduction of photophysical properties. Thus all PtTA complexes have the longest decay lifetime in DCM, as supported by Figure 2.1-b,d,f. Consequently, DCM will be utilized as the solvent to dissolve PtTA complexes for subsequent experiments.

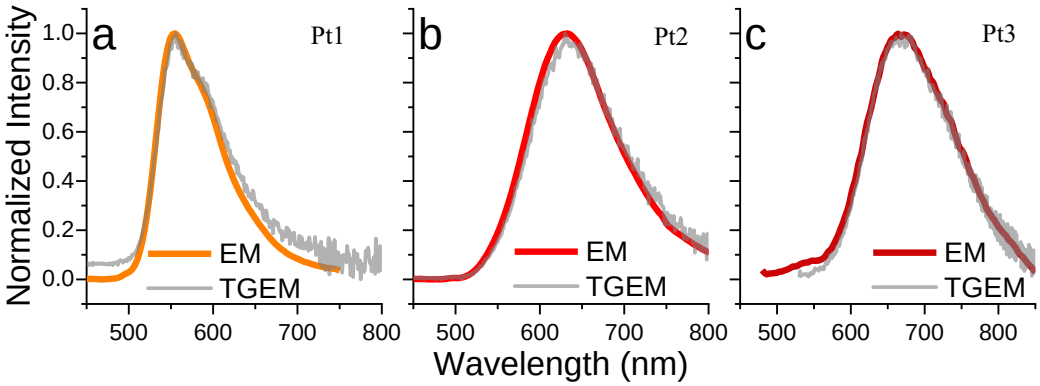

Figure 2.2. Steady-state emission spectra and time-gated (TG=5 μs) emission spectra of (a) Pt1, (b) Pt2 and (c) Pt3 in optically diluted DCM solution (10 μM, 298 K), though signals from Pt2 and Pt3 were very weak.

In addition to the medium effect,[77] the basic photophysical properties of the three PtTA complexes can be observed in DCM solutions in Figure 2.1. Under 430 nm ultraviolet light, the emission maxima for Pt1, Pt2, and Pt3 are located at 555 nm, 633 nm, and 678 nm, respectively. All PtTA complexes exhibit the longest lifetime in DCM: Pt1 (1.7 μs), Pt2 (0.48 μs), and Pt3 (0.077 μs), with almost monoexponential decay shapes. Time-gated emission spectra in Figure 2.2 further confirm the phosphorescent origins for each PtTA complex, as the weak emission collected after a 5 μs time-gate upon cessation of laser illumination overlaps well with the normal steady-state emission.

Dominated by intramolecular charge transfer processes, planar Pt(II) terpyridine chromophores have been shown to undergo significant modulation of photoluminescence by systematically tuning structural fragments,[78] including the metal center and ancillary ligands.[76, 79, 80] Through changes in the acetylide ancillary ligand, the emission of PtTA complexes was successfully tuned

from 555 nm (Pt1) to 690 nm (Pt3). The electron density of the acetylide ligand, increasing from hydroxylacetylide to naphthylacetylide, directly influences the optical transitions, as evidenced by differences in the lowest absorption band (Figure 2.3-a), which reflect the changes of ground state electronic properties among the three PtTA complexes.[81-83]

Previous research has demonstrated that for PtTA complexes, the highest occupied molecular orbital (HOMO) is mainly contributed by metal and acetylide orbitals, while the lowest unoccupied molecular orbital (LUMO) is extensively influenced by terpyridine localized orbitals.[81] Therefore, the absorption of PtTA complexes under ambient conditions displays low-energy absorption bands originating from Pt(II) metal to ligands charge transfer (MLCT) transitions.[74] The potential of metal-centered oxidation may also be sensitive to the nature of acetylide ligands, with higher σ-donor strength resulting in more negative ligand oxidation potentials for the metal center.[84] Consequently, a more red-shifted absorption band is observed in Figure 2.3-a, as the acetylide ligand changes from hydroxide (Pt1) to naphthalene (Pt3).

In general, effective modulation of the three PtTA complexes absorption, phosphorescence emission and lifetime were achieved by appropriately altering the acetylide ancillary ligands.

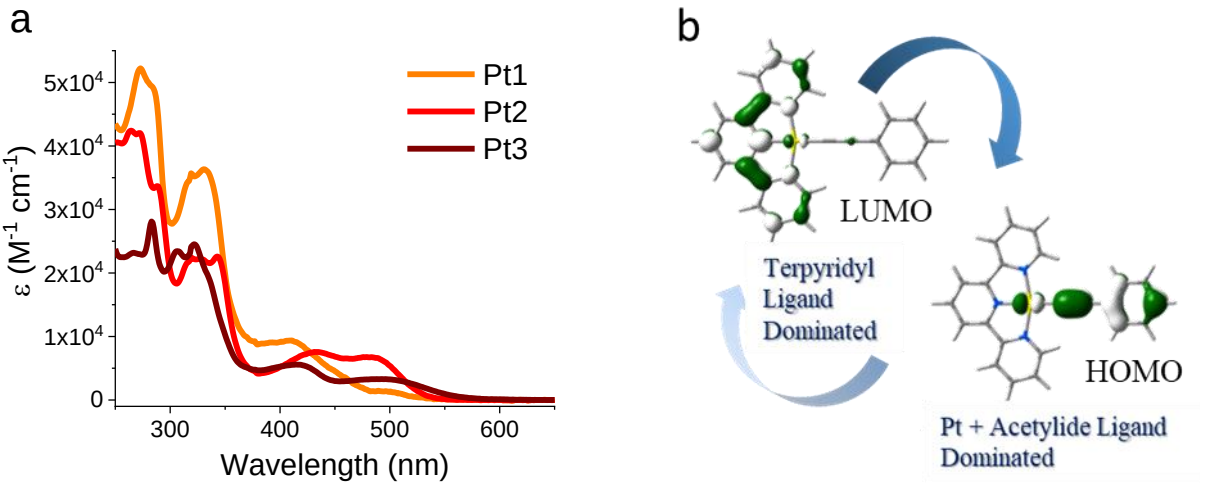

Figure 2.3. (a) Absorption spectra of PtTA complexes showing the absorption coefficient values, in optically diluted DCM solutions. (b) Illustration of photoexcited state of Pt2 analogue between terpyridyl ligand dominated (LLCT) and Pt-acetylide ligand dominated (MLCT) conditions.

2.2.2 Excited State of PtTA Complexes

In addition to confirming the successful modulation of the optical properties of PtTA complexes, understanding the triplet excited state of each complex is crucial for further investigations. Cryogenic conditions were employed to inhibit molecular relaxation and probe the triplet emissions. However, as depicted in Figure 2.4, all three PtTA complexes exhibit similar emission spectra, suggesting closely positioned lowest unoccupied molecular orbitals (LUMO) and similar optical transitions when solvent effects and dissipation influences are restricted. This indicates the predominant contribution from the terpyridine ligand,[83, 84] making it challenging to effectively determine the triplet excited state of different PtTA complexes using frozen media alone, as it stems from a complicated intramolecular charge-transfer process.[85]

Instead, the triplet energies of the PtTA complexes were determined from their phosphorescence spectra,[70] as shown in Figure 2.1. Typically, the peak of the highest energy phosphorescence band is used as an estimate for the triplet energy.

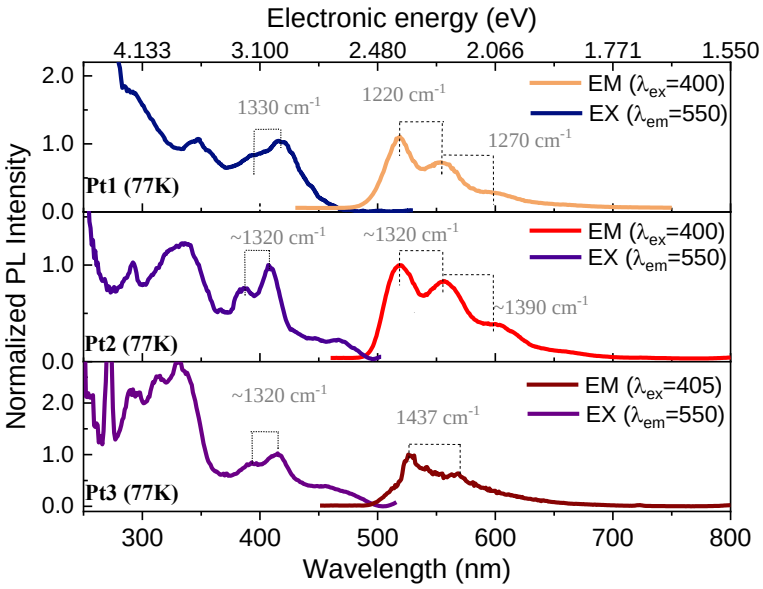

Figure 2.4. Steady-state emission and excitation curves for Pt1, Pt2, and Pt3 in glassy propylene glycol (in liquid nitrogen, 77K). PtTA complexes were dissolved in DCM at first and then mixed with propylene glycol in a volume ratio of DCM/PG = 5/95 vol%.

However, for PtTA complexes with broad and unstructured phosphorescence spectra, the triplet energy levels were estimated from the phosphorescence onset wavelength (80% of maxima). This method is based on previous theoretical calculations and empirical tests on a Pt2 analog system.[73, 86] The triplet energy levels were determined to be $E_{T\text{-}Pt1}$ = 2.30 eV, $E_{T\text{-}Pt2}$ = 2.07 eV, and $E_{T\text{-}Pt3}$ = 1.92 eV, corresponding to the phosphorescence onset wavelengths of 540 nm for Pt1, 600 nm for Pt2, and 646 nm for Pt3.

2.3 Molecular Interactions and Triplet Energy Transfer

2.3.1 Photophysical Properties of PtTA[CS_2PF_6]

With the success in the modulation of PtTA phosphorescent emission, we step to investigating molecular interactions between CS and PtTA. In Figure 2.5, the addition of two molar equivalents of CS did not significantly alter the emission shape or maxima position of the PtTA complexes. The identical MLCT absorption bands are highly overlapped with excitation curves, which indicates the maintenance of mono-chromophoric systems.

This implies that photoexcitation and emission are originated from PtTA complexes, rather than from dimers, ion pairs with CS or other impurities, thus demonstrating a high-fidelity reproduction of optical performances stemming from PtTA complexes in PtTA[CS_2PF_6] solutions.

However, noticeable quenching effects were observed, as evidenced in Figure 2.5 (a) and (b) for Pt1[CS_2PF_6] and Pt2[CS_2PF_6].

Hence, a systematic investigation into the molecular interaction mechanism between CS and PtTA complexes is needed.

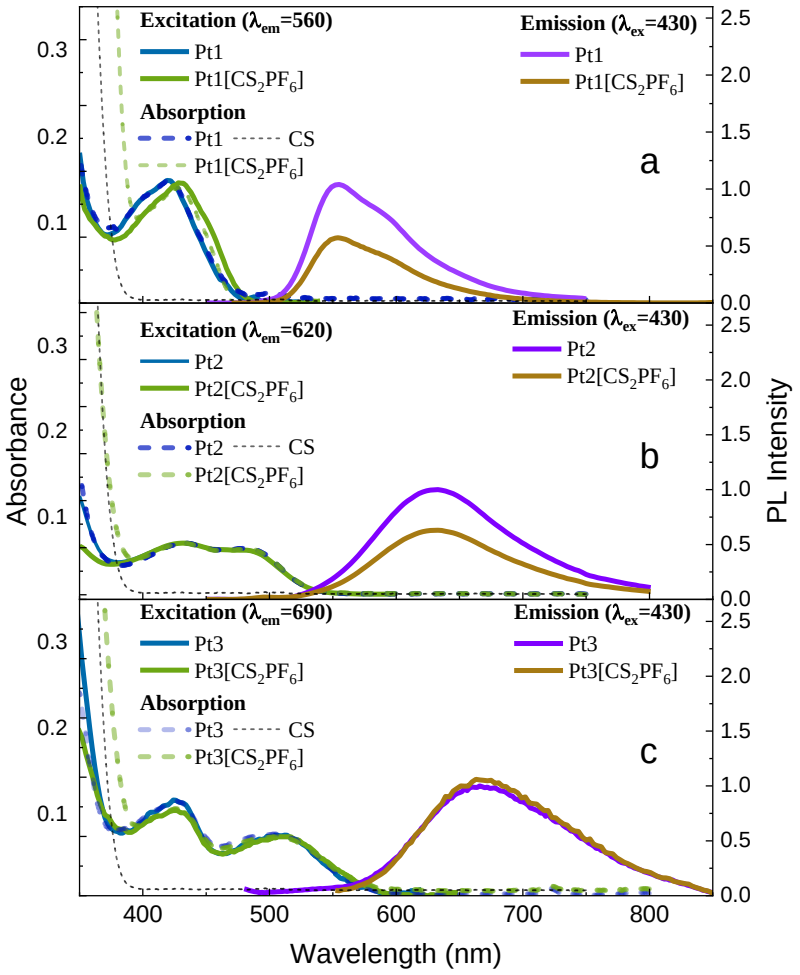

Figure 2.5. Steady state (emission, excitation and absorption) of (a) Pt1 and Pt1[CS_2PF_6] , (b) Pt2 and Pt2[CS_2PF_6] and (c) Pt3 and Pt3[CS_2PF_6] (10 μM, DCM, 298 K). Absorption and excitation curves are normalized to compare the overlap. Steady state emission are also normalized in proportional to the original intensity ratio .

2.3.2 Stern-Volmer Plots

Stern-Volmer experiments were conducted for each PtTA complex with varying concentrations of tetrabutylammonium-cyanostar (TBA[CS_2PF_6]).[25, 70] As illustrated in Figure 2.6 and Figure 2.7, steady-state spectra, decay curves, and absorption curves demonstrate quenching of lifetime and relative QY (absorption-normalized PL intensity). These parameters were plotted on the same Stern-Volmer graph in Figure 2.8. For Pt1 (Figure 2.8-a) and Pt2 (Figure 2.8-b), both plots exhibit close overlap with long-range linearity and similar slopes. However, the Stern-Volmer plots for Pt3 (Figure 2.8-c) show a less pronounced changing tendency. The bimolecular quenching constants (k_q) for both reacting pairs **Pt1**[CS_2PF_6]-TBA[CS_2PF_6] and **Pt2**[CS_2PF_6]-TBA[CS_2PF_6] were calculated using the Stern-Volmer equation:

$$\frac{\tau_0}{\tau} = \frac{I_0}{I} = 1 + k_q \tau_0 [Q] \tag{2-1}$$

where τ_0 and τ represent luminescent lifetimes without and with the presence of the quencher, respectively, while I_0 and I denote luminescent intensities without and with the presence of the quencher. The diffusional quenching constant is represented by k_q, and [Q] indicates the concentration of the quencher. In this report, the values of I_0 and I were calibrated using the corresponding absorbance value at the excitation wavelength.[14, 15]

The k_q for τ_0/τ and I_0/I are equivalently presented for both **Pt1**[CS_2PF_6]-TBA[CS_2PF_6] and **Pt2**[CS_2PF_6]-TBA[CS_2PF_6] systems, indicating a dynamic quenching feature. Thereby the bimolecular quenching constant k_q for **Pt1**[CS_2PF_6]-TBA[CS_2PF_6] and **Pt2**[CS_2PF_6]-TBA[CS_2PF_6] are 9×10^9 $M^{-1} \bullet s^{-1}$ and 1×10^{10} $M^{-1} \bullet s^{-1}$, respectively.

Previous studies on energy transfer reactions to CS have provided robust confirmation of the origins of triplet-triplet energy transfer.[70] Therefore, in this case, the quenching constant k_q can be regarded as the triplet energy transfer constant k_{TET}, as the triplet-triplet energy transfer requires actual collisions in the form of Dexter exchange.[71] Additionally, a higher triplet excitation energy of the donor is required. As demonstrated by Fredrik and co-workers' research,[70] the triplet energy of the $[CS_2PF_6]^-$ complex is 2.0 eV. Therefore, the triplet energies of Pt1 (2.30 eV) and Pt2 (2.07 eV) both meet the exothermic TET requirement, hereby lead to k_{TET} approaching the diffusion-limited rate $k_{diff} = 1 \times 10^{10}$ $M^{-1} \bullet s^{-1}$.[15, 25]

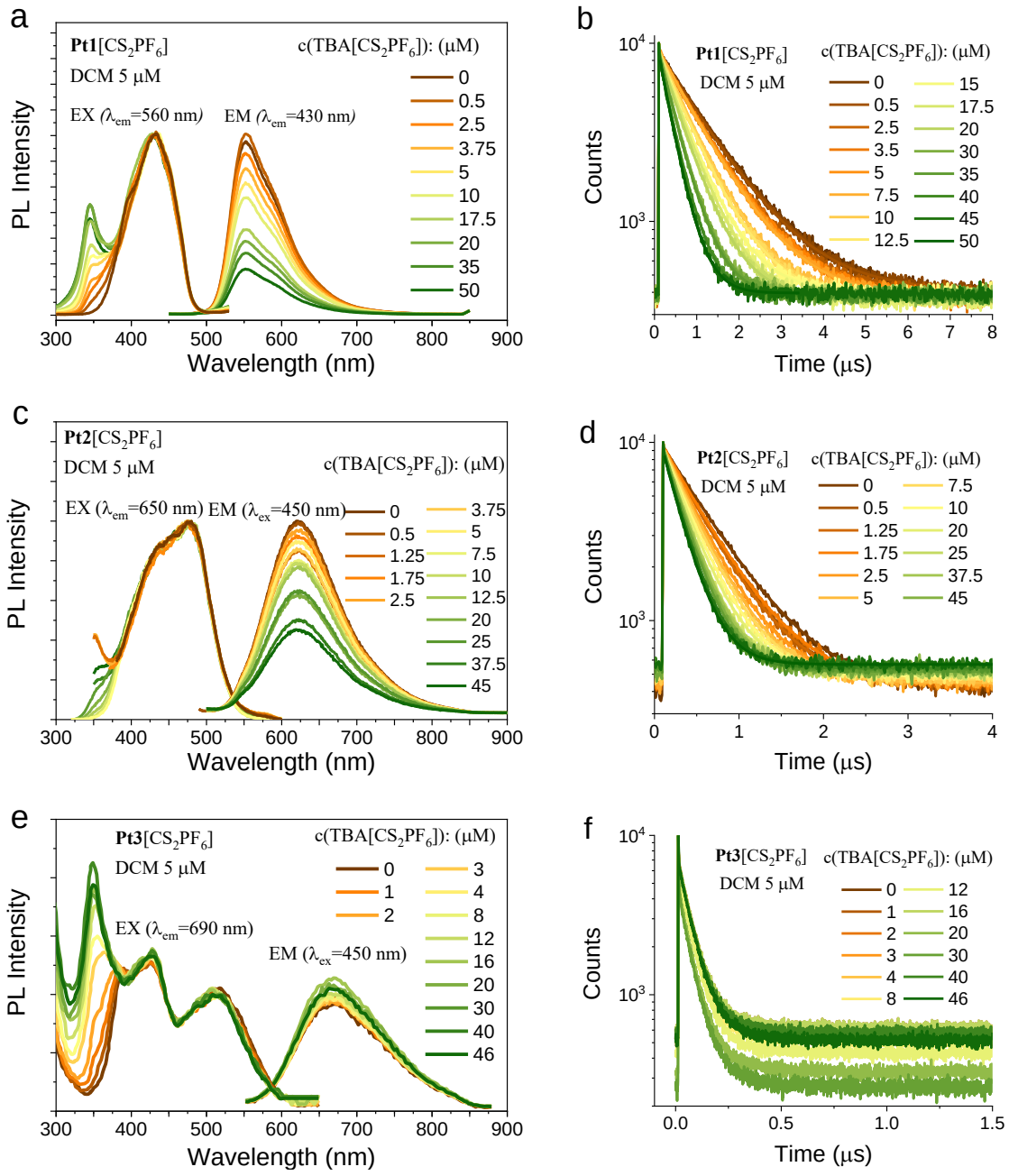

Figure 2.6. Steady state optical spectra and TCSPC decay curves for Stern-Volmer titration experiments of (a, b) **Pt1**[CS_2PF_6]-TBA[CS_2PF_6], (c, d) **Pt2**[CS_2PF_6]-TBA[CS_2PF_6] and (e, f) **Pt3**[CS_2PF_6]-TBA[CS_2PF_6]. The concentration of PtTA[CS_2PF_6] was fixed at 5 µM in DCM, different concentrations of TBA[CS_2PF_6] were added separately. Instrumental setup for decay curves was: λ_{ex}=450 nm λ_{em}=560 nm for **Pt1**[CS_2PF_6]-TBA[CS_2PF_6] in (b), λ_{ex}=450 nm λ_{em}=620 nm for **Pt2**[CS_2PF_6]-TBA[CS_2PF_6] in (d), λ_{ex}=450 nm λ_{em}=690 nm for **Pt3**[CS_2PF_6]-TBA[CS_2PF_6] in (f).

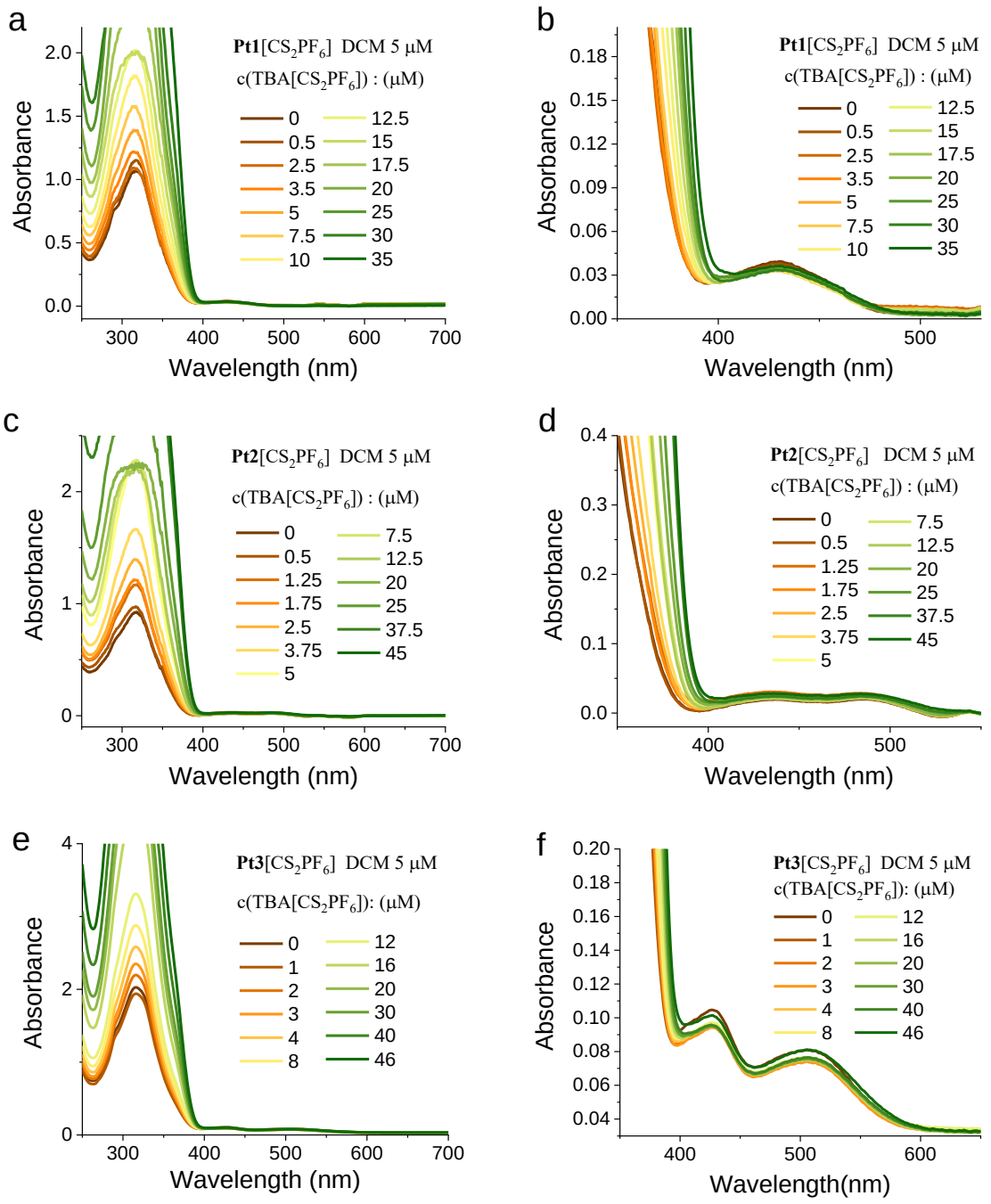

Figure 2.7. Absorption curves for Stern-Volmer titration experiments of (a, b) **Pt1**[CS_2PF_6]-TBA[CS_2PF_6], (c, d) **Pt2**[CS_2PF_6]-TBA[CS_2PF_6] and (e, f) **Pt3**[CS_2PF_6]-TBA[CS_2PF_6], The concentration of PtTA[CS_2PF_6] was fixed at 5 μM in DCM.

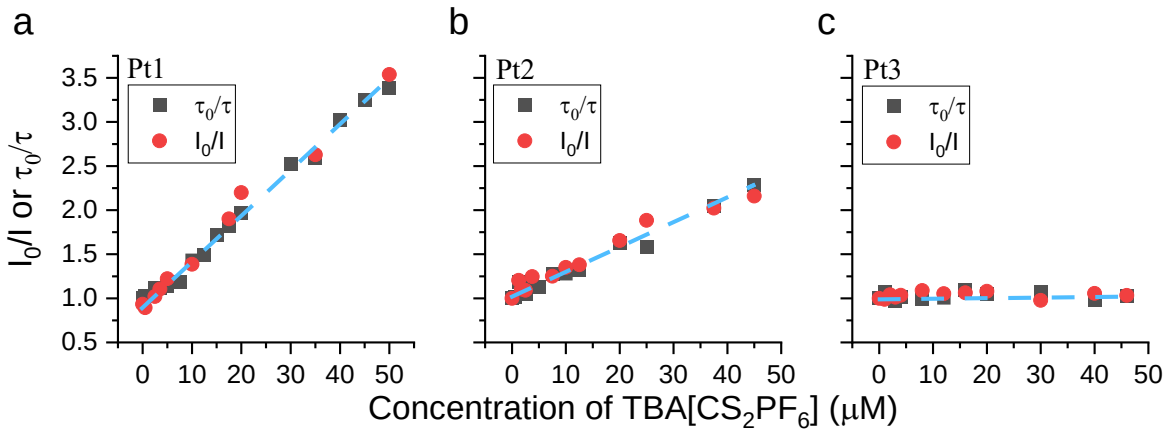

Figure 2.8. Stern-Volmer plots (lifetime and emission intensity) for PtTA: (a)-**Pt1**, (b)-**Pt2** and (c)-**Pt3** (5 μM in DCM) as the function of increasing concentration of TBA[CS_2PF_6] at room temperature. Emission intensities were normalized with respect to the absorbance at the excitation wavelength.

Different to **Pt1**[CS_2PF_6]-TBA[CS_2PF_6] and **Pt2**[CS_2PF_6]-TBA[CS_2PF_6], **Pt3**[CS_2PF_6]-TBA[CS_2PF_6] shows a relatively unchanged tendency. This observation suggests that the triplet energy transfer process is less efficient from the triplet state of Pt3 (1.92 eV) to that of [CS_2PF_6]$^-$ (2.0 eV), which is in agreement to the exothermic nature of triplet energy transfer.[14]

The comparisons among three Stern-Volmer quenching systems provide important insight on comprehending energy transfer from phosphorescent PtTA to cyanostar. Moreover, they potentially benchmark a pathway for selectively avoid transferring triplet energy to cyanostar.

Table 2.1. Fitted linear functions from Stern-Volmer plots of PtTA[CS_2PF_6]-TBA[CS_2PF_6]

Sample	Fitted Function		R-square (COD)	k_q ($M^{-1}s^{-1}$)
Pt1[CS_2PF_6]-TBA[CS_2PF_6]	τ_0/τ	y=0.942+0.050 × x	0.9937	8.55E+09
	I_0/I	y=0.931+0.052 × x	0.9882	8.89E+09
Pt2[CS_2PF_6]-TBA[CS_2PF_6]	τ_0/τ	y=1.028+0.027 × x	0.9779	1.06E+10
	I_0/I	y=1.092+0.026 × x	0.9644	1.02E+10
Pt3[CS_2PF_6]-TBA[CS_2PF_6]	τ_0/τ	y=1.021+0.00025 × x	0.0108	---
	I_0/I	y=1.031+0.00031 × x	0.0187	---

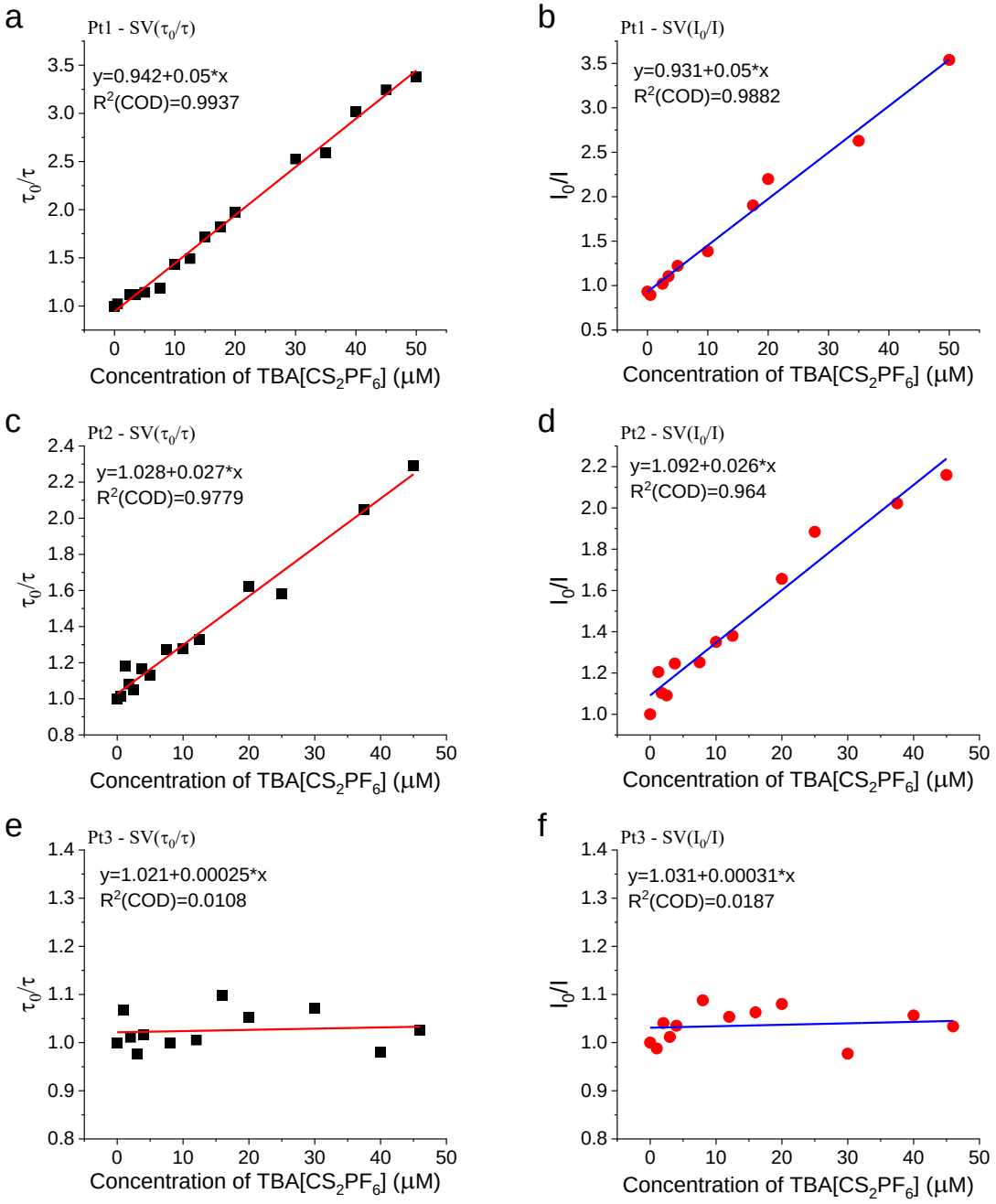

Figure 2.9. Fitted lines for Stern-Volmer quenching plots of PtTA[CS_2PF_6]-TBA[CS_2PF_6] systems.

2.4 Conclusions

In this chapter, we delved into the molecular interactions between cyanostar and phosphorescent chromophores (PtTA) through Stern-Volmer quenching experiments, which support previous investigations on CS triplet state energy and thus elucidate a selection rule for choosing phosphorescent dyes to sustain phosphorescence in SMILES structures.

Our findings from the Stern-Volmer titration experiments revealed that efficient triplet energy transfer from phosphorescent dyes to CS occurs when the triplet state energy level of the dye surpasses that of CS ($E_{T\text{-}dye} > E_{T\text{-}CS}$). Conversely, when $E_{T\text{-}dye} < E_{T\text{-}CS}$, a less efficient triplet energy transfer process is observed. These findings suggest that the alterations in quenched emission were primarily attributed to triplet energy transfer processes. Ultimately, to minimize the loss of phosphorescent emission due to energy transfer to CS, it is advisable to choose chromophores with triplet state energy levels presumed to be lower than 2.0 eV.

Chapter 3

Selectively Restoring Phosphorescence in PtTA-SMILES

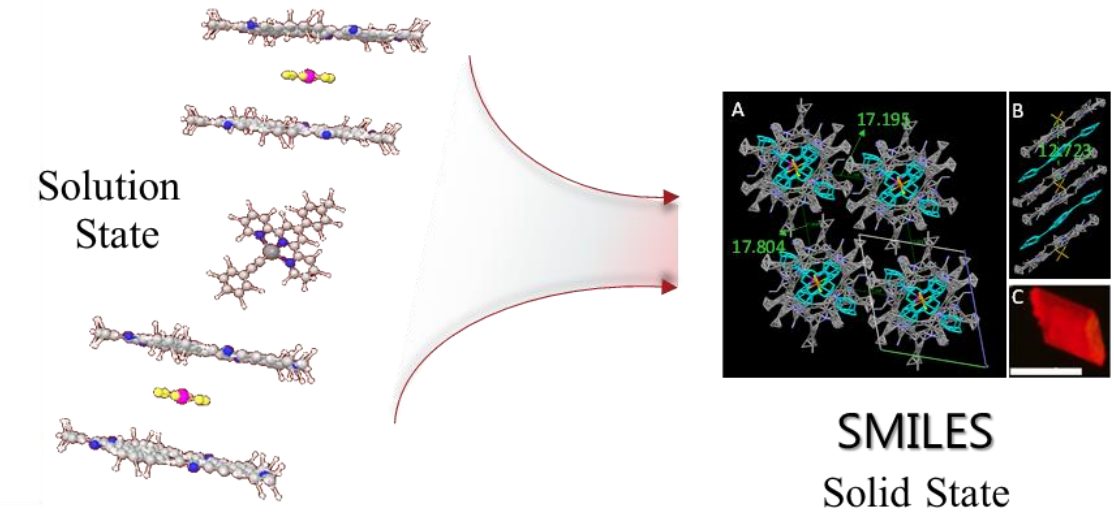

Chapter Acknowledgement

The PtTA complexes were synthesized by Dr. Niels Bisballe and Marko H. Nowack in Prof. Bo W. Laursen group (University of Copenhagen). The cyanostar was synthezied in Prof. Amar H. Flood group (Indiana University). All crystalline and nanoparticles synthesis, spectroscopic measurements, and data analysis were conducted by Yang Wang at the University of Copenhagen. This chapter contributes to the publication manuscript: *Turning on Molecular Phosphorescence in Materials by Supramolecular Organization in Small-Molecule Ionic Isolation Lattices*.

3.1 Motivation for Phosphorescent PtTA-SMILES Solids

With the foundational investigations into the bimolecular interactions between cyanostar and PtTA complexes, in this chapter, the primary focus lies on examining the guiding principle for selectively avoiding the transfer of triplet energy to cyanostar in solid-state SMILES. The experiments aim to prove that phosphorescence can be sustained by utilizing phosphorescent dyes whose triplet state energy is lower than 2.0 eV - the triplet state energy of cyanostar. Therefore, in this chapter, three PtTA complexes were employed to generate PtTA-SMILES solid emitters and to assess the potential triplet energy transfer, as illustrated in Scheme 3.1. Additionally, the formation of phosphorescent SMILES was tracked by measuring solid samples with different molar ratios of PtTA and cyanostar, thus to understand the deactivation pathways in phosphorescent SMILES and hereby to explore the phosphorescence emission in SMILES solids.

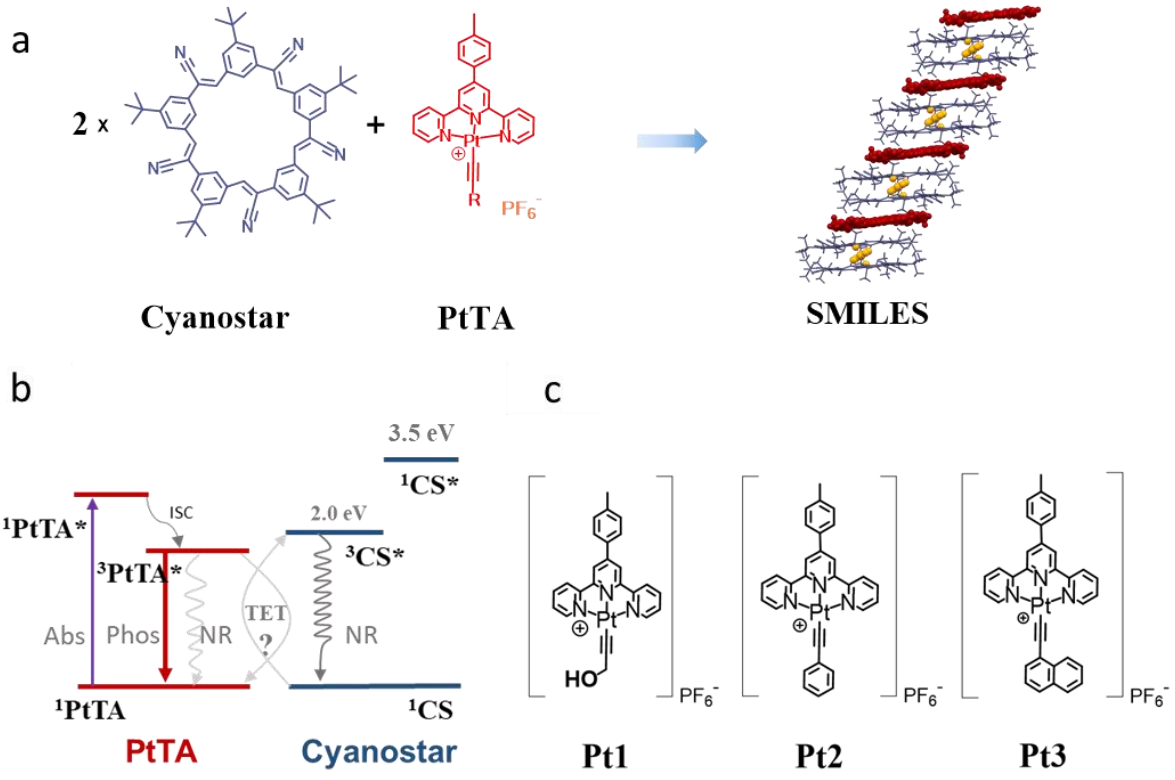

Scheme 3.1. (a) Illustration of the formation and structure of SMILES, 2:1 anion complexes are formed from CS and PF_6^- ions that in solids packs alternating with the planar PtTA dyes. (b) Relative energy state of cyanostar and sensitization of the CS triplet state via triplet energy transfer (TET) in the format of Dexter exchange. (c) Molecular structures of three PtTA compounds: **Pt1**, **Pt2** and **Pt3**.

3.2 Characterizations on PtTA-SMILES Crystals

3.2.1 Preparation of PtTA-SMILES Crystals

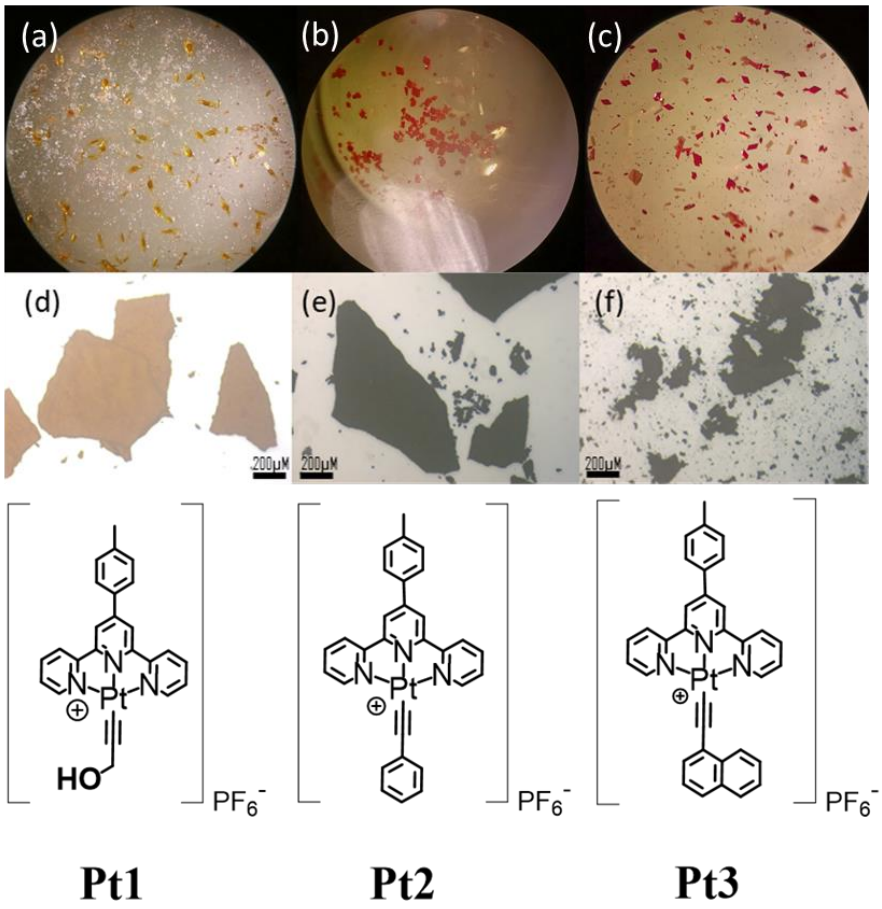

Figure 3.1. Micrographs of crystals under microscope for (a) **Pt1**-SMILES, (b) **Pt2**-SMILES and (c) **Pt3**-SMILES. Powders (neat aggregates) for (d) Pt1, (e) Pt2, (f) Pt3 under microscope (excitation resource: white light, scale bar: 200 μm). Chemical structures of each PtTA complex are also listed below.

To confirm the spatial isolated chromophore structure in the SMILES solids, single crystal structures of all three PtTA-SMILES materials were prepared (Figure 3.1). A notable difference in color was observed for PtTA-SMILES crystals, especially when compared to the neat aggregates of the corresponding PtTA complex. The **Pt1**-SMILES crystal exhibits a yellow color, resembling the orange color of Pt1 neat aggregates. In contrast, as both Pt2 and Pt3 neat aggregates appear as brownish powder, Pt2-SMILES crystals are bright red, and Pt3-SMILES crystals appear as dark red color.

The single crystal XRD analyses revealed the characteristic charge-by-charge stacking structure in PtTA-SMILES crystals (Figure 3.2). Notably, the crystal structure of Pt2-SMILES exhibited alternating intercalated stacking arrangements. This charge-by-charge packing of cationic Pt2 chromophore with $[CS_2PF_6]^-$ complex mirrored previous findings on fluorescent SMILES crystal structures,[1] indicating a unified alternative stacking structure for PtTA-SMILES materials. Moreover, the intermolecular distances between Pt2 molecules were sufficiently large to facilitate efficient spatial isolation between dyes and minimize potential exciton coupling. Similar conclusions are expected to be drawn for **Pt1**-SMILES and **Pt3**-SMILES single crystals, pending further crystallography analysis from collaborators.

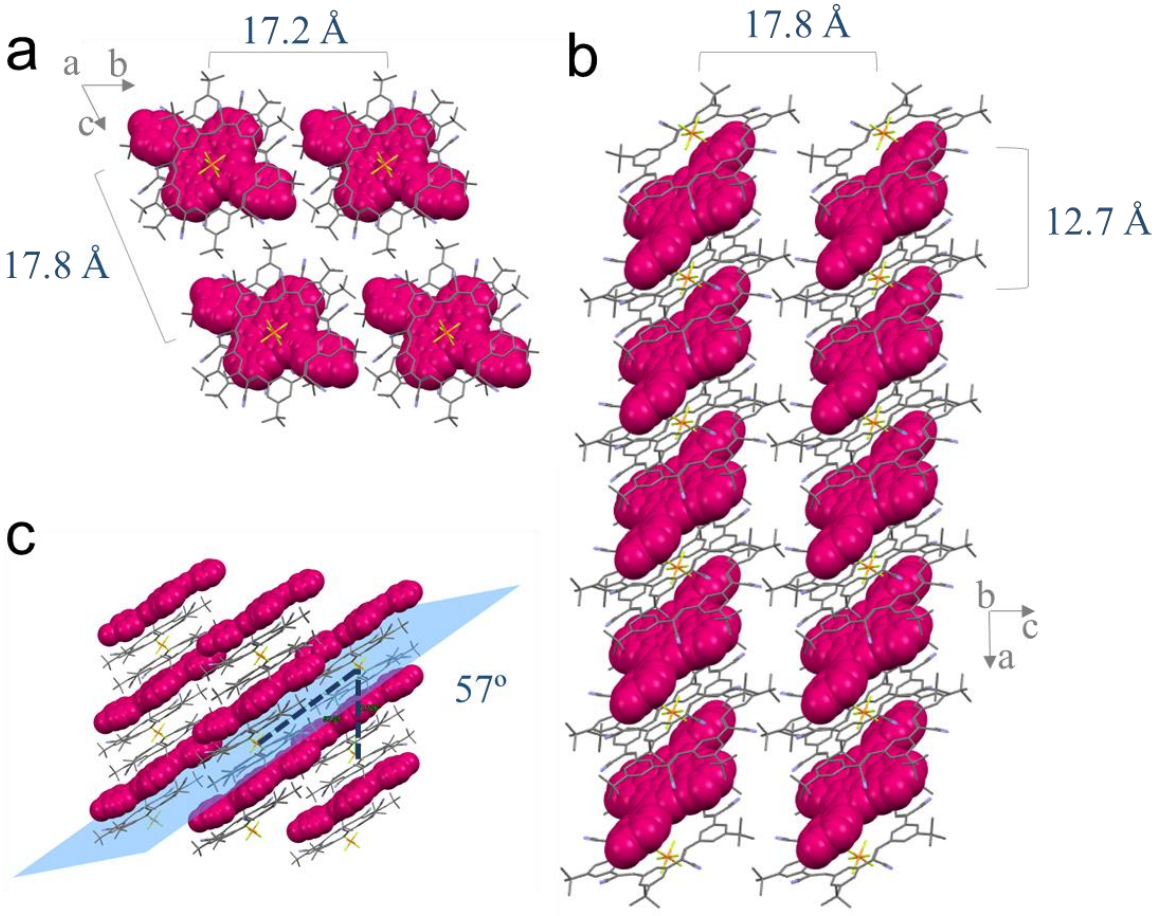

Figure 3.2. Molecular packing in **Pt2•CS_2PF_6** SMILES crystal based on single crystal XRD characterizations, The unit is Ångstroms for numbers in a and b. the **Pt2** cation is shown in red space filling mode and $CS_2PF_6^-$ as stick structure mode.

3.2.2 Photophysical Properties of PtTA Solids

One of the fundamental and essential applications of SMILES materials is to restore the emissive performances of dyes in densely packed aggregates, as observed in dilute solutions. For PtTA complexes, the triplet energy of chromophores' excited states undergoes different fates with CS in dilute solutions. To verify both the emission reinstatement and energy transfer process in SMILES solids, an investigation on PtTA-SMILES solids is of utmost importance for a conclusive confirmation of the phosphorescent SMILES strategy.

Figure 3.3 displays the steady-state and time-resolved measurements on PtTA-SMILES crystal samples. **Pt1**-SMILES exhibits weak luminescence, with the emission maximum closely matching that of Pt1 neat aggregates, rather than mimicking the solution state emission (Figure 3.3-a). However, for **Pt2**-SMILES and **Pt3**-SMILES, both crystals exhibit luminescence under a microscope, and also reproduce emission curves similar to the corresponding solution state emission (Figure 3.3-c, d), with emission maxima at 635 nm and 670 nm, respectively. Interestingly, both **Pt2**-SMILES and **Pt3**-SMILES crystals also demonstrate a narrower bandwidth (FWHM, full width at half maximum) in solid-state emission. The excitation spectra of all three SMILES show an apparent red-shifted band, which cannot be clearly assigned yet, although proposed explanations may include shifted MLCT transitions in tightly stacked lattices,[87] and size-dependent spectral deformations due to inner filter effects.[28]

Compared to neat aggregates, embedding Pt2 and Pt3 into SMILES evidently restores the intrinsic single molecular emission and improves the quantum yield (QY) and lifetime (Table 3.1 and Figure 3.3-f, g). Particularly for Pt3, the increase in QY and lifetime in SMILES is more than 10 times higher compared to the single molecular solution state. Therefore, we eventually obtained two emissive phosphorescent SMILES crystals: **Pt2**-SMILES (λ_{em} = 635 nm, Φ = 0.04, τ = 1.5 μs) and **Pt3**-SMILES (λ_{em} = 670 nm, Φ = 0.05, τ = 2.2 μs), whose photophysical properties surpass both the single molecular state and pure chromophoric aggregate properties.

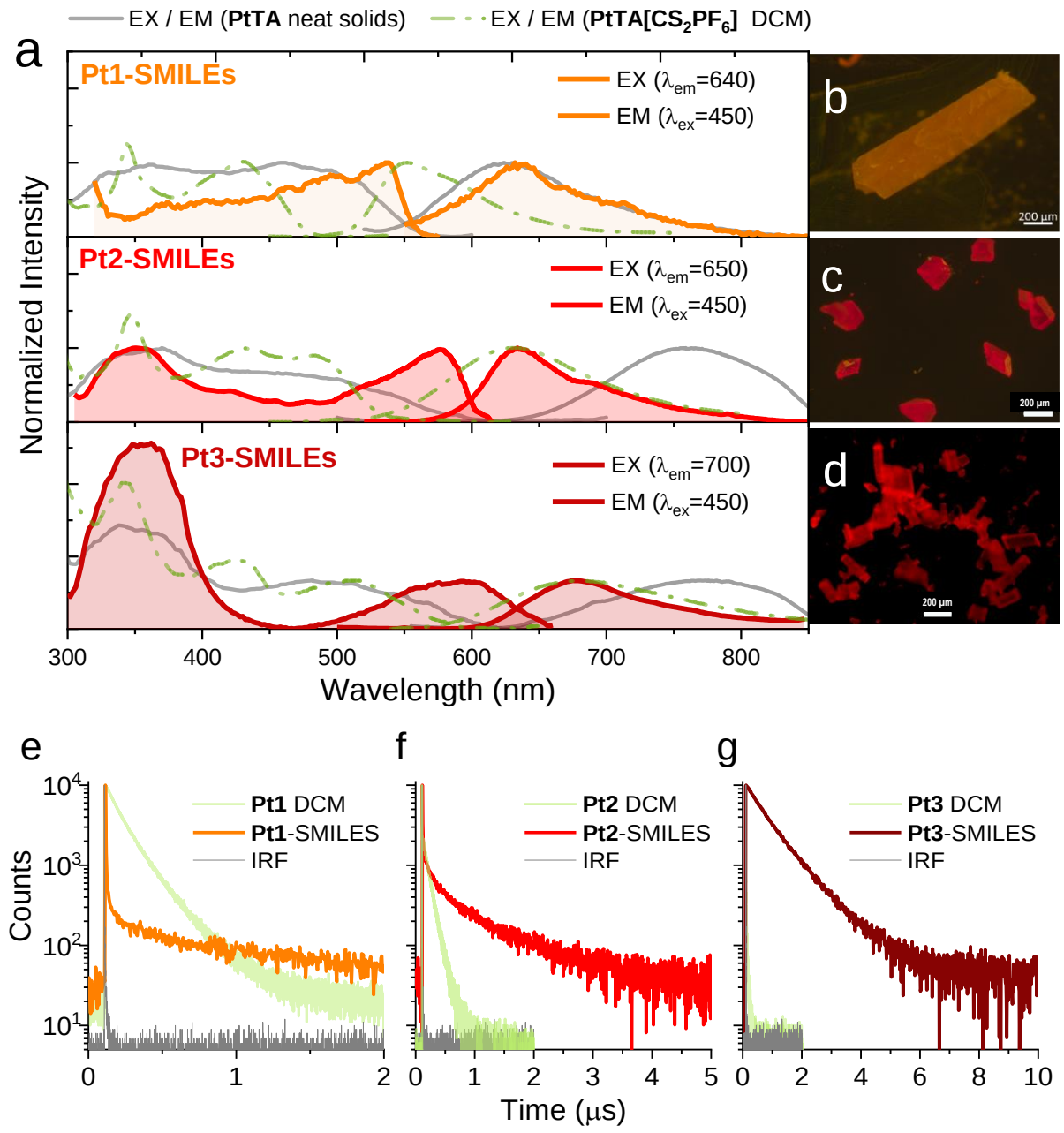

Figure 3.3. (a) Steady-state optical properties of PtTA-SMILES crystals in comparison with optical properties of PtTA in DCM solution and PtTA aggregates. Pictures of crystal (b) Pt1-SMILES, (c) Pt2-SMILES and (c) Pt3-SMILES under microscope by using 475 nm band pass filter for excitation and 510 nm long pass filter in the emission path. Decay curves of crystal (e) Pt1-SMILES, (f) Pt2-SMILES and (g) Pt3-SMILES in comparison with corresponding decay curves of PtTA in solution state. 532 nm long pass filter was used for decay curves characterizations in order to screen out scattering signals.

The radiative rate in SMILES crystals ($k_r \approx 3\times10^4$ s^{-1}) is identical to that of solutions, indicating that the improved quantum yields can be attributed to significantly reduced non-radiative rates $k_{nr} \approx 5\times10^5$ s^{-1} (**Pt2**-SMILES: 6.4×10^5 s^{-1} and **Pt3**-SMILES: 4.7×10^5 s^{-1}), as shown in Table 3.1.[88] This value thus serves as an upper limit on any triplet energy transfer (TET) process in SMILES of Pt2 and Pt3, potentially also for Pt1 even if the luminescence in Pt1-SMILES is difficult to be measured.

Considering that Pt2 triplet emisison in solution was quenched by $[CS_2PF_6]^-$ with a diffusion-limited rate of 9×10^9 M^{-1}s^{-1} , it suggests that the triplet state energy of $[CS_2PF_6]^-$ must be higher in the solid state than in solution, so that the phosphorescence emitted from Pt2 will not be efficiently quenched by $[CS_2PF_6]^-$ via triplet energy transfer in solids. This may be explained by the lowering of the effective triplet state energy of $[CS_2PF_6]^-$ in solution due to out-of-plane deformations, as investigated by preliminary calculations on the triplet state energy of cyanostar.[70] Thus, the upper threshold for triplet state energy of $[CS_2PF_6]^-$ complexes in solution lies between Pt2 and Pt3 ($E_{T,limit} \approx 2.0$ eV), but in SMILES solids, this threshold lies between Pt1 and Pt2 ($E_{T,limit} \approx 2.2$ eV), likely due to the structural confinement of CS in SMILES.

In summary, the spectroscopic measurements reinforce two key facts: 1) efficient triplet energy transfer and 2) effective emission reinstatement in PtTA-SMILES solids. The crucial determination of these differences lies in the triplet state energy ($E_{T\text{-}PtTA}$) of the PtTA complexes in comparison to $E_{T\text{-}CS}$. When $E_{T\text{-}PtTA} > E_{T\text{-}CS}$, as observed in Pt1, efficient triplet energy transfer occurs from Pt1 to cyanostar or the $[CS_2PF_6]^-$ complexes in solid lattices. Conversely, when $E_{T\text{-}PtTA} < E_{T\text{-}CS}$, such as in Pt3, triplet energy transfer is not prominently observed in SMILES crystals, and instead, spatially isolated and rigidified configurations reinstate or even enhance the emissive properties of Pt3 in SMILES. In cases where $E_{T\text{-}PtTA} \approx E_{T\text{-}CS}$, although the triplet energy transfer process was diffusion-controlled between Pt2 and cyanostar in DCM solution, **Pt2**-SMILES crystals still exhibit a noticeable reproduction of bright Pt2 single molecular emission. Further insights will be provided, based on the disentanglement of deactivation processes in the formation of PtTA-SMILES solids.

Table 3.1. Photophysical properties of PtTA solutions, PtTA-SMILES crystals and solids.

Samples (Composition)		λ_{em} (nm)	τ (ns)	Φ_{em} (%)	k_r (s^{-1}) $\times 10^4$	k_{nr} (s^{-1}) $\times 10^4$	τ_0 (μs)
Solution (DCM, 5μM)	**Pt1**[PF_6]	555	1751	5.3	3.1	54	32.8
	Pt2[PF_6]	633	483	1.5	3.0	200	33.1
	Pt3[PF_6]	678	77	0.2	3.0	1300	33.3
Solution (DCM, 5μM)	**Pt1**[CS_2PF_6]	554	1138	3.4	3.0	85	33.2
	Pt2[CS_2PF_6]	633	462	1.4	3.0	210	33.2
	Pt3[CS_2PF_6]	672	80	0.3	2.9	1000	34.4
SMILES Single crystals	**Pt2**[CS_2PF_6]	635	1500	4.4	2.9	64	34.5
	Pt3[CS_2PF_6]	670	2200	5.4	2.9	47	35.1
Dropcast solids	**Pt2**[PF_6]	770	42	0.3	7.6	2370	13.1
	Pt3[PF_6]	780	95	0.7	7.8	1080	12.8
	Pt2[CS_2PF_6]	640	549	1.7	3.0	179	33.3
	Pt3[CS_2PF_6]	680	958	2.8	2.9	101	34.7
SMILES NPs	**Pt3**[$CS_{2.5}PF_6$]	675	990	3.1	3.1	98	31.9

*Rate constants calculated as $k_r = (\Phi/100)/\tau$, $k_{nr} = (1-\Phi/100)/\tau$, $\tau_0 = \tau/(\Phi/100)$[86]

3.3 Formation of PtTA-SMILES Solids

To fully understand the reinstated luminescence in PtTA-SMILES solids, especially for **Pt2**-SMILES and **Pt3**-SMILES, it is important to examine various factors such as intramolecular versus intermolecular influences, and radiative versus nonradiative processes. The intrinsic intramolecular factors that govern the emissivity of PtTA complexes have been extensively studied in the solution state, in the last chapter. And cyanostar offers well-defined spatial isolation to mitigate dye-dye interactions. Therefore, our focus now shifts to investigating the radiative and non-radiative deactivation pathways within PtTA-SMILES solids,[86, 88, 89] to gain a comprehensive understanding of how the SMILES strategy selectively modulates the phosphorescence of PtTA complexes in solid emitters.

We conducted titration experiments on PtTA-SMILES solids (**PtTA**•CS_x), gradually increasing the molar ratio of CS/PtTA (0~3) in the solution mixture, and drop-casting each solution onto galss slides (Figure 3.4). The samples vary from neat PtTA aggregates (**PtTA**•CS_0) without any cyanostar, to **PtTA**•CS_3 solids with excess cyanostar. In Figure 3.4-a, it suggests that for **Pt2**•CS_x and **Pt3**•CS_x, the addition of cyanostar gradually transformed the characteristic red-shifted emission of PtTA aggregates (PtTA dimers) to the solution-like emission of SMILES crystals.

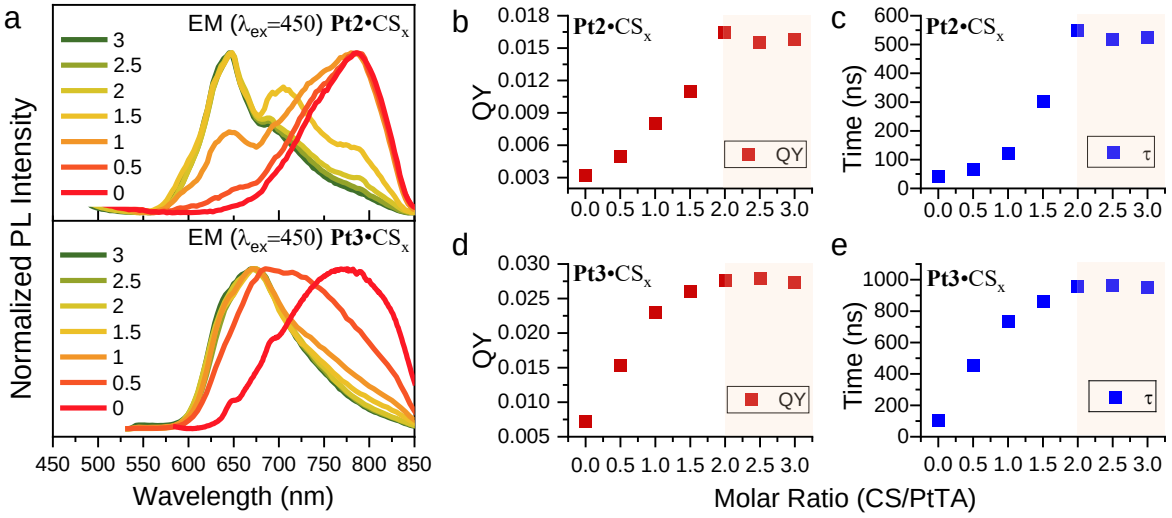

Figure 3.4. (a) Steady-state emission spectra of drop-cast solids with increasing molar ratio of CS/PtTA. (b) Quantum yields and (c) lifetime of **Pt2**•CS_x solids as a function of the molar ratio of CS/Pt2. (d) Quantum yields and (e) lifetime of **Pt3**•CS_x solids as a function of the molar ratio of CS/Pt3. Lifetime measurements were conducted with detector set at the wavelengths of each emission maximum.

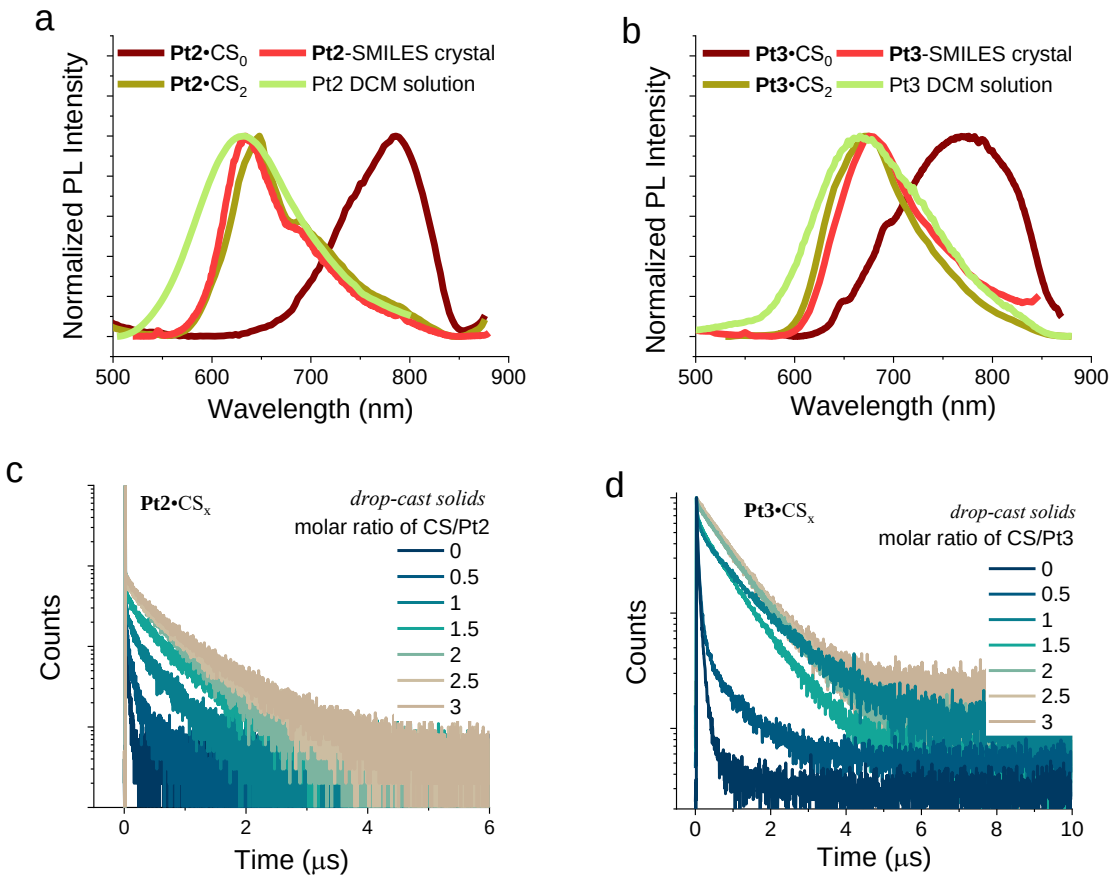

Figure 3.5. Emission spectra of (a) **Pt2**•CS_0, **Pt2**•CS_2 dropcast solids, **Pt2**-SMILES single crystal and Pt2 in DCM solution; (b) **Pt3**•CS_0, **Pt3**•CS_2 dropcast solids, **Pt3**-SMILES single crystal and Pt3 in DCM solution. The illumination was λ_{ex}=450 nm. Decay curves of drop-cast solids samples for (c) **Pt2**•CS_x and (d) **Pt3**•CS_x. Instrumental setup were λ_{ex}=450 nm, with λ_{em} from emission maxima.

Spectroscopic characterizations for all drop-cast samples are exhibited in Figure 3.4 and Figure 3.5, with detailed information on photophysical properties provided in Table 3.2. It indicates that the increase of cyanostar equivalents in **PtTA**•CS_x is accompanied by increases in Φ and τ (Figure 3.4-b,c,d,e). At 2.0 molar equivalents of CS, the emission spectra resemble those of the SMILES crystals (as shown by the overlay spectra in Figure 3.5-a,b). Φ and τ also reach constant values at 2.0 molar equivalents of CS, albeit somewhat lower than those found for single crystal samples (Table 3.2). This observation aligns with previous findings of generally lower emission quantum yields for spin-coated and drop-cast samples of fluorescent SMILES, where more structural defects compared to single crystals lead to increased non-radiative deactivations.[10, 26]

The above interpretation is supported by the calculated radiative rates (k_r) for the samples, which perfectly match those found for Pt2 and Pt3 in solution and SMILES crystals (Figure 3.6 and Table 3.2). And it indicates that once the CS to PtTA molar ratio reaches 2.0, the ion pair between cationic dyes and cyanostar-anion complex (PtTA•[CS_2PF_6]) is formed. The titration of CS into PtTA solids clearly demonstrates that effective decoupling of the PtTA complexes occurs at 2.0 equivalents, which results in similar optical properties as those in PtTA-SMILES crystals.

The investigation on radiative and non-radiative processes facilitates our understanding of the steric effect and spatial isolation exerted by CS. Without active energetic interactions with CS, such as TET,[90] the rigidified PtTA chromophores in the solid state helps reinstate the radiative and non-radiative factors as in intrinsic single molecular conditions.[91-93] Therefore, it allows the

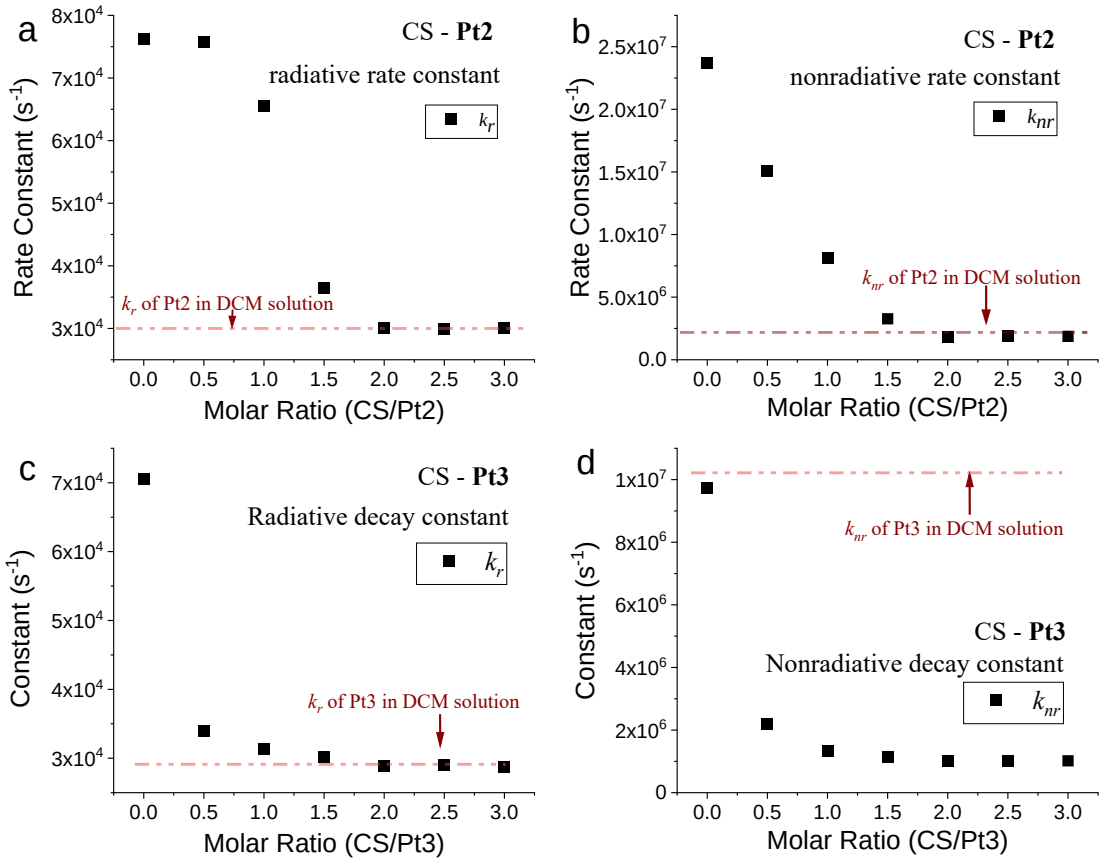

Figure 3.6. Deactivation rate constants of (a) radiative and (b) nonradiative processes of Pt2 in solid conditions with different molar ratio of CS, and (c) radiative and (d) nonradiative processes of Pt3 in solid conditions with different molar ratio of CS, respectively. The inserted lines are rate constants of separate deactivation processes of Pt2 or Pt3 in DCM solution.

solids to reproduce solution-like emission. For floppy dyes with a large intrinsic k_{nr}, as Pt3 showcases, the steric effect in SMILES is proven to be much more effective in alleviating non-radiative deactivation,[94] which apparently strengthens the emission in Pt3-SMILES solids.

Table 3.2. Photophysical properties of PtTA•CS_x solids.

PtTA•CS_x (Composition)		λ_{em} (nm)	τ (ns)	Φ (%)	k_r (s^{-1}) $\times 10^4$	k_{nr} (s^{-1}) $\times 10^4$	τ_0 (μs)
0	**Pt2**•CS_0	770	42	0.32	7.6	2373	13
0.5	**Pt2**•$CS_{0.5}$	770	66	0.5	7.6	1508	13
1.0	**Pt2**•$CS_{1.0}$	650, 750	122	0.8	6.6	813	15
1.5	**Pt2**•$CS_{1.5}$	650, 700	302	1.1	3.6	327	27
2.0	**Pt2**•$CS_{2.0}$	650	549	1.65	3.0	179	33
2.5	**Pt2**•$CS_{2.5}$	650	517	1.55	3.0	190	33
3.0	**Pt2**•$CS_{3.0}$	650	526	1.58	3.0	187	33
0	**Pt3**•CS_0	780	92	0.72	7.8	1079	13
0.5	**Pt3**•$CS_{0.5}$	700	451	1.53	3.4	218	29
1.0	**Pt3**•$CS_{1.0}$	680	735	2.3	3.1	133	32
1.5	**Pt3**•$CS_{1.5}$	680	861	2.6	3.0	113	33
2.0	**Pt3**•$CS_{2.0}$	680	958	2.76	2.9	102	35
2.5	**Pt3**•$CS_{2.5}$	680	961	2.79	2.9	101	34
3.0	**Pt3**•$CS_{3.0}$	680	953	2.74	2.9	102	35

*Rate constants calculated as $k_r = (\Phi/100)/\tau$, $k_{nr} = (1-\Phi/100)/\tau$, $\tau_0 = \tau/(\Phi/100)$[86]

3.4 Phosphorescent PtTA-SMILES Nanoparticles

To validate the practical application of phosphorescent SMILES solid emitters, we adopted the well-established SMILES nanoparticle methodology,[11, 12] with particular focus on Pt3-SMILES, which exhibits the largest phosphorescence emission improvement compared to the other two PtTA-SMILES solid materials. Hereby the Pt3-SMILES nanoparticles were synthesized as illustrated in Scheme 3.2, detailed protocol is described in Appendix 1.7.

As shown in Figure 3.7, we find that Pt3-SMILES nanoparticles (NPs) exhibit similar optical properties to the crystals. Pt3-SMILES NPs emit at 670 nm (Φ=0.01), and their excitation curve shows a red-shifted band compared to that of Pt3 in the solution state, although the bathochromic effect is weakened in Pt3-SMILES NPs compared to single crystals. This difference may be attributed to the size differences of absorbers for single crystals and polycrystalline within nanoparticles. The polycrystalline structure of Pt3-SMILES in the core of nanoparticles likely generates more energetic traps at grain boundaries and inside the emitter, correspondingly, we observe a slight decrease of lifetime in Pt3-SMILES NPs, but it is still maintained at a satisfactory level (~900 ns). For morphological determinations, Pt3-SMILES NPs exhibit a uniform size distribution with an average size of ~26 nm. Overall, the fabrication of Pt3-SMILES NPs provides a promising platform for the development of longer emissive phosphorescent probes.

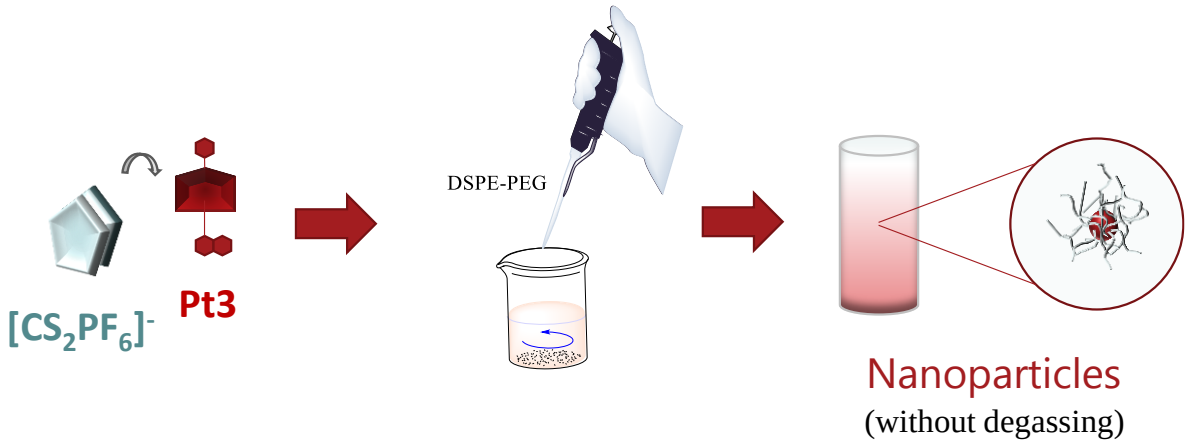

Scheme 3.2. Preparation protocol for making Pt3-SMILES nanoparticles. DSPE-PEG refers to 1, 2-distearoyl-sn-glycero-3-phosphoethanolamine-poly(ethylene glycol).

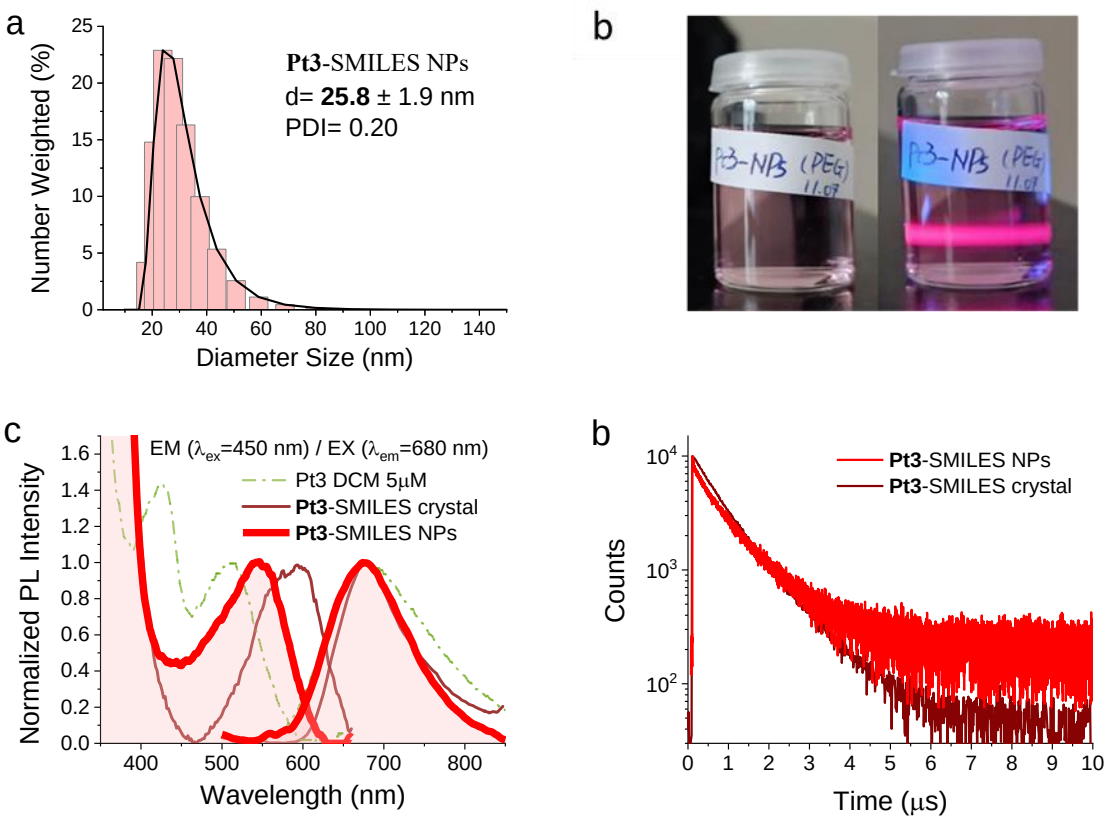

Figure 3.7. (a) Dynamic light scattering (DLS) measurements on **Pt3**-SMILES nanoparticles size distribution. (b) Picture of **Pt3**-SMILES NPs aqueous solution illuminated by 405 nm laser. (c) Steady-state optical properties and (d) Decay curves of **Pt3**-SMILES nanoparticles in comparison to **Pt3** in DCM (10 μM) and **Pt3**-SMILES crystal. The decay curves were collected with a setup of λ_{ex}=450 nm, λ_{em}=690 nm.

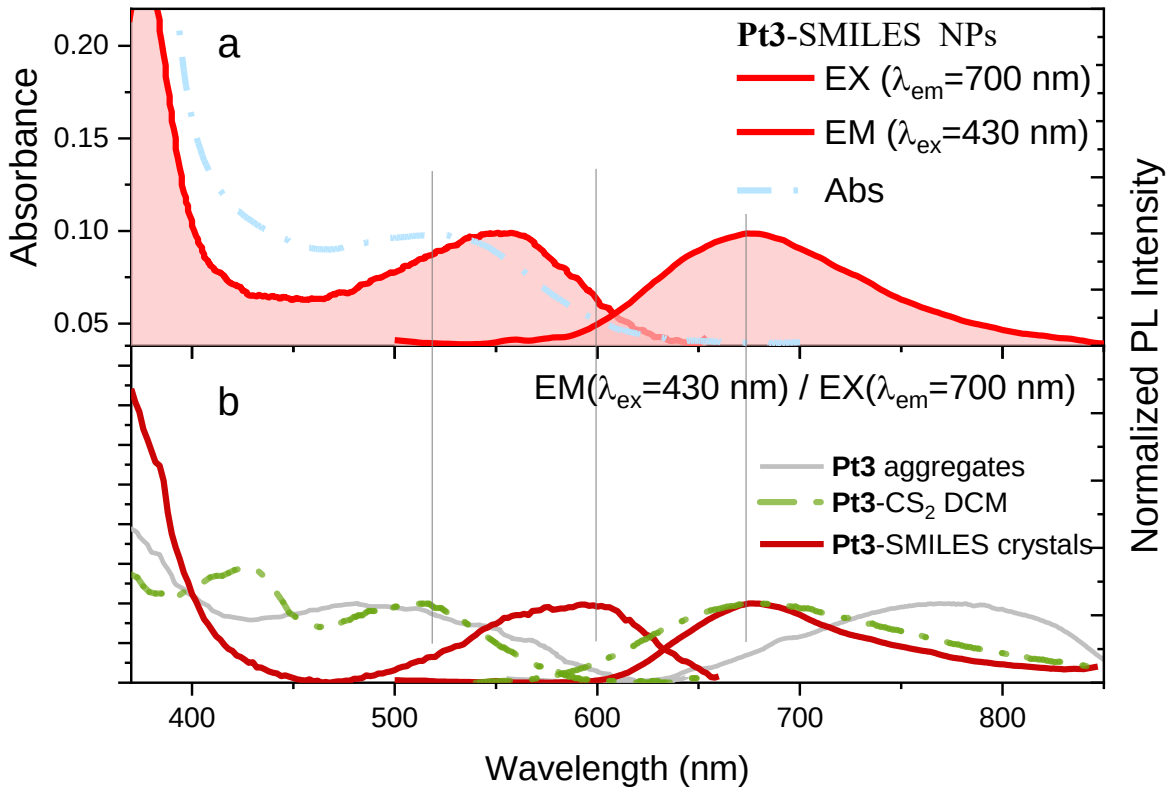

Figure 3.8. Steady state optical properties of **Pt3**-SMILES nanoparticles in comparison with emission and excitation curves of **Pt3**[CS_2PF_6] in DCM solution, **Pt3**-SMILES crystal and **Pt3** neat aggregates, all measured at room temperature. λ_{ex}=430 nm for emission curves and λ_{ex}=700 nm for excitation curves.

3.5 Conclusions

In this research, we have demonstrated the efficiency of the SMILES strategy in reliably transferring phosphorescence emission from dilute solution to high-density solids. By combining cyanostar (CS) with three PtTA chromophores, whose triplet state energies span across the calculated CS triplet energy ($E_{T\text{-}CS}$), we have achieved the reproduction of bright phosphorescence emission in **Pt2**-SMILES and **Pt3**-SMILES crystals and solid samples.

The crucial reason inducing the different emissivity in three PtTA-SMILES crystals lies in comparison between the triplet state energy ($E_{T\text{-}PtTA}$) of the PtTA complexes and $E_{T\text{-}CS}$. When $E_{T\text{-}PtTA}$ is larger than $E_{T\text{-}CS}$, efficient triplet energy transfer occurs from PtTA to cyanostar or the $[CS_2PF_6]^-$ complexes in solids, as observed in the quenched emission within Pt1-SMILES crystal. Conversely, when $E_{T\text{-}PtTA}$ is smaller than $E_{T\text{-}CS}$, such as in Pt3-SMILES, triplet energy transfer is less efficient, but instead CS induces an effective spatial isolation and protection for Pt3 chromophores to enhance the phosphorescence emission. Therefore, based on our experimental findings, it is advisable to select phosphorescent chromophores with triplet energy levels lower than $E_{T\text{-}CS}$ (2.0 eV), to generate emissive phosphorescent SMILES solid emitters.

Additionally, for the enhanced phosphorescence observed in Pt3-SMILES, our explorations into the radiative and non-radiative deactivation processes were conducted by measuring the **PtTA•**CS_x solids, which highlight how the steric effect exerted by SMILES confines the non-radiative pathways and improves the emissivity of Pt3 by up to 10 times. Consequently, we propose and validate a proof of concept for selectively harnessing phosphorescent chromophores' emission and long-lived decay in high-density solids using the SMILES method. Additionally, the development of brightly red-color emissive Pt3-SMILES nanoparticles (NPs) presents exciting prospects for the application of SMILES in microsecond-range phosphorescent probes.

PART II

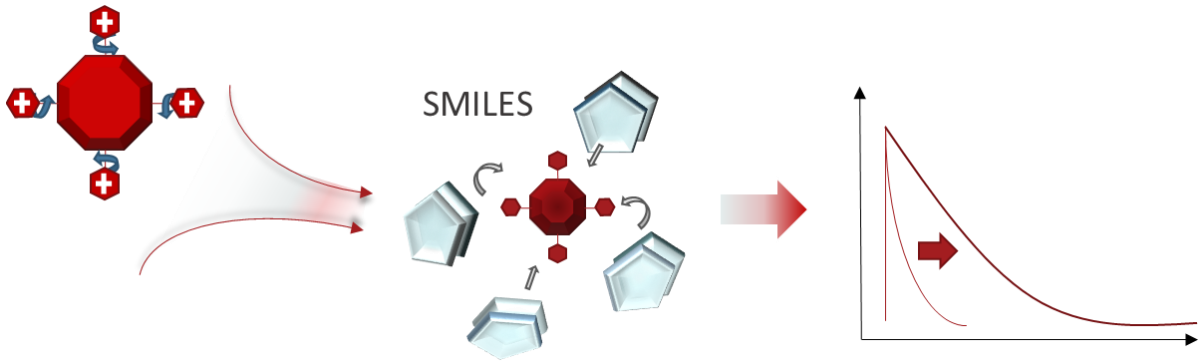

Chapter 4

Boosting Phosphorescence in Porphyrin-Based SMILES

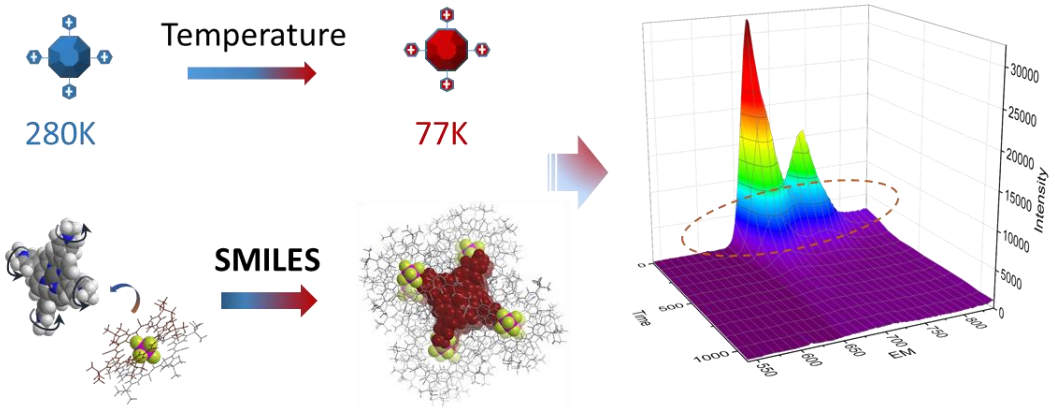

Chapter Acknowledgement

The porphyrin complex (Por4) was synthesized by Marko H. Nowack in Prof. Bo W. Laursen group (University of Copenhagen). The cyanostar was synthesized in Prof. Amar H. Flood group (Indiana University). All crystalline and nanoparticle synthesis, spectroscopic measurements, and data analysis were conducted by Yang Wang at the University of Copenhagen. This chapter contributes to the manuscript in Appendix 4.

4.1 Background and Motivation

Following the promising results in producing long-lived (~10^{-6}s) phosphorescent Pt3-SMILES, we continued the investigation in phosphorescent SMILES to encompass longer lifetimes. Majority of recent observations regarding SMILES have been liminted to utilizing monocationic dyes to form charge-by-charge stacking structures.[10, 62] This leads to the question of whether multicationic dyes could also be effective in the SMILES strategy.

In this chapter, we focus our investigations on generating solid emitters with phosphorescent SMILES that possess optical properties such as red emission and long lifetimes in the milisecond range. After screening a series of dyes, a metalloporphyrin compounds: *Palladium(III)–5,10,15,20–(tetra-N-methyl-4-pyridyl) porphyrin* (denoted as Por4), was chosen to form SMILES, as illustrated in Scheme 4.1.

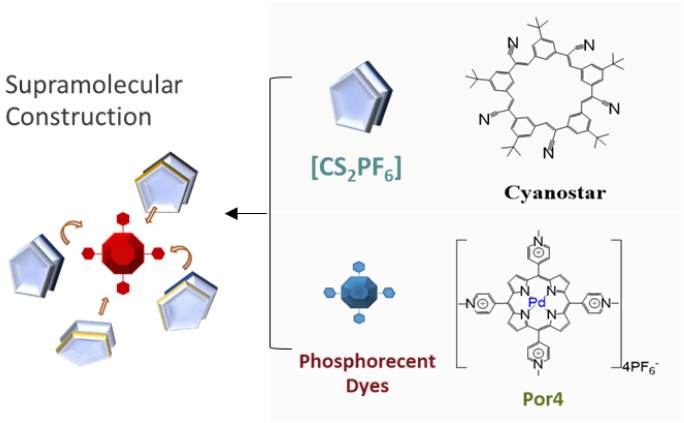

Scheme 4.1. Illustration of the supramolecular construction of Por4-SMILES using Por4 and CS.

Por4 has been studied as a biosensor for detecting intermolecular interactions with bio-based macromolecules like DNA, peptides.[95-98] However this metalloporphyrin typically exhibits a combined fluorescence and phosphorescence, with weak triplet emission.[99-101] There has been limited exploration on modulating Por4 optical properties without altering its chemical structure. Recent reports suggest that enclosing Por4 within macromolecules or oligomers will enhance its phosphorescence.[102, 103] Such as the bimolecular interactions between Por4 and DNA has shed light on the significant impact on enhancing Por4 phosphorescent emission via intermolecular interactions.[104-106] Based on this knowledge, we proposed that the cofacial stacking structure in SMILES may potentially boost Por4 optical properties, and to generate a phosphorescent SMILES materials via effectively reinstating or enhancing Por4 triplet state emission.

4.2 Basic Photophysical Properties in Solution State

4.2.1 Photophysical Properties of Por4

To investigate the photophysical properties of Por4, we performed steady-state absorption, emission, excitation spectra, and time-resolved experiments in solution state (MeCN and H_2O).[107-109] To differentiate the coexisting fluorescence and phosphorescence in Por4 emission, decay-associated spectra (DAS) were also practiced.[15]

In Figure 4.1, the absorption spectra of Por4 in both organic solvent MeCN (acetonitrile) and H_2O display the typical porphyrin Soret band (417 nm) and Q band (521 nm). However, the emission spectra of Por4 are different in MeCN and H_2O. In MeCN (Figure 4.1-a), Por4 exhibits four distinct emission peaks (570 nm, 620 nm, 650 nm, and 720 nm). In H_2O, Por4 emits at 570 nm, 620 nm, and a broad peak at 700 nm. The difference between emission curves occurs in the range 650~750 nm, where the peak broading occurs.

Decay curves of Por4 suggest the coexistence of fluorescence and weak phosphorescence. Upon monitoring the fluorescence at different wavelength, it is observed that the lifetimes are different. In MeCN, it is observed that the lifetimes vary from a short decay curve approaching the instrument response function (IRF) ($\tau < 0.1$ ns) at λ_{em}= 580 nm, to a mono-exponential decay curve with a lifetime of 10 ns at λem=720 nm. Additionally, at λ_{em}=720 nm, a long decay component assigned to phosphorescence is also observed, with a lifetime of 0.25 μs. For Por4 in H_2O, the lifetimes for the coexisting fluorescence and phosphorescence are similar to that observed in MeCN, though the utmost of fluorescence lifetime is shorter (5.2 ns), and with multi-exponential decay curve. On the contrary, the phosphorescence lifetime of Por4 in H_2O is 1.51 μs at λ_{em}=720 nm, which is longer than in MeCN.

To assign the origin of fluorescence and phosphorescence emission for Por4, deoxygenation experiments were conducted for Por4 in both MeCN and H_2O, as presented in Figure 4.2. Upon degassing via nitrogen purging, the emission of Por4 in both MeCN and H_2O exhibited enhancement in the range of 650~800 nm, however, the two emission bands at 580 nm and 620 nm were relatively unchanged. Corresponding to the improved emission intensity at 650~800 nm, the long lifetime components at λ_{em}=720 nm were prolonged, as well.

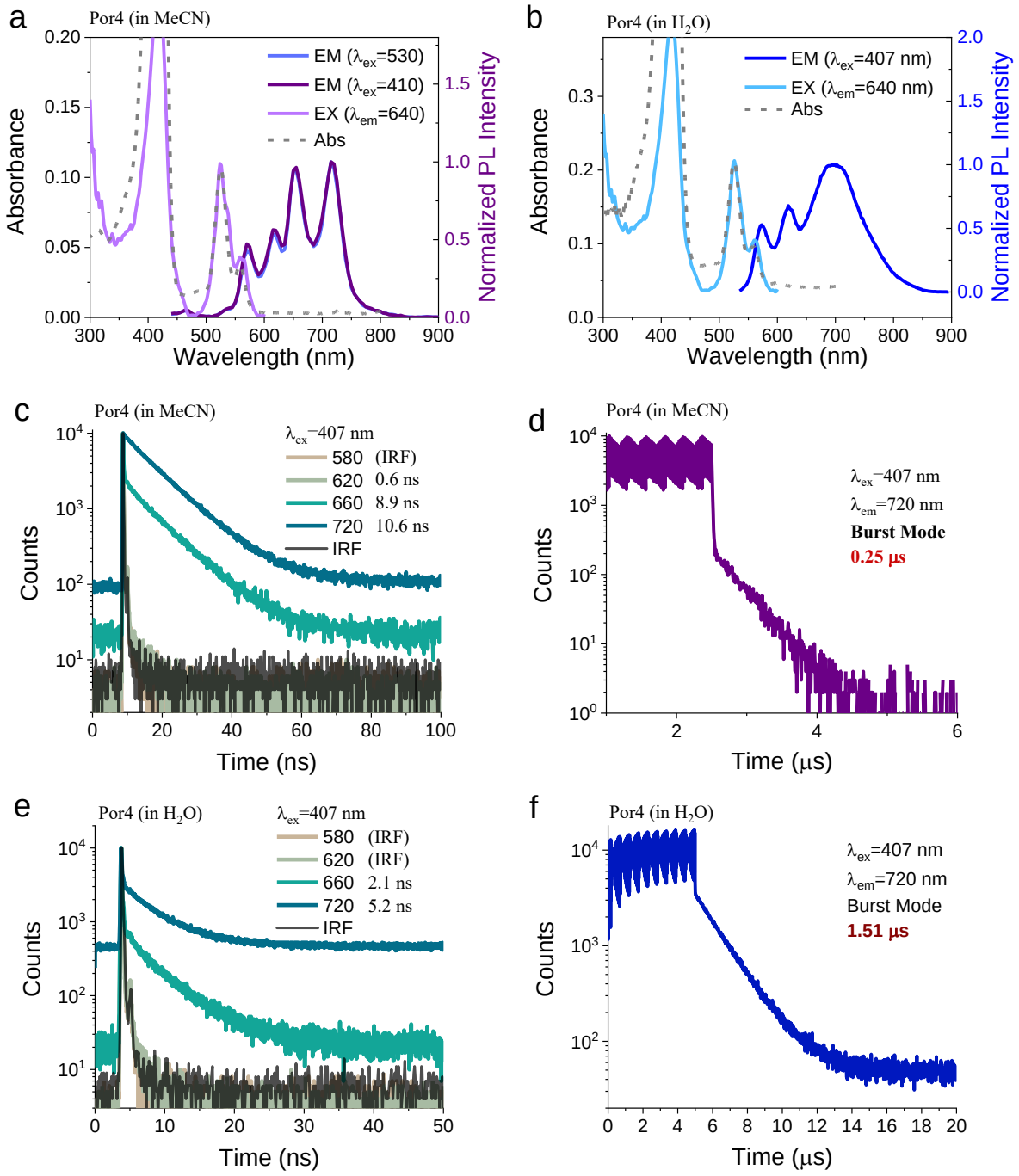

Figure 4.1. Photophysical properties of Por4 at an optically diluted concentration (5 μM), in MeCN and in H_2O. Steady-state properties of absorption, emission, and excitation curves for Por4 in (a) MeCN and (b) H_2O, the emission and excitation curves were normalized to the emission at 616nm. (c-d) Time-resolved decay curves for Por4 in MeCN, by using laser at λex=407nm, detectors were set at wavelengths of 570 nm, 620 nm, 655 nm, and 720 nm, separately. Burst mode was used to collect phosphorescence signals in (d). (e-f) Time-resolved decay curves for Por4 in H_2O, by using laser at λ_{ex}=407 nm, detectors were set at wavelengths of 570 nm, 620 nm, 655 nm, and 720 nm, separately. Burst mode was used to collect phosphorescence signals in (f).

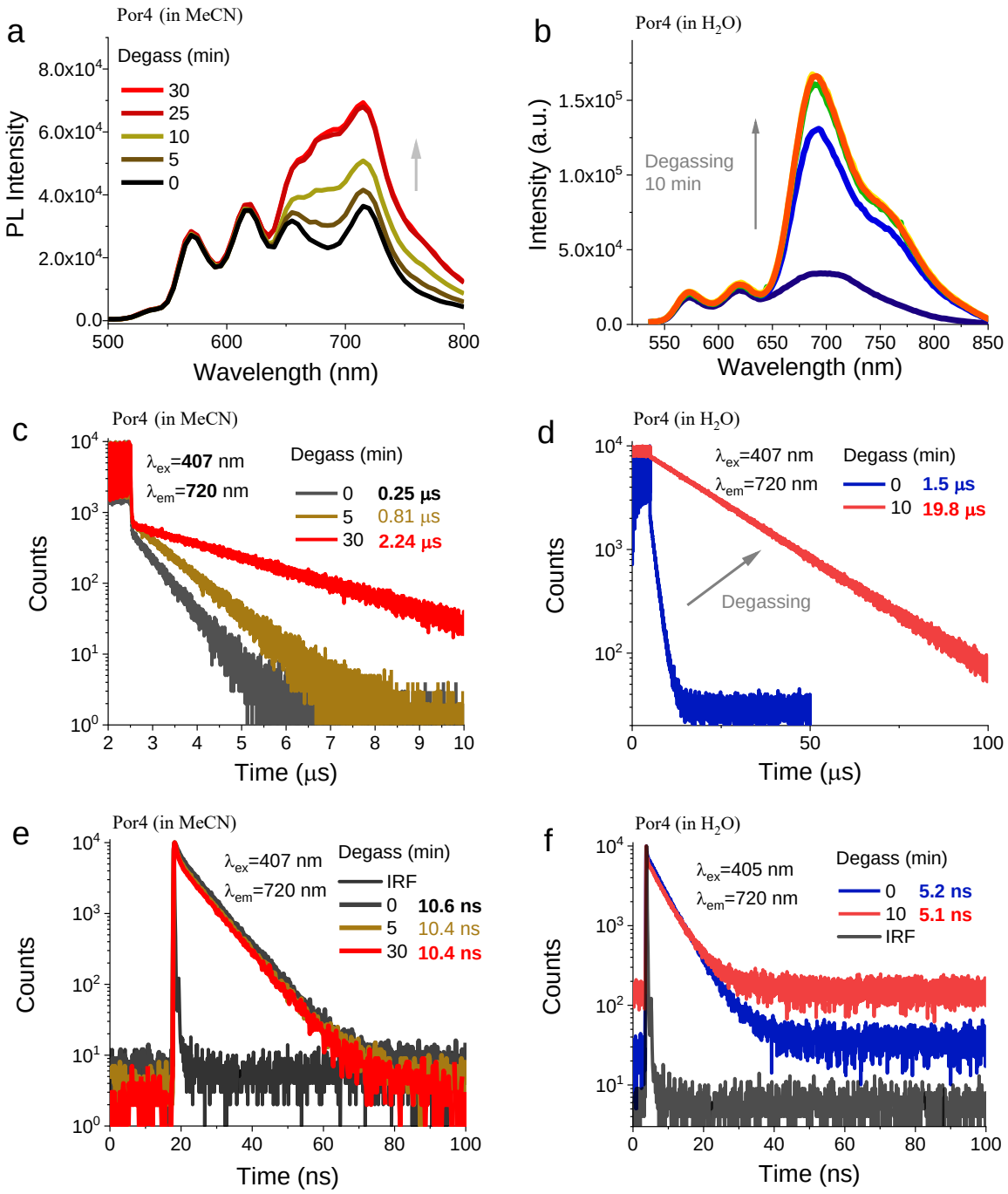

Figure 4.2. Deoxygenation experiments for Por4 in MeCN (5 µM) and H_2O (5 µM). (a) Emission curves for Por4 in MeCN upon degassing via N_2 purging for 30 minutes. (b) Emission curves for Por4 in H_2O upon degassing for 10 minutes. Phosphorescence decay curves at λ_{em}=720 nm, for Por4 being degassed in (c) MeCN for 30 minutes and in (d) H_2O for 10 minutes. Fluorescence decay curves at λ_{em}=720 nm, for Por4 being degassed in (e) MeCN for 30 minutes and in (f) H_2O for 10 minutes. For all measurements, excitation was λ_{ex}=407 nm.

Supplementary Note: ***Burst Mode***

PicoQuant's pulsed diode laser heads are designed for high repetition rates in the MHz range, enabling rapid measurements of fluorescence lifetimes ranging from picoseconds to nanoseconds. However, extending measurements to longer lifetimes in the millisecond range typically requires low repetition rates, which may not be efficiently achieved with diode lasers due to their limited pulse energy. Consequently, such measurements often resort to pulsed Xenon flash lamps, necessitating additional excitation hardware with a suitable monochromator.

Alternatively, the FluoTime 300 offers a unique "burst mode" capability, eliminating the need for extra hardware while enabling millisecond-range lifetime measurements. In burst mode, the diode laser emits a variable number of pulses at MHz repetition rates before being deactivated to allow sample emission detection. This process concentrates the laser energy into fewer but stronger pulses, effectively exciting a large number of molecules for fluorescence detection by the FluoTime 300. Consequently, phosphorescence and other excited states with extended lifetimes can be accurately measured without requiring additional excitation sources. *(from PicoQuant)*

Figure 4.2 indicates the degassing process enhanced the long decay component of Por4 in both MeCN and H_2O. In MeCN, the component increased from 0.25 μs to 2.24 μs after 30 minutes degassing, while in H_2O, it increased from 1.5 μs to 19.8 μs after just 10 minutes degassing. Meanwhile, the fast decay component at λ_{em}=720 nm remained constant, indicating the origin as fluorescence, with the long decay component attributed to phosphorescence, displaying lifetimes in the microsecond range. Previous studies suggest that introducing heavy metals into porphyrins enhances intersystem crossing efficiency, leading to room temperature phosphorescence. Emission bands in the 650~850 nm range are likely from triplet emission, although inconsistent lifetimes in different solvents may stem from solvation effects altering molecular rotational freedom, as well as coordination binding between heavy metals and porphyrins.

To specify the compositions of fluorescence and phosphorescence in Por4 emission, decay-associated spectra (DAS) were obtained by collecting decay curves for each wavelength (Figure 4.3-a).[10, 15, 110] The different decay components were subsequently deconvoluted. The distribution of amplitudes assigning to the same lifetime components is displayed as the function of emission wavelength. Figure 4.3-b illustrates the fitted emission curves assigned to fluorescence and phosphorescence, hereby the contribution to Por4 emission from both origins can be visualized. Additionally, for emission bands at 570 nm and 620 nm, decay curves all approach IRF, and the excitation spectra suggest the origins for emission bands within such range are different from the emission in the range of 650~850 nm. Therein, to facilitate the exploration on Por4 phosphorescence emission, less attention was focused on emission bands within 570~620 nm.

In Figure 4.3, the DAS characterization of Por4 in H_2O indicates overlapped positioning of two fitted emission curves in the range of 620~850 nm, which are assigned to fluorescence (~5 ns) and phosphorescence (~1.5 µs), respectively. When the Por4's emission in MeCN is also compared to the fitted DAS fluorescence and phosphorescence curves, the vibrational peaks of the fitted fluorescence curve correlate well to the two emission peaks at 660 nm and 720 nm for Por4 emission in MeCN. The fitted phosphorescence curve in MeCN is not directly evident under ambient condition. However, degassing Por4 in MeCN solution leads to a newly emerged peak at 680 nm, which matches the maximum of the fitted phosphorescence curve. Thus, it is concluded that both fluorescence and phosphorescence emission coexisting for Por4 in both MeCN and H_2O. In H_2O, the phosphorescence band is more pronounced than in MeCN.

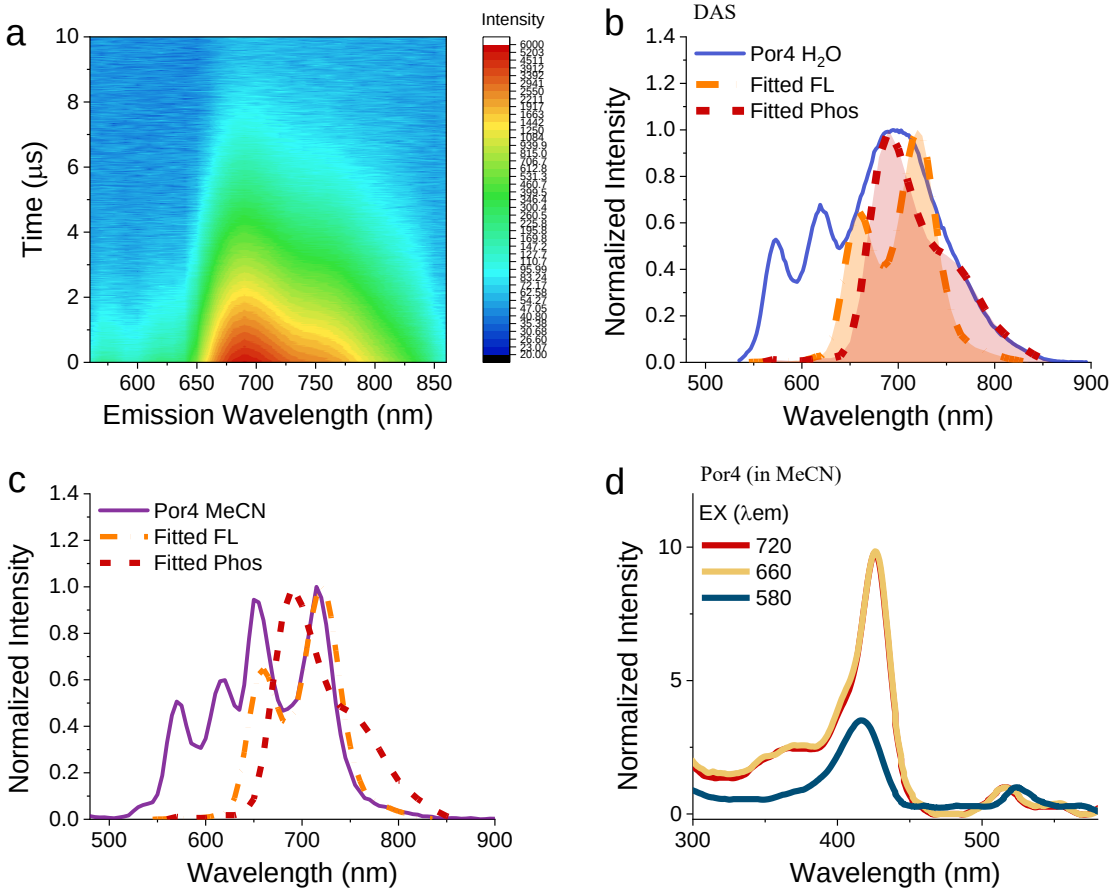

Figure 4.3. (a) Plot of decay curves as the function of emission wavelength - TRES (Time-Resolved Emission Spectra), based on the data from DAS (decay-associated spectra) measurements. (b) Emission curves of Por4 in H_2O (5 µM), and the fitted fluorescence and phosphorescence bands assigned to lifetime components of ~5 ns and ~1.5 µs, respectively. (c) Comparison among the emission curve of Por4 in MeCN (5 µM), and the fitted fluorescence and phosphorescence bands. (d) Excitation curves of Por4 in MeCN, with dector set at 580 nm, 660 nm and 720 nm.

4.2.2 Bimolecular Interactions between Por4 and CS

Given the sensitivity of Por4 emission to environmental changes, the addition of a macromolecule can potentially alter Por4's emission through changes in the microenvironment or energy- and electron-transfer processes.[111] To investigate the potential influences of CS, Stern-Volmer experiments were conducted to examine bimolecular interactions between CS and Por4.

Since the good solvents for Por4 and DCM are different, a mixture of MeCN and DCM is used for the Stern-Volmer titration experiments. Before conducting Stern-Volmer experiments, trials were performed to compare the photophysical properties of Por4 before and after CS was added. In Figure 4.4, the addition of CS did not change the Por4 emission, and the excitation curve overlaps well with the absorption band, suggesting a single chromophore system with no ground state interaction and disturbances (Figure 4.4-a). The extinction spectra suggest that the addition of CS into Por4 sustains Por4 identical absorption bands with added features of CS (Figure 4.4-b). The Por4-CS_2 absorption suggest a proportional increase of the CS band at 320 nm as a function of added CS molar equivalents. Additionally, solutions containing both Por4 and CS still present the coexistence of fluorescence and phosphorescence (Figure 4.4-c, d). The solvent-induced effect on Por4's phosphorescence lifetime results in an increase from 0.25 μs in pure MeCN to 0.53 μs in mixed MeCN/DCM (50%/50%). The fluorescence lifetime was relatively unchanged: 8.3 ns in pure MeCN and 8.0 ns in mixed MeCN/DCM (50%/50%). The addition of eight equivalents of CS did not alter Por4's fluorescence features (Figure 4.4-c,d).

The Stern-Volmer experiment were conducted with a low concentration of Por4 chromophores (2.5×10^{-6} μM). Por4 was well dissolved with addition of CS, a diffusive interaction with CS is expected, in a dynamic and collisional process. In Figure 4.5-a, a progressive increase in the absorption band at 314 nm is apparent, which is attributed to CS, whereas all absorption bands related to Por4 remained constant. The ratio of absorbance between the CS band at 314 nm and the two Por4 bands at 418 nm and 525 nm proved to have a linear relationship up to a molar ratio of 10 for CS/Por4 (Figure 4.5-b). This indicates that the solubility is sufficient for measurements and the subsequent analysis is reliable. Despite the observations in absorption spectra, both the emission curves, excitation curves and phosphorescent decay curves of Por4 remained relatively unchanged in the presence of CS (Figure 4.5-c,d,e,f).

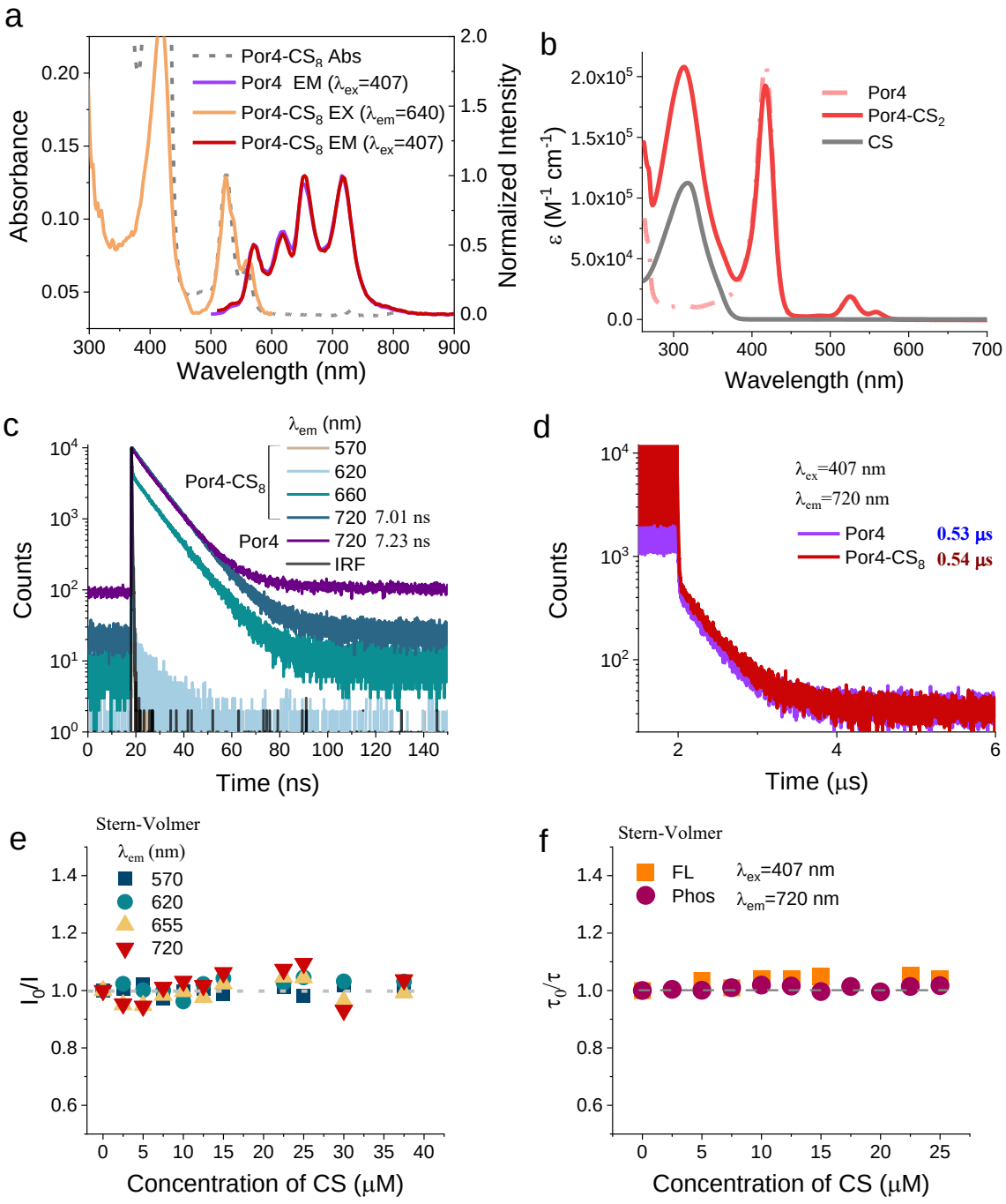

Figure 4.4. (a) Absorption spectra of Por4 and Por4-CS_8 in MeCN/DCM (5 μM). (b) Extinction values of Por4, CS and Por4-CS_2. Por4-CS_2 is used to showcase the add-up of CS in the function of composition, as the comparison of add-up effect is more direct compared to Por4-CS_8. (c) Decay curves of Por4-CS_8 in MeCN/DCM (5 μM), λ_{ex}=407 nm, λ_{em}=570 nm, 620 nm, 655 nm, and 720 nm, respectively. (d) Decay curves of Por4 and Por4-CS_8 in MeCN/DCM (5 μM), λ_{ex}=407 nm, λ_{em}=720 nm, burst mode was used. (e-f) Stern-Volmer plots for (f) luminescence intensity I_0/I and (f) lifetime τ_0/τ.

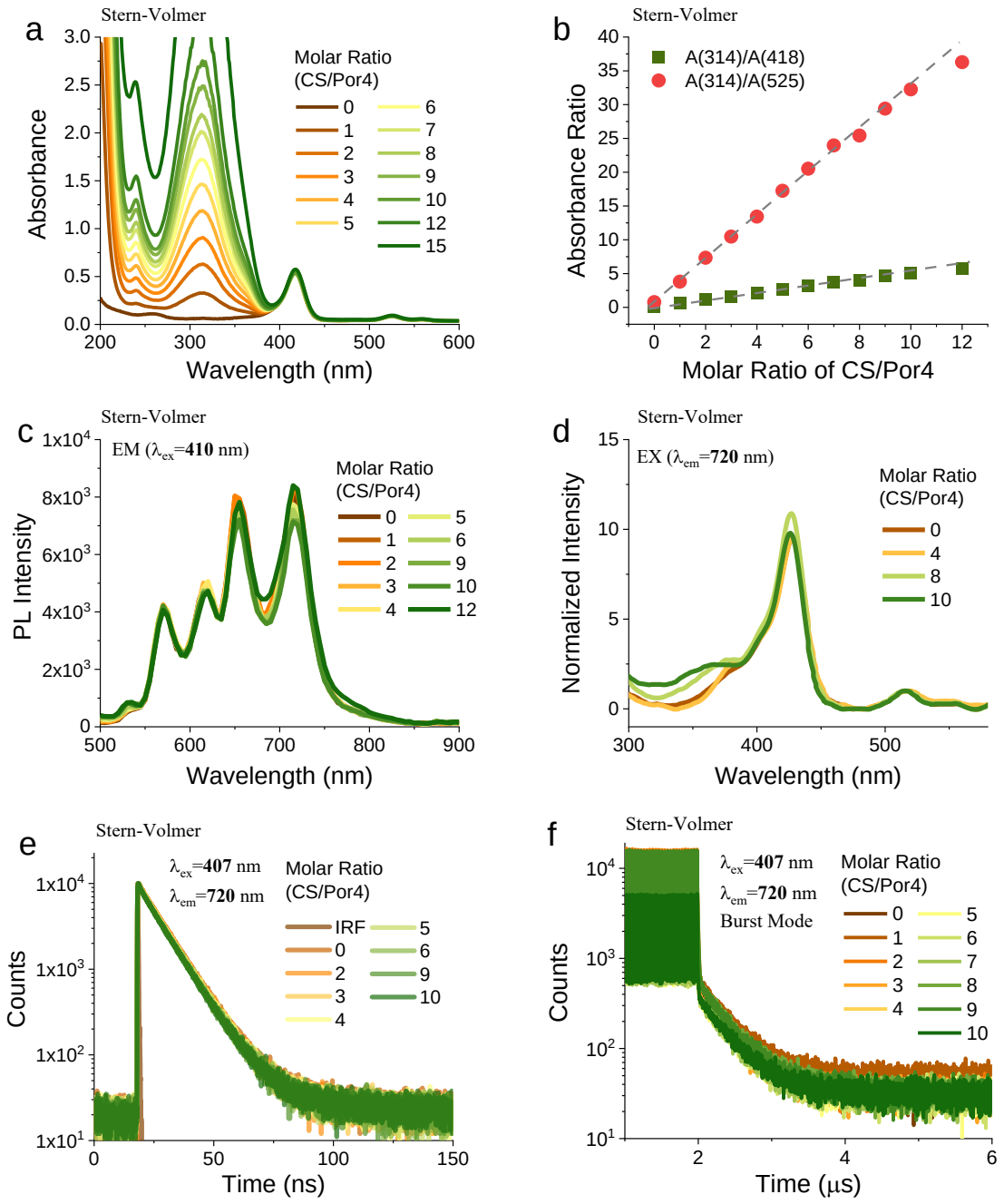

Figure 4.5. (a) Absorption spectra for Stern-Volmer titration between Por4 and CS. (b) Absorbance ratio between bands at 314 nm and 418 nm, 314 nm and 525 nm. (c) Emission spectra (λ_{ex}=410 nm) and (d) Excitation curves (λ_{em}=720 nm) for Stern-Volmer titration, all excitation curves were normalized to the band intensity at 525 nm. (e,f) Decay curves for Stern-Volmer titration, λ_{ex}=450 nm for both types of measurements, (e) for fluorescence and (f) for phosphorescence by using burst mode.

In general, as CS was gradually added into Por4 solutions, no apparent alterations in Por4 emission or lifetime is occurred, as corroborated by the flat Stern-Volmer plots based on intensity (I_0/I) and lifetime (τ_0/τ) in Figure 4.5-c and Figure 4.5-d.

According to the Stern-Volmer equation:

$$\frac{I_0}{I} = \frac{\tau_0}{\tau} = 1 + k_q \tau_0 [Q] \quad (4\text{-}1)$$

In which the I_0 and I refer to the luminescence intensity of chromophore (Por4) without and with the presence of quencher (CS), τ_0 and τ refer to the luminescence intensity of chromophore (Por4) without and with the presence of quencher (CS), k_q is the bimolecular quenching constant, [Q] is the concentration of quencher.

Overall, Stern-Volmer plots for both intensity (I_0/I) and lifetime (τ_0/τ) suggest that k_q=0, therefore no efficient energy transfer process occurred within the Por4 and CS bimolecular interactions.

4.3 Phosphorescence in Por4-SMILES

Adhering to the well-developed SMILES synthetic protocol, where the molar ratio between CS and mono-cationic dye is 2.5,[11, 12] the synthesis of Por4-SMILES adopted a molar ratio of CS/Por4=10 on account of the tetra-cationic charge balance. The concentrated mixture of CS and Por4 in the MeCN/DCM (50%/50%) solvent system was placed in the dark until large crystals emerged. Por4-SMILES nanoparticles were prepared by adding amphiphilic polymer (DSPE-PEG_{2000}) into the mixture of CS and Por4, in which DSPE-PEG_{2000} constitutes 60 wt% of the whole mixed chemicals. The solution of mixtures was evaporated thoroughly, then redissolved by THF and injected into milli-Q water while being accompanied by ultrasonication. Detailed preparation steps can be referred to Appendix 1.7.

Figure 4.6 displays the photophysical properties of Por4-SMILES crystals and nanoparticles. Compared to the weak phosphorescence emission in MeCN or H_2O, both Por4-SMILES crystals and nanoparticles emit identical strong phosphorescence bands with a maximum at 690 nm, and the signature of such emission band resembles the phosphorescence component in DAS

characterizations (Figure 4.3). Correspondingly, the lifetime for this emission band in Por4-SMILES is much prolonged than that in the solution state, both lifetimes of Por4-SMILES crystal (0.37 ms) and Por4-SMILES nanoparticles (0.26 ms) suggest efficient improvement by two orders of magnitude compared to Por4 phosphorescence lifetime in solution state (in MeCN: 0.25 μs, in H_2O: 1.51 μs). Additionally, the quantum yields of Por4 phosphorescence are also increased when Por4 is embedded into SMILES, from 0.03% for Por4 in MeCN to 0.96% for Por4-SMILES nanoparticles and 1.20% for Por4-SMILES crystal, which is about two orders of magnitude enhancement. The enhancement in phosphorescence is assigned to the unique SMILES stacking structure, where Por4's rotational flexibility is highly confined, and effects of singlet oxygen are prevented.[103, 106]

Following such a proposal, efforts were put to understand the molecular packing structure of Por4-SMILES. However, the attempts to characterize the crystal structure were unsuccessful due to weak diffraction signals and lattice disorders. To elucidate the stoichiometry between CS and Por4 within the Por4-SMILES crystals, those single crystals were re-dissolved into organic solvents and a relative absorbance ratio between the CS band and Por4 band was calculated, against a standardized titration plot (Figure 4.7-b). The re-dissolved Por4-SMILES crystal shows that the molar composition with CS accounts for 88%, which represents a molar ratio of CS/Por4=7.33, approaching the expected molar ratio of CS/Por4=8. Considering the charge balance considerations, the structure of Por4-SMILES is still proposed as the format of $Por4[CS_2PF_6]_4$.

Compared to the Por4 neat aggregates, even though the decay curve of Por4 powders contain a long-lifetime component with an averaged lifetime of 0.2 ms, the emissivity is extremely weak, the QY is not detectable accurately. On the contrary, the Por4-SMILES crystal exhibits strong phosphorescence with a QY of 1.2% (the QY for Por4 in MeCN is 0.03%). Thus the phosphorescence emitted from Por4-SMILES crystals represents a stronger enhancement of Por4 triplet emission, instead of the effect exerted by dimerization.

The Por4-SMILES nanoparticles can have practical use for bio-imaging applications. Figure 4.6-c shows the size distribution of Por4-SMILES nanoparticles centered around 37 nm. Besides, Por4-SMILES nanoparticles also show good stability for long-term storage, wherein the phosphorescence is well sustained even after being stored for two months (Figure 4.7-e,f), which suggests an efficient regularity by using the synthetic method.

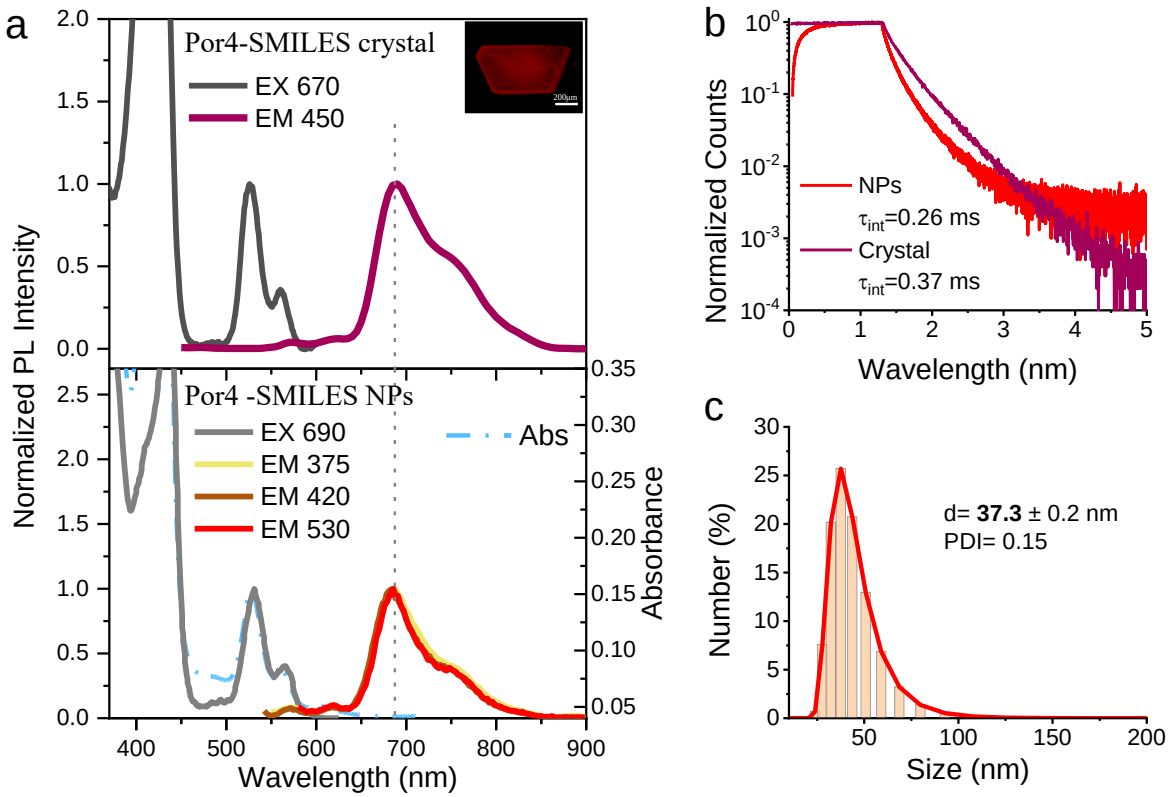

Figure 4.6. (a) Steady state photophysical properties of Por4-SMILES crystal and Por4-SMILES NPs. The number after 'EM' is the wavelength used for illumination, and the number after 'EX' is the wavelength being detected. Inserted picture is the fluorescence micrograph of Por4-SMILES crystal under microscope, scale bar is 200 µm. (b) Decay curves of Por4-SMILES crystal and Por4-SMILES NPs, excitation wavelength was 450 nm, detector emission wavelength was 700 nm. (c) Dynamic light scattering measurements of Por4-SMILES NPs, number-averaged size distribution is presented. PDI is the polydispersity index.

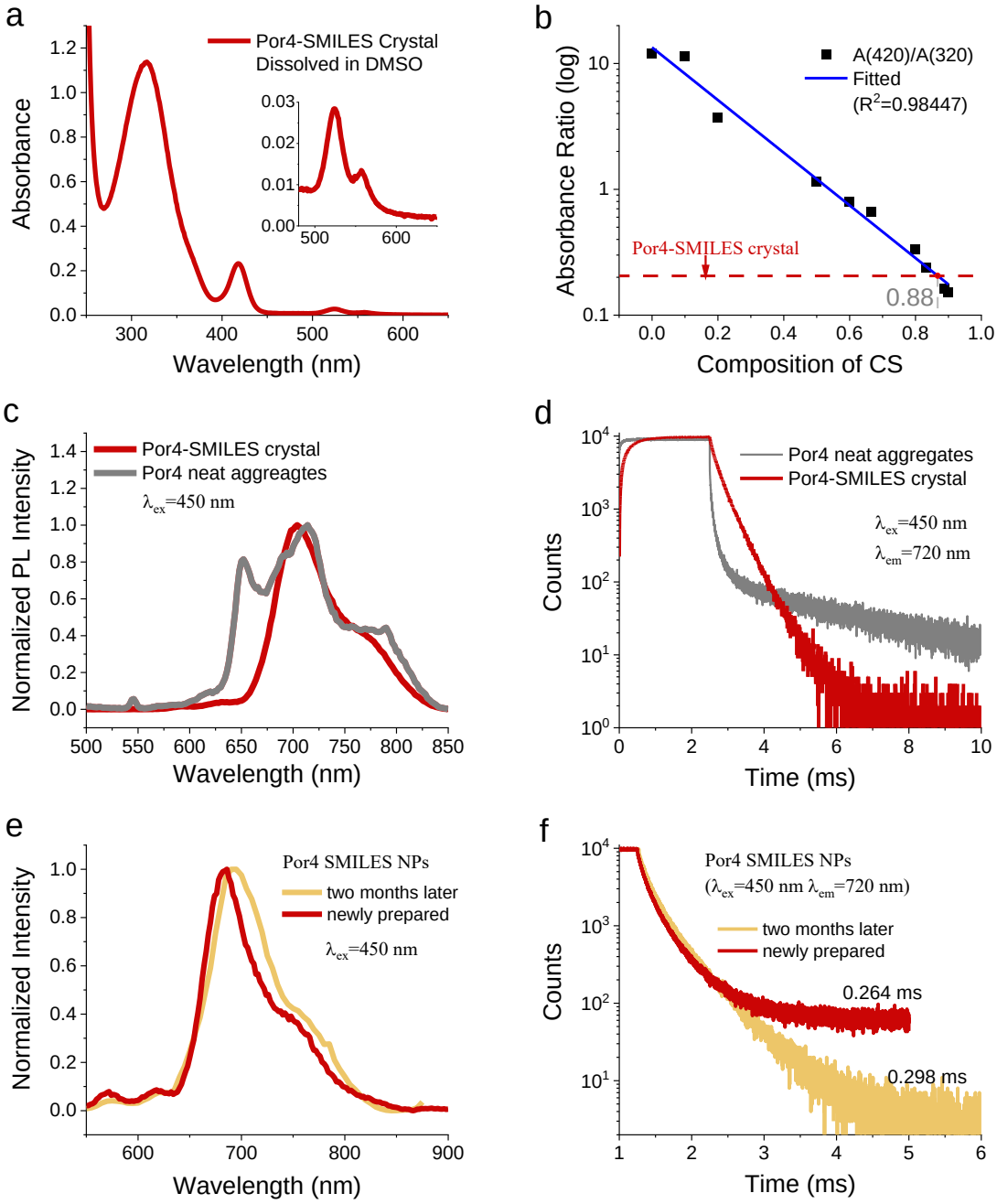

Figure 4.7. (a) Absorption curve of Por4-SMILES single crystal being re-dissolved. (b) Absorbance ratio between band 314 nm (CS) and 420 nm (Por4) as the function of CS composition. The solvent was MeCN/DCM (50/50 vol%). (c,d) Comparisons between Por4-SMILES single crystal and Por4 neat aggregates: (c) emission spectra, λ_{ex}=450 nm and (d) decay spectra, λ_{ex}=450 nm, λ_{em}=710 nm, burst mode was used for TCSPC measurements. (e,f) Photophysical stability comparison between freshly prepared Por4-SMILES NPs and sample being stored for two months: (e) steady state emission spectra λ_{ex}=450 nm. (f) decay spectra, λ_{ex}=450 nm, λ_{em}=710 nm, burst mode was used.

4.4 Explorations on the Enhanced Triplet Emission

To fully understand the origins of the desired long-lived red emission in Por4-SMILES, which is originally weak in solution state Por4, detailed elaborations on photophysical properties are highly required, especially the triplet excited state is of great importance. Therein cryogenic condition was applied to stimulate efficient depopulation of Por4's triplet excited state with inhibited thermal decay.[21, 112, 113] The utilization of a cryogenic environment facilitates reinstating the intrinsic triplet emission of Por4 and helps with compare the SMILES effect in enhancing Por4 intrinsic phosphorescence.

4.4.1 Intrinsic Triplet Emission of Por4

At 77K (liquid nitrogen), Por4 exhibits intense phosphorescence, with emission bands at 670 nm and 742 nm (Figure 4.8-a, f), accompanied by a remarkable lifetime of 1.36 ms (Figure 4.8-b). The excitation curve follows the shape similar to that observed at room temperature solutions and Por4-SMILES, as depicted in Figure 4.8-f. The long decay of Por4 at cryogenic conditions indicates that the triplet excitons can survive longer (1.36 ms), such a long lifetime has rarely been reported for Por4.

When the liquid nitrogen was removed, and allowed thaw, a fast decrease of phosphorescence intensity was observed, and the emission bands at 670 nm and 742 nm gradually merged to a main peak at ~690 nm. Eventually the phosphorescent emission diminished to a level comparable to the fluorescence emission bands at 568 nm and 614 nm, which were relatively unchanged in response to temperature alterations (Figure 4.8-a). Correspondingly, the intensity drop of phosphorescence emission is accompanied by a fast decrease of lifetime, from 1.39 ms at 77K to 1.79 μs at around 273 K. Comparisons of photophysical properties are tableted in Table 4.1.

The abovementioned phenomenon suggests that Por4's phosphorescent emission is highly dependent on the environmental changes, and the fluorescence is much more stable regardless of the external changes, or less pronounced of the fluorescence derivation in comparison to the drastic changes of the phosphorescence from 77K to 273 K.

Interestingly, when the freeze-thaw experiment (Figure 4.8-a) is correlated to the comparisons among optical performances of Por4 in different conditions (MeCN solution, SMILES and frozen PG), as depicted in Figure 4.8-c, d, e, f, the optical performances of Por4-SMILES mimics an intermediate phase of Por4 in the freeze-thaw transition, where the typical phosphorescent emission is strongly displayed with a maximum at 690 nm, and the possesses a lifetime in the range of 1.79 μs ~ 1.39 ms. Distinct from the weak phosphorescence emission and short lifetime in solutions, Por4's triplet emission was sufficiently reinstated in the cryogenic environment and in SMILES, which both prolonged the phosphorescence lifetime to the ms range.

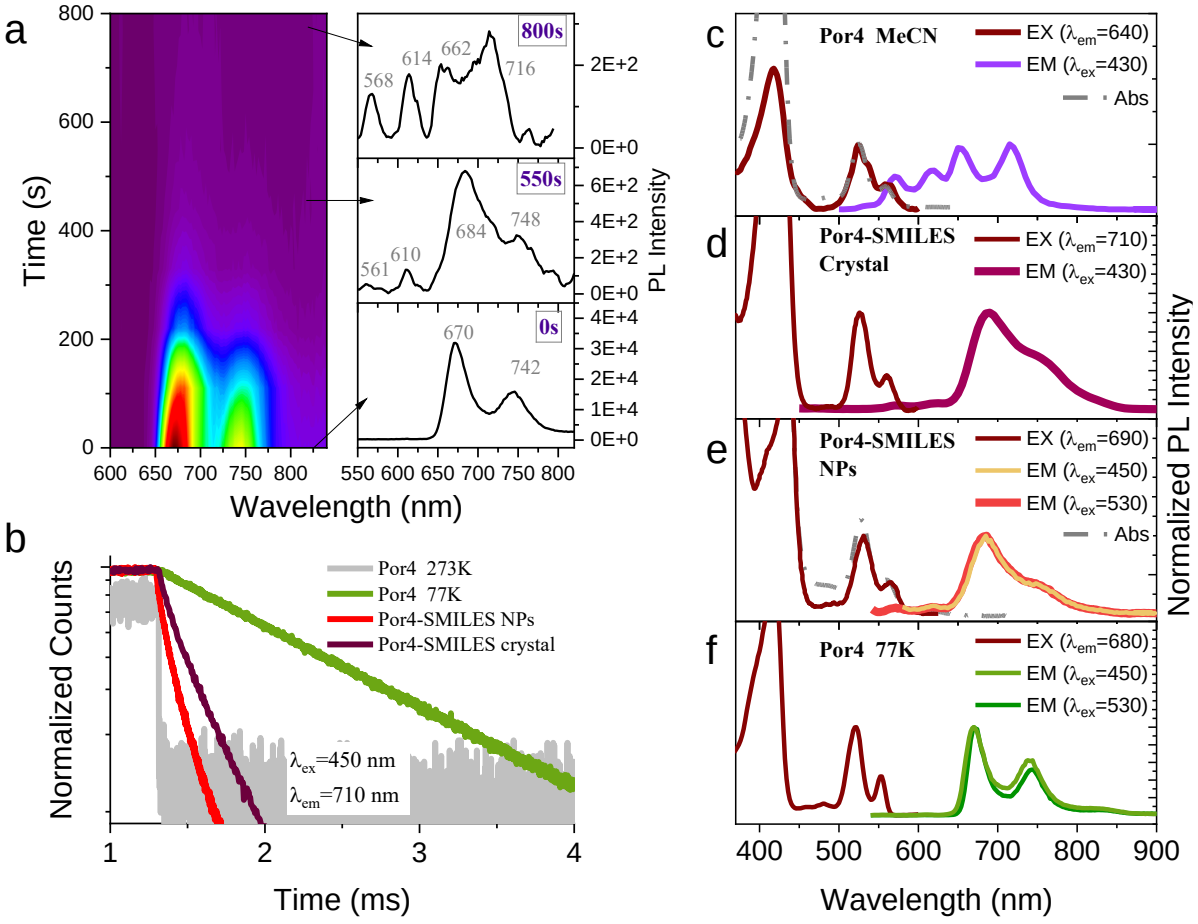

Figure 4.8. (a) Time correlated emission spectra of Por4 in MeCN/PG (10/90 vol%) in a freeze-thaw experiment transiting from 77K (liquid nitrogen) to 273K (removal of liquid nitrogen), and selected emission curves at specific moments (0s, 550s, 800s upon melting). (b) Decay curves of Por4 and Por4-SMILES at different conditions, the excitation wavelength was 450nm, detector was set at 710 nm. Burst mode was used to collected the long-lived photons. (c-f) Comparisons of steady state photophysical properties of Por4 and Por4-SMILES in different conditions.

The similarity between the SMILES effect and cryogenic condition in strengthening Por4 triplet emission is not supposed to be perceived as a sole coincidence. Conversely, the rigidified environment arising from densely stacked structures in SMILES and confined molecular movement in the frozen state should be recognized as the main reasons contributing to the enhanced Por4 phosphorescence. Such observations corroborate to the increase of Por4 phosphorescence emission in several previous researches, via encapsulation of Por4 by macromolecules such as DNA and peptides, generating spatial confinement on Por4's rotational freedom and exclusion to solvent molecules.[104, 105]

Table 4.1. Photophysical properties of Por4 solutions and Por4-SMILES samples

Sample		λ_{em} (nm)	τ (λ_{em}=720 nm)	
			FL	Phos
Por4 (MeCN)	Before degass	570, 616, 652, 716	10.6 ns	0.25 μs
	After degass	568, 614, 715	10.4 ns	2.24 μs
Por4 (H_2O)	Before Degass	573, 621, 691	5.2 ns	1.51 μs
	After Degass	573, 621, 697	5.1 ns	19.80 μs
Por4 (PG/MeCN)	273K	570, 616, 652, 716	IRF	1.79 μs
	77K	670, 742	IRF	1.39 ms
Por4 SMILES Crystal		692	IRF	0.37 ms
Por4 SMILES NPs	Before Degass	694	IRF	0.30 ms
	After Degass	696	IRF	0.46 ms

*Absolute QY. Por4(MeCN): 0.03%, Por4 SMILES NPs before degass: 0.96%, Por4 SMILES crystal: 1.2%.

4.4.2 Analysis on Deactivation Pathways

The photoexcited state process in Por4-SMILES can be schematically depicted in the Jablonski diagram Figure 4.9-a.[15] For chromophoric Por4, after photoexcitation, the excitons at excited state undergo different deactivation pathways: (a) directly decay from singlet excited state to ground state, radiating fluorescence; (b) undergo intersystem crossing to populate triplet excited state and experience radiative emission as long-lived phosphorescence. Meanwhile, the radiative deactivations also encounter competitive non-radiative processes including energy dissipation via molecular vibration or heat, or via interactions with quenching species. For Por4-SMILES, the non-radiative deactivation pathways are mainly three aspects: (1) energy dissipation via Por4 molecular vibration from triplet excited state to ground state by intersystem crossing process, the rate constant is denoted as $k_{ISC(nr)}$; (2) excitons quenched by O_2, the rate constant is denoted as $k_{Q(O2)}$; And (3) bimolecular interactions with CS and hereby induce triplet energy transfer, the rate constant is denoted as k_{TET}.

Considering all the deactivation pathways, the average lifetime of Por4 for fluorescence (τ_{Fl}) and phosphorescence (τ_{Phos}) can be presented as the following equations:

$$\tau_{Fl} = \frac{1}{k_{Fl}+k_{nr}} \tag{4-2}$$

$$\tau_{Phos} = \frac{1}{k_{Phos}+k_{ISC(nr)}+k_{TET}+k_{Q(O_2)}} \tag{4-3}$$

Herein, Por4 phosphorescence is sensitive and can be easily affected by a range of factors, Por4 fluorescence is less sensitive to such factors.

The Stern-Volmer titration experiments have given evidence that the triplet energy transfer between Por4 and CS is not feasible in the bimolecular interactions and the factor of k_{TET} can be ruled out. Therein the non-radiative pathways influencing phosphorescence emissions of Por4 and Por4-SMILES are $k_{ISC(nr)}$ and $k_{Q(O2)}$.

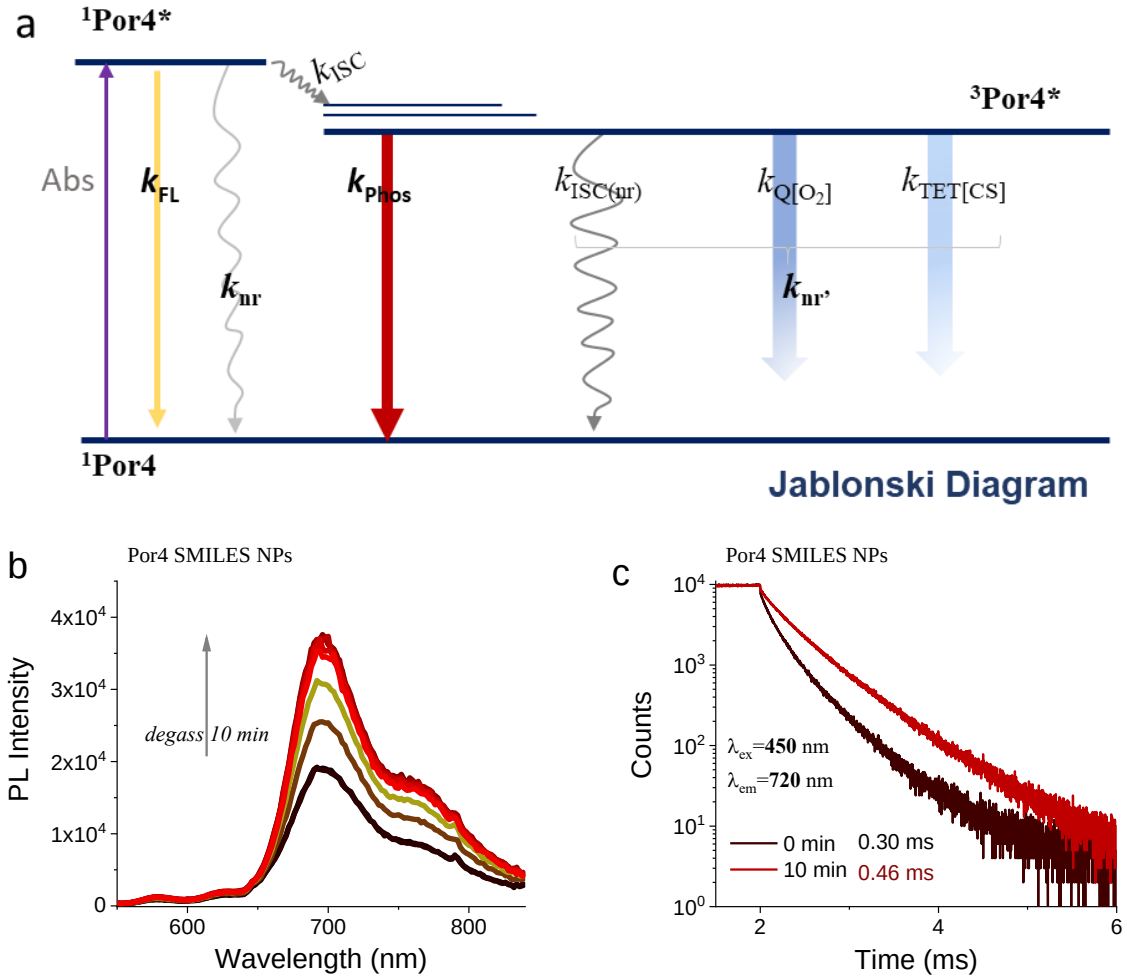

Figure 4.9. (a) Scheme of Jablonski energy diagram for Por4 photoexcitation processes. Degassing experiments for Por4-SMILES NPs for 10 minutes: (b) emission spectra, λ_{ex}=407 nm. (c) Decay curves, λ_{ex}=450 nm, λ_{em}=720 nm, burst mode was used.

As tabulated in the Table 4.1, the deoxygenation for Por4 solutions is only capable of improving the lifetime by a factor of 10, and is far from the two orders of magnitude enhancement exerted by SMILES or the cryogenic conditions. The common point for both strategies is the rigidified matrix that constrains Por4's conformational flexibility. The molecular rotation/vibration movements can potentially induces non-radiative dissipation of excited state energy from T_1 to S_0, thus such confinement on conformational flexibility can be understood as effectively reducing $k_{ISC(nr)}$. Hereby, $k_{Q(O2)}$ is determined as less affective as $k_{ISC(nr)}$ does in the whole non-radiative pathways.

And finally, the SMILES is confirmed as effectively boosting Por4's phosphorescence, for both emissivity and lifetime, on account of the efficient spatial confinement on chromophores'

rotational freedom and effectively reducing non-radiative pathways. The relocation of the metalloporphyrin into a more hydrophobic microenvironment near the macromolecular host (CS) plays a crucial role. This relocation, combined with the confinement of geometrical flexibilities within the lattices, efficiently restricts the rotational and vibrational freedom of the metalloporphyrin. As a result, Por4's non-radiative decay pathways are circumvented. Furthermore, the metalloporphyrin becomes spatially isolated and shielded from external quenchers such as solvent and oxygen upon complexation with CS, leading to the enhancement of its triplet emission.

4.5 Conclusions

This chapter discusses the construction of self-assembled tetracationic metalloporphyrin (Por4) into densely packed SMILES structure, which resulted in a remarkable enhancement of Por4 phosphorescence emission, with lifetimes reaching the millisecond range. Specifically, we obtained Por4-SMILES crystal (λ_{em}=690 nm, τ=0.37 ms, Φ=1.2%) and Por4-SMILES nanoparticles (λ_{em}=690 nm, τ=0.30 ms, Φ=0.96%). Notably, till date, achieving such long-lived red emission of Por4 was possible only under cryogenic conditions.

Our investigations into Por4's intrinsic photophysical properties and interactions with CS yielded valuable insights. We discovered that the enhanced phosphorescence in SMILES primarily results from effective confinement on the nonradiative deactivations of triplet excitons. This confinement likely stemmed from the reduction of Por4's conformational flexibilities within the SMILES stacking structures, and protecting/shielding Por4 from external oxygen.

The discovery in Por4-SMILES proves an effective method for regulating and boosting phosphorescence without complicated chromophore modification or functionalization on chromophores' scaffold. Moreover, it offers a practical approach for adapting ultralong decay luminescence in densely packed supramolecular systems. The generation of Por4-SMILES nanoparticles additionally addresses the demand for long-lifetime detection required for bioimaging applications.

PART III

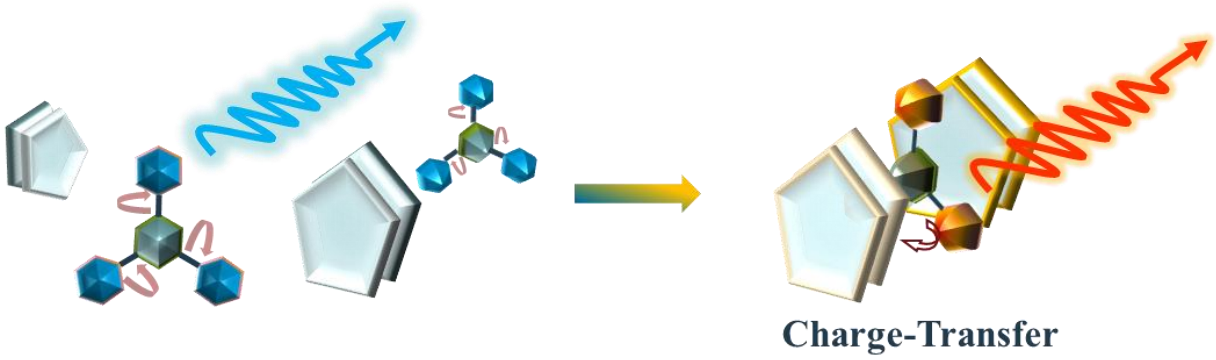

Chapter 5

Long-Lived Excited State in SMILES via Charge-Transfer Transition

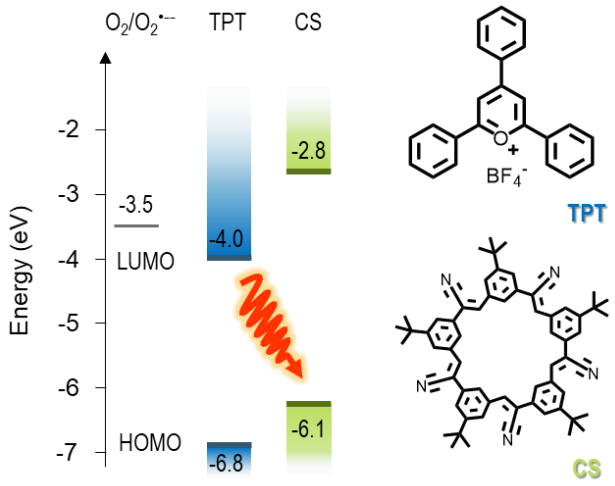

Chapter Acknowledgement

The preliminary experiments focusing on the photophysical properties of TPT[CS_2BF_4] ion pairs formed in solvents with varying polarity were performed by previous master student Sina Borgi in Prof. Bo W. Laursen group (University of Copenhagen). The cyanostar (CS) was synthesized in Prof. Amar H. Flood group (Indiana University). All solids preparation experiments, spectroscopic measurements, and data analysis were conducted by Yang Wang at the University of Copenhagen. This chapter partially contributes to the manuscript in Appendix 5.

5.1 Background and Motivation

The strategy of SMILES (*Small-Molecule Ionic Isolation Lattices*) is utilized to reduce strong coupling of cationic chromophores by spatially and electronically isolate them into the charge-by-charge alternating lattices, which enables the reproduction of the dilute solution optical properties into solid emitters.[1, 10] X-ray characterizations of SMILES crystals prove the successful spatial isolation of cationic dyes by stacking with $CS_2 \bullet X^-$ anionic complexes. Owing to the wide electronic window (with reduction and oxidation processes at -1.94 V and +1.50 V versus ferrocene, as in Figure 5.1), $CS_2 \bullet X^-$ can accommodate many fluorophores such as oxazine, pyridine, rhodamine, as long as their HOMO (Highest Occupied Molecular Orbitals) and LUMO (Lowest Unoccupied Molecular Orbitals) locate within the 3.5 V electronic window of $CS_2 \bullet X^-$.[1] Cases where the chromophore's frontier orbitals locate outside of the anionic complex electronic window, SMILES strategy is not expected to be functioning for reinstating solution-alike properties in solid emitters. Nevertheless, for dyes with deep HOMO or high LUMO than that of the $CS_2 \bullet X^-$ electronic window, efficient charge transfer-transition between dyes and $CS_2 \bullet X^-$ may induce new emission band with favorable features.

For TOTA, a triangulenium cationic dye whose HOMO locates lower than that of $[CS_2X]^-$, in 2017,[114] we discovered that the co-assembly of TOTA and CS generates an orange emission band (630 nm), which is distinct to both TOTA's solution state emission (530 nm) and crystal emission (548 nm). Such red-shifted emission band also displays a prolonged lifetime of ~25 ns, compared to the lifetime (12 ns) of TOTA emission band. The new emission band was explained as hierarchical assembled structure of $(\mathbf{TOTA} \bullet [CS_2BF_4])_n$, and contributed from π-stack enhanced oligomerization, since the ion-pair complexation of $\mathbf{TOTA}^+[CS_2BF_4]^-$ leads to apparent quenching, which is illustrated in Figure 5.1-a.

With the explorations on $[CS_2X]^-$ electronic window, TOTA's HOMO is energy-mismatched for SMILES effect, DFT (density functional theory) calculations reveal that the HOMO of the $\mathbf{TOTA} \bullet [CS_2BF_4]$ ion-paired assembly is predominantly situated on the cyanostar-anion complex rather than on the dye.[1] Conversely, LUMO of the ion-paired assembly is found to be predominantly located on the TOTA dye (Figure 5.1-b). Herein confirms that charge-transfer transition is the dominative mechanism for the new redshifted emission band.

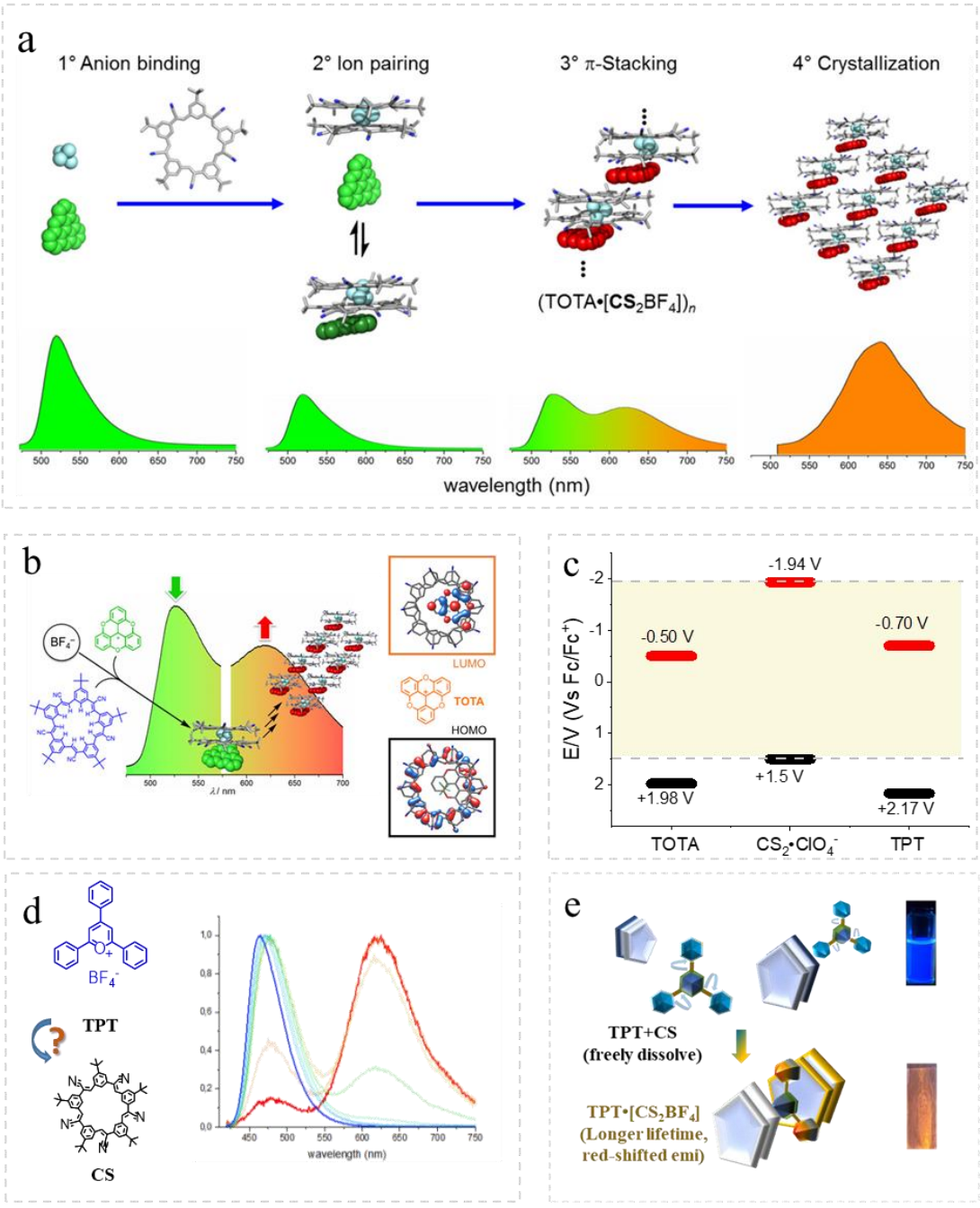

Figure 5.1. (a) Illustration of emission transformation from TOTA molecule to hierarchical structure of **TOTA•**[CS_2BF_4] contact ion pairs as reported in *JACS 139, 6226-6233 (2017)*. (b) Scheme illustrating the new emission band in **TOTA**-SMILES is induced by charge-transfer transition, as supported by DFT calculations showing the HOMO is located on the cyanostar-anion complex instead of the dye, and the LUMO of the ionpaired assembly is situated on the TOTA dye. (c) Energy level diagram showing positions of frontier orbitals mapped using electrochemistry, which suggests both TOTA's and TPT's frontier orbitals located outside of the CS_2X^- complex's electronic window. (d-e) Illustrations of emission changes for **TPT•** [CS_2BF_4] ion pair formation, approached by gradually varying solvent from DCM to 95%:5% benzene:DCM, done by Sina Borgi (unpublished).

Following the TOTA-SMILES, our group continued the explorations on charge-transfer transition in SMILES ion-paired assemblies. Though, such systems do not strictly follow the electronic isolation rule for SMILES strategy, they have a potential to create new redshifted emission, and accompanied with prolonged luminescent lifetime for practical applications of solid emitters. **TPT**[BF_4] (*2,4,6-Triphenylpyrylium Tetrafluoroborate*) was chosen on account of its planar shape, the symmetric scaffold and high charge density on the center to facilitate alternative stacking structure instead of forming segregation, in addition to the commercial availablility and wide usage in optoelectrical materials. Importantly, the molecular frontier orbital of **TPT**[BF_4] positions similarly to that of **TOTA**[BF_4], which means **TPT**[BF_4] HOMO sits lower than that of CS_2•X^-, as shown in Figure 5.1-c.[115] Therefore it is expected to witness charge-transfer transition in **TPT**•[CS_2BF_4] ion pair assembly. Our previous group member, Sina Borgi investigated the formation of **TPT**•[CS_2BF_4] ion pair in solution state, by gradually decreasing solvent polarity from 100% DCM to 95%:5% Benzene:DCM. The preliminary investigation on **TPT**•[CS_2BF_4] ion pair narrates a similar phenomenon as for **TOTA**•[CS_2BF_4] ion pair: a newly emerged red-shifted emission band for **TPT**•[CS_2BF_4] ion pair (λ_{em}=620 nm) is observed, with a much longer lifetime (13.1 ns in solution, 70.9 ns in thin film), in comparison to optical properties of TPT (λ_{em} = 480 nm, τ = 3 ns).

As has been confirmed in **TOTA**-SMILES solids and preliminary work on **TPT**-SMILES solutions, the charge-transfer transition in such ion pair assembly systems contributes to the new emission band with prolonged lifetime, but less efforts were focused on tracking the long-lived excited state and the underlying deactivation processes (radiative and nonradiative pathways). Apart from that, it has shown that both ion pairs **TOTA**$^+$[CS_2BF_4]$^-$ and **TPT**$^+$[CS_2BF_4]$^-$ in solution state are prone to undergo quenching, which creates uncertainty for a high-fidelity tracking of the charge-transfer transition in the solution state.

To further investigate the charge-transfer transition in SMILES, especially to continue explorations on **TPT**-SMILES, we have three aspects to highlight in this chapter:

(1) We focus more on the long-lived excited state in **TPT**-SMILES, which is induced by charge-transfer transition, especially tracking the formation of such a long-lived excited state.

(2) Investigation of the photophysical properties is mainly based on solid samples, to avoid uncertainties arising from quenching in solutions.

(3) We track the transformation from monomer TPT to hierarchical (**TPT**•[CS_2BF_4])n structure, by varying the molar ratio of CS/TPT in solids, therein the photophysical property changes are stemmed from different close contacts between TPT dimers and **TPT**•[CS_2BF_4] ion pairs. Proposed species representing different interaction modes are illustrated in Figure 5.2-c. Such gradual probing approach facilitates our understanding of intrinsic emissivity of variable hierarchical **TPT**•CS_x structures in real fabrication scenarios.

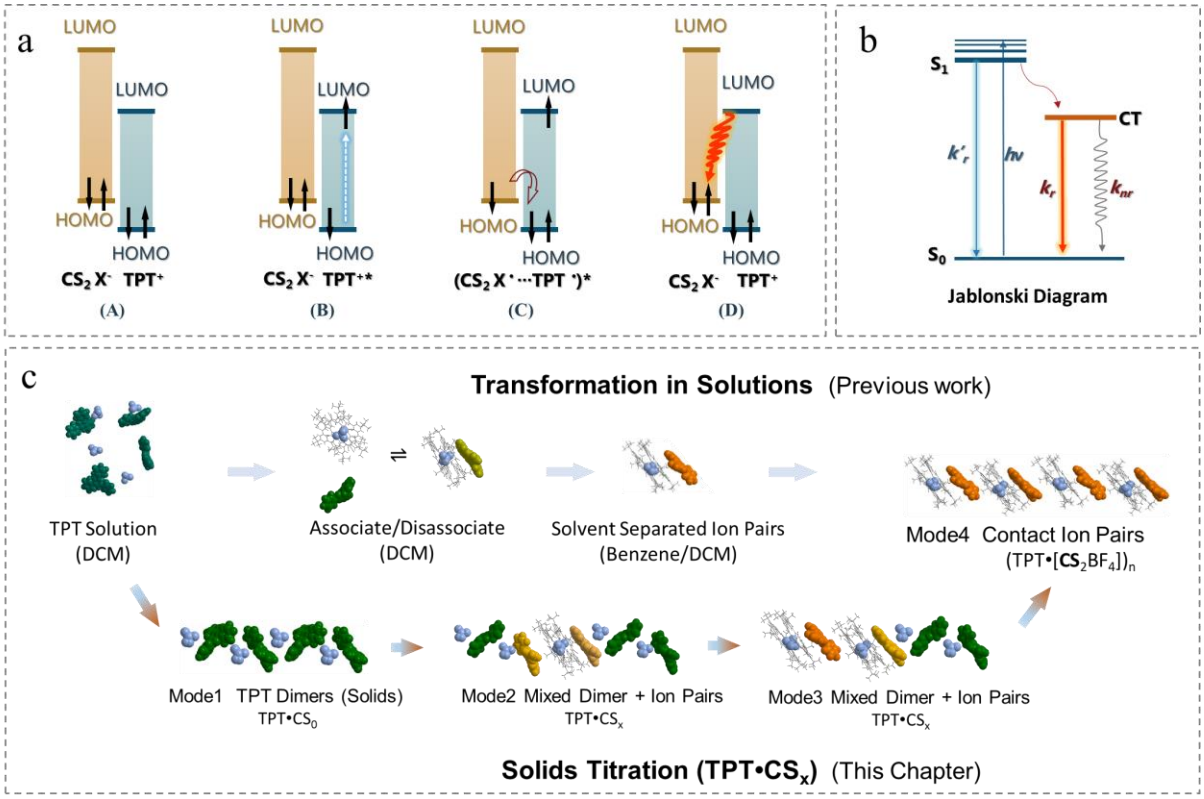

Figure 5.2. (a) Illustration of molecular orbital (MO) diagram for charge transfer transition. The scheme illustrates the steps involved in the charge-transfer mechanism: (**1**) Upon photoexcitation,an electron being photoexcited from TPT^+ HOMO to LUMO, labeled as TPT^+ *. (**2**) Within close contacts between TPT^+ * and $[CS_2BF_4]^-$, an electron migrated from adjacent $[CS_2BF_4]^-$ HOMO to the vacancy of TPT HOMO, therein induce forming into exciplex, an intermediate radical pair ($[CS_2BF_4]^{\bullet}\cdots TPT^{\bullet}$)*. (**3**) Excited TPT^+ relaxes back to ground state via photon emission, herein, electron from TPT^+ LUMO to $[CS_2BF_4]^-$ HOMO. (b) Jablonski diagram of charge transfer transition, k_r and k_r' refer to radiative rate constants for charge transfer induced radiation and the intrinsic TPT fluorescence. (c) Methods for transforming TPT solution to **TPT**-SMILES, which contains the hierarchical structure of contact ion pairs of (**TPT**•[CS_2BF_4])$_n$, by either reducing the polarity of solvents or by using drop-cast solids. For the solids titration method, we propose various putative species of **TPT**•CS_x (x=0~3) solids composing different interaction modes between TPT dimers and **TPT**•[CS_2BF_4] ion pairs. The green ones represent TPT dimers, the yellow ones represent TPT molecules approached by both dimers and [CS_2BF_4] ion pairs, the orange ones represent TPT being stacked by [CS_2BF_4] ion pairs.

5.2 Bimolecular Charge-Transfer Transition

When delving into the topic of charge-transfer transition, electron donor-accepter systems will be the main focus. These systems consist of matched electron donors (D) and electron acceptors (A).[19, 116-118] When the components are identical, the system is classified as an excimer, whereas non-identical components form an exciplex system.[69] The electron donors and acceptors in these systems readily form a charge-transfer state, facilitating charge separation, transfer, and radical ion generation when exposed to external photoexcitations. The gradual charge migration and recombination of radicals stabilize the excited state and lead to long-lasting luminescence.[118, 119]

The pair of electron donor and accepter in a typical exciplex system undergo electrostatic interactions and electron migrations upon close contacts, which generate intermediate radical ion pairs. A new photon radiates along with the intermediate species recombination process, such charge-transfer transition can be simply elaborated as the following (5-1):

$$A + D \xrightarrow{h\nu} A^* + D \xrightarrow{CT} \left(A^{\delta-} \cdots D^{\delta+}\right) \rightarrow A + D + h\nu \tag{5-1}$$

As mentioned above, this chapter focuses on specific SMILES materials, in which the cationic chromophores possess HOMO locating below that of CS_2X^- anionic complex, therein the model of charge-transfer transition needs to be updated to ionic donor and acceptor pairs.

$$A^+ + D^- \xrightarrow{h\nu} A^{+*} + D^- \xrightarrow{CT} (A^\bullet \cdots D^\bullet)^* \rightarrow A^+ + D^- + h\nu \tag{5-2}$$

Eventually it can be theorized for the **TPT•**[CS_2BF_4] ion pair as following (Figure 5.2-a):

$$TPT^+ + CS_2X^- \xrightarrow{h\nu} TPT^{+*} + CS_2X^- \xrightarrow{CT} (TPT^\bullet \cdots CS_2X^\bullet)^* \rightarrow TPT^+ + CS_2X^- + h\nu \tag{5-3}$$

Figure 5.2-b also displays such charge-transfer emission in **TPT**-SMILES from the perspective of Jablonski diagram.

With the fundamental information of charge-transfer transition in **TPT**-SMILES being well perceived from theoretical models in procedures (5-2), previous group member Sina's work indicates the formation of **TPT•**[CS_2BF_4] ion pair is the main reason for the unique charge-transfer

emission band. The transformation from freely dissolved dyes to assembled species with CS are specified as following:[114]

$$\mathbf{TPT}^{+}[BF_4]^{-} \rightleftharpoons \mathbf{TPT}^{+} + BF_4^{-} \quad \text{(in DCM, blue emission)} \quad (5\text{-}4)$$

$$2\mathbf{CS} + BF_4^{-} \rightleftharpoons [\mathbf{CS}_2\ BF_4]^{-} \quad \text{(in DCM)} \quad (5\text{-}5)$$

$$[\mathbf{CS}_2\ BF_4]^{-} + \mathbf{TPT}^{+} \rightleftharpoons \mathbf{TPT}^{+}[\mathbf{CS}_2\ BF_4]^{-} \quad \text{(in Benzene/DCM, Quenched)} \quad (5\text{-}6)$$

$$n\ \mathbf{TPT}^{+}[\mathbf{CS}_2\ BF_4]^{-} \rightleftharpoons (\mathbf{TPT}\bullet[\mathbf{CS}_2BF_4])_n \quad \text{(in solids, orange emission)} \quad (5\text{-}7)$$

The previous method of forming **TPT•**$[CS_2BF_4]$ ion pair was by altering solvent polarity, which actually increases the uncertainty owing to the photobleaching of emissive species (5-6). Such strong quenching/photobleaching phenomenon has been observed for **TOTA**-SMILES.[114] To probe the formation of charge-transfer emission, it was suggested to utilize a higher ordered contact ion pairs structure, for example the solids of **TOTA**-SMILES containing (**TOTA•**$[CS_2BF_4])_n$, as shown in Figure 5.2-c.

To track the formation of charge-transfer emission in **TPT**-SMILES, we adapted the method of using solids titration, which is to drop-cast solutions containing different molar ratio of CS and TPT, and specify the changes of photophysical properties by measuring the solid samples. Such method reduces the chances of getting emissive species quenched, and also provides a different perspective to understand the transformation from freely dissolved TPT to hierarchically assembled species (**TPT•**$[CS_2BF_4])_n$, as shown in Figure 5.2-c. We proposed several modes to describe the differences of emissive species, from TPT neat aggregates (TPT dimer, Mode 1), different mixed species of TPT dimers and **TPT•**$[CS_2BF_4]$ ion pairs (Mode 2 and Mode 3) and eventually the purely contact ion pairs (**TPT•**$[CS_2BF_4])_n$ (Mode 4).

Apart from the solids titration method, we also used polystyrene film to embed and isolate the ion pairs of **TPT•**$[CS_2BF_4]$. Polystyrene resembles the low polarity matrix of benzene and highly induces the close contact between $\mathbf{TPT}^{+}$ and $[\mathbf{CS}_2BF_4]^{-}$, therein **TPT•**$[CS_2BF_4]$ ion pair will be stabilized and protected within polystyrene, instead of in solutions, the intermediate radicals ($TPT^{\bullet}$ or $[CS_2BF_4]^{\bullet}$) have a chance to disassociate, then being attacked and have the charge-transfer emission quenched.

5.3 Charge-Transfer Emission in TPT-SMILES

We start by observing the difference in optical properties between TPT and **TPT**-SMILES in different conditions. Samples containing TPT and two molar equivalents of CS are named as TPT-CS_2 to indicate the chemical composition. In the absorption spectra (Figure 5.3-a), for both solutions containing TPT and TPT-CS_2, the TPT's lowest lying absorption band (420 nm) is almost unchanged. Absorption of TPT-CS_2 solution shows the CS typical absorption band at higher energy (320 nm). In polystyrene film, the TPT absorption band is at the same position as in the

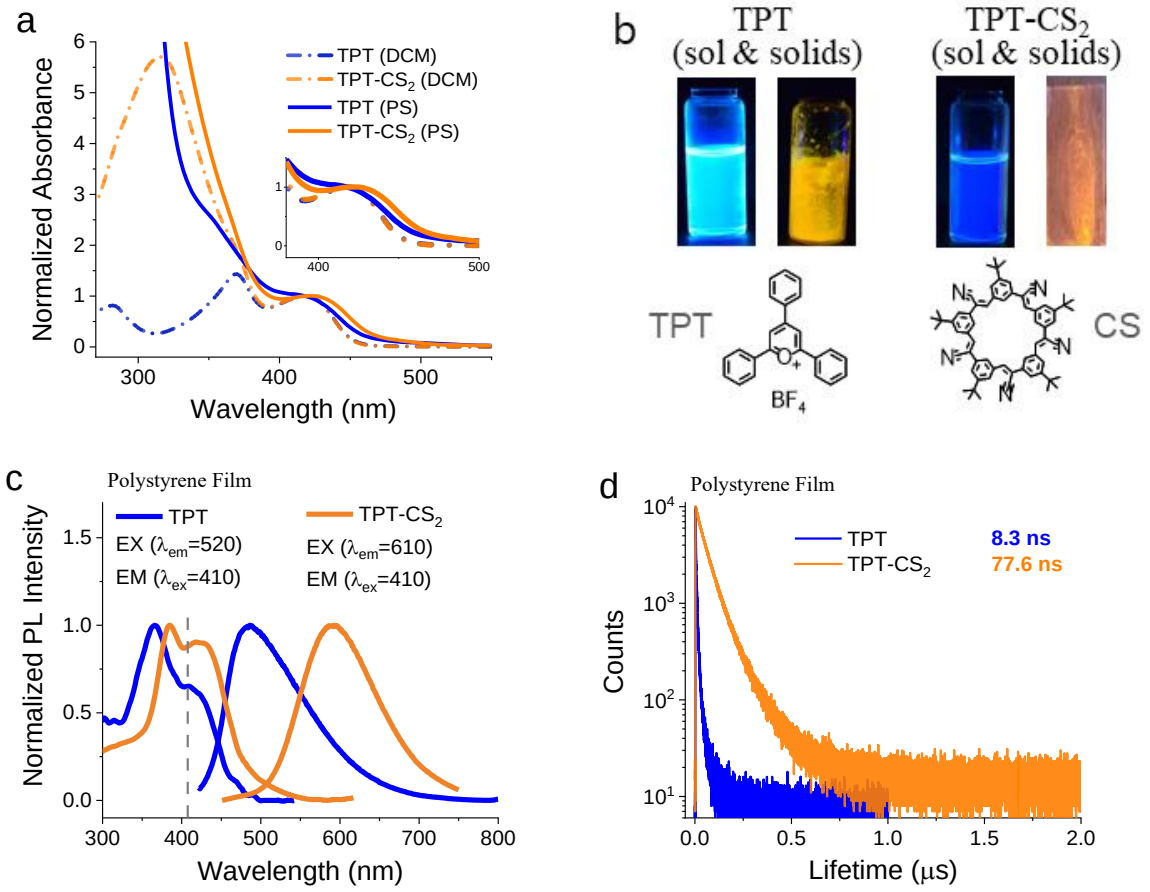

Figure 5.3. (a) Absorption spectra of TPT and TPT-CS_2 in DCM solutions. (b) Chemical structures of TPT and CS. Illustration of TPT and TPT-CS_2 in solution state and solid state under the illumination of 365nm ultraviolet light. (c) Emission and excitation curves of TPT and TPT-CS_2 in polystyrene thin films, λ_{ex}=410 nm for both emission curves, λ_{em}=520 nm for excitation curve of TPT, λ_{em}=610 nm for excitation curve of TPT-CS_2. (d) TCSPC decay curves for TPT (λ_{em}=520 nm) and TPT-CS_2 (λ_{em}=620 nm) in polystyrene thin films, laser light λ_{ex}=407 nm was used for excitation.

solution state, and absorption curve of TPT-CS_2 exhibits a red-shift (~5nm) as compared to the solution state, owing to the generation of **TPT•**[CS_2BF_4] ion pair.

Figure 5.3-b displays the blue emission color of both TPT and TPT-CS_2 in solution state. In solids, TPT neat aggregates shows yellow emission, and TPT-CS_2 shows orange emission. Such phenomenon of red-shifted emission in solids is supported by emission spectra in Figure 5.3-c, in which TPT polystyrene film emits with maximum at 480 nm, locating similarly to the previously reported TPT emission in solution state. Compared to TPT, TPT-CS_2 polystyrene film emission maximum locates at 600 nm, which is close to the **TPT•**[CS_2BF_4] ion pairs emission at 620 nm.

The red-shifted emission band in TPT-CS_2 polystyrene film is accompanied with a much longer lifetime (77.6 ns) than the lifetime of TPT in polystyrene film (8.3 ns) and in solutions (3.1 ns), as shown in Table 5.1. The long lifetime of TPT-CS_2 polystyrene film emission is also also much longer than the lifetime measured for **TPT•**[CS_2BF_4] ion pairs in 95%:5% Benzene:DCM (13.1 ns), suggesting that the encapsulation of polystyrene sustains the long-lived excited state. And such long-lived red-shifted emission is induced by charge-transfer transition happened within the closely contacted ion pair **TPT•**[CS_2BF_4].

Based on the abovementioned confirmation of charge-transfer emission in **TPT**-SMILES solids or polystyrene film, charge-transfer transition prompts a prolonged excited state which decays much longer than molecular TPT, by at least ten fold improvement. Therein we also explored on the potential participancy of triplet states.

Under cryogenic condition (Figure 5.4), both TPT (dissolved in propylene glycol) and **TPT**-SMILES (TPT-CS_2 solids dispersed in propylene glycol) emit differently compared to that measured at room temperature. TPT emits at 450 nm with a diffuse band at 520 nm, the blue-shifted emission maximum is proposed to be the result of confined rotational freedom of TPT and changes in the dielectric. **TPT**-SMILES emits the charge-transfer emission at 620 nm, though residual emission from TPT exists, possibly because of the re-dissolved TPT molecules. In Figure 5.4-b, the excitation curves for bands at TPT (480 nm) and **TPT**-SMILES (620 nm) differ from each other, suggesting the different origins of these two emissions.

In Figure 5.4-c and d, TPT emission at cryogenic conditions has a lifetime of 3 ns for whole emission range. For **TPT**-SMILES, the decay curves for emission at 600~680 nm suggests a long-

lived lifetime reaching around 100 ns, though for the residual part, the lifetime are ~15 ns. In general, we conclude that the generation of distinct charge-transfer emission in **TPT**-SMILES prolongs the original TPT's lifetime to a two orders higher level, though the long decay component still falls in the range of nanosecond, accompanied with the intrinsic long lifetime (τ_0=520 ns) for **TPT**-SMILES solids (Table 5.1), which is still shorter than typical phosphorescence lifetimes, we thus propose the charge-transfer emission in **TPT**-SMILES basically involves singlet state.

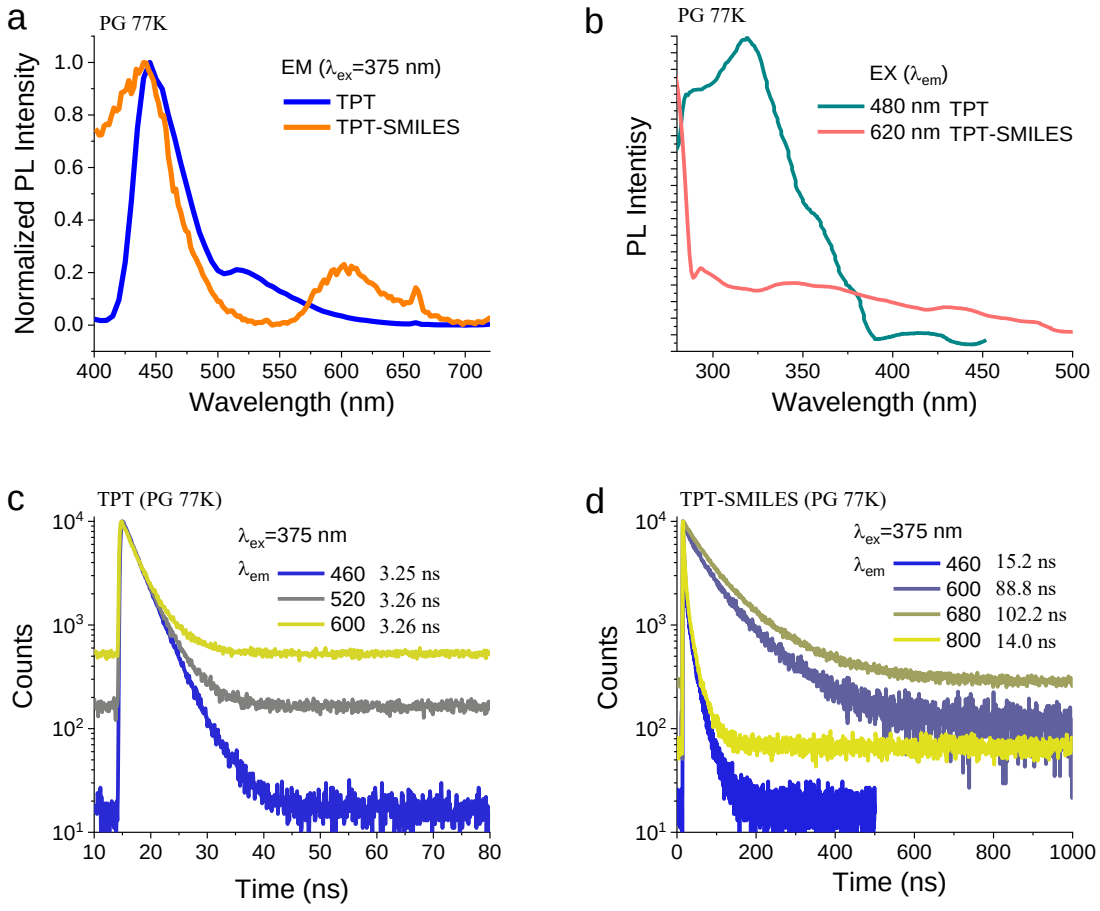

Figure 5.4. (a) Emission spectra of TPT chromophore and **TPT**-SMILES (TPT-CS_2) powders in frozen propylene glycol (PG) at 77K (by using liquid nitrogen), excitation wavelengh was 375 nm. TPT was dissolved in DCM then dissolved into PG, **TPT**-SMILES powders were made from dropcast solids and suspended into PG with good stability. (b) Excitation spectra of TPT and **TPT**-SMILES powders in frozen propylene glycol at 77K (liquid nitrogen), with detector set at 480 nm for TPT and 620 nm for **TPT**-SMILES. (c) TCSPC decay curves for TPT in frozen PG, with detector set at 460 nm, 520 nm and 600 nm, respectively. (d) TCSPC decay curves for **TPT**-SMILES powders in frozen PG, with detector set at 460 nm, 600 nm, 680 nm and 800 nm, respectively.

5.4 Formation of the Long-Lived Excited State

5.4.1 Emission Changes

Figure 5.5 presents the fluorescent emission spectra of dropcast solids samples containing different molar ratio of TPT and CS (denoted as **TPT•**CS_x, x=0~3), and the absorption spectra of corresponding sample's stock solution (in DCM) before being dropcast onto glass (Figure 5.3-a). The linearity of absorbance ratio between typical TPT band (418 nm) and CS band (317 nm) ensures the stepwise addition of CS. In Figure 5.5-c, we compare the emission curves among **TPT•**CS_x solids, a systematic red-shifted is observed for the emission maximum, from the TPT neat aggregated solids (565 nm) to **TPT•**CS_3 solids (620 nm), the emission maximum shifting stops at the molar ratio CS/TPT=2, as the emission maxima of **TPT•**CS_2, **TPT•**$CS_{2.5}$ and **TPT•**CS_3 solids all locate at 620 nm.

To track the emission changes from single molecular TPT to assembled **TPT•**$[CS_2BF_4]$ ion pairs and higher order oligomerization (**TPT•**$[CS_2BF_4])_n$, the emission spectra of TPT (polystyrene film) and samples containing **TPT•**$[CS_2BF_4]$ ion pairs (polystyrene film and solution) were recorded. The monomeric TPT and TPT-CS_2 polystyrene film samples emit at 490 nm and 600 nm, respectively, whereas **TPT•**$[CS_2BF_4]$ ion pair in solution emits at 620 nm.

Compared to the TPT monomer emission (490 nm), TPT neat aggregated solids (Mode 1, TPT dimers) show a red-shifted emission maximum at 565 nm. As the molar ratio of CS/TPT increases, the emissive species gradually forms **TPT•**$[CS_2BF_4]$ ion pairs, which are mixed with TPT dimers, as proposed in Figure 5.2-c Mode 2 and Mode 3. Correspondingly, the increased proportion of **TPT•**$[CS_2BF_4]$ ion pairs is reflected by the emission changes from 565 nm to 620 nm in a systematic manner. Once the molar ratio of CS/TPT is beyond 2, **TPT•**$[CS_2BF_4]$ ion pairs start becoming the dominative emissive species, and the hierarchically contacted ion pairs (**TPT•**$[CS_2BF_4])_n$ all emit identically as the emission of **TPT•**$[CS_2BF_4]$ ion pairs in solution.

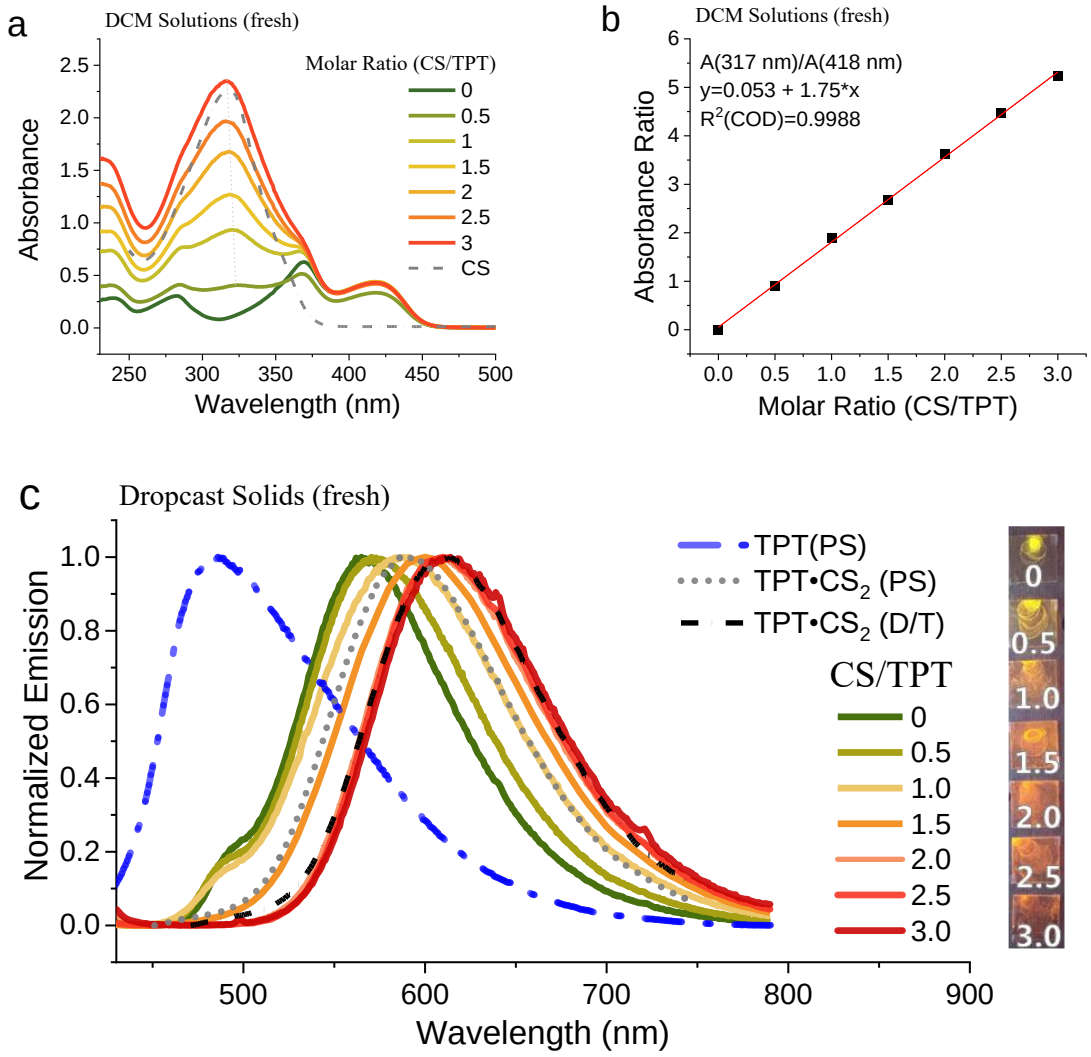

Figure 5.5. (a) Absorption spectra of solutions with different molar ratio of **TPT**[BF_4] and CS, in dichloromethane at the concentration of 10 µM of **TPT**[BF_4] and (b) Plot of absorbance at 317 nm in the function of CS/TPT molar ratio. (c) Emission spectra (λ_{ex}=405 nm) of dropcast solids with different molar ratio of TPT and CS, and corresponding pictures under illumination of 365 nm ultraviolet light. Long dashed (— -) and dotted (•••••) curves refer to TPT and TPT-CS_2 drop-cast polystyrene thin films, short dashed (– • –) curve refers to **TPT**•[CS_2BF_4] in solvent mixture of dichloromethane(D) and toluene(T) (D/T-10/90 vol%).

5.4.2 Lifetime Changes

With the understanding of the emission changes in mind, it is important to delve deeper into the excited state via measurements of luminescence lifetime. For lifetime measurements on **TPT**•CS_x solids (Figure 5.6), decay curves measured at each sample's emission maximum indicate a gradually prolonged lifetime as a function of CS/TPT molar ratio, increasing from 7 ns (**TPT**•CS_0, TPT neat aggregates) to 56 ns (**TPT**•CS_2 solids), then reaches a lifetime plateau once the molar ratio of CS/TPT is larger than 2 (Figure 5.6-b). In order to reduce the potential artefacts arising from the scattering and reabsorption in highly reflective solid emitters, we monitored lifetime

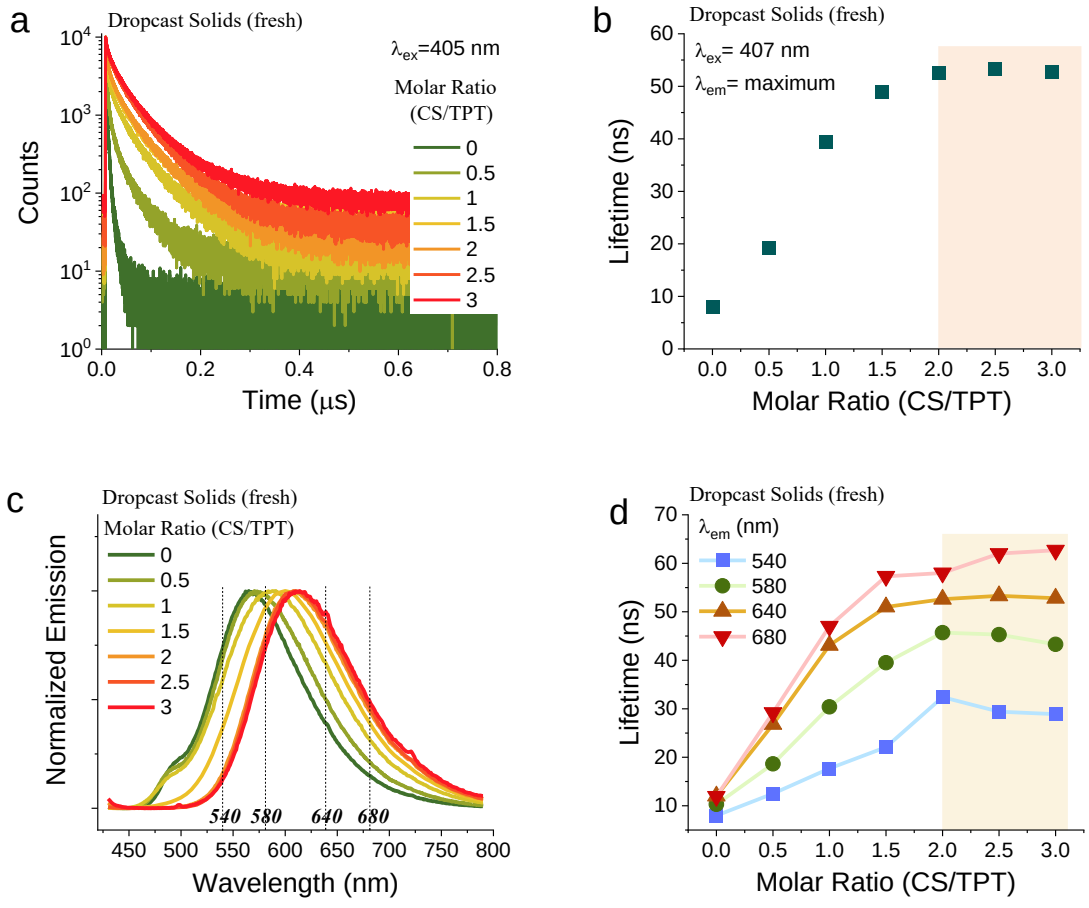

Figure 5.6. (a) TCSPC decay curves of **TPT**•CS_x solids (x=0, 0.5, 1, 1.5, 2, 2.5, 3), and corresponding intensity averaged lifetime plot (b), with the detector set at the maximum of each emission curve. (d) Intensity averaged lifetime plots for **TPT**•CS_x solids, with detector set at wavelength of 540 nm, 580 nm, 640 nm, and 680 nm, as shown in emission curves (c) to indicate the general tendency of lifetime changes with whole emission range covered.

changes at different emission wavelengths (540 nm, 580 nm, 640 nm and 680 nm), as displayed in Figure 5.6-c. Regardless of the detection position, the increase follows the same trend by reaching plateau when the molar ratio CS/TPT ≥ 2 (Figure 5.6-d), which represents an equilibrium of emissive state on account of forming contact ion pairs (**TPT**•$[CS_2BF_4]$)$_n$.

We confirm that the long-lived emission state arises from the addition of CS into TPT, which leads to a much longer lifetime (65 ns in solids) than the both parental components. As CS is added into TPT, and **TPT**•$[CS_2BF_4]$ ion pair formed in solids, the excited state of emissive species is prolonged. The lifetime (7 ns) of TPT dimers (*Mode 1*) is gradually replaced by a much longer lifetime (~53 ns) arising from charge-transfer transition in contact ion pairs (**TPT**•$[CS_2BF_4]$)$_n$ (*Mode 4*).

5.5 Analysis on Charge Transfer Transition

Unravelling the charge transfer mechanism in **TPT**-SMILES system can be nontrivial if solely based on the steady state measurements and lifetime data. In order to further unravel the excited state of charge-transfer emission, radiative and nonradiative rates were evaluated for samples including **TPT**•CS_x dropcast solids, TPT and TPT-CS_2 in polystyrene film and solution, as shown in Table 5.1 and Figure 5.7.

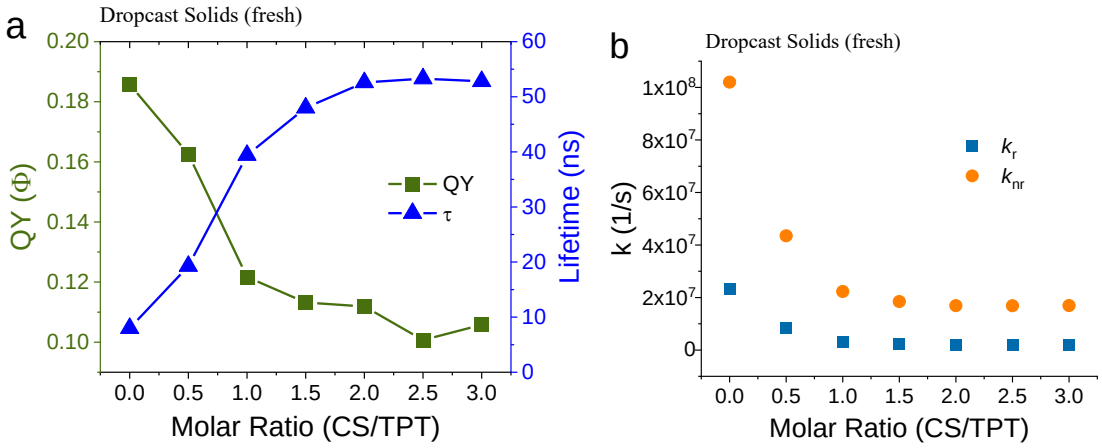

Figure 5.7. (a) Lifetime (detector set at emission maxima) and QYs of **TPT**•CS_x solids (x=0, 0.5, 1.0, 1.5, 2.0, 2.5, 3.0). (b) Radiative and non-radiative constants calculated from lifetime and QYs.

Table 5.1. Photophysical properties of samples.

Sample (composition)		λ_{em} (nm)	Φ(%)[c]	τ (ns)	k_r (s^{-1})[d] ($\times 10^5$)	k_{nr} (s^{-1})[d] ($\times 10^5$)	τ_0 (ns)[d]
Solution[a]	TPT (DCM)	480	58.0	3.1	1883	1364	5
	TPT[CS_2BF_4] (95:5 B:D) [b]	620	2.0	13.1	15	746	657
Polystyrene film	TPT	490	24.7	8.3	298	907	34
	TPT•CS_2	600	14.2	77.6	18	111	546
Dropcast solids	TPT•CS_0	565	18.6	8.0	233	1020	43
	TPT•$CS_{0.5}$	572	16.3	19.3	84	435	118
	TPT•CS_1	588	12.2	39.4	31	223	324
	TPT•$CS_{1.5}$	600	11.3	48.0	24	185	424
	TPT•CS_2	610	11.2	52.6	21	169	470
	TPT•$CS_{2.5}$	615	10.1	53.3	19	168	529
	TPT•CS_3	618	10.3	52.8	20	169	514

a): cited from preliminary research done by Sina Borgi, *Thesis- Ionpair and Solid-state Emitters Based on Bimolecular Charge-Transfer Systems*, 2020, 09.
b): 95:5 B:D refers to 95%:5% Benzene:DCM solvent mixture.
c): The quantum yields were obtained by absolute method, using integrating sphere.
d): calculations for k_r, k_{nr}, τ_0. $k_r=\Phi/\tau$, $k_{nr}=(1-\Phi)/\tau$, $\tau_0=\tau/\Phi$

5.5.1 Photophysical Analysis on the Long-Lived State

Figure 5.7-a exhibits the QY and lifetime of **TPT**•CS_x dropcast solids as a function of CS/TPT molar ratio. A steep decrease of QY occur during the initial formation of **TPT**•[CS_2BF_4], during which the QY drops from 18.6% (TPT dimer, **TPT**•CS_0) to 12.2% (**TPT**•CS_1). The QY decrease slows down when the molar ratio of CS/TPT is large than 1.5, with QY eventually reaches 10% for **TPT**•CS_3.

Analogous to QY changes, the lifetime of **TPT**•CS_x dropcast solids shows a steep increase from 8 ns (**TPT**•CS_0)to 53 ns (TPT•CS_2), then reaches a plateau as the molar ratio of CS/TPT is larger than 2. Based on the QY and lifetime data, we calculated the corresponding rate constants for

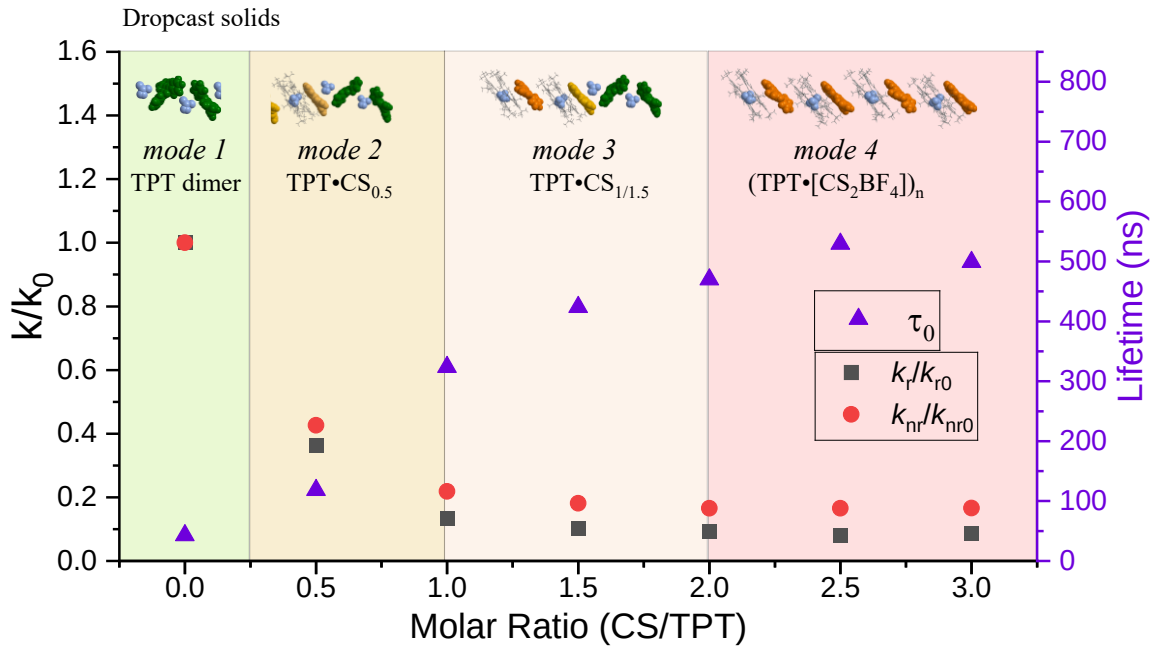

Figure 5.8. Illustration of the putative species within the dropcast **TPT**•CS_x solids and being classified into four modes. Deactivation rate constants ratio (k/k_0) and intrinsic lifetime (τ_0) as a the function of molar ratio CS/TPT, k_0 refers to k_r or k_{nr} for TPT•CS_0, k refers to k_r or k_{nr} for **TPT**•CS_x (x=0.5, 1, 1.5, 2, 2.5, 3) derived from Figure 5.7-b and Table 5.1.

radiative (k_r) and nonradiative (k_{nr}) deactivation pathways (Figure 5.7-b), and also the intrinsic lifetime τ_0 (Table 5.1) which represents an identical lifetime of exciton's fate without the interference of nonradiative pathways.

Comparing to the samples in solution state and polystyrene film (Table 5.1), we can obtain a more holistic view on the photophysical property changes of the transformation from TPT to **TPT**•[CS_2BF_4] ion pairs, as proposed of different modes for emissive species (Figure 5.8).[114]

(***Mode 1***) When we compare the TPT monomer in DCM solution and in TPT dimers in polystyrene film, it is observed that the formation of dimers changes the radiative rate constant (k_r) by a factor of 6, owing to the strong coupling of frontier orbitals of closely packed dyes. Concomitantly, the formation of dimer also reduces the nonradiative constant (k_{nr}). Hereby the photophysical properties of the TPT dimer, as presented in Mode 1,.are well investigated.

The comparison between **TPT**•[CS_2BF_4] in solvent system and in polystyrene film implies that the k_r for both scenarios are similar, and k_{nr} is effectively reduced by the protection of polymer. The intrinsic lifetime (τ_0) for **TPT**•[CS_2BF_4] in solution is larger than in polystyrene system,

however still in the same order. Therefore the photophysical properties of the ion pairs **TPT•**[CS_2BF_4], which represents the constituting unit for the hierarchical structure of Mode 4, are also well investigated. With the rate constants of TPT dimer and the ion pairs **TPT•**[CS_2BF_4] being confirmed, which refer to the beginning and ending phase of structure transformation. A deeper exploration is to focus on the modes containing mixed TPT dimers and **TPT•**[CS_2BF_4] ion pairs.

(***Mode 2***) Mode 2 represent a minor fraction of [CS_2BF_4]$^-$ ion pairs and the majority propotion of TPT dimers, it can be compared to **TPT•**$CS_{0.5}$. Herein certain TPT molecules adjacent to the [CS_2BF_4] ion pairs undergo charge delocalization with CS, however simultaneously exhibits intermolecular interactions with other TPT molecules, therein apparent changes of the deactivation processes can be reflected, with k_r =8.4 × 10^6 s^{-1} (30% of TPT dimer's k_r=2.3 × 10^7 s^{-1}), k_{nr} =4.4 × 10^7 s^{-1} (40% of TPT dimer's k_{nr}=1.0 × 10^8 s^{-1}), τ_0=118 ns (270% of TPT dimer's τ_0=43 ns).

(***Mode 3***) Mode 3 represents coexistence of [CS_2BF_4]$^-$ ion pairs and TPT dimers, and refers to samples of **TPT•**CS_1 and **TPT•**$CS_{1.5}$. In this mode, TPT closely contacts with [CS_2BF_4]$^-$ ion pairs, thereby strengthen the charge delocalization with CS and promote charge-transfer induced emission. In this condition, according to the decreasing tendency shown in Figure 5.6, the fast decrease of both k_r and k_{nr} slows down, reaching a level that k_r is in the range of 2.4 × 10^6 ~ 3.1 × 10^6 s^{-1} (10% of TPT dimer's k_r), k_r is in the range of 1.85 × 10^7 ~ 2.23 × 10^7 s^{-1} (20% of TPT dimer's k_{nr}), τ_0 is in the range of 324 ~ 424 ns (ten times of TPT dimer's τ_0).

(***Mode 4***) Mode 4 represents the eventual formation of hierarchical contact ion pairs (**TPT•**[CS_2BF_4])$_n$, and refers to samples including **TPT•**CS_2, **TPT•**$CS_{2.5}$ and **TPT•**CS_3. In this scenario, we observe the changing tendency for k_r and k_{nr} reaches a plateu, with k_r =2.0 × 10^6 s^{-1} (8.5% of TPT dimer's k_r), k_{nr} =1.7 × 10^7 s^{-1} (17% of TPT dimer's k_{nr}), τ_0=520 ns (twelve times of TPT dimer's τ_0).

Thus, we tracked the formation of hierarchical (**TPT•**[CS_2BF_4])$_n$ structures in a stepwise manner in dropcast solid samples, and eventually confirmed the drastically changed optical performance compared to monomer or dimer of TPT, whose origin lies in having totally different radiative and non-radiative processes. By cofacial stacking with [CS_2BF_4]$^-$ ion pairs, and charge delocalization with CS, a long-lived emissive state is achieved via charge-transfer transition, with a distinct τ_0=520 ns.

5.5.2 Photodegraded Intermediate Species

As specified in the model of charge-transfer transition for **TPT**-SMILES, the ionic donor and acceptor pairs are prone to form into radicals ($TPT^{\bullet}$ and $CS_2^{\bullet}$) after the charge-transfer transition occur, for such intermediate species Coulombic attraction is no longer dominating the bimolecular interactions. Without external forces leading intermediate radicals to close contact and step into recombination, they may disassociate and expose to environmental quenchers, which explains the apparent quenching/photobleaching phenomenon of **TPT**$^{+}[CS_2BF_4]^{-}$ and **TOTA**$^{+}[CS_2\ BF_4]^{-}$ in solutions.[120] The transient disassociation of intermediate radical species may circumvent generating a stable charge-transfer emission, and we discovered that $CS_2^{\bullet}$ is the main radical to be attacked.

In Figure 5.9, absorption spectra of solution samples (**TPT**•CS_x) being placed in light for seven days suggest the identical CS absorption band is diminished, but TPT absorption band is relatively stable (Figure 5.7-a). And such 'old' solutions being drop-cast into solids also failed to exhibit the red-shifted emission as in Figure 5.5, instead all samples emit at the same maximum as the TPT dimer (Figure 5.7-b). Correspondingly, the lifetime of these samples are much shorter compared to freshly prepared **TPT**•CS_x solids (Figure 5.7-c,d). Figure 5.7-d indicates that as higher molar equivalents of CS existed with TPT, the lifetime decrease of charge-transfer emission band is more apparent. Monitoring the photo-degradation in undried matrix containing polystyrene and DCM (Figure 5.7-e,f) exhibits the charge-transfer emission gradually diminished and approaches TPT dimer emission. In general, abovementioned observation suggests that the quenching of **TPT**$^{+}[CS_2\ BF_4]^{-}$ charge-transfer emission is mainly arising from attacks on $CS_2^{\bullet}$ and CS structure decomposition.

Therefore, once being transformed into solids, **TPT**-SMILES can steadily emit the long-lived charge-transfer emission. Such observation also corroborates with **TOTA**•$[CS_2BF_4]$ ion pairs, where a quenched emission is perceived in solution state, however a stable unquenched emission is observed for (**TOTA**•$[CS_2BF_4])_n$ solids with long-lived emissive state.

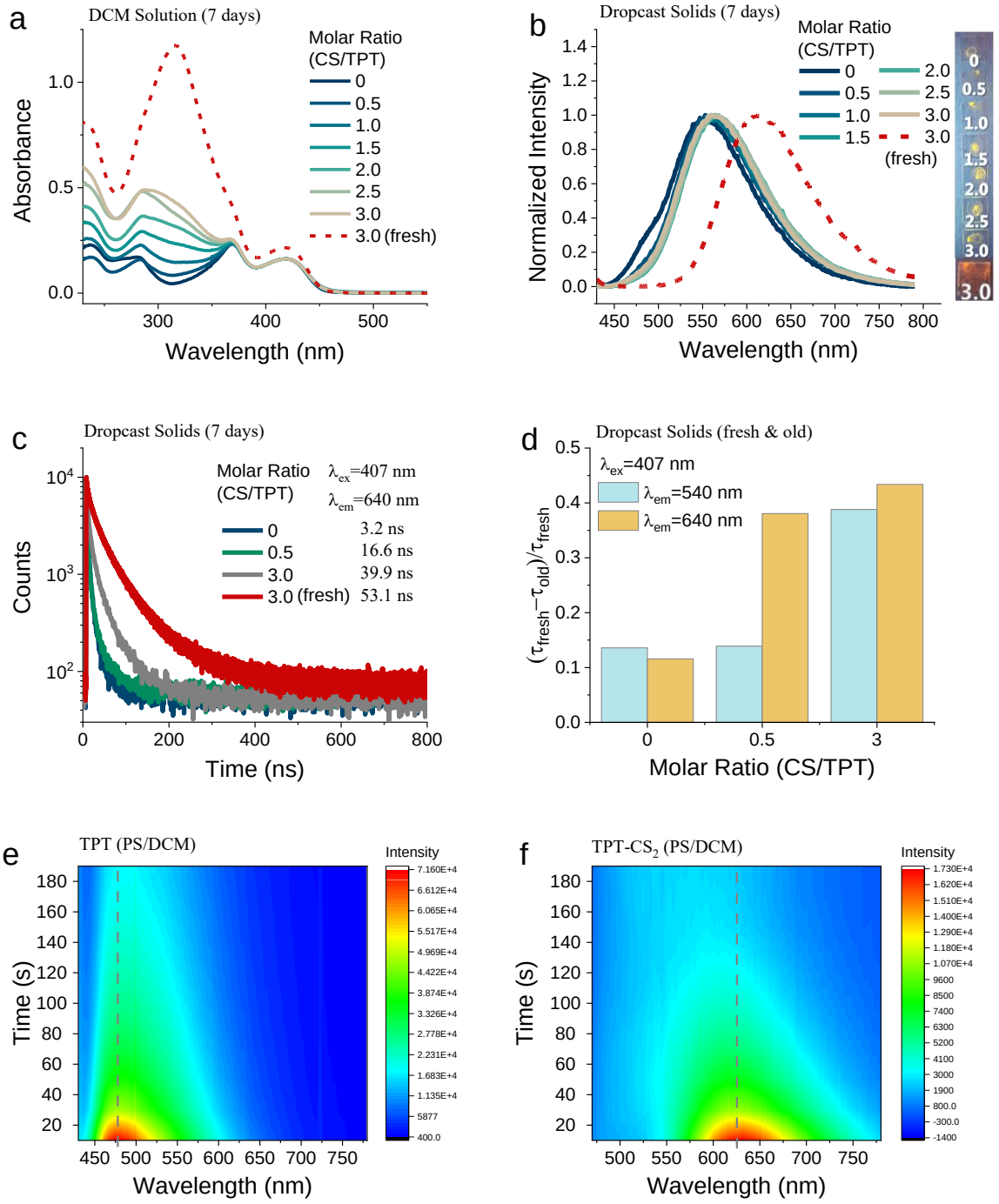

Figure 5.9. (a) Absorption spectra of **TPT**•CSx solutions (DCM 5 mM) and stored for 7 days with exposure to natural lights. (b) Emission curves of corresponding drop-cast solid samples. (c) Decay curves of old solid samples **TPT**•CS_x (x=0, 0.5, 3.0) in comparison to freshly prepared **TPT**•CS_3. (d) The decrease of lifetime in old solid samples (solution samples placed for 7 days) compared to freshly prepared samples (τ_{fresh} for fresh samples of **TPT**•CS_0 **TPT**•$CS_{0.5}$ **TPT**•CS_3, separately), lifetime were measured at λ_{em}=540 nm and 640 nm. (e-f) Time correlated emission spectra of (e) TPT and (f) TPT-CS_2 in undried polystyrene film (PS/DCM: 2/98 vol%), illuminated by laser light (λ_{ex}=407 nm).

5.6 Conclusions

In this chapter, we explored the long-lived charge-transfer emissive state in **TPT**-SMILES solids, which occurs as TPT HOMO is energetically lower than CS_2•X^- HOMO. The prolonged lifetime and red-shifted emission induced by charge-transfer are characterized in **TPT**•CS_x solids in a stepwise solids titration. Based on previous research on analogous **TOTA**-SMILES, we propose different modes of emissive species, containing different interactions between TPT dimers and **TPT**•[CS_2BF_4] ion pairs. We confirm that the addition of CS into TPT efficiently induces charge delocalization and extends the exciton's fate, thereby generating a long-lived (~80 ns) and red-shifted (620 nm) emission with an intrinsic lifetime reaching 520 ns.

In general, this exploration on the prolonged exciton's fate by intermolecular charge-transfer transition within SMILES solid emitters extended our understanding on a new pathway of utilizing SMILES strategy, which does not follow the previous assigned 'HOMO-LUMO window' rule, but still generates long-lived emission which can be beneficial to applications including photocatalysis and optoelectrical materials.

Concluding Remarks

This thesis aims to explore the attainment of long-lived luminescence in SMILES-based structures by focusing on two main aspects: Firstly, it aims to protect the triplet emission of phosphorescent dyes by suppressing non-radiative pathways. Secondly, electronic donor-acceptor systems are created in SMILES to facilitate the formation of exciplexes, involving charge-transfer transitions between fluorescent dyes and CS, which generate identical charge-transfer emission with prolonged luminescence lifetime.

Part I: Interactions between CS and Phosphorescent Dyes, and Phosphorescent SMILES

Part I of the thesis delves into fundamental investigations of the bimolecular interactions between cyanostar (CS) and a series of mono-cationic phosphorescent dyes (PtTA). This research is pivotal for understanding the dynamics of these interactions, particularly concerning energy transfer processes and the involved triplet state energy levels. Stern-Volmer experiments are conducted to elucidate the triplet state energy level of CS, providing crucial insights into its suitability as a host molecule for phosphorescent dyes. By studying these interactions in solution, a benchmark is established where the energy of the triplet state of the dye ($E_{T\text{-}dye}$) is less than the triplet state energy level of CS ($E_{T\text{-}CS}$= 2.0 eV), ensuring efficient prevention of triplet energy transfer to CS. This lays the groundwork for the subsequent exploration of achieving phosphorescent SMILES solid emitters.

The utilization of three PtTA complexes in phosphorescent SMILES solid emitters aligns with the established triplet energy matching criterion observed in the solution state. Successful generation of Pt3-SMILES crystals and nanoparticles with improved emission and prolonged lifetime marks the initiation of the phosphorescent SMILES. Detailed investigations suggest that bypassing Pt3's non-radiative deactivation pathways in SMILES significantly contributes to the enhanced phosphorescence observed in Pt3-SMILES compared to Pt3 in the solution state. Thus, the phosphorescent SMILES strategy has been fundamentally established by utilizing mono-cationic phosphorescent dyes.

Part II: Exploration of Phosphorescent SMILES with Metalloporphyrin Dyes

In Part II, a multi-cationic metalloporphyrin dye (Por4) is employed to explore phosphorescent SMILES with more complex charge-by-charge stacking structures and longer lifetimes. This section builds upon the findings of Part I, aiming to enhance the phosphorescence of metalloporphyrin dyes within SMILES structures. The effectiveness of SMILES in enhancing the phosphorescence of metalloporphyrin dyes is demonstrated, showcasing its potential as an alternative to cryogenic conditions for achieving strong phosphorescence. Through the synthesis of Por4-SMILES crystals and nanoparticles, the weak phosphorescence of Por4 observed in solution, accompanied by fluorescence, is significantly improved. These nanoparticles emit red phosphorescence with millisecond-range lifetimes, highlighting the utility of SMILES in extending the luminescence lifetime of metalloporphyrin dyes.

Part III: Utilizing Exciplex Formation to Prolong Luminescence Lifetimes

In contrast to the previous sections focusing on monitoring chromophores' triplet emission, Part III explores the utilization of exciplex formation to prolong fluorophores' luminescence lifetimes. Exciplex formation involves charge-transfer transitions between fluorescent dyes and CS, resulting in identical charge-transfer emission with prolonged luminescence lifetime. This section tracks the charge-transfer transition by measuring solid samples with various molar ratios of CS and fluorophore (TPT), ultimately confirming the long-lived excited state originating from the charge-transfer mechanism. This approach offers a promising strategy for achieving long-lived luminescence in SMILES-based structures, expanding the range of luminescent lifetimes available for bio-imaging applications and other relevant fields.

Despite the promising concepts and experimental data presented in these chapters, several challenges still persist in the development of phosphorescent SMILES. Firstly, the bulky nature of phosphorescent chromophores poses a significant challenge as they have a high propensity for self-aggregation. This complicates the crystal engineering process for phosphorescent SMILES self-assemblies, presenting practical challenges in achieving desired structures. Additionally, the phosphorescent chromophores utilized in the initial chapters exhibit low absorption coefficients, limiting the potential for further enhancement of brightly emissive phosphorescent SMILES.

Efforts to improve the brightness of phosphorescent SMILES emission through the introduction of different dopants have been explored. These dopants aim to facilitate the energy transfer process, directing photons absorbed from highly absorbing fluorophores to phosphorescent dyes. However, many empirical doping strategies have failed to yield the desired results. In some cases, fluorescent dopants were unable to efficiently induce energy transfer to the phosphorescent acceptor, despite significant spectral overlap. In other instances, even if the energy transfer process occurred, as evidenced by the reduction in the fluorophore's lifetime, the resulting phosphorescent emission remained weak due to quenching phenomena.

Moreover, while the formation of charge-transfer emission in SMILES is feasible by simply mixing compounds to form solids, translating this long-lived emission into nanoparticles presents challenges. The emission tends to be quenched in aqueous solutions, complicating the development of long-lived charge-transfer emission in SMILES nanoparticles.

Overall, significant progress has been made in achieving long-lived luminescent SMILES and has the potential to inspire further investigations on long-lived luminescence in similar supramolecular constructs. Further modulation of this property and extending its applications for practical usage pose pivotal and urgent challenges. Ensuring the stabilization of the long-lived excited state in various conditions, particularly in the presence of abundant quenchers, remains a critical objective for future research in this field.

References

[1] C. R. Benson, L. Kacenauskaite, K. L. VanDenburgh, W. Zhao, B. Qiao, *Plug-and-Play Optical Materials from Fluorescent Dyes and Macrocycles*. *Chem*. **2020**, 6, 1978-1997.

[2] S. Lee, C. H. Chen, A. H. Flood, *A pentagonal cyanostar macrocycle with cyanostilbene CH donors binds anions and forms dialkylphosphate [3]rotaxanes*. *Nat Chem*. **2013**, 5, 704-710.

[3] M. Yamashina, M. M. Sartin, Y. Sei, M. Akita, S. Takeuchi, *Preparation of Highly Fluorescent Host-Guest Complexes with Tunable Color upon Encapsulation*. *J Am Chem Soc*. **2015**, 137, 9266-9269.

[4] F. Wurthner, T. E. Kaiser, C. R. Saha-Moller, *J-aggregates: from serendipitous discovery to supramolecular engineering of functional dye materials*. *Angew Chem Int Ed Engl*. **2011**, 50, 3376-3410.

[5] S. Varghese, S. K. Park, S. Casado, R. C. Fischer, R. Resel, *Stimulated Emission Properties of Sterically Modified Distyrylbenzene-Based H-Aggregate Single Crystals*. *J Phys Chem Lett*. **2013**, 4, 1597-1602.

[6] N. J. Hestand, F. C. Spano, *Expanded Theory of H- and J-Molecular Aggregates: The Effects of Vibronic Coupling and Intermolecular Charge Transfer*. *Chem Rev*. **2018**, 118, 7069-7163.

[7] X. Ding, C. Wei, L. Wang, J. Yang, W. Huang, *Multicomponent flexible organic crystals*. *SmartMat*. **2023**.

[8] Y. Wang, H. Wu, W. Hu, J. F. Stoddart, *Color-Tunable Supramolecular Luminescent Materials*. *Adv Mater*. **2022**, 34, e2105405.

[9] T. L. Mako, J. M. Racicot, M. Levine, *Supramolecular Luminescent Sensors*. *Chem Rev*. **2019**, 119, 322-477.

[10] L. Kacenauskaite, S. G. Stenspil, A. H. Olsson, A. H. Flood, B. W. Laursen, *Universal Concept for Bright, Organic, Solid-State Emitters Doping of Small-Molecule Ionic Isolation Lattices with FRET Acceptors*. *J Am Chem Soc*. **2022**, 144, 19981-19989.

[11] J. Chen, S. G. Stenspil, S. Kaziannis, L. Kacenauskaite, N. Lenngren, *Quantitative Energy Transfer in Organic Nanoparticles Based on Small-Molecule Ionic Isolation Lattices for UV Light Harvesting*. *ACS Applied Nano Materials*. **2022**, 5, 13887-13893.

[12] J. Chen, S. M. A. Fateminia, L. Kacenauskaite, N. Baerentsen, S. Gronfeldt Stenspil, *Ultrabright Fluorescent Organic Nanoparticles Based on Small-Molecule Ionic Isolation Lattices*. *Angew Chem Int Ed Engl*. **2021**, 60, 9450-9458.

[13] H. Yong, N. Zotev, J. M. Ruddock, B. Stankus, M. Simmermacher, *Observation of the molecular response to light upon photoexcitation*. *Nat Commun*. **2020**, 11, 2157.

[14] B. Valeur, M. N. Berberan-Santos, *Molecular Fluorescence*. (2012).

[15] J. R. Lakowicz, *Principles of Fluorescence Spectroscopy*. (2006).

[16] J. R. Lakowicz, G. Piszczek, J. S. Kang, *On the possibility of long-wavelength long-lifetime high-quantum-yield luminophores*. *Anal Biochem*. **2001**, 288, 62-75.

[17] J. Gierschner, S. Varghese, S. Y. Park, *Organic Single Crystal Lasers: A Materials View*. *Advanced Optical Materials*. **2015**, 4, 348-364.

[18] C. Wu, D. T. Chiu, *Highly fluorescent semiconducting polymer dots for biology and medicine*. *Angew Chem Int Ed Engl*. **2013**, 52, 3086-3109.

[19] M. Kasha, *Characterization of electronic transitions in complex molecules*. *Discussions of the Faraday Society*. **1950**, 9.

[20] IUPAC, *Kasha Rule: Polyatomic molecular entities luminesce with appreciable yield only from the lowest excited state of a given multiplicity*. **2006**.

[21] M. A. El-Sayed, *Triplet state. Its radiative and nonradiative properties*. *Accounts of Chemical Research*. **1967**, 1, 8-16.

[22] X. D. Wang, O. S. Wolfbeis, R. J. Meier, *Luminescent probes and sensors for temperature*. *Chem Soc Rev*. **2013**, 42, 7834-7869.

[23] T. Itoh, *Fluorescence and phosphorescence from higher excited states of organic molecules*. *Chem Rev*. **2012**, 112, 4541-4568.

[24] Q. Zhao, F. Li, C. Huang, *Phosphorescent chemosensors based on heavy-metal complexes*. *Chem Soc Rev*. **2010**, 39, 3007-3030.

[25] M. H. Gehlen, *The centenary of the Stern-Volmer equation of fluorescence quenching: From the single line plot to the SV quenching map*. *Journal of Photochemistry and Photobiology C: Photochemistry Reviews*. **2020**, 42.

[26] J. Gierschner, J. Shi, B. Milián-Medina, D. Roca-Sanjuán, S. Varghese, *Luminescence in Crystalline Organic Materials: From Molecules to Molecular Solids*. *Advanced Optical Materials*. **2021**, 9, 2002251.

[27] M. G. Lagorio, *Determination of Fluorescence Quantum Yields in Scattering Media*. *Methods Appl Fluoresc*. **2020**, 8.

[28] S. Kumar Panigrahi, A. Kumar Mishra, *Inner filter effect in fluorescence spectroscopy: As a problem and as a solution*. *Journal of Photochemistry and Photobiology C: Photochemistry Reviews*. **2019**, 41, 100318.

[29] J. Tao, D. Liu, J. Jing, H. Dong, L. Liu, *Organic Single Crystals with High Photoluminescence Quantum Yields Close to 100% and High Mobility for Optoelectronic Devices*. *Adv Mater*. **2021**, 33, e2105466.

[30] P. Yu, Y. Zhen, H. Dong, W. Hu, *Crystal Engineering of Organic Optoelectronic Materials*. *Chem*. **2019**, 5, 2814-2853.

[31] Q. Liao, Q. Li, Z. Li, *The Key Role of Molecular Packing in Luminescence Property: from Adjacent Molecules to Molecular Aggregates*. *Adv Mater*. **2023**, e2306617.

[32] M. Kasha, H. R. Rawls, M. Ashraf El-Bayoumi, *The exciton model in molecular spectroscopy*. *Pure and Applied Chemistry*. **1965**, 11, 371-392.

[33] J. L. Bricks, Y. L. Slominskii, I. D. Panas, A. P. Demchenko, *Fluorescent J-aggregates of cyanine dyes: basic research and applications review*. *Methods Appl Fluoresc*. **2017**, 6, 012001.

[34] Z. Z. Li, L. S. Liao, X. D. Wang, *Controllable Synthesis of Organic Microcrystals with Tunable Emission Color and Morphology Based on Molecular Packing Mode*. *Small*. **2018**, 14.

[35] J. Gierschner, S. Y. Park, *Luminescent distyrylbenzenes: tailoring molecular structure and crystalline morphology*. *Journal of Materials Chemistry C*. **2013**, 1.

[36] J. Li, G. Wang, X. Chen, X. Li, M. Wu, *Manipulation of Triplet Excited States in Two-Component Systems for High-Performance Organic Afterglow Materials*. *Chemistry*. **2022**, 28, e202200852.

[37] P. C. Nandajan, H. J. Kim, S. Casado, S. Y. Park, J. Gierschner, *Insight into Water-Soluble Highly Fluorescent Low-Dimensional Host-Guest Supramolecular Polymers: Structure and Energy-Transfer Dynamics Revealed by Polarized Fluorescence Spectroscopy*. *J Phys Chem Lett*. **2018**, 9, 3870-3877.

[38] X. Ma, J. Wang, H. Tian, *Assembling-Induced Emission: An Efficient Approach for Amorphous Metal-Free Organic Emitting Materials with Room-Temperature Phosphorescence*. *Acc Chem Res*. **2019**, 52, 738-748.

[39] Z. Wu, J. Nitsch, T. B. Marder, *Persistent Room-Temperature Phosphorescence from Purely Organic Molecules and Multi-Component Systems*. *Advanced Optical Materials*. **2021**, 9, 2100411.

[40] Z. Huang, X. Ma, *Tailoring Tunable Luminescence via Supramolecular Assembly Strategies*. *Cell Reports Physical Science*. **2020**, 1.

[41] M. J. Gu, X. N. Han, Y. Han, C. F. Chen, *Strategies for Constructing Macrocyclic Arene-Based Color-Tunable Supramolecular Luminescent Materials*. *Chempluschem*. **2024**, e202400023.

[42] D. Sun, Y. Wu, X. Han, S. Liu, *The host-guest inclusion driven by host-stabilized charge transfer for construction of sequentially red-shifted mechanochromic system*. *Nat Commun*. **2023**, 14, 4190.

[43] R. N. Dsouza, U. Pischel, W. M. Nau, *Fluorescent dyes and their supramolecular host/guest complexes with macrocycles in aqueous solution*. *Chem Rev*. **2011**, 111, 7941-7980.

[44] X. Y. Lou, S. Zhang, Y. Wang, Y. W. Yang, *Smart organic materials based on macrocycle hosts*. *Chem Soc Rev*. **2023**, 52, 6644-6663.

[45] C. J. Pedersen, *Cyclic polyethers and their complexes with metal salts*. *Journal of the American Chemical Society*. **2002**, 89, 2495-2496.

[46] Z. Niu, H. W. Gibson, *Polycatenanes*. *Chem Rev*. **2009**, 109, 6024-6046.

[47] H. G. Fu, H. Y. Zhang, H. Y. Zhang, Y. Liu, *Photo-controlled chirality transfer and FRET effects based on pseudo[3]rotaxane*. *Chem Commun (Camb)*. **2019**, 55, 13462-13465.

[48] X. Ma, H. Tian, *Stimuli-responsive supramolecular polymers in aqueous solution*. *Acc Chem Res*. **2014**, 47, 1971-1981.

[49] J. Liu, Y. Lan, Z. Yu, C. S. Tan, R. M. Parker, *Cucurbit[n]uril-Based Microcapsules Self-Assembled within Microfluidic Droplets: A Versatile Approach for Supramolecular Architectures and Materials*. *Acc Chem Res*. **2017**, 50, 208-217.

[50] Z. Y. Zhang, Y. Liu, *Ultralong room-temperature phosphorescence of a solid-state supramolecule between phenylmethylpyridinium and cucurbit[6]uril*. *Chem Sci*. **2019**, 10, 7773-7778.

[51] Z. Y. Zhang, Y. Chen, Y. Liu, *Efficient Room-Temperature Phosphorescence of a Solid-State Supramolecule Enhanced by Cucurbit[6]uril*. *Angew Chem Int Ed Engl*. **2019**, 58, 6028-6032.

[52] H. Nie, Z. Wei, X. L. Ni, Y. Liu, *Assembly and Applications of Macrocyclic-Confinement-Derived Supramolecular Organic Luminescent Emissions from Cucurbiturils*. *Chem Rev*. **2022**, 122, 9032-9077.

[53] D. Li, F. Lu, J. Wang, W. Hu, X. M. Cao, *Amorphous Metal-Free Room-Temperature Phosphorescent Small Molecules with Multicolor Photoluminescence via a Host-Guest and Dual-Emission Strategy*. *J Am Chem Soc*. **2018**, 140, 1916-1923.

[54] T. Jiang, X. Wang, J. Wang, G. Hu, X. Ma, *Humidity- and Temperature-Tunable Multicolor Luminescence of Cucurbit[8]uril-Based Supramolecular Assembly*. *ACS Appl Mater Interfaces*. **2019**, 11, 14399-14407.

[55] S. Shinkai, *Calixarenes - the third generation of supramolecules*. *Tetrahedron*. **1993**, 49, 8933-8968.

[56] M. Xue, Y. Yang, X. Chi, Z. Zhang, F. Huang, *Pillararenes, a new class of macrocycles for supramolecular chemistry*. *Acc Chem Res*. **2012**, 45, 1294-1308.

[57] M. A. H. Muhammed, L. K. Cruz, A. H. Emwas, A. M. El-Zohry, B. Moosa, *Pillar[5]arene-Stabilized Silver Nanoclusters: Extraordinary Stability and Luminescence Enhancement Induced by Host-Guest Interactions*. *Angew Chem Int Ed Engl*. **2019**, 58, 15665-15670.

[58] L. Yang, P. Langer, E. S. Davies, M. Baldoni, K. Wickham, *Synthesis and characterisation of rylene diimide dimers using molecular handcuffs*. *Chem Sci*. **2019**, 10, 3723-3732.

[59] A. H. Flood, *Creating molecular macrocycles for anion recognition*. *Beilstein J Org Chem*. **2016**, 12, 611-627.

[60] E. M. Fatila, E. B. Twum, A. Sengupta, M. Pink, J. A. Karty, *Anions Stabilize Each Other inside Macrocyclic Hosts*. *Angew Chem Int Ed Engl*. **2016**, 55, 14057-14062.

[61] L. M. Azofra, J. Elguero, I. Alkorta, *Stabilisation of dianion dimers trapped inside cyanostar macrocycles*. *Phys Chem Chem Phys*. **2020**, 22, 11348-11353.

[62] P. Deshmukh, S. Satapathy, E. Michail, A. H. Olsson, R. Bushati, *Plug-and-Play Molecular Approach for Room Temperature Polariton Condensation*. *ACS Photonics*. **2024**.

[63] J. Zhao, W. Wu, J. Sun, S. Guo, *Triplet photosensitizers: from molecular design to applications*. *Chem Soc Rev*. **2013**, 42, 5323-5351.

[64] X. Yan, H. Peng, Y. Xiang, J. Wang, L. Yu, *Recent Advances on Host-Guest Material Systems toward Organic Room Temperature Phosphorescence*. *Small*. **2022**, 18, e2104073.

[65] C. A. Mitchell, R. W. Gurney, S.-H. Jang, B. Kahr, *On the Mechanism of Matrix-Assisted Room Temperature Phosphorescence*. *Journal of the American Chemical Society*. **1998**, 120, 9726-9727.

[66] Y. Li, G. Baryshnikov, F. Siddique, P. Wei, H. Wu, *Vibration-Regulated Multi-State Long-Lived Emission from Star-Shaped Molecules*. *Angew Chem Int Ed Engl*. **2022**.

[67] W. Ye, H. Ma, H. Shi, H. Wang, A. Lv, *Confining isolated chromophores for highly efficient blue phosphorescence*. *Nat Mater*. **2021**, 20, 1539-1544.

[68] X. Sun, Y. D. Yang, X. L. Chen, A. H. Sun, J. F. Xiang, *Macrocycle-Based Crystalline Sponge that Stabilizes and Lights Up Cationic Aggregation-Caused Quenching Dyes*. *Advanced Optical Materials*. **2021**, 9.

[69] T. Förster, *Excimers*. *Angewandte Chemie International Edition in English*. **1969**, 8, 333-343.

[70] F. Edhborg, A. Olesund, V. Tripathy, Y. Wang, T. Sadhukhan, *Triplet States of Cyanostar and Its Anion Complexes*. *J Phys Chem A*. **2023**, 127, 5841-5850.

[71] P. J. Wagner, I. Kochevar, *Triplet energy transfer. III. How efficient is diffusion-controlled triplet energy transfer*. *Journal of the American Chemical Society*. **2002**, 90, 2232-2238.

[72] R. Akaba, K. Ohshima, Y. Kawai, Y. Obuchi, A. Negishi, *Triplet-mediated electron transfer oxygenation of stilbene derivatives with 2,4,6-triphenylpyrylium tetrafluoroborate*. *Tetrahedron Letters*. **1991**, 32, 109-112.

[73] Q. Z. Yang, L. Z. Wu, Z. X. Wu, L. P. Zhang, C. H. Tung, *Long-lived emission from platinum(II) terpyridyl acetylide complexes*. *Inorg Chem*. **2002**, 41, 5653-5655.

[74] F. Guo, W. Sun, Y. Liu, K. Schanze, *Synthesis, photophysics, and optical limiting of platinum(II) 4'-tolylterpyridyl arylacetylide complexes*. *Inorg Chem*. **2005**, 44, 4055-4065.

[75] V. W. Yam, K. M. Wong, N. Zhu, *Solvent-induced aggregation through metal...metal/pi...pi interactions: large solvatochromism of luminescent organoplatinum(II) terpyridyl complexes*. *J Am Chem Soc*. **2002**, 124, 6506-6507.

[76] V. W. Yam, *Molecular design of transition metal alkynyl complexes as building blocks for luminescent metal-based materials: structural and photophysical aspects*. *Acc Chem Res*. **2002**, 35, 555-563.

[77] K. M. Wong, W. S. Tang, X. X. Lu, N. Zhu, V. W. Yam, *Functionalized platinum(II) terpyridyl alkynyl complexes as colorimetric and luminescence pH sensors*. *Inorg Chem*. **2005**, 44, 1492-1498.

[78] X. J. Liu, J. K. Feng, J. Meng, Q. J. Pan, A. M. Ren, *A Theoretical Investigation of Substituent Effects on the Absorption and Emission Properties of a Series of*

Terpyridylplatinum(II) Acetylide Complexes. *European Journal of Inorganic Chemistry*. **2005**, 2005, 1856-1866.

[79] A. Y. Tam, W. H. Lam, K. M. Wong, N. Zhu, V. W. Yam, *Luminescent alkynylplatinum(II) complexes of 2,6-bis(N-alkylbenzimidazol-2'-yl)pyridine-type ligands with ready tunability of the nature of the emissive states by solvent and electronic property modulation*. *Chemistry*. **2008**, 14, 4562-4576.

[80] C. W. Hsu, C. C. Lin, M. W. Chung, Y. Chi, G. H. Lee, *Systematic investigation of the metal-structure-photophysics relationship of emissive d10-complexes of group 11 elements: the prospect of application in organic light emitting devices*. *J Am Chem Soc*. **2011**, 133, 12085-12099.

[81] E. Shikhova, E. O. Danilov, S. Kinayyigit, I. E. Pomestchenko, A. D. Tregubov, *Excited-state absorption properties of platinum(II) terpyridyl acetylides*. *Inorg Chem*. **2007**, 46, 3038-3048.

[82] F. N. Castellano, I. E. Pomestchenko, E. Shikhova, F. Hua, M. L. Muro, *Photophysics in bipyridyl and terpyridyl platinum(II) acetylides*. *Coordination Chemistry Reviews*. **2006**, 250, 1819-1828.

[83] X. Wang, S. Goeb, Z. Ji, F. N. Castellano, *Excited state absorption properties of Pt(II) terpyridyl complexes bearing pi-conjugated arylacetylides*. *J Phys Chem B*. **2010**, 114, 14440-14449.

[84] A. A. Rachford, S. Goeb, R. Ziessel, F. N. Castellano, *Ligand localized triplet excited states in platinum(II) bipyridyl and terpyridyl peryleneacetylides*. *Inorg Chem*. **2008**, 47, 4348-4355.

[85] X. Han, L. Z. Wu, G. Si, J. Pan, Q. Z. Yang, *Switching between ligand-to-ligand charge-transfer, intraligand charge-transfer, and metal-to-ligand charge-transfer excited states in platinum(II) terpyridyl acetylide complexes induced by pH change and metal ions*. *Chemistry*. **2007**, 13, 1231-1239.

[86] W. H. Lam, E. S. Lam, V. W. Yam, *Computational studies on the excited states of luminescent platinum(II) alkynyl systems of tridentate pincer ligands in radiative and nonradiative processes*. *J Am Chem Soc*. **2013**, 135, 15135-15143.

[87] K. Li, G. S. Ming Tong, Q. Wan, G. Cheng, W. Y. Tong, *Highly phosphorescent platinum(ii) emitters: photophysics, materials and biological applications*. *Chem Sci*. **2016**, 7, 1653-1673.

[88] G. S. Tong, C. M. Che, *Emissive or nonemissive? A theoretical analysis of the phosphorescence efficiencies of cyclometalated platinum(II) complexes*. *Chemistry*. **2009**, 15, 7225-7237.

[89] S. Goeb, V. Prusakova, X. Wang, A. Vezinat, M. Salle, *Phosphorescent self-assembled Pt(II) tetranuclear metallocycles*. *Chem Commun (Camb)*. **2011**, 47, 4397-4399.

[90] C. H. Tao, N. Zhu, V. W. Yam, *Room-temperature phosphorescence and energy transfer in luminescent multinuclear platinum(II) complexes of branched alkynyls*. *Chemistry*. **2005**, 11, 1647-1657.

[91] H. Yang, H. Li, L. Yue, X. Chen, D. Song, *Aggregation-induced phosphorescence emission (AIPE) behaviors in PtII(C^N)(N-donor ligand)Cl-type complexes through restrained D2d deformation of the coordinating skeleton and their optoelectronic properties*. *Journal of Materials Chemistry C*. **2021**, 9, 2334-2349.

[92] Y. S. Wong, M. Ng, M. C. Yeung, V. W. Yam, *Platinum(II)-Based Host-Guest Coordination-Driven Supramolecular Co-Assembly Assisted by Pt...Pt and pi-pi Stacking Interactions: A Dual-Selective Luminescence Sensor for Cations and Anions*. *J Am Chem Soc*. **2021**, 143, 973-982.

[93] A. S. Law, L. C. Lee, M. C. Yeung, K. K. Lo, V. W. Yam, *Amyloid Protein-Induced Supramolecular Self-Assembly of Water-Soluble Platinum(II) Complexes: A Luminescence Assay for Amyloid Fibrillation Detection and Inhibitor Screening*. *J Am Chem Soc*. **2019**, 141, 18570-18577.

[94] W.-S. Tang, X.-X. Lu, K. M.-C. Wong, V. W.-W. Yam, *Synthesis, photophysics and binding studies of Pt(ii) alkynyl terpyridine complexes with crown ether pendant. Potential luminescent sensors for metal ions*. *Journal of Materials Chemistry*. **2005**, 15.

[95] A. M. Brun, A. Harriman, *Energy- and Electron-Transfer Processes Involving Palladium Porphyrins Bound to DNA. Journal of the American Chemical Society*. **1994**, 116, 10383-10393.

[96] M. Aoudia, M. A. J. Rodgers, *Photoprocesses in Self-Assembled Complexes of Oligopeptides with Metalloporphyrins*. *Journal of the American Chemical Society*. **1997**, 119, 12859-12868.

[97] D. B. Papkovsky, T. C. O'Riordan, *Emerging applications of phosphorescent metalloporphyrins*. *J Fluoresc*. **2005**, 15, 569-584.

[98] H. M. Anula, E. Myshkin, A. Guliaev, C. Luman, E. O. Danilov, *Photo processes on self-associated cationic porphyrins and plastocyanin complexes 1. Ligation of plastocyanin tyrosine 83 onto metalloporphyrins and electron-transfer fluorescence quenching*. *J Phys Chem A*. **2006**, 110, 2545-2559.

[99] E. Nyarko, N. Hanada, A. Habib, M. Tabata, *Fluorescence and phosphorescence spectra of Au(III), Pt(II) and Pd(II) porphyrins with DNA at room temperature*. *Inorganica Chimica Acta*. **2004**, 357, 739-745.

[100] R. R. Valiev, V. N. Cherepanov, V. Y. Artyukhov, D. Sundholm, *Computational studies of photophysical properties of porphin, tetraphenylporphyrin and tetrabenzoporphyrin*. *Phys Chem Chem Phys*. **2012**, 14, 11508-11517.

[101] A. Barbieri, E. Bandini, F. Monti, V. K. Praveen, N. Armaroli, *The Rise of Near-Infrared Emitters: Organic Dyes, Porphyrinoids, and Transition Metal Complexes*. *Top Curr Chem (Cham)*. **2016**, 374, 47.

[102] T. Biver, S. Aydinoglu, D. Greco, F. Macii, *Mechanistic details on Pd(II)/5,10,15,20-tetrakis(1-methyl-4-pyridyl)porphyrin complex formation and reactivity in the presence of DNA. Monatshefte für Chemie - Chemical Monthly*. **2017**, 149, 175-183.

[103] P. M. Keane, J. M. Kelly, *Ground and excited state interactions of metalloporphyrin PtTMPyP4 with polynucleotides [poly(dG-dC)]2 and [poly(dA-dT)]2*. *Photochem Photobiol Sci*. **2016**, 15, 980-987.

[104] C. I. V. Ramos, A. R. Monteiro, N. M. M. Moura, M. A. F. Faustino, T. Trindade, *The Interactions of H(2)TMPyP, Analogues and Its Metal Complexes with DNA G-Quadruplexes-An Overview*. *Biomolecules*. **2021**, 11.

[105] H. Zhao, L. Zang, Q. Liu, B. Ma, M. Kou, *Enhancement of the room temperature phosphorescence of metalloporphyrins using imidazole as a triplet state protector*. *Journal of Luminescence*. **2018**, 194, 29-32.

[106] A. G. Moiseev, E. A. Margulies, J. A. Schneider, F. Belanger-Gariepy, D. F. Perepichka, *Protecting the triplet excited state in sterically congested platinum porphyrin*. *Dalton Trans*. **2014**, 43, 2676-2683.

[107] N. M. Barbosa Neto, D. S. Correa, L. De Boni, G. G. Parra, L. Misoguti, *Excited states absorption spectra of porphyrins – Solvent effects*. *Chemical Physics Letters*. **2013**, 587, 118-123.

[108] M. Uttamlal, A. S. Holmes-Smith, *The excitation wavelength dependent fluorescence of porphyrins*. *Chemical Physics Letters*. **2008**, 454, 223-228.

[109] M. Taniguchi, J. S. Lindsey, D. F. Bocian, D. Holten, *Comprehensive review of photophysical parameters (ε, Φf, τs) of tetraphenylporphyrin (H2TPP) and zinc tetraphenylporphyrin (ZnTPP) – Critical benchmark molecules in photochemistry and photosynthesis*. *Journal of Photochemistry and Photobiology C: Photochemistry Reviews*. **2021**, 46.

[110] J. E. Loefroth, *Time-resolved emission spectra, decay-associated spectra, and species-associated spectra*. *The Journal of Physical Chemistry*. **1985**, 90, 1160-1168.

[111] K. Kano, K. Fukuda, H. Wakami, R. Nishiyabu, R. F. Pasternack, *Factors Influencing Self-Aggregation Tendencies of Cationic Porphyrins in Aqueous Solution*. *Journal of the American Chemical Society*. **2000**, 122, 7494-7502.

[112] D. Sasikumar, A. T. John, J. Sunny, M. Hariharan, *Access to the triplet excited states of organic chromophores*. *Chem Soc Rev*. **2020**, 49, 6122-6140.

[113] G. Baryshnikov, B. Minaev, H. Agren, *Theory and Calculation of the Phosphorescence Phenomenon*. *Chem Rev*. **2017**, 117, 6500-6537.

[114] B. Qiao, B. E. Hirsch, S. Lee, M. Pink, C. H. Chen, *Ion-Pair Oligomerization of Chromogenic Triangulenium Cations with Cyanostar-Modified Anions That Controls Emission in Hierarchical Materials*. *J Am Chem Soc*. **2017**, 139, 6226-6233.

[115] N. A. Romero, D. A. Nicewicz, *Organic Photoredox Catalysis*. *Chem Rev*. **2016**, 116, 10075-10166.

[116] H. J. Worner, C. A. Arrell, N. Banerji, A. Cannizzo, M. Chergui, *Charge migration and charge transfer in molecular systems*. *Struct Dyn*. **2017**, 4, 061508.

[117] C. P. Hsu, *The electronic couplings in electron transfer and excitation energy transfer*. *Acc Chem Res*. **2009**, 42, 509-518.

[118] S. Garain, S. N. Ansari, A. A. Kongasseri, B. Chandra Garain, S. K. Pati, *Room temperature charge-transfer phosphorescence from organic donor-acceptor co-crystals*. *Chem Sci*. **2022**, 13, 10011-10019.

[119] F. Coppola, P. Cimino, A. Petrone, N. Rega, *Evidence of Excited-State Vibrational Mode Governing the Photorelaxation of a Charge-Transfer Complex*. *J Phys Chem A*. **2024**.

[120] C. J. Bender, *Theoretical models of charge-transfer complexes*. *Chemical Society Reviews*. **1986**, 15.

Acknowledgment

Few of us can thrive without a nurturing relationship with ourselves, yet leading a fulfilling life often demands persistent courage to embrace various risks, which include the adventurous journey of completing a PhD. As I wrote down my plans at the beginning of university life, envisioning the pursuit of a PhD, I could not foresee the challenges that lay ahead. Now, ten years later, as I stand at the end of this pursuit, I realize it marks not only an end but also a new beginning.

Throughout my three-year journey in pursuing PhD, I am deeply grateful to MSCA (Prof. Maria Skłodowska-Curie) and KU for providing opportunities for international applicants. Meanwhile, the collaboration with Prof. Bo W. Laursen in the past three years is destined to be memorable.

Special thanks are owed to Dr. Laura Kačenauskaitė and Dr. Cecilia Cerretani for their invaluable instrumental training and encouragement, to Dr. Rasmus K. Jacobsen for sharing important lab survival tips, to Marko H. Nowack, Dr. Niels Bisballe, Dr. Maria S. Thomsen and Dr Fredrik Edhborg for their fruitful scientific collaborations. Gratitude also extends to Vibe Drostgaard and Dr. Lu Wang for their patient guidance both prior to and following my arrival in Denmark. I also owe great gratitude to Dr. Abbey M. Philip for his important assistance with thesis proofreading and knowledge sharing, as well as Prof. Leila Lo Leggio, Niels Vissing Holst, and Lone Mortensen for their support. I also appreciate the collaborative efforts with groups from Sweden (Prof. Bo Albinsson's group) and the US (Prof. Amar H. Flood's group).

To my colleagues and friends who enriched my experience through engaging discussions on various topics, including culture and politics, I extend my heartfelt thanks. Besides, the interesting people from the ground floor, whose endeavors frequently left me surprised! For the heart-warming experiences with my international/Danish friends and Chinese counterparts, my appreciation goes to you all, especially ‘Expert Expat’ Βασί (Vasileios), Cecilia, Dalma, Gabriele, Giacomo, María Paula and Aliaksandr, Amilie, Axel, Fuxue, Jonas, Julian, Kapil, Ruifang, Simin, Siyu, Zhe and many others... The memories of our chats, walks, trips, dinners, hugs and laughters will be well preserved, thank you!

Moreover, I am grateful for the companionship and encouragement from Jurica, Danyang, Bochen, and the unwavering support from Mr. Zhucheng He (CAUC), Prof. Hengwei Lin (NIMTE), Ms. Nan Zhang (CAUC), and my dear parents, whose support always lightened up my navigation pathways.

And importantly, thank you for being alive and witness all these, dear Yang Wang! Eventually but not finally, to dear readers, I hope this book will inspire you to be more interested in yourself than in the book itself, then gradually more than yourself. :)

List of Publications

Publication/manuscripts related to projects included in this thesis:

1] Edhborg, F.; Olesund, A.; Tripathy, V.; Wang, Y.; Sadhukhan, T.; et al. *Triplet States of Cyanostar and Its Anion Complexes*. J Phys Chem A 2023, 127 (28), 5841-5850. (published, in Appendix 2)

2] Yang Wang, Marko H. Nowack, Niels Bisballe, Maria S. Thomsen, Maren Pink, Amar H. Flood, Bo W. Laursen. *Turning on Molecular Phosphorescence in Materials by Supramolecular Organization in Small-Molecule Ionic Isolation Lattices*. (manuscript, in Appendix 3)

3] Yang Wang, Marko H. Nowack, Amar H. Flood, Bo W. Laursen. *Boosting Triplet Emission in Porphyrin-Based Supramolecular Structures of Small-Molecule Ionic Isolation Lattices*. (manuscript, in Appendix 4)

4] Yang Wang, Sina Borgi, Amar H. Flood, Bo W. Laursen. *Long-Lived Excited State via Charge-Transfer Transition in Small-Molecule Ionic Isolation Lattices*. (manuscript, in Appendix 5)

Appendix

Appendix 1: Experimental Parts

Appendix 2: Publication –Triplet State of Cyanostar

Appendix 3: Manuscript – PtTA-SMILES

Appendix 4: Manuscript – Por4-SMILES

Appendix 5: Manuscript – TPT-SMILES

Appendix 1: Experimental Parts

§1.1 Spectroscopic Methods

Steady-state: UV-Vis absorption spectra were measured with a Cary 300 spectrophotometer. Corrected photoluminescence spectra were obtained by a PTI Instruments spectrofluorimeter. All photophysical measurements were conducted at ambient temperature, 22 ± 2 ℃. All luminescent solution samples were measured in 1 cm2 anaerobic quartz cells.

TCSPC lifetime measurements were obtained by time-correlated single-photon counting on a PTI Instruments-FluoTime 300, the instrument response function was collected using a dilute solution of Ludox at the detection wavelength. Reconvolution of the fluorescence decay and instrumental response function (IRF) was performed on the Edinburgh software in conjunction with lifetime fitting. Finally, the data was exported and plotted by using Origin 2020. Average, amplitude-weighted fluorescence lifetimes were calculated using parameters resolved from the fits as: $\tau = \sum A \times \tau_i$, where τ is the lifetime component and A is its corresponding fractional amplitude.

Fluorescence microscopy: All micrographs of solid materials were taken using Zeiss fluorescence microscope, equipped with KL 2500 LCD halogen lamp as an excitation source, a LD EC Epiplan-NEOFLUAR 50x/0.55 HD DIC objective, and an AxioCam MRc camera from Zeiss. Excitation (475 ± 20 nm) and emission (510 nm LP) filters were used in the excitation and detection path, respectively. Fluorescence and white light images of the crystals were taken using Axio Scope fluorescence microscope from ZEISS equipped with AxioCam MRc camera (ZEISS) and KL2500 LCD halogen light source from Schott. All steady-state spectra were corrected for excitation power and detection efficiency. Absolute quantum yields of crystalline samples were measured by using an integrating sphere in a Horiba Jobin Yvon Fluoreolog-3 spectrofluorometer.

DLS measurements were obtained by Dynamic Light Scattering Zetasizer Pro Instrument (Malvern Panalytic).

§1.2 Stern-Volmer Quenching Experiments

(1) Stern-Volmer quenching experiments for PtTA

The preparation of samples for Stern-Volmer quenching experiments is described as follows:

1) Prepare PtTA (50 μM, DCM) solution, then filter with hydrophobic PTFE filters (0.22 μm).

2) 200 μL of PtTA (50 μM, DCM) was mixed with different volumes of TBA[CS_2PF_6] (50 μM or 100 μM, DCM).

3) DCM was added to adjust all the solutions to reach a fixed volume of 2 mL. The concentration of PtTA was set at 5 μM for diluted samples, and CS concentration varied from 0 μM to 45 μM.

(2) Stern-Volmer quenching experiments for Por4

1) Prepare Por4 (50 μM, MeCN) and CS (50 μM, DCM) solutions, then filter with hydrophobic PTFE filters (0.22 μm).

2) 200 μL of Por4 (50 μM, MeCN) was mixed with different volumes of CS (50 μM, DCM), ranging from 0 μL to 3600 μL.

3) MeCN was added to adjust all the solutions to a fixed volume of 4 mL. The concentration of Por4 was set at 5 μM for diluted samples, and CS concentration varied from 0 μM to 45 μM.

§1.3 Solid Sample Preparation and Measurements

Solid sample preparation:

1) *Drop-cast solids on glass slids*: for measurements on solids, dropcast precursor solutions or suspension of solids (in heptane) on glass, then evaporate the solvents slowly.
2) *Dispersed in viscous matrix*: for measurements on neat aggregates and crystals optical properties (especially QY and τ), viscous matrix (propylene glycol, PG) was used to disperse crystallites for measurements.

QY: All quantum yield measurements were conducted with absolute method by using Integrating Sphere.

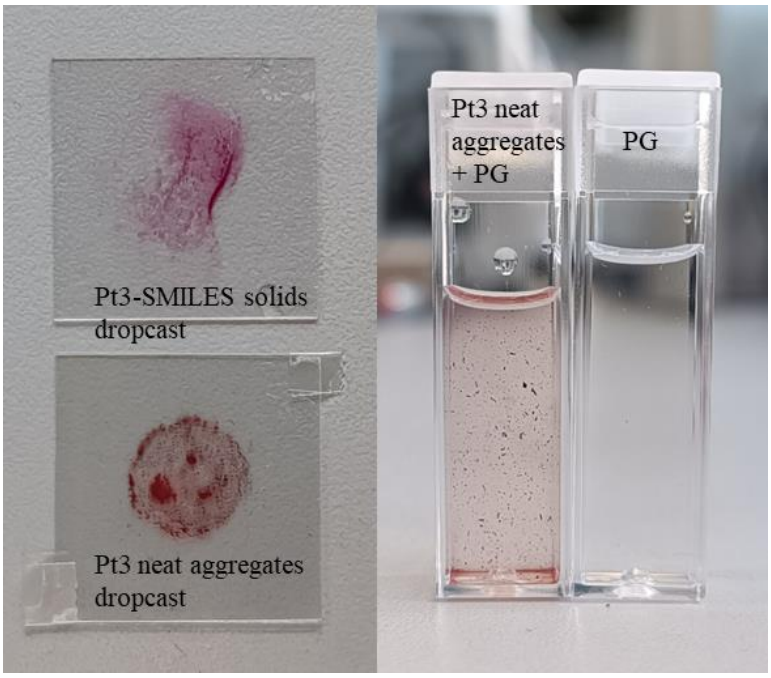

Figure §1. Comparison between solid samples on glass slids and in PG

§1.4 Synthesis of PtTA Complexes

General remarks: ^{1}H-NMR spectra were acquired on 500 MHz instruments by Bruker. Chemical shifts for ^{1}H-NMR spectra are reported relative to TMS, or referenced to the solvent residual peak for DMSO-d_6 (δ = 2.50 ppm). HRMS was recorded on an ESPMALDI-FT-ICR instrument equipped with a 7 T magnet (the instrument was calibrated using sodium trifluoroacetate cluster ions prior to acquiring the spectra) or a MicroTOF-QII-system using ESP (calibrated using formic acid). Methanol was dried over 3 Å mol. sieves for 48 h prior to use. 4'-(4-Tolyl)-2,2′:6′,2″-terpyridine (**S1**) and other reagents and solvents were obtained from commercial suppliers and used without further purification.

Synthesis of S2 : *Platinum(II) 4'-(4-tolyl)-2,2':6',2'' terpyridine chloride*

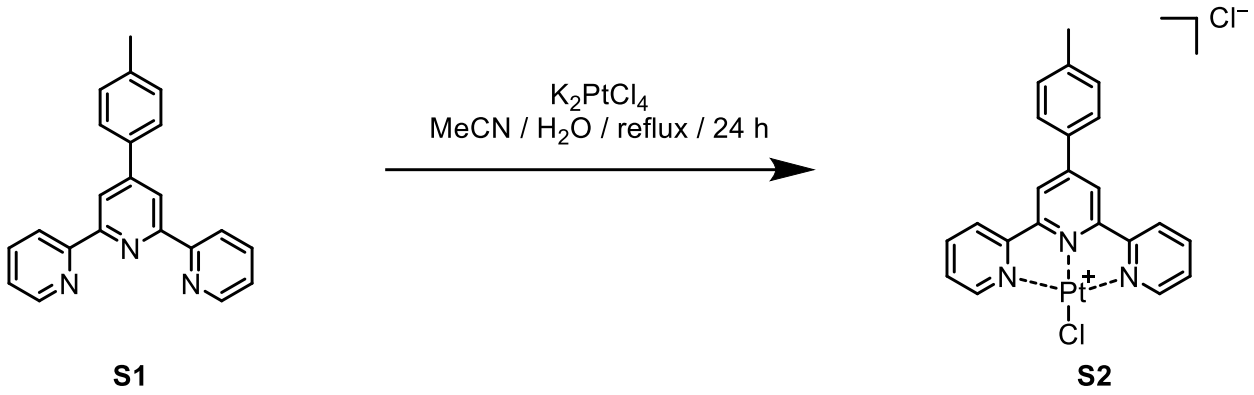

S1 **S2**

S2 was synthesized from **S1** according to a previously reported literature procedure[1].

^{1}H NMR (500 MHz, DMSO-*d6*):	δ = δ =8.98 (s, 2H), 8.93 (d, *J* = 5.6 Hz, 2H), 8.87 (d, *J* = 8.0 Hz, 2H), 8.54 (t, *J* = 7.9 Hz, 2H), 8.14 (d, *J* = 7.8 Hz, 2H), 7.96 (t, *J* = 6.7 Hz, 2H), 7.50 (d, *J* = 7.8 Hz, 2H), 2.45 (s, 3H).

Synthesis of Pt1: *Platinum(II) 4'-(4-tolyl)-2,2':6',2''-terpyridine methanolacetylide hexafluorophosphate*

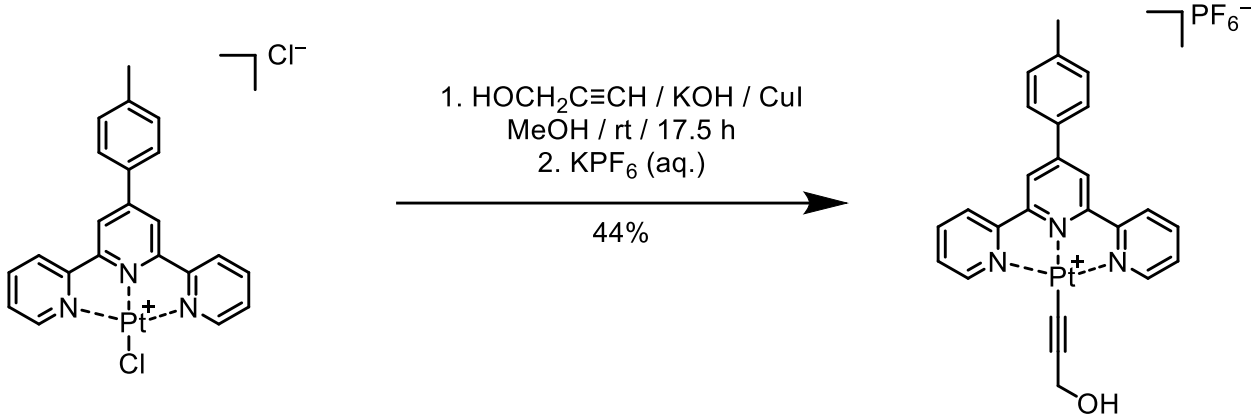

S2 **Pt1**

Pt1 was synthesized from **S2** according to a previously reported literature procedure[1]. The ^{1}H-NMR Signals are consistent with previous literature reports [1].

^{1}H-NMR (500 MHz, DMSO-*d6*)	δ =8.98 (s, 2H), 8.93 (d, J = 5.6 Hz, 2H), 8.87 (d, J = 8.0 Hz, 2H), 8.54 (t, J = 7.9 Hz, 2H), 8.14 (d, J = 7.8 Hz, 2H), 7.96 (t, J = 6.7 Hz, 2H), 7.50 (d, J = 7.8 Hz, 2H), 2.45 (s, 3H).

Synthesis of Pt2 : *Platinum(II) 4'-(4-tolyl)-2,2':6',2''-terpyridine phenylacetylide hexafluorophosphate*

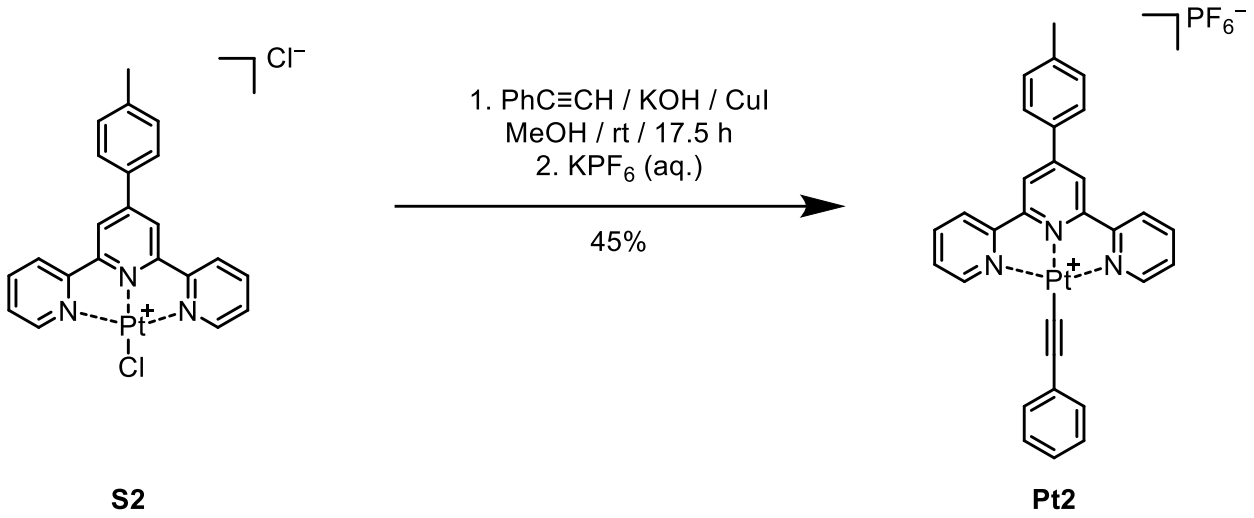

S2 **Pt2**

Pt2 was synthesized from **S2** according to modified literature procedure[2].

Synthetic processes: Phenylacetylene (25 µL, 0.23 mmol) and KOH (14 mg, 0.25 mmol) were combined in dry MeOH (15 mL, 0.01 M) in a dry round-bottomed flask under moderate stirring at room temperature. After 1 h, **S2** (101 mg, 0.159 mmol) and CuI (6.6 mg, 0.034 mmol) were added and the resulting yellow solution turned orange within 10 minutes. After 17.5 h the orange-brown reaction mixture was quenched by pouring KPF_6 (0.2 M). The resulting precipitate was isolated by filtration and washed with water (3 × 25 mL). The precipitate was then eluted off the filter with MeCN. The solution was reduced to 50 mL by evaporation of excess solvent, before the mixture was sonicated and poured into MeOH (150 mL) under vigorous stirring. Stirring was halted for the red precipitate to settle and was then isolated by filtration, followed by washing of the precipitate with MeOH (3 x 25 mL). This gave the titled compound **Pt2** as a red solid (58 mg, 0.072 mmol, 45 %).

^{1}H NMR (500 MHz, DMSO-*d6*):	δ = 9.18 (d, *J* = 5.6 Hz, 2H), 9.03 (s, 2H), 8.88 (d, *J* = 8.0 Hz, 2H), 8.55 (t, *J* = 7.9 Hz, 2H), 8.13 (d, *J* = 7.9 Hz, 2H), 7.94 (t, *J* = 6.7 Hz, 2H), 7.53-7.48 (m, 4H), 7.36 (t, *J* = 7.5 Hz, 2H), 7.28 (t, *J* = 7.5 Hz, 1H), 2.45 (s).

Synthesis of Pt3: *Platinum(II) 4'-(4-tolyl)-2,2':6',2''-terpyridine naphthylacetylide hexafluorophosphate*

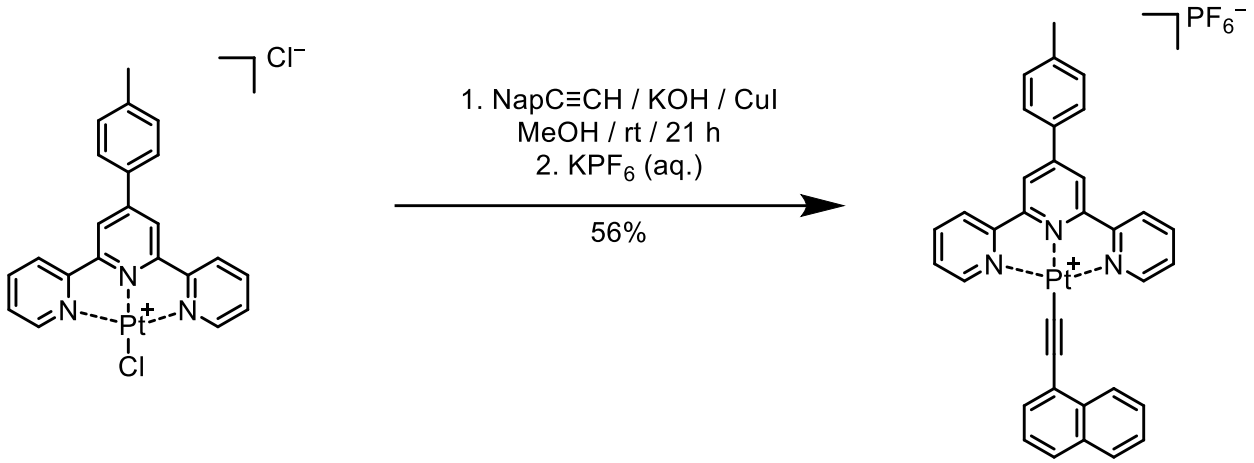

S2 **Pt3**

Pt3 was synthesized from **S2** according to modified literature procedures[3].

Synthetic processes: NapC≡CH (50 µL, 0.35 mmol) and KOH (17.5 mg, 0.35 mmol) were dissolved in MeOH (20 mL) and stirred at room temperature for 1 h. **S2** (106 mg, 0.167 mmol) and CuI (4.5 mg, 0.02 mmol) were added to the dark red solution, whereupon the solution turned dark orange over 10 min. The reaction mixture was stirred at room temperature for 21 h and poured into KPF_6 (0.2 M aq, 200 mL) under stirring. The dark red precipitate was filtered off, washed with H_2O (3 × 30 mL) and eluted off the filter with MeCN (200 mL). The solvent was concentrated in vacuo to 100 mL and sonicated for 5 min to redissolve the formed precipitate. The resulting solution was poured into Et_2O (300 mL) and stirred at rt for 2 h. The dark red precipitate was filtered off, washed with Et_2O (2 × 25 mL), eluted off the filter with MeCN, concentrated and dried in vacuo to yield **Pt3** as a dark red powder (81.2 mg, 0.094 mmol, 56%).

^{1}H NMR (500 MHz, DMSO-*d6*): δ (ppm) = 2.45 (s, 3H, $ArCH_3$), 7.47-7.52 (m, 3H, 3 × ArH), 7.58 (t, 1H, J = 7.4 Hz, 1H), 7.63 (t, J = 7.5 Hz, 1H), 7.73 (d, J = 7.1 Hz, 1H), 7.86 (d, J = 8.3 Hz, 1H), 7.95 (q, J = 8.0 Hz, 2H), 8.12 (d, J = 7.8 Hz, 1H), 8.50 (d, J = 8.4 Hz, 1H), 8.53 (t, J = 8.0 Hz, 1H), 8.88 (d, J = 8.0 Hz, 1H), 9.03 (s, 1H), 9.22 (d, J = 5.6 Hz, 1H).

^{1}H-NMR (500 MHz, DMSO-*d*$_6$):.

S2

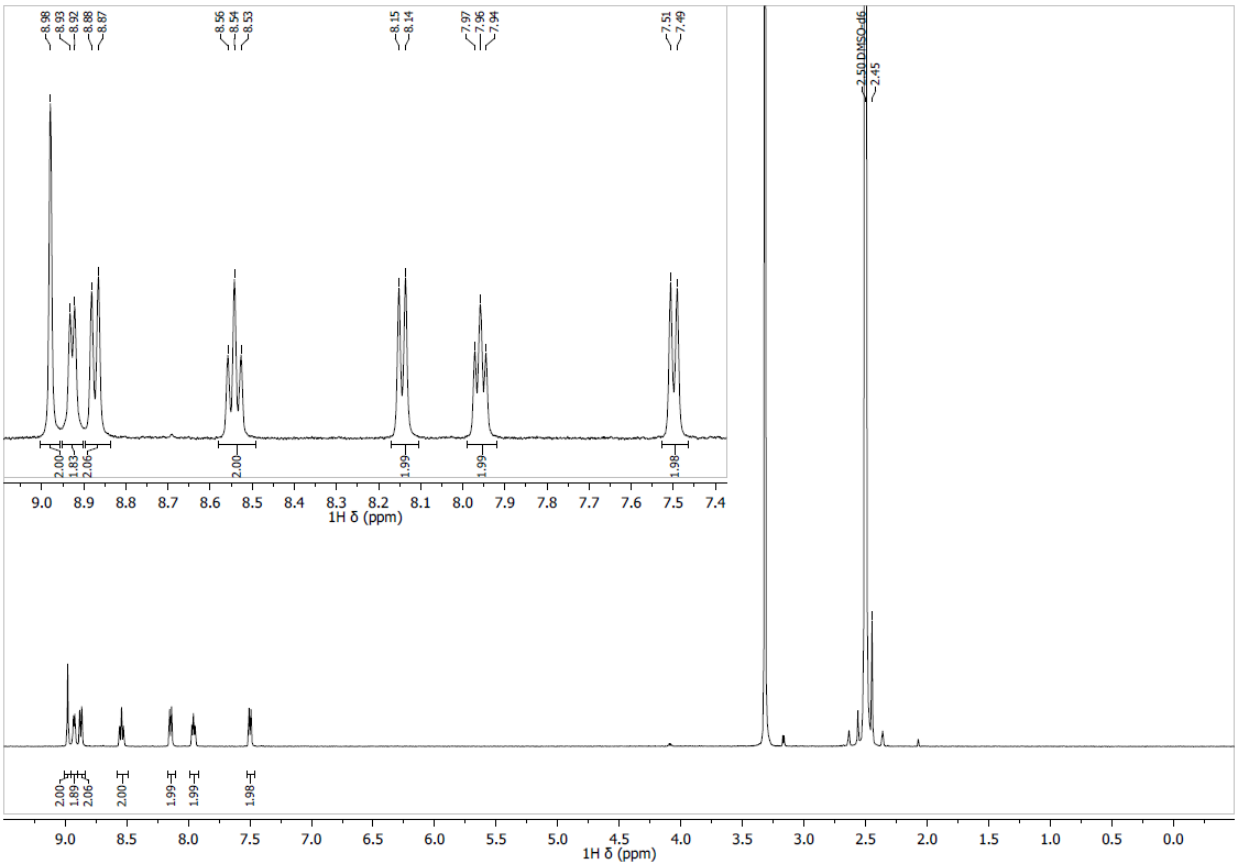

Figure §2. ^{1}H-NMR spectra of **S2** (500 MHz, DMSO-*d6*)

Pt1

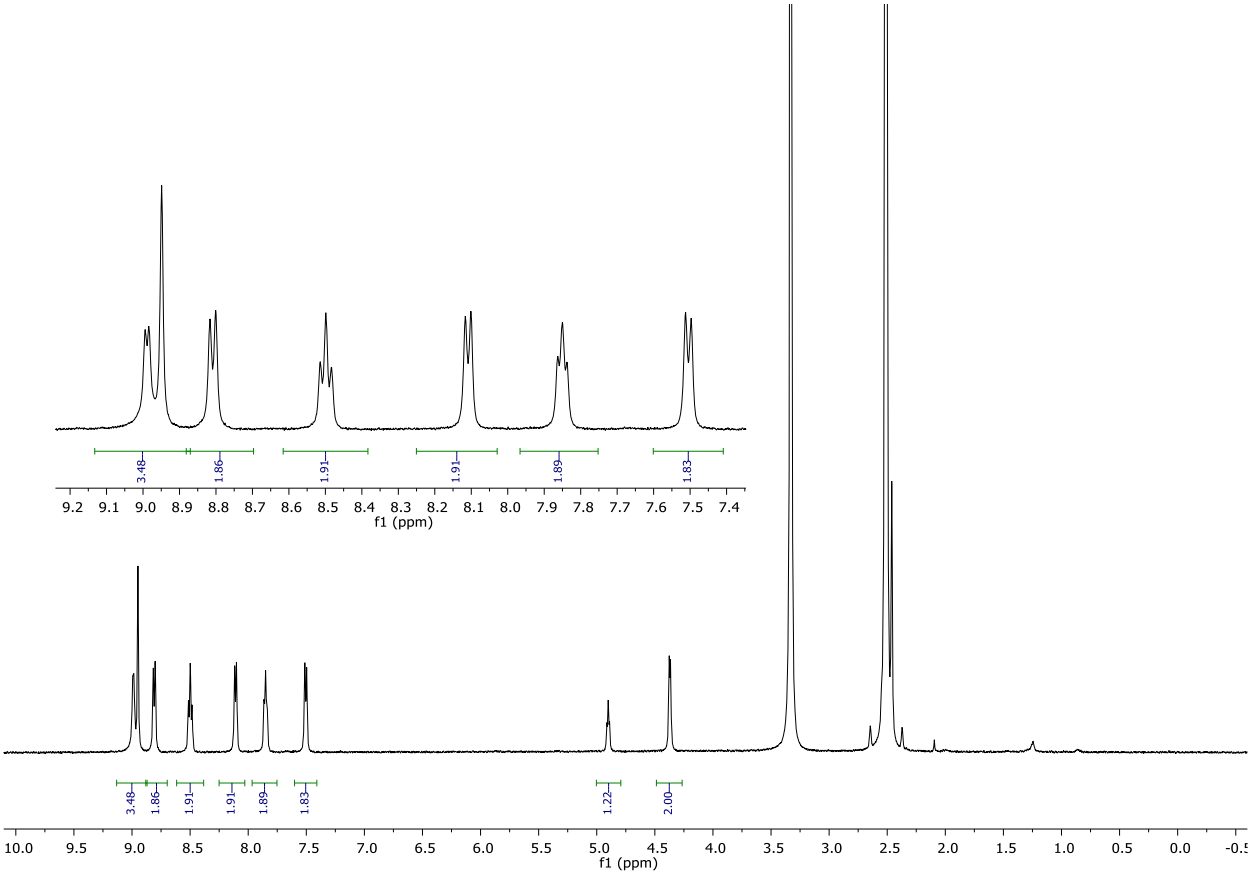

Figure §3. ^{1}H-NMR spectra of **Pt1** (500 MHz, DMSO-*d6*)

Pt2

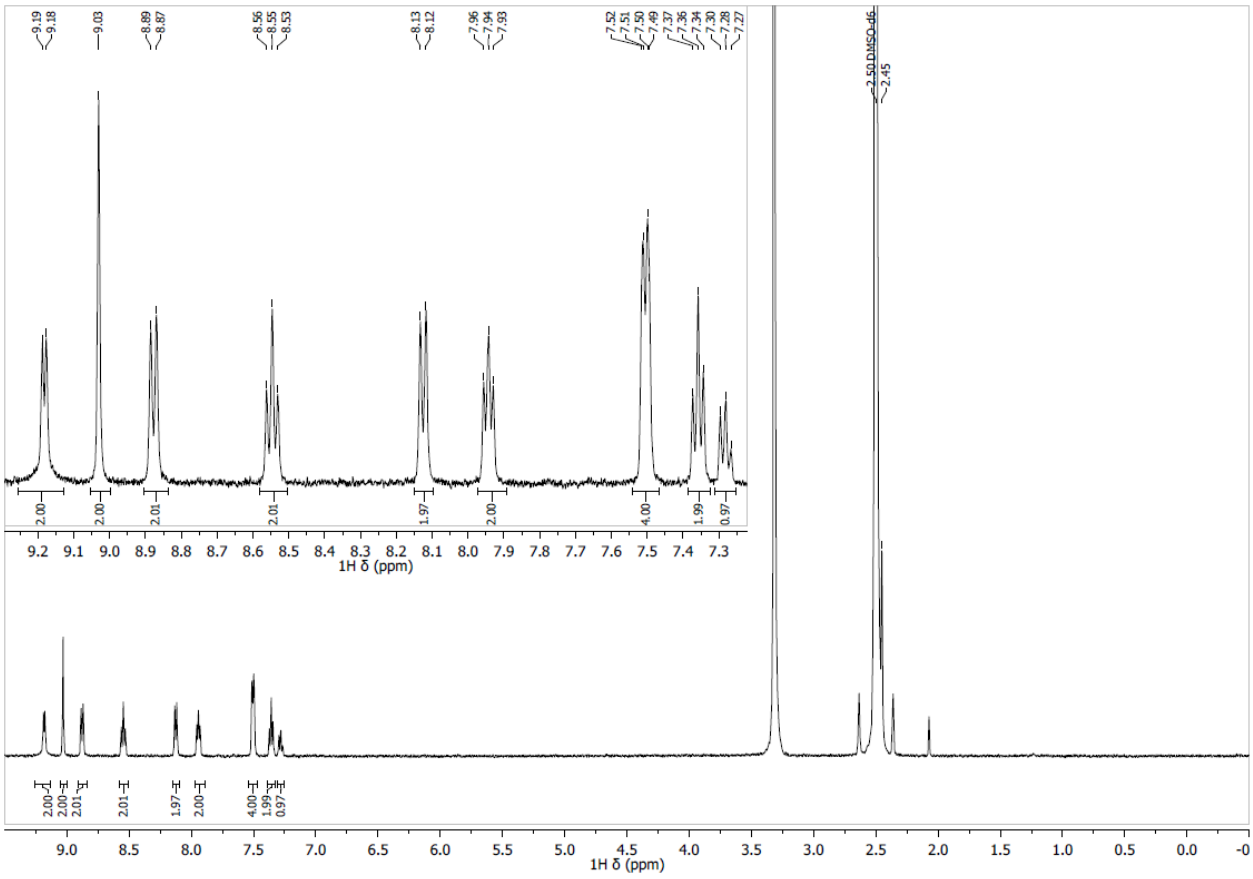

Figure §4. ^{1}H-NMR spectra of **Pt2** (500 MHz, DMSO-*d6*)

Pt3

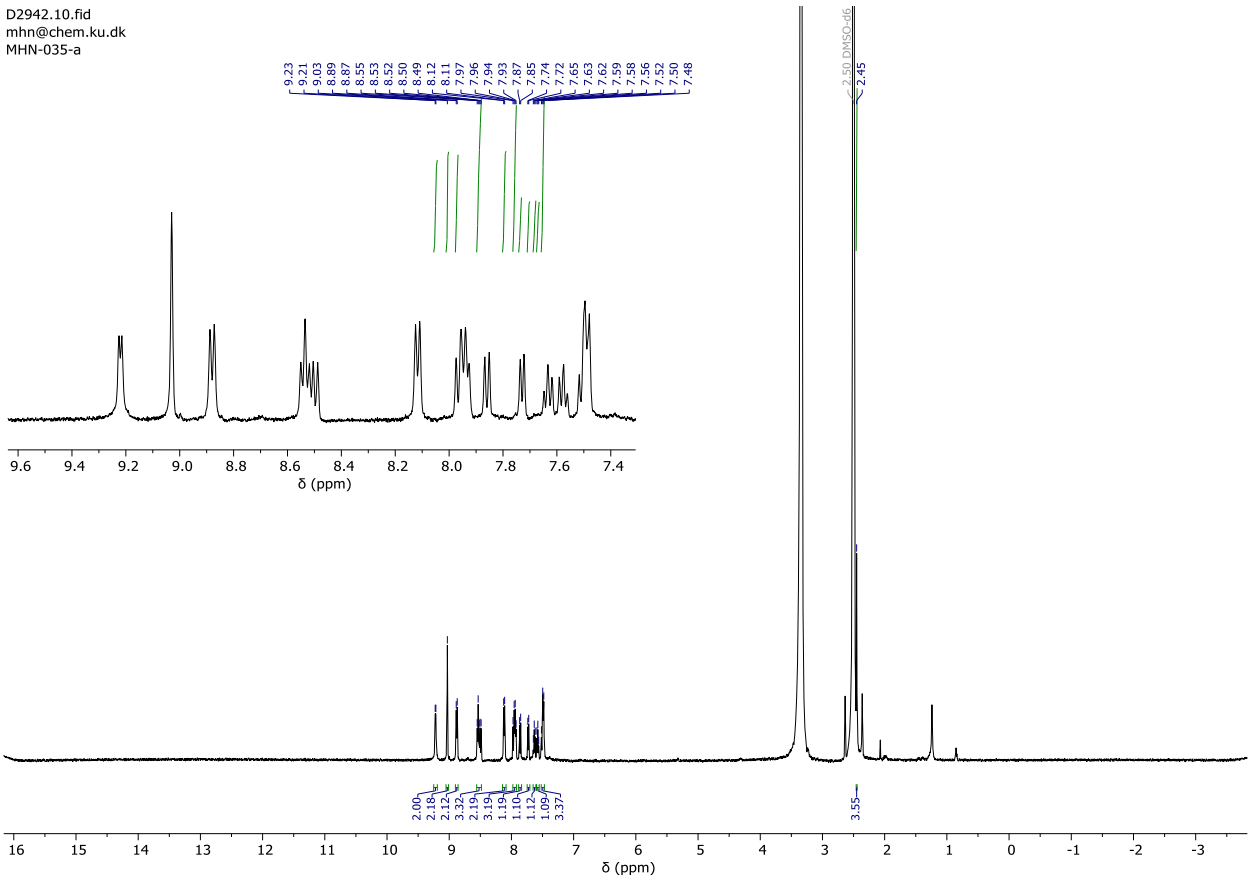

Figure §5. ^{1}H-NMR spectra of **Pt3** (500 MHz, DMSO-*d6*)

§1.5 Synthesis of Por4 Complex

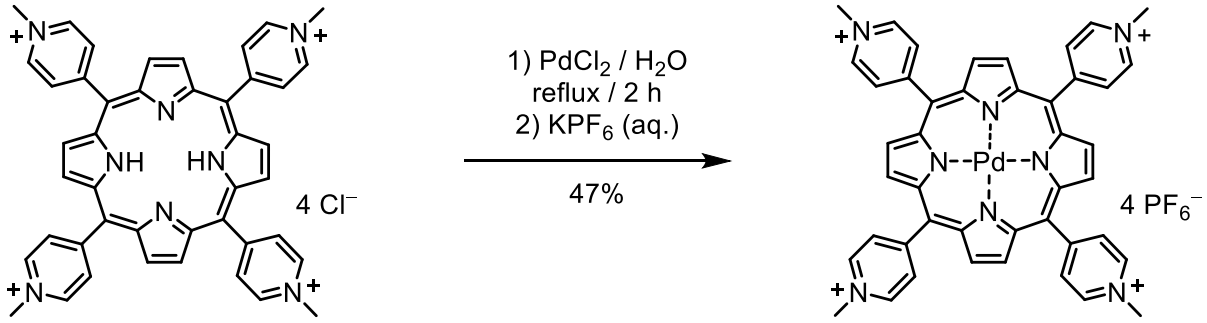

1 **2**

1 (204.0 mg, 0.248 mmol) and $PdCl_2$ (58.3 mg, 0.329 mmol) were suspended in H_2O (10 mL). The suspension was heated to reflux under N_2 for 2 h. The reaction progress was followed by UV-Vis absorption spectroscopy, as the change in the Soret band in characteristic (420 nm to 416 nm). The suspension was cooled to rt and filtered. The precipitate was washed with H_2O (3 × 5 mL). KPF_6 (0.2 M, 5 mL) was added to the filtrate under stirring, causing **2** to precipitate. The suspension was stirred at rt for 30 min and filtered. The precipitate was washed with H_2O (3 × 5 mL). The solid was eluted off the filter with MeCN and the solvent was evaporated in vacuo. The dark red solid was dried in vacuo o.n. to yield **2** (158.1 mg, 0.116 mmol, 47%).

^{1}H-NMR (CD_3CN, 500 MHz): δ (ppm) = 9.07 (d, 8H, *J* = 6.2 Hz, Ar*H*), 8.97 (s, 8H, Por*H*), 8.76 (d, 8H, *J* = 6.2 Hz, 8H, Ar*H*), 4.68 (s, 12H, N^+CH_3).

^{19}F-NMR (CD_3CN, 470 MHz): δ (ppm) = −72.9 (d, J = 708 Hz, PF_6^-)

UV-Vis absorption of reaction mixture

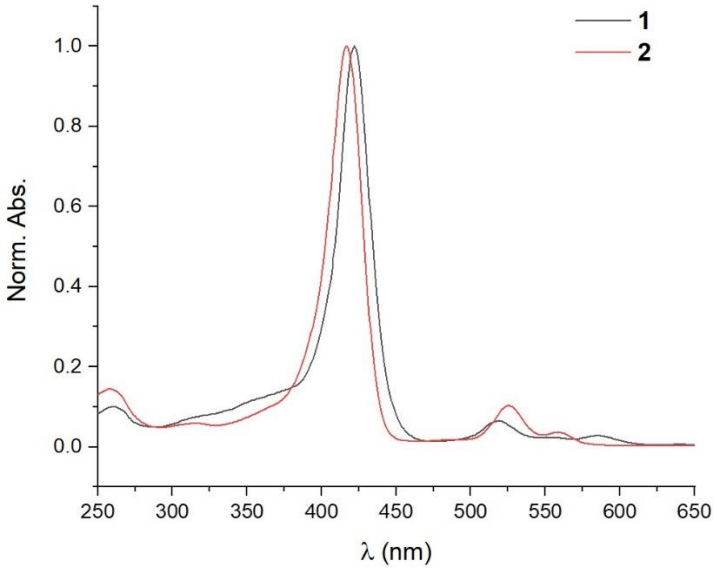

Figure §6. Absorption spectra of **Por4** (2) and the starting porphyrin compound (1)

^{1}H-NMR

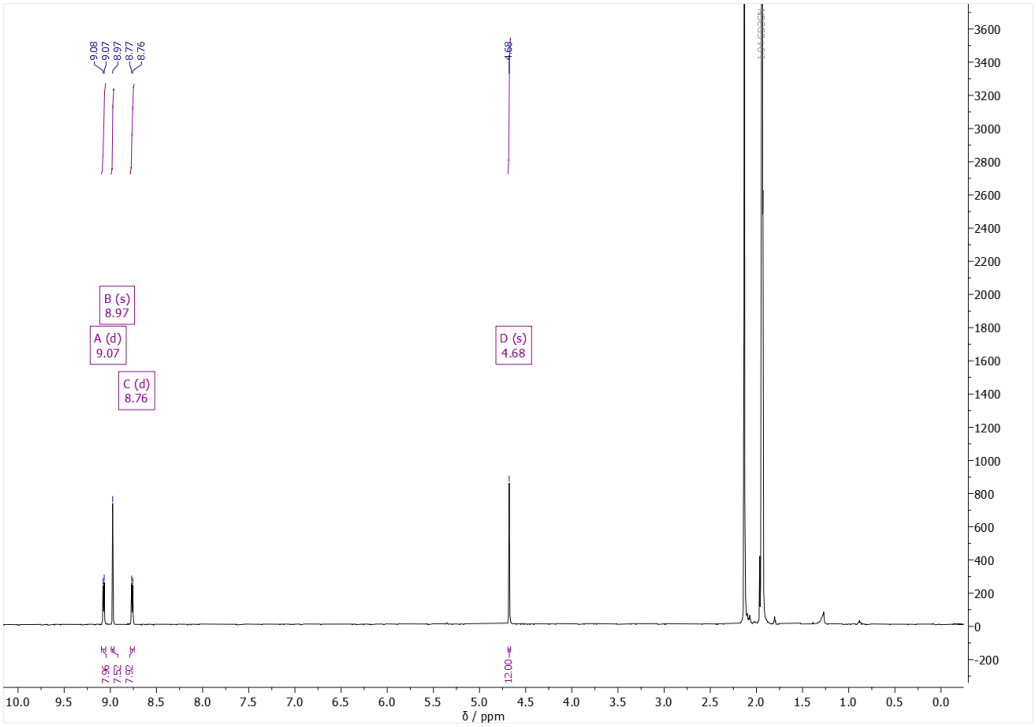

Figure §7. ^{1}H-NMR spectra of **Por4** (500 MHz, CD_3CN-*d6*)

^{19}F-NMR

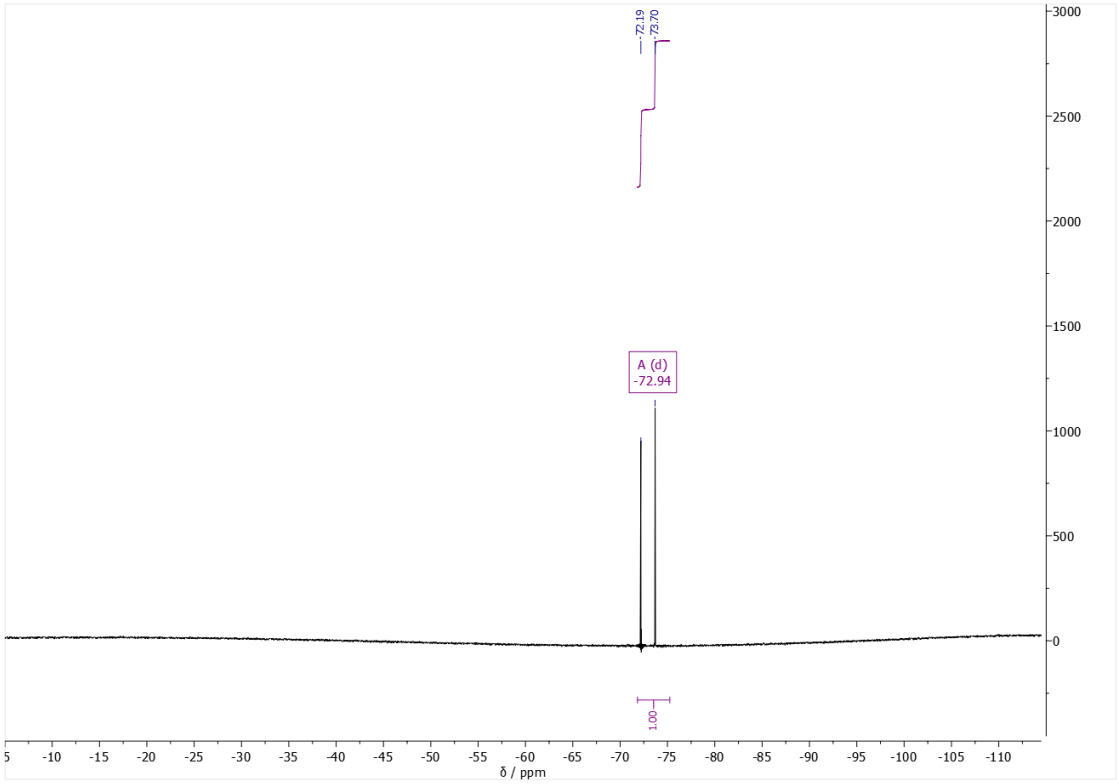

Figure §8. ^{19}F-NMR spectra of **Por4** (470 MHz, CD_3CN-*d6*)

§1.6 Synthetic Method of SMILEs Crystals

1.6.1 Preparation of PtTA-SMILES single crystals:

5 mL of CS (1mM, DCM), and 4 mL of PtTA complex (0.5 mM, MeCN) were both filtered through hydrophobic PTFE filters (0.22μm), then mixed together in a 20 mL vial. After being ultrasonicated for 10 minutes, the vial was left until crystals emerged.

1.6.2 Preparation of PtTA-SMILEs large-scale crystalline solids:

The antisolvent crystallization method was used for the preparation of PtTA-SMILMES solids. A detailed protocol can be described as follows:

10 mL of PtTA complex (0.5 mM, MeCN), and two molar equivalences of CS, which is 12.5 mL of CS (1mM, THF) were mixed in a 100 mL flask. The flask was ultrasonicated for 15 minutes before 20 mL diethyl ether was slowly added, ultrasonication was maintained during ether addition and for another 20 minutes afterwards. The flask was left still for 48~72 h before rotary evaporation was applied to slowly remove the solvent and obtain crystalline powders. The system vapor pressure was 140 mPa to ensure both the acetonitrile and tetrahydrofuran can be evaporated simultaneously. Rotated flask slowly at a speed of 50-100 rpm until nearly one-third of the solvent evaporated, when powders started to emerge. Collected the powders and filtered them on filter paper by diethyl ether, finally drying up the solids, the yields were about 85%.

Characterizations on species from large-scale crystalline engineering: The graph below illustrates the emissive properties of different fractions of Pt2-SMILES crystalline solids produced under different conditions (A1-A3), reflecting various species emerged in the evaporation process. A1 represents powders collected at a slow rotatory speed of 50 rpm and low pressure of 140 mPa, ensuring the simultaneous removal of THF and MeCN. A2 was generated with the same rotatory speed but a higher vapor pressure of 220 mPa, resulting in the rapid removal of MeCN. A3, on the other hand, was produced at a faster rotatory speed of 120 mPa and a high vapor pressure of 220 mPa, leading to the quick removal of MeCN and the formation of dark brownish Pt2 neat aggregates.

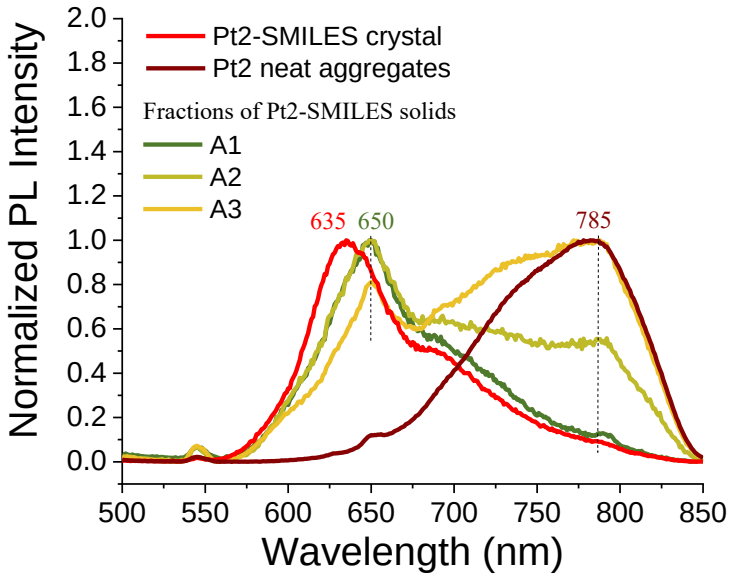

Figure §9. Emission spectra of different fractions from Pt2-SMILES crystal engineering process

1.6.3 Preparation of Por4-SMILES single crystals:

4 mL of Por4 complex (0.5 mM, MeCN) and 10 molar equivalence of CS which is 10 mL of CS (1 mM, DCM) were both filtered by hydrophobic PTFE filters (0.22 μm), then mixed in a 20 mL vial. After 10 minutes of ultrasonication, the vial was placed in darkness until crystals emerged.

§1.7 Synthetic Method of SMILEs Nanoparticles

1.7.1 Pt3-SMILES NPs:

1) **Pt3** (0.2 mM, MeCN) and CS (1 mM, DCM) were mixed by following the molar ratio of CS/Pt3=2.5. DCM was added to keep **Pt3**[$CS_{2.5}PF_6$] concentration at 50 μM.

2) 2mL Pt3[$CS_{2.5}PF_6$] (50 μM) and 0.7 mL DSPE-PEG (1 mg/mL, DCM) were mixed, and DSPE-PEG accounted for 60% of total weight. Then thoroughly evaporate the solvent mixture. 2mL THF was added to dissolve the evaporated solids with the assistance of ultrasonication.

3) The prepared precursor solution was injected into a vial containing 10 mL distilled water, as the ultrasonication and ice-bathing were used simultaneously, then kept ultrasonication for 15 minutes.

4) Place the sample in vials without covered lid for overnight, in order to evaporate the THF.

1.7.2 Por4-SMILES NPs:

1) Por4 (0.2 mM, MeCN) and CS(1 mM, THF) were prepared with the help of ultrasonication and filtering (0.22 μM, hydrophobic filter). 2 mL Por4 and 4 mL CS were mixed together, with the addition of 2 mL MeCN, a **Por4**-CS_{10} precusor solution (50 μM) was obtained.

2) 2 mL **Por4**-CS_{10} (50 μM) and 1.3 mL DSPE-PEG (1 mg/mL) were mixed together, then evaporated the solvent by using N_2 gas with slow speed, which lasted for about 15 minutes, pinky reddish solids gradually emerged with observable red emission under 410nm laser illumination.

3) 2 mL THF was added to dissolve the reddish solids, the solution was then injected into 10 mL distilled water, accompanied by ultrasonication for about 15 minutes.

4) Place the sample in vials without covered lid for overnight, in order to evaporate the THF.

§1.8 Single Crystal XRD Characterizations

Data collection for Pt2-SMILES single crystal

A red crystal (approximate dimensions 0.244 × 0.129 × 0.078 mm^3) was placed onto the tip of a MiTeGen loop and mounted on a Bruker Venture D8 diffractometer equipped with a Photon100 detector at 173 K. The data collection was carried out using Mo Kα radiation (graphite monochromator) with a frame time of 10 seconds and a detector distance of 34 mm.

Ten sections of frames were collected with 1º ω and φ scans. A total of 768 frames were collected. The total exposure time was 2.13 hours. The frames were integrated with the Bruker SAINT software package[4] using a narrow-frame algorithm. The integration of the data using a triclinic unit cell yielded a total of 89148 reflections to a maximum θ angle of 25.23° (0.83 Å resolution), of which 13070 were independent (average redundancy 6.821, completeness = 99.1%, Rint = 15.70%, Rsig = 8.86%) and 8415 (64.38%) were greater than $2\sigma(F^2)$.

The final cell constants of a = 12.726(3) Å, b = 17.196(4) Å, c = 17.808(4) Å, α = 69.868(9)°, β = 89.933(10)°, γ = 84.522(11)°, volume = 3640.1(15) Å3, are based upon the refinement of the XYZ-centroids of 9928 reflections above 20 σ(I) with 4.424° < 2θ < 44.47°. Data were corrected for absorption effects using the Multi-Scan method (SADABS)[5]. The ratio of minimum to maximum apparent transmission was 0.853. The calculated minimum and maximum transmission coefficients (based on crystal size) are 0.7860 and 0.9240. Please refer to Table S7 for additional crystal and refinement information.

Structure solution and refinement

The space group P-1 was determined based on intensity statistics and systematic absences. The structure was solved and refined using the SHELX suite of programs.[6,7] An intrinsic-methods solution was calculated, which provided most non-hydrogen atoms from the E-map. Full-matrix least squares / difference Fourier cycles were performed, which located the remaining non-hydrogen atoms. All non-hydrogen atoms were refined with anisotropic displacement parameters. The hydrogen atoms were placed in ideal positions and refined as riding atoms with relative isotropic displacement parameters. Disorder was refined for all components of the structure; sets of restraints and constraints were applied.

Remaining electron density indicated that solvent was present in the structure; difference electron density patterns suggests the presence of partially lost solvent in the structure, specifically heptane and MeCN. However, such a model refined with a strong sets of restraints and constraints did not converge to a chemically sensible structure. Therefore, the solvent models were removed, and structure was investigated for solvent accessible areas[8]. One large void was found in the unit cell at approximately ½ 0 0 (407 $Å^3$ or 11% per unit cell) to contain 106 electrons. For comparison, MeCN occupies ca. 47 $Å^3$ with 15 electrons and heptane occupies ca. 94 $Å^3$ with 71 electrons[8]. The contribution of the unidentified solvent to the structure factors was assessed by back-Fourier transformation[9] and the data were corrected accordingly. The refinement using the modified dataset improved the overall structure and R1 by about 4 %.

The final anisotropic full-matrix least-squares refinement on F^2 with 1069 variables converged at R1 = 7.07%, for the observed data and wR2 = 17.43% for all data. The goodness-of-fit was 1.031. The largest peak in the final difference electron density synthesis was 0.856 $e^-/Å^3$ and the largest hole was -0.744 $e^-/Å^3$ with an RMS deviation of 0.066 $e^-/Å^3$. On the basis of the final model, the calculated density was 1.185 g/cm^3 and F(000), 1350 e^-.

Figure §10. Mounted specimen

Table §1 . Single crystal information of **Pt2-SMILES**	
Formula	**0.25(C_{32} N_2 Pt_2),0.25(F_6 P),0.5(C_{70} N_5)**
Crystal system	P 1 (2) **Triclinic**
Cell length	a 12.723(3) b 17.195(4) c 17.804(4)
Cell angle	a 69.867(9) b 89.912(10) g 84.526(11)
Cell vol (Å^3)	**3638.3**

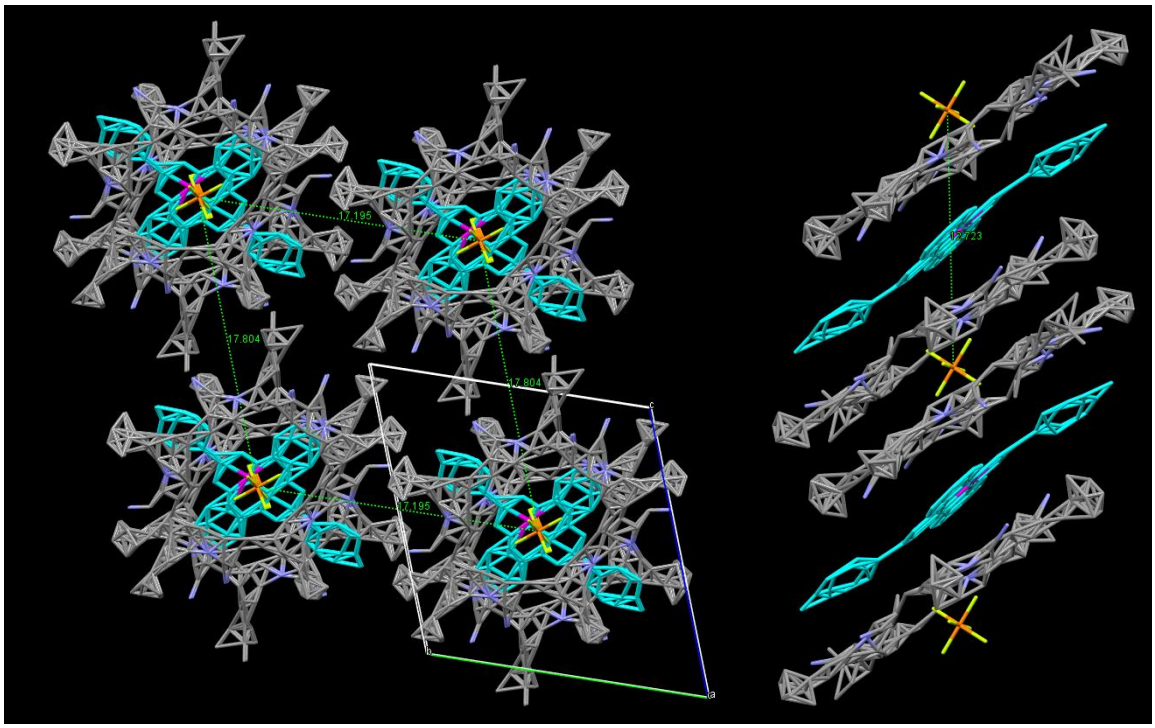

Figure §11. Molecular stacking structures of Pt2-SMILES crystals

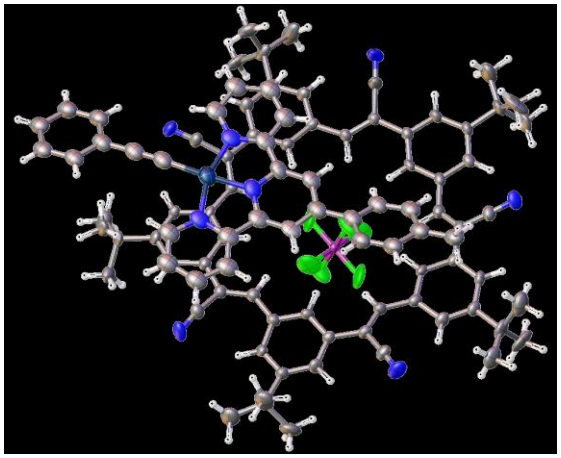

Figure §12. Formula unit, disorder omitted, molecules at special positions are shown as complete molecules.

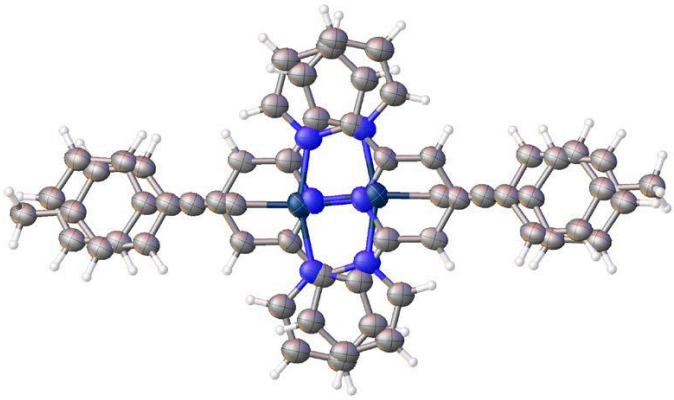

Figure §13. Pt-2 complex disorder

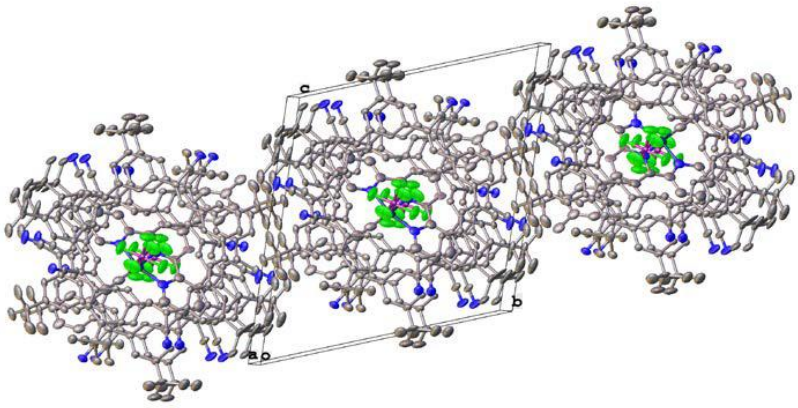

Figure §14. Cell plot, view along a.

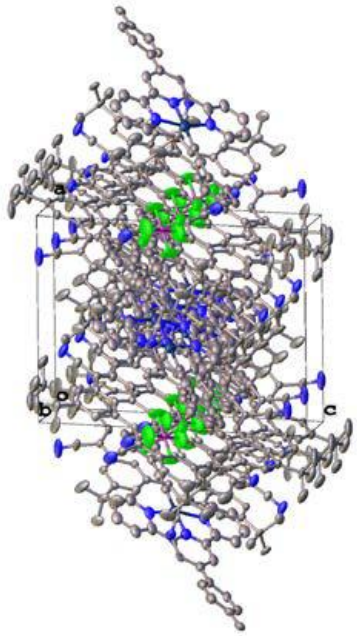

Figure §15. Cell plot, view along *b*.

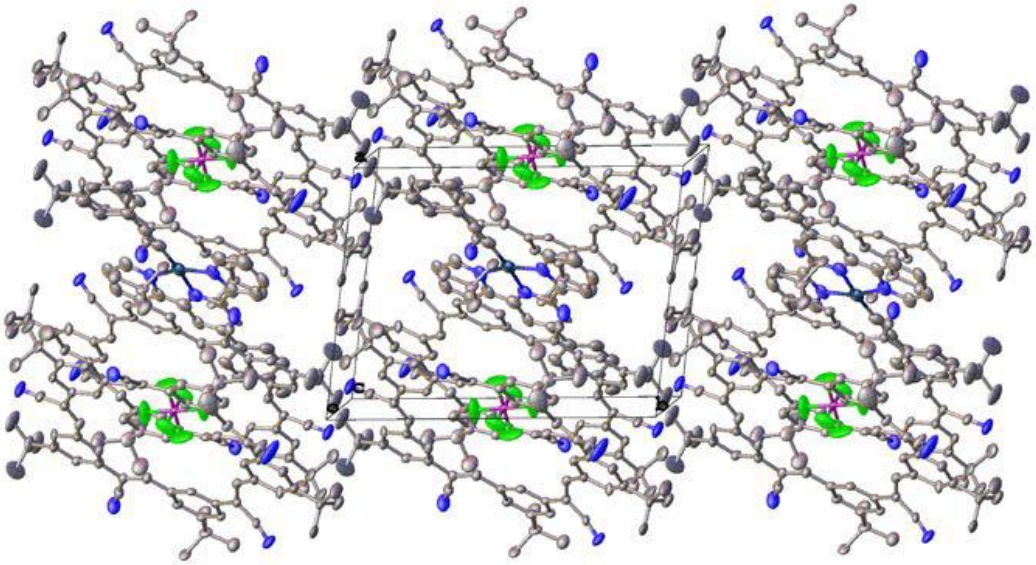

Figure §16. Cell plot, view along *c*.

Table §2. Crystal data and structure refinement for Pt2-SMILES single crystal

Empirical formula	C160 H152 F6 N13 P Pt	
Formula weight	2597.00	
Crystal color, shape, size	red rod, 0.244 × 0.129 × 0.078 mm^3	
Temperature	100(2) K	
Wavelength	0.71073 Å	
Crystal system, space group	Triclinic, P-1	
Unit cell dimensions	a = 12.726(3) Å	α = 69.868(9)°.
	b = 17.196(4) Å	β = 89.933(10)°.
	c = 17.808(4) Å	γ = 84.522(11)°.
Volume	3640.3(15) $Å^3$	
Z	1	
Density (calculated)	1.185 Mg/m^3	
Absorption coefficient	1.036 mm^{-1}	
F(000)	1350	
Data collection		
Diffractometer	Venture D8, Bruker	
Source	IμS, with focusing Helios optics	
Detector	Photon100	
Theta range for data collection	1.608 to 25.228°.	
Index ranges	-15<=h<=15, -20<=k<=20, -21<=l<=21	
Reflections collected	89148	
Independent reflections	13070 [R_{int} = 0.1570]	
Observed Reflections	8415	
Completeness to theta = 25.228°	99.1 %	
Solution and Refinement		
Absorption correction	Semi-empirical from equivalents	
Max. and min. transmission	0.7452 and 0.6360	
Solution	Intrinsic methods	
Refinement method	Full-matrix least-squares on F^2	
Weighting scheme	$w = [\sigma^2 Fo^2 + AP^2 + BP]^{-1}$, with	
	$P = (Fo^2 + 2\,Fc^2)/3$, A = 0.0585, B = 6.7578,	
Data / restraints / parameters	13070 / 2927 / 1069	
Goodness-of-fit on F^2	1.031	
Final R indices [I>2σ(I)]	R1 = 0.0707, wR2 = 0.1520	
R indices (all data)	R1 = 0.1229, wR2 = 0.1743	
Largest diff. peak and hole	0.856 and -0.744 $e.Å^{-3}$	

Goodness-of-fit = $[\Sigma[w(F_o^2 - F_c^2)^2]/N_{observns} - N_{params})]^{1/2}$, all data.

R1 = $\Sigma(|F_o| - |F_c|) / \Sigma |F_o|$. $wR2 = [\Sigma[w(F_o^2 - F_c^2)^2] / \Sigma [w(F_o^2)^2]]^{1/2}$

§1.9 References for Experimental Parts

[1] Guo, F., et al., *Synthesis, photophysics, and optical limiting of platinum(II) 4'-tolylterpyridyl arylacetylide complexes.* Inorg Chem, 2005. **44**(11): p. 4055-65.

[2] Yang, Q.Z., et al., *Long-lived emission from platinum(II) terpyridyl acetylide complexes.* Inorg Chem, 2002. **41**(22): p. 5653-5.

[3] Tam, A.Y., et al., *Luminescent alkynylplatinum(II) complexes of 2,6-bis(N-alkylbenzimidazol-2'-yl)pyridine-type ligands with ready tunability of the nature of the emissive states by solvent and electronic property modulation*. Chemistry, 2008. 14(15): p. 4562-76.

[4] SAINT V8.40A (2020), Bruker AXS, Madison, WI.

[5] L. Krause, R. Herbst-Irmer, G. M. Sheldrick, D. Stalke, *Comparison of silver and molybdenum microfocus X-ray sources for single-crystal structure determination*. J. Appl. Cryst., 2015. 48: p. 3-10.

[6] G. M. Sheldrick, *SHELXT--Integrated space-group and crystal-structure determination*. Acta Cryst, 2015. A71: p. 3-8.

[7] G. M. Sheldrick, *Crystal structure refinement with SHELXL*. Acta Cryst, 2015. C71: p. 3-8.

[8] A. Immirzi, B. Perini, *Prediction of density in organic crystals*. Acta Cryst, 1977. A33: p. 216-218.

[9] A.L. Spek, *PLATON SQUEEZE: a tool for the calculation of the disordered solvent contribution to the calculated structure factors*. Acta Cryst. 2015. C71: p. 9-18.

Publications/Manuscripts

Related to projects included in this thesis

Appendix 2-a: Publication – Triplet State of Cyanostar

THE JOURNAL OF PHYSICAL CHEMISTRY A
A JOURNAL OF THE AMERICAN CHEMICAL SOCIETY

pubs.acs.org/JPCA Article

Triplet States of Cyanostar and Its Anion Complexes

Published as part of The Journal of Physical Chemistry A virtual special issue "Krishnan Raghavachari Festschrift".

Fredrik Edhborg, Axel Olesund, Vikrant Tripathy, Yang Wang, Tumpa Sadhukhan, Andrew H. Olsson, Niels Bisballe, Krishnan Raghavachari, Bo W. Laursen, Bo Albinsson,* and Amar H. Flood*

Cite This: J. Phys. Chem. A 2023, 127, 5841−5850 Read Online

ACCESS | Metrics & More | Article Recommendations | Supporting Information

ABSTRACT: The design of advanced optical materials based on triplet states requires knowledge of the triplet energies of the molecular building blocks. To this end, we report the triplet energy of cyanostar (**CS**) macrocycles, which are the key structure-directing units of small-molecule ionic isolation lattices (SMILES) that have emerged as programmable optical materials. Cyanostar is a cyclic pentamer of covalently linked cyanostilbene units that form π-stacked dimers when binding anions as 2:1 complexes. The triplet energies, E_T, of the parent cyanostar and its 2:1 complex around PF_6^- are measured to be 1.96 and 2.02 eV, respectively, using phosphorescence quenching studies at room temperature. The similarity of these triplet energies suggests that anion complexation leaves the triplet energy relatively unchanged. Similar energies (2.0 and 1.98 eV, respectively) were also obtained from phosphorescence spectra of the iodinated form, **I-CS**, and of complexes formed with PF_6^- and IO_4^- recorded at 85 K in an organic glass. Thus, measures of the triplet energies likely reflect geometries close to those of the ground state either directly by triplet energy transfer to the ground state or indirectly by using frozen media to inhibit relaxation. Density functional theory (DFT) and time-dependent DFT were undertaken on a cyanostar analogue, **CSH**, to examine the triplet state. The triplet excitation localizes on a single olefin whether in the single cyanostar or its π-stacked dimer. Restriction of the geometrical changes by forming either a dimer of macrocycles, $(CSH)_2$, or a complex, $(CSH)_2{\cdot}PF_6^-$, reduces the relaxation resulting in an adiabatic energy of the triplet state of 2.0 eV. This structural constraint is also expected for solid-state SMILES materials. The obtained T_1 energy of 2.0 eV is a key guide line for the design of SMILES materials for the manipulation of triplet excitons by triplet state engineering in the future.

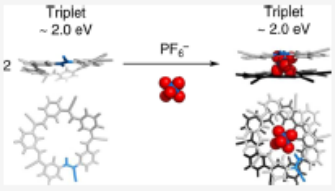

INTRODUCTION

The triplet (T) states of organic molecules[1−3] are integral to the function of materials with advanced optical properties.[4,5] Topical examples include photon upconversion, singlet fission, and thermally activated delayed fluorescence, which are considered potential elements of next-generation technologies for solar energy capture and information processing.[6−14] These materials also rely on the transfer of energy to and from singlet (S) states. Consequently, knowledge of the relative energies of each state and the extent to which these states are modified by packing into high-density solids[15,16] are important fundamental properties. While packing rarely alters triplet states, it often leads to exciton coupling with substantial deterioration in the properties of singlet states.[17−20] Without a strategy to mitigate exciton coupling,[21,22] heavy losses in quantum efficiency are observed. Our recent discovery of small-molecule, ionic isolation lattices (SMILES)[23] produced a reliable strategy to mitigate this coupling. This discovery led to the creation of the brightest nanoparticles[24] and fluorescent materials[25,26] stemming from uncoupled singlet states. Thus, the opportunity for creating materials composed of organic molecules in high-density solids with both well-defined triplet and singlet energies can now be considered. Investigation of this opportunity, however, requires characterization of the triplet energies of SMILES materials.

The construction of SMILES materials relies on charge-by-charge packing[22] of cationic dyes to isolate and decouple them from each other.[27] For this purpose, we use cyanostar macrocycles[28] (**CS**, Figure 1a,b) to bind the dye's counter anion (X^-, Figure 1c) and generate 2:1 anionic complexes. These negatively charged complexes stack into an alternating lattice with the cationic dyes. Thus, the first step to using SMILES as an optical material for manipulating triplet excitation is to determine the triplet energies of the structure-directing cyanostar macrocycles and the anion-bound complexes present in the SMILES lattices.[23] We do this here by using quenching studies, phosphorescence (Phos) spectra, and time-dependent density functional theory (TD-

Received: April 24, 2023
Revised: June 23, 2023
Published: July 10, 2023

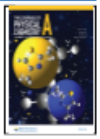

https://doi.org/10.1021/acs.jpca.3c02701
J. Phys. Chem. A 2023, 127, 5841−5850

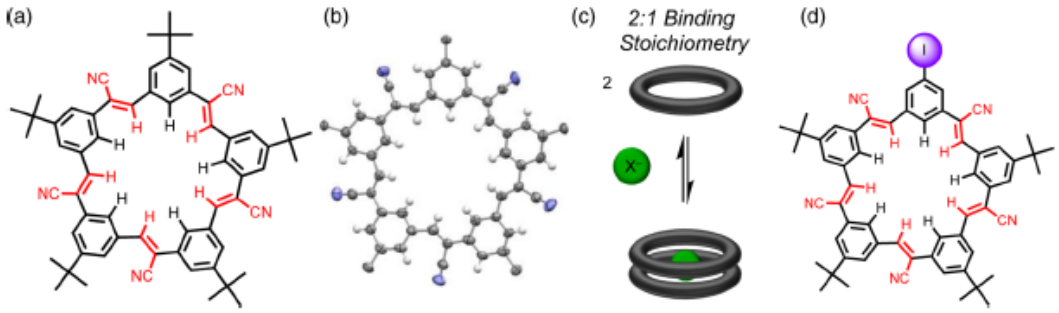

Figure 1. (a) Chemical and (b) crystal structure of cyanostar (**CS**) macrocycles. *tert*-Butyl groups have been removed for simplicity. (c) Preferred binding equilibria of cyanostar as a 2:1 complex around anions (X^-, green) of the right size, e.g., PF_6^-. (d) Chemical structure of iodo-cyanostar (**I-CS**).

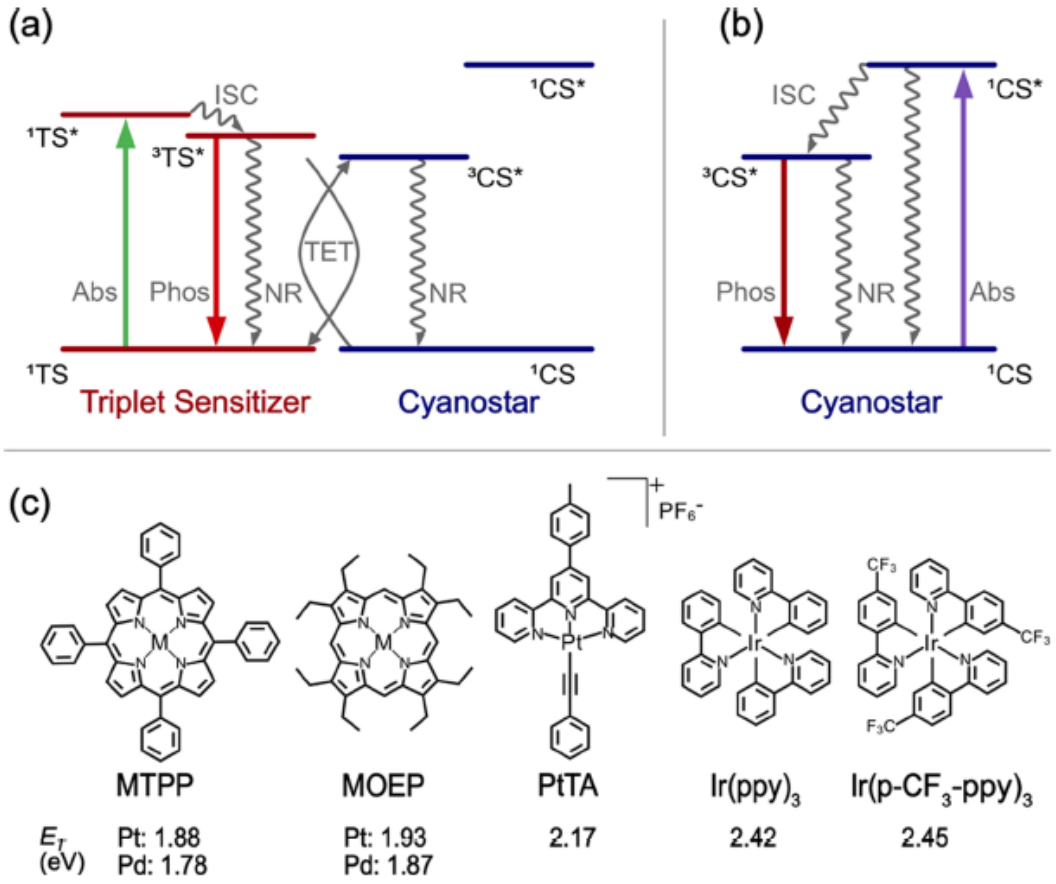

Figure 2. Simplified Jablonski diagrams illustrating the two different methods for determination of the cyanostar triplet energy using (a) Phos quenching with TET from a series of triplet sensitizers (TS) with known triplet state (^{3}TS*) energies, and (b) cyanostar Phos, populating the cyanostar triplet excited state by intersystem crossing (ISC) from the photoexcited singlet excited state (^{1}CS*). Photophysical processes shown are absorption (Abs), Phos, and nonradiative deactivation (NR). (c) Molecular structures of triplet donors; M = Pd, Pt for MOEP and MTPP.

DFT) to show that the triplet energy of cyanostar and its anion-driven complexes are both around 2.0 eV.

The chromophoric units in the cyanostar are five *trans*-cyanostilbenes. Stilbene and its derivatives have been thoroughly studied and they are the archetypical cis−trans isomerizing olefins.[29] These compounds often display twisted excited states and are subject to conformational heterogeneity.[30,31] The lowest photoexcited triplet state energies for many monomolecular stilbene derivatives have been reported both from triplet energy transfer (TET) experiments as well as Phos in low-temperature glasses;[32] however, no literature was found reporting the excited triplet energy for the specific *trans*-cyanostilbene derivative present in cyanostar.

https://doi.org/10.1021/acs.jpca.3c02701
J. Phys. Chem. A 2023, 127, 5841−5850

The triplet states of cyanostar have not previously been measured. The cyanostar macrocycle, its anion-binding properties,[28,33−36] and its packing in SMILES crystals have been well described.[23,24] The parent cyanostar is monomolecular in solution. It displays rapid interconversion between ∼300 low-energy conformations as revealed by molecular dynamics, DFT, and confirmed using the nuclear Overhauser effect.[37] The cyanostar has five cyanostilbenes in cross-conjugation with each other. Consistent with the optical spectroscopy of cyanostilbene,[38] cyanostar displays a low-quantum yield fluorescence band at 410 nm (3.3 eV) at room temperature.[23] Upon binding size-matched anions, like PF_6^-, it forms a discrete 2:1 complex.[28] In this form, the two macrocycles are π-stacked and display a ∼36° rotational offset from each other on account of interlocking steric contacts defined by the five *tert*-butyl substituents. While the number of conformations is reduced in the complex, it retains thermal access to many local minima with dynamically varying torsion angles indicative of a relatively flexible ground state.[37,39] Nevertheless, the stability of the 2:1 anion complex with the PF_6^- anion is remarkably high, recorded at 10^{12} M^{-2}. The stability of this complex, $\mathbf{CS}_2{\cdot}PF_6^-$, is generally accepted to increase in less polar solvents, like dichloromethane (DCM).[34,40] When studying anion binding, a spectroscopically and redox-inert cation such as tetrabutylammonium (TBA^+) is typically used. Further lowering of the solution polarity drives favorable ion pairing of the anionic 2:1 complexes with the counter cation.[41] Chloroform and aromatic solvents typically support these tight ion pairs.[35,41] The resulting 2:1:1 species, $\mathbf{CS}_2{\cdot}PF_6{\cdot}$TBA, is the elementary unit of crystal structures observed with various anions. They are also the units that compose the SMILES materials where the inert cations are replaced with optically active dyes.[23] Thus, the triplet energies of the 2:1 and 2:1:1 building blocks are key to laying the groundwork for designing triplet-based optical materials.

Herein, we describe an experimental and computational study of the first excited triplet state energies of cyanostar and its 2:1 cyanostar-anion complexes. Phos quenching (Figure 2a) using a Sandros analysis[42] was used to estimate the triplet excited state energies of cyanostar (1.96 eV) and the corresponding anionic complex (2.02 eV) revealing an insignificant change in the triplet energies upon complexation. The triplet energies (2.0 eV) match the one measured using Phos (Figure 2b) from cyanostar and its iodo-substituted variant (iodo-cyanostar, **I-CS**, Figure 1d) in low-temperature glasses. Both processes likely probe transitions between structurally similar S_0 and T_1 states. Computational studies using DFT and TD-DFT were performed to complement the experimental results and investigate the geometry of the cyanostar in the ground and excited states. This study is the first exploration into the triplet state and Phos properties of cyanostar and lays the foundation for the design of SMILES materials exploiting the triplet manifold.

METHODS

The synthesis of PtTA was based on established procedures. Stern−Volmer analyses conducted for the Phos quenching studies were performed in tetrahydrofuran (THF) at room temperature. Phos spectra of cyanostar and its complexes were measured in 2-methyltetrahydrofuran (MeTHF) at 85 K. DFT calculations have been performed to investigate the geometries and electronic states of the parent cyanostar as well as some of its relevant associated species. Structures were optimized at the B3LYP-D3BJ/6-31G level of theory for the cyanostar, **CSH**, its dimer, $(\mathbf{CSH})_2$, and the 2:1 complex, $(\mathbf{CSH})_2{\cdot}PF_6^-$. Single point calculations were performed on the optimized geometries using CAM-B3LYP-D3BJ/6-31+G(d). A CPCM continuum solvation model was used. For further details, please refer to the Supporting Information.

RESULTS AND DISCUSSION

Determining the Triplet Energy of Cyanostar Using Phos Quenching. The triplet energy of a molecule can be determined by measuring the rate constant of TET from a triplet donor of known triplet energy, the so-called Sandros method.[42] Assuming dynamic, diffusion-mediated energy transfer, the rate constant of TET, k_{TET}, depends on the energy difference between the triplet excited state of the donor, $E_{T,D}$, and the acceptor, $E_{T,A}$, as described by the Sandros equation

$$k_{TET} = \frac{k_{diff}}{1 + \exp(-(E_{T,D} - E_{T,A})/k_B T)} \quad (1)$$

Here, k_B is the Boltzmann constant, T is the temperature, and k_{diff} is the diffusion-controlled rate of collision between donor and acceptor. Equation 1 shows that k_{TET} approaches k_{diff} when the energetic driving force of TET increases, but k_{TET} decreases exponentially when $E_{T,A} > E_{T,D}$, i.e., when TET from the donor to acceptor is energetically uphill.

Using a set of triplet energy donors (Figure 2c) with a range of known triplet energies, the unknown triplet energy of an acceptor can be determined from the measured k_{TET} rate constants after fitting to the Sandros equation (eq 1). If the donor molecules are phosphorescent, the rate of TET can be calculated from the Phos intensity (or Phos lifetime) of the donor, measured in absence (I_0, τ_0) and in the presence of the acceptor (I, τ). The rate constant of TET, k_{TET}, is calculated by assuming dynamic quenching and using the Stern−Volmer relationship (eq 2), where $[A]$ is the concentration of the acceptor.

$$\frac{I_0}{I} = \frac{\tau_0}{\tau} = 1 + \tau_0 k_{TET}[A] \quad (2)$$

Rate constants of TET to cyanostar, **CS**, and its anion complex $\mathbf{CS}_2{\cdot}PF_6^-$, were measured using a series of phosphorescent triplet energy donors, including four metal porphyrins, two iridium(III) complexes and a platinum(II) complex (Figure 2c). The donor molecules platinum(II) octaethylporphyrin (PtOEP), palladium(II) octaethylporphyrin (PdOEP), platinum(II) tetraphenylporphyrin (PtTPP), palladium(II) tetraphenylporphyrin (PdTPP), *tris*(2-phenylpyridine)iridium(III) [$Ir(ppy)_3$], *tris*(2-*p*-trifluoromethylphenylpyridine)iridium(III) [$Ir(p\text{-}CF_3\text{-}ppy)_3$], and platinum(II) terpyridylphenylacetylide (PtTA) have triplet energies spanning from 1.7 to 2.4 eV, as determined from the peak or onset of their Phos emission (see the Supporting Information for details). This range of triplet energies were found to span the expected triplet state energy of cyanostar, thereby allowing the Sandros method to accurately determine its triplet energy.

The measured values of k_{TET} for cyanostar, **CS**, and its complex, $\mathbf{CS}_2{\cdot}PF_6^-$, as a function of the donor energies can be plotted versus the donor triplet energies (Figure 3). All Phos quenching measurements were performed in THF, except for the PtTA which was conducted in DCM on account of

https://doi.org/10.1021/acs.jpca.3c02701
J. Phys. Chem. A 2023, 127, 5841−5850

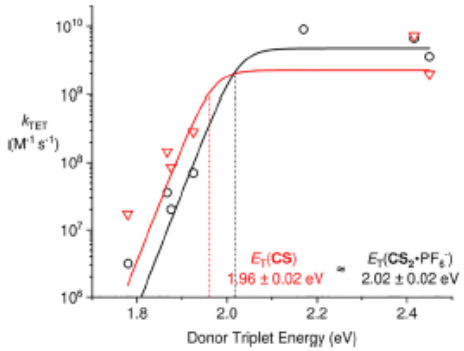

Figure 3. Sandros plots associated with the **CS** macrocycle (red triangles) and its anionic complex $\mathbf{CS_2}$·PF_6^- (black circles) using PtOEP, PdTPP, PtTPP, PdTPP, $Ir(ppy)_3$, and $Ir(p\text{-}CF_3\text{-}ppy)_3$ in THF and using PtTA in DCM as energy donors. Donor concentration was approximately 5−10 μM with the cyanostar concentration ranging from 10 to 500 μM for the generation of the Stern−Volmer quenching plots (SI). Solid lines show fits to eq 1.

solubility. Each data point corresponds to a series of Phos quenching experiments (see Stern−Volmer plots, Figures S2 and S3 and Table S1). For the mono-molecular cyanostar, **CS**, the best fit to eq 1 gives a triplet energy of 1.96 eV ± 0.02 eV. Here, the error is obtained from the data fitting. The estimated triplet energy of cyanostar is similar to the triplet energy of *trans*-stilbene,[32,43] indicating weak electronic communication on the triplet surface between the five meta-connected cyanostilbene subunits making up the cyanostar molecule. Using the same method, the triplet energy of the corresponding 2:1 complex, $\mathbf{CS_2}$·PF_6^-, was estimated to be 2.02 ± 0.02 eV from the fitted data (Figure 3). The minor and insignificant change in triplet energy upon anion-driven dimerization is consistent with the minor anion-induced change seen in the UV−vis Abs spectrum.[28] It should be noted that the error presented for these numbers is the standard error of fitting and should not be considered as the accuracy of the received triplet energy value. A rough estimate of the accuracy can instead be achieved by iteratively fitting the data in the Sandros plots (Figure 3) with a fixed value of the triplet energy to study how much the triplet energy can be varied and still result in a reasonable fit. With this simple method, the accuracy of the determined triplet energy is estimated to be ±0.05 eV. Further discussion about the accuracy of the method is given below.

Phos from Cyanostar. To provide an independent measure of the triplet energy of the cyanostar and its anion complex, we also measured their Phos spectra, which gives a more direct readout of the triplet energy. Similar to *trans*-stilbene, the cyanostar itself is not phosphorescent in liquid solution at room temperature but becomes very weakly phosphorescent in a low-temperature glass and in the presence of a heavy atom.[43] The low-temperature glass is expected to freeze out the conformational dynamics, whether they involve local distortions in the ground state as seen by MD[37] or twisting in the excited states. The glasses also inhibit bimolecular quenching from residual oxygen. As a result, we expect to increase Phos by lowering the rate of non-radiative decay from the triplet state (Figure 2b). We also expect the cyanostar to be frozen into a distribution of conformations at low temperature. Prior DFT studies[37] showed us that the cyanostar is not perfectly flat but instead has access to various conformations. In each of these, the cyano-olefin groups tilt either above or below the macrocycle's mean plane. The most stable conformations of the cyanostar have two non-neighboring olefins tilted above the plane and three below (Figure 4a). There are multiple combinations of this ruffled

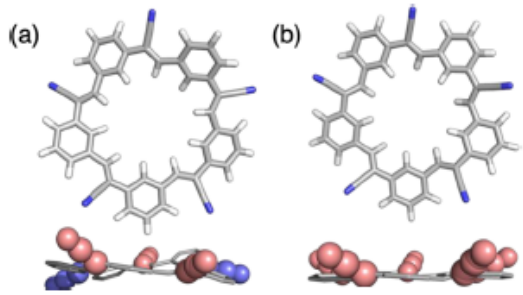

Figure 4. (a) Lowest-energy conformation of the cyanostar monomer. (b) Lowest energy conformation of one of the cyanostar macrocycles within a 2:1 cyanostar complex around a diglyme guest molecule. Geometries calculated with DFT as described previously.[37]

conformation for an overall 10-fold degeneracy. Based on Boltzmann statistics, there is ∼9% population in each of the 10 conformers at 85 K. Higher-energy conformations (totaling 10%) have similar tilts but across different combinations of olefins. In total, there is a high degree of conformational heterogeneity in the cyanostars. When examined in the complex, when two macrocycles are π stacked, the preferred conformation changes (Figure 4b) and while the number of conformations reduce, they are still plentiful in number.

In this study, two different approaches were used to induce Phos in the cyanostar. First, we covalently substituted the macrocycle with iodine[44] to make iodo-cyanostar (**I-CS**, Figure 1). Second, we leveraged cyanostar's facility for anion binding to use periodate, IO_4^-, in the formation of a 2:1 anion complex.[28] The iodine atoms were used as a means to exploit the heavy atom effect to enhance ISC and thereby increase the population of the triplet excited states from the photoexcited singlet excited state (Figure 2b), as well as to enhance the rate of Phos.[45] In the case of IO_4^-, this anion provided a non-covalent mechanism of influencing ISC. Spectra were recorded for the mono-molecular iodo-cyanostar, the anion complex of **I-CS** using the non-heavy atom PF_6^- anion, $(\mathbf{I\text{-}CS})_2$·PF_6^-, and a dimer of the parent cyanostar with a periodate anion, $\mathbf{CS_2}$·IO_4^-. All measurements were performed at 85 K in a frozen organic glass of MeTHF. Under these conditions, we assume **I-CS** to be frozen into 10+ conformations with the cyano groups tilted above and below the ring (vide supra). In the complexes, the conformational landscape is far simpler. All 10 cyano groups on both cyanostars are tilted away from the π-stacked seam (Figure 4b). In both the complexed and uncomplexed cyanostars, the low-energy barriers seen by MD (1.5 kcal/mol) suggest that there will be a distribution of many different tilt angles in the low-temperature glasses. We also assume that formation of contact ionpairs, e.g., $\mathbf{CS_2}$·IO_4·TBA, will be favored on entropic grounds as the temperature is lowered down to the glass transition temperature of MeTHF (137 K) and ultimately in the glass.

The Phos spectra of the iodinated cyanostar and the anion complexes (Figure 5) were recorded using time-gated

https://doi.org/10.1021/acs.jpca.3c02701
J. Phys. Chem. A 2023, 127, 5841−5850

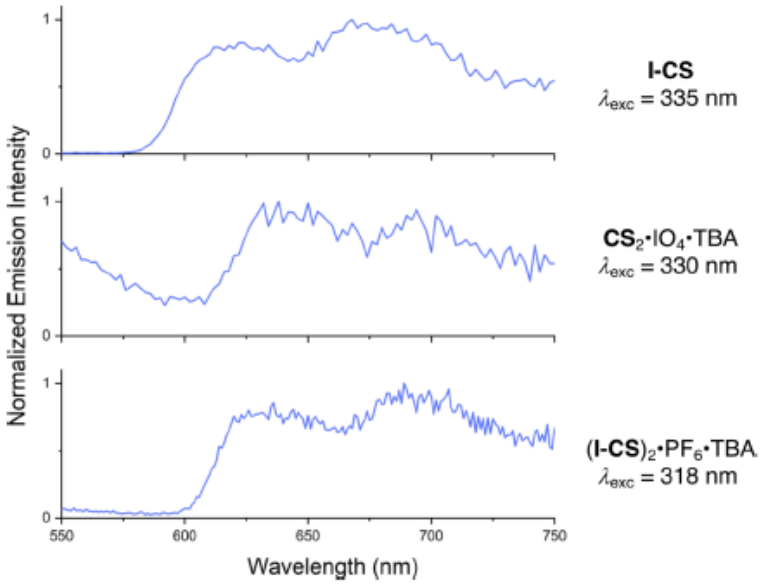

Figure 5. Phos spectra of **I-CS**, CS_2·IO_4·TBA, and $(I\text{-}CS)_2$·PF_6·TBA. Spectra recorded in MeTHF (~20−40 μM) at 85 K at various excitation wavelengths as noted.

emission. Therein, the sample is excited with a short excitation pulse and the emission signal is recorded after a time delay in order to exclude any short-lived emission signals like fluorescence. The emission spectrum of **I-CS** (Figure 5) shows clear Phos in the region of 600−750 nm with two resolved vibronic bands centered at 620 and 675 nm. The triplet energy level is estimated from the position of the highest energy Phos band (620 nm), which corresponds to 2.0 eV. The emission spectra of the anion-induced dimers, CS_2·IO_4·TBA and $(I\text{-}CS)_2$·PF_6·TBA show Phos in the same region with two vibronic bands, but with lower intensity and lower signal-to-noise ratio. The energy of the highest-energy Phos band (635 and 625 nm) for CS_2·IO_4·TBA and $(I\text{-}CS)_2$·PF_6·TBA, respectively, corresponds to a triplet energy of 1.95 and 1.98 eV. The emission intensity seen at shorter wavelengths for CS_2·IO_4·TBA and $(I\text{-}CS)_2$·PF_6·TBA is assigned to the tail of the strong fluorescence which could not be eliminated totally in the gated emission. This interpretation is supported by the close spectral resemblance of the emission tail in the 500−600 nm region and the steady-state fluorescence spectrum (Figure S4). Low-intensity Phos precluded measurements of the quantum yields. The Phos emission decay was measured (Figure S5) for **I-CS** and $(I\text{-}CS)_2$·PF_6·TBA but could not be measured for CS_2·IO_4·TBA stemming from the lower emission intensity. The Phos decay could be fitted to a biexponential decay with an average lifetime (amplitude weighted) of 0.50 ms for **I-CS**, and 0.30 ms for $(I\text{-}CS)_2$·PF_6·TBA (Table S2).

The estimates of the triplet energies are closely matched. The Phos spectra of the two different cyanostar complexes (Figure 5) are similar, which suggest that iodine substitution only adds a small (~30 meV) perturbation to the triplet energy. The triplet energies of cyanostar determined from the Phos spectra match with the triplet energy of substituted stilbenes, E_T ~ 2.0 eV.[32] This resemblance suggests that the meta linkage between the five cyanostilbenes present in the cyanostar leads to triplet states localized on one stilbene unit as supported from calculation. The close resemblance between the measured triplet energies of the cyanostar monomer and its anion complex, from both the emission quenching and Phos experiments, show that π-stacked dimerization of the cyanostar only induces a minor shift in the triplet energy.

The triplet energy estimated from quenching studies matches low-temperature Phos despite probing different processes (Figure 2a,b). The first is a Dexter energy-transfer excitation from the singlet ground state of cyanostar to its first triplet excited state, while the second is a radiative decay from the excited triplet state of the cyanostar that is likely frozen in a ground state-like geometry. Given the matching energies, both processes likely probe transitions between similar S_0 and T_1 states with modest geometrical distortion between them.

Even though both methods give very similar estimates of the triplet energies, the accuracy of the two methods needs to be considered. The accuracy of the Sandros method depends on how well the triplet energies of the donors have been determined as well as the accuracy in the estimation of the rate constant of TET derived from the Phos quenching experiments. Furthermore, the Sandros method assumes free diffusion of both the donor and acceptor and that all donors−acceptor pairs share the same diffusion limited rate constant of energy transfer, k_{diff}. More donor molecules could, of course, be included in the study to get more data points in the Sandros plot. However, the six or seven donors included in this study are considered sufficient to provide an estimate of the cyanostar-based triplet energies. As already noted, these donors span a suitable range of triplet energies. This range enables access to a rate constant close to the diffusion limit[1] for TET of ~5×10^9 M^{-1} s^{-1} when $E_{T,A} < E_{T,D}$ and to triplet energies giving a TET rate constant that is 2 or 3 orders of magnitude lower when $E_{T,A} > E_{T,D}$.

The Phos spectra of the cyanostar gives an estimate of the triplet energy of the molecule in a solid environment at low temperature likely locked in a ground state-like geometry. This situation could be quite different from a fully relaxed triplet state obtained in liquid solution at room temperature. For the

https://doi.org/10.1021/acs.jpca.3c02701
J. Phys. Chem. A 2023, 127, 5841−5850

Table 1. Experimental Triplet Energies Obtained from Various Forms of the Cyanostar in Various Physical States

compound	solvent	state	T/K	E_T/eV	τ/ms[a]	experiment[b]
CS	THF	liquid	RT	1.96 ± 0.05		TET
$CS_2{\cdot}PF_6^-$	THF	liquid	RT	2.02 ± 0.05		TET
I-CS	MeTHF	glass	85	2.0	0.50	phos
$CS_2{\cdot}IO_4{\cdot}$TBA	MeTHF	glass	85	1.95		phos
$(\text{I-CS})_2{\cdot}PF_6{\cdot}$TBA	MeTHF	glass	85	1.98	0.30	phos

[a]Average lifetime (amplitude weighted). [b]Measured using TET by Stern−Volmer quenching of triplet states (1.78−2.45 eV) according to the Sandros method. Uncertainties determined from a sensitivity analysis. Phos experiments conducted using time-gated emission.

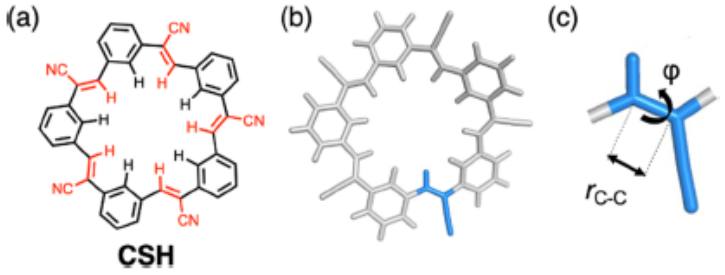

Figure 6. (a) Structure of modified cyanostar (**CSH**). (b,c) Definition of the torsion angle and the C═C bond coordinate that deform in the excited states of cyanostar and its complexes.

quenching studies the experimental situation is quite different, but is also expected to involve **CS** and $CS_2{\cdot}X^-$ complexes in ground state geometries.[46] Thus, geometry relaxation of the T_1 state is highly prohibited in both cases (though for different reasons), which may explain the close match of the triplet energies between the two methods (Table 1). From this argument, we conclude that the triplet excited state energy of both the cyanostar and its anion complexes is close to 2.0 eV when major geometry changes are prohibited. This situation also corresponds to the cyanostar complexes in SMILES materials. Thus, this T_1 energy is relevant for the design of SMILES materials that incorporate phosphorescent dyes and for the manipulation of triplet excitons.

Calculations on the Singlet and Triplet Excited States. DFT calculations were performed to investigate the electronic states of the parent cyanostar and its complexes as well as the structure of the excited states that were not probed experimentally. TD-DFT was employed to obtain excited singlet state properties including the excitation and emission energies along with the associated oscillator strengths. The *tert*-butyl groups of cyanostar were replaced with hydrogen atoms in the model compound **CSH** (Figure 6a) to reduce the computational cost at very little loss in accuracy.

Structures were optimized at the B3LYP-D3BJ/6-31G level of theory for the cyanostar, **CSH**, its dimer, $(\text{CSH})_2$, and the 2:1 complex, $(\text{CSH})_2{\cdot}PF_6^-$. Polarization functions were added to the anion to accommodate the hypervalent phosphorous atom. Single-point calculations were performed on the optimized geometries using CAM-B3LYP-D3BJ/6-31+G(d). DCM (ε = 8.93) was used as the solvent in conjunction with a CPCM continuum solvation model. This model should be representative of low polarity solvents. A modest change in solvent polarity, such as for THF (ε = 7.58), is expected to have insignificant impact on our results.

The behavior of the ground state singlet (S_0) of **CSH** has been analyzed previously.[37] There are many low-lying conformers (332) within a small energy window (2.3 kcal/mol) undergoing rapid interconversion. Each of them has a ruffled semi-planar geometry. The deviation from planarity stems from non-zero dihedrals in the C−C single bonds connecting the phenylene units and the olefin units. In the ground state of the cyanostar and its complexes, the olefin's C═C double bond (defined in blue, Figure 6b,c) is mostly untwisted with a dihedral angle close to ∼0° (varying between 0 and 5° in the different conformations). Despite these small deviations from planarity and the conformational heterogeneity, **CSH** is shape persistent as a result of the relatively small average change in molecular geometry across these conformations.[37] Considering both the pseudo-degenerate character of the 332 ground state conformers (relative to the typical scale of electronic states, ∼50 kcal/mol) and the macrocycle's shape persistence, the effect of these conformers on the energies of the various singlet and triplet states is assumed to be negligible in our current work.

The optical Abs was examined using the ground state geometry (Figure 7a). The cyanostar structure has pseudo-five-

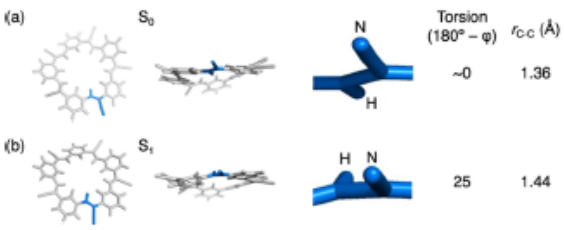

Figure 7. Structural characteristics of the (a) S_0 and (b) S_1 states obtained by DFT and TD-DFT, respectively.

fold symmetry, and it is convenient to consider the behavior expected from C_5 symmetry. Analysis of the first five excited states shows that the first excited state, S_1, is non-degenerate, while the second and third excited states, S_2 and S_3, are close in energy (pseudo-degenerate), as are the S_4 and S_5 states. The excitation energy corresponding to the $S_0 \rightarrow S_1$ transition is 3.6 eV albeit with a low oscillator strength (f = 0.004). The S_2 and

https://doi.org/10.1021/acs.jpca.3c02701
J. Phys. Chem. A 2023, 127, 5841−5850

S_3 states lie at 3.8 eV with very high oscillator strengths (f = 2.2). This finding is consistent with the lowest-energy UV−vis Abs maximum of **CS** measured at 3.8 eV. The S_4 and S_5 states lie at 3.9 eV with small oscillator strengths (f = 0.04 and 0.02, respectively).

The rate of internal conversion from S_2 to S_1 is usually rapid and emission is therefore expected to occur from the S_1 state. Thus, geometry optimization of the S_1 state was carried out using TD-DFT (see the Supporting Information for details). Compared to the geometry of the S_0 state (Figure 7a), the optimized geometry of the cyanostar in its S_1 state (Figure 7b) shows one of the five olefins is twisted from 0 to 25° and the double bond is elongated from 1.36 to 1.44 Å. This change in geometry is similar to half the elongation from a double bond (1.34 Å in ethylene) to a single bond (1.54 Å in ethane) suggesting a bond order of 1.5. The transition energy for emission from this S_1 state to the S_0 state (at the S_1 geometry) is found to be 2.9 eV. This finding is consistent with the fluorescence spectral maximum of **CS** observed at ∼3.0 eV. Thus, the calculated singlet manifolds are consistent with experimental observations.

Unlike fluorescence, Phos originates from an excited state of different spin symmetry (triplet, T) and can be calculated directly using standard ground-state DFT methods. As a model of the possible features we might expect, it is common for stilbenes to be twisted about the C═C double bond in the excited state, consistent with the expected cis−trans isomerization.[47] An analogous feature becomes prominent in the triplet state of the mono-molecular **CSH** (Figure 8a). Therein,

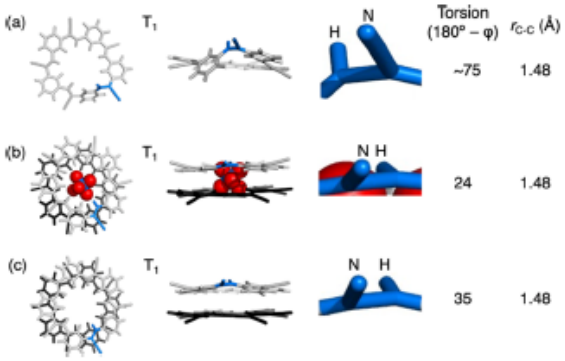

Figure 8. Structural characteristics of the triplet (T_1) states of (a) **CSH**, (b) the anion complex $(\mathbf{CSH})_2{\cdot}PF_6^-$, and (c) cyanostar dimer $(\mathbf{CSH})_2$ obtained by DFT.

the triplet state shows a substantial ∼75° twisting about a C═C double bond in one of the five cyanostilbene units. Such a state has an adiabatic energy difference between excited triplet (T_1) and ground (S_0) state at their respective geometries of 1.7 eV. However, the geometry change is so large that it will have very little Franck−Condon overlap with the ground state.

The Phos studies were carried out at low temperature (85 K) in a glassy solid, which will restrict movements in the cyanostar, like twisting. We expect the pseudo-rigid environment of the glass to be replicated in the calculated 2:1 complex $(\mathbf{CSH})_2{\cdot}PF_6^-$ (Figure 8b), which has been studied experimentally as $(\mathbf{CS})_2{\cdot}PF_6^-$. In this case, reduced twisting in the calculated structure likely emerges from a combination of the steric constraints of the adjacent macrocycle and the sum of stabilizing interactions from the π stacking and the CH···PF_6^- hydrogen bonding counteracting the tendency to rotate. We observe (Figure 8b) a reduction in the triplet's twist angle to only 24°. The adiabatic energy is now calculated to be 2.0 eV, some 0.3 eV higher than the triplet state of **CSH**. The less twisted triplet state of $(\mathbf{CSH})_2{\cdot}PF_6^-$ likely has a more reasonable Franck-Condon overlap with the ground singlet state.

In order to further model the uncomplexed cyanostar in the absence of the anion, we carried out two sets of studies. In the first, we studied the geometry of the stacked cyanostar dimer, $(\mathbf{CSH})_2$ (Figure 8c). This species is not necessarily expected to be present in solution but serves as a surrogate to replicate the steric constrains imposed by other species, like the glassy solvent. The dimer was obtained by removing the anion from the complex and reoptimizing the geometry. Again, the twisting is smaller (only 35°) than the single macrocycle, but it retains the 0.12 Å extension in the olefin. The energy of this triplet is at 1.9 eV, showcasing again how the degree of shape change correlates with the triplet energy. Further analysis of the character of the triplet excited state in this stacked cyanostar dimer $(\mathbf{CSH})_2$ shows the excitation is almost completely localized on one of the two cyanostar macrocycles. The other macrocycle is playing a passive role with respect to the electronic excitation. When the passive cyanostar is removed, the distorted cyanostar again shows a triplet energy close to 2.0 eV. If, however, it is allowed to relax, it forms the highly twisted triplet seen earlier in the isolated cyanostar (Figure 8a).

Calculations show that less twisted T_1 states of $(\mathbf{CSH})_2$ and $(\mathbf{CSH})_2{\cdot}PF_6^-$ have triplet energies close to 2 eV and that twisting correlates with lowering of the triplet energy. Since the glassy solvent restricts rotation, such a state could explain the experimental observations in the parent cyanostar too. In order to study the properties of a pseudo-planar triplet state, we carried out a potential energy scan to explore the dependence of the triplet energy on the most relevant geometrical parameters. A comparison of S_0 and T_1 geometries reveals that the most significant geometry change occurs only in a few coordinates (Figure 9, R_1, R_2, $r_{C=C}$, and φ). The change in the

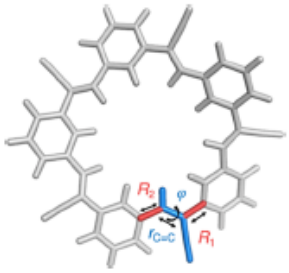

Figure 9. Bonds and dihedral angle next to the C═C bond in the stilbene unit undergoing rotation also change. All the coordinates undergoing significant change are highlighted.

three neighboring bond lengths are correlated with each other. As $r_{C=C}$ increases (by 0.12 Å) on going to the triplet state, both R_1 and R_2 decrease (by 0.05−0.06 Å), consistent with the conjugation across the three bonds.

We performed a stepwise relaxation along the triplet T_1 state from the ground state (S_0) geometry to the pseudo-planar triplet state by fixing the dihedral φ and relaxing the other

https://doi.org/10.1021/acs.jpca.3c02701
J. Phys. Chem. A 2023, 127, 5841−5850

three structural parameters. The scan involved 10 geometrical steps in **CSH** (Figure 10).

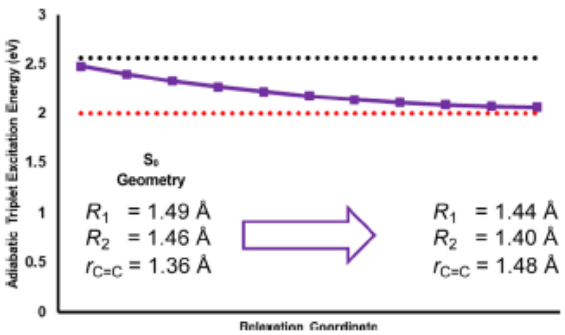

Figure 10. Stepwise relaxation from ground state (S_0) geometry to pseudo-planar triplet geometry of **CSH**, obtained by freezing the dihedral φ. 10 steps were taken, each changing each of the three coordinates by a tenth of the range. At each point, triplet state is optimized while keeping R_1, R_2, $r_{C=C}$, and φ fixed.

The relaxation of R_1, R_2, and $r_{C=C}$ without twisting brings the triplet state down to 2.06 eV, which is close to the experimental value. Restriction in the twisting also shows this state is higher in energy relative to the twisted form of **CSH** by 0.36 eV. It is interesting to note that the terminal (C_1–C_4) bond distance between neighboring phenylene units is changed very little (<0.01 Å) in this scan, due to the opposing effects of the different bond lengths. Thus, the final constrained triplet geometry is changed very little from the ground state geometry. Consistently, we observe that the energy of the untwisted **CSH** triplet (2.06 eV) closely matches that of the $(\mathbf{CSH})_2{\cdot}PF_6^-$ triplet (2.0 eV). This similarity matches the triplet energies measured using the low-temperature Phos in the glassy solids for **I-CS** (2.0 eV) and $(\mathbf{I\text{-}CS})_2{\cdot}PF_6{\cdot}$TBA (1.98 eV).

The results from our calculations are consistent with the findings from both types of experiments reported in this study. The TET (Figure 2a) is related to a vertical excitation from a ground-state cyanostar geometry, ^{1}**CS**, to a triplet state, ^{3}**CS*** (with similar geometry). For the Phos, it involves vertical de-excitation from cyanostar in an excited triplet state. However, its geometry is expected to closely resemble the ground state in the frozen glass on account of restricted motions in this physical state. Thus, both processes likely probe transitions between states with ground state-like geometries, consistent with their matching triplet energies at ~2.0 eV. This consistency extends to the similar 2.0 eV triplet energy for the single macrocycle and the complexes. The only reasonable explanation for the observation is that Phos from these two forms of the cyanostar are the same is that their geometries are also the same. This interpretation can be best accommodated if the geometries both resemble those of the ground states.

In summary, the DFT studies show that large differences in the triplet energies determined using TET and low-temperature Phos will only occur if there are large-scale geometry changes. Thus, as also shown by the DFT studies, reductions in large scale motions, whether by complexation or increased viscosity, raise the triplet energy. The observations from experiment indicate that the differences in triplet energies measured using the different methods and between the various forms of the cyanostar are negligible. For this reason, the triplet states of cyanostar and its complexes that are populated by TET closely resemble the ground state geometry. Furthermore, the triplet states that are populated in low-temperature glasses also resemble the ground state geometry.

■ CONCLUSIONS

The triplet energy of both cyanostar and its anion-bound complexes is 2.0 eV when probed using experiments that correspond closely to their ground state geometries. This energy was observed using room-temperature TET quenching studies, which effectively excite the molecules from their ground states to the first triplet state. The same energy was observed using low-temperature (85 K) Phos, which corresponds to light emission from the first triplet state frozen into the ground-state geometry. Therefore, both processes likely probe transitions between S_0 and T_1 states that are in similar ground-state geometries. DFT and TD-DFT provided insights into the role of relaxation on the triplet energy. Full relaxation of a single cyanostar shows a triplet energy of 1.7 eV with one of the olefins twisted and elongated. Upon formation of a 2:1 anion complex, relaxation remains localized on one olefin with the degree of twisting much reduced from 75 to 24° and resulting in a higher 2.0 eV energy for the triplet state. In addition, iodination had a minor effect on the triplet energies while improving the phosphorescent intensity consistent with the heavy atom effect. Use of heavy-element anions like periodate, IO_4^-, was also explored as a means to enhance ISC though the covalently incorporated iodine atom had a more substantial effect. These findings indicate that the primary mode of anion-induced packing of cyanostar macrocycles seen in solid-state SMILES materials has a major impact on the triplet energies by preventing large structural relaxation. These findings provide a blueprint for triplet state engineering in cyanostar-based SMILES defined by a 2.0 eV triplet window in structurally constrained SMILES materials.

■ ASSOCIATED CONTENT

Supporting Information

The Supporting Information is available free of charge at https://pubs.acs.org/doi/10.1021/acs.jpca.3c02701.

Atomic coordinates for **CSH** S_0 (XYZ)

Atomic coordinates for **CSH** S_1 (XYZ)

Atomic coordinates for the **CSH** triplet (XYZ)

Atomic coordinates for the $(\mathbf{CSH})_2{\cdot}PF_6^-$ triplet (XYZ)

Synthesis of PtTA, Phos quenching data, Stern–Volmer plots, Phos spectra, computational chemistry methods, energies, and atomic coordinates (PDF)

Atomic coordinates for the $(\mathbf{CSH})_2$ triplet (XYZ)

■ AUTHOR INFORMATION

Corresponding Authors

Bo Albinsson – *Department of Chemistry and Chemical Engineering, Chalmers University of Technology, Gothenburg 41296, Sweden;* orcid.org/0000-0002-5991-7863; Email: balb@chamlers.se

Amar H. Flood – *Department of Chemistry, Indiana University, Bloomington, Indiana 47405, United States;* orcid.org/0000-0002-2764-9155; Email: aflood@iu.edu

https://doi.org/10.1021/acs.jpca.3c02701
J. Phys. Chem. A 2023, 127, 5841−5850

Authors

Fredrik Edhborg – *Department of Chemistry and Chemical Engineering, Chalmers University of Technology, Gothenburg 41296, Sweden;* orcid.org/0000-0001-5168-2935

Axel Olesund – *Department of Chemistry and Chemical Engineering, Chalmers University of Technology, Gothenburg 41296, Sweden;* orcid.org/0000-0003-1202-7844

Vikrant Tripathy – *Department of Chemistry, Indiana University, Bloomington, Indiana 47405, United States;* orcid.org/0000-0002-3246-0680

Yang Wang – *Nano-Science Center & Department of Chemistry, University of Copenhagen, Copenhagen 2100, Denmark;* orcid.org/0000-0003-0867-2752

Tumpa Sadhukhan – *Department of Chemistry, Indiana University, Bloomington, Indiana 47405, United States; Department of Chemistry, SRM Institute of Science and Technology, Chennai 603203, India*

Andrew H. Olsson – *Department of Chemistry, Indiana University, Bloomington, Indiana 47405, United States*

Niels Bisballe – *Nano-Science Center & Department of Chemistry, University of Copenhagen, Copenhagen 2100, Denmark;* orcid.org/0000-0002-4476-5481

Krishnan Raghavachari – *Department of Chemistry, Indiana University, Bloomington, Indiana 47405, United States;* orcid.org/0000-0003-3275-1426

Bo W. Laursen – *Nano-Science Center & Department of Chemistry, University of Copenhagen, Copenhagen 2100, Denmark;* orcid.org/0000-0002-1120-3191

Complete contact information is available at: https://pubs.acs.org/10.1021/acs.jpca.3c02701

Notes

The authors declare no competing financial interest.

■ ACKNOWLEDGMENTS

A.H.F. and K.R. thank the National Science Foundation for support (DMR-2118423). B.A. is grateful to the Swedish Energy Agency (46526-1) and Swedish Research Council for providing financial support. B.W.L. thanks the Danish Council of Independent Research (DFF-0136-00122B). Y.W. thanks the European Union's Horizon 2020 research and innovation programme under the Marie Skłodowska-Curie grant agreement no. 801199.

■ REFERENCES

(1) Lakowicz, J. R. *Principles of Fluorescent Spectroscopy*; Springer, 2006.

(2) Beery, D.; Schmidt, T. W.; Hanson, K. Harnessing Sunlight via Molecular Photon Upconversion. *ACS Appl. Mater. Interfaces* **2021**, *13*, 32601−32605.

(3) Hanna, M. C.; Nozik, A. J. Solar conversion efficiency of photovoltaic and photoelectrolysis cells with carrier multiplication absorbers. *J. Appl. Phys.* **2006**, *100*, 074510.

(4) Di, D.; Romanov, A. S.; Yang, L.; Richter, J. M.; Rivett, J. P. H.; Jones, S.; Thomas, T. H.; Abdi Jalebi, M.; Friend, R. H.; Linnolahti, M.; et al. High-performance light-emitting diodes based on carbene-metal-amides. *Science* **2017**, *356*, 159−163.

(5) Kimura, K.; Miwa, K.; Imada, H.; Imai-Imada, M.; Kawahara, S.; Takeya, J.; Kawai, M.; Galperin, M.; Kim, Y. Selective triplet exciton formation in a single molecule. *Nature* **2019**, *570*, 210−213.

(6) Smith, M. B.; Michl, J. Singlet Fission. *Chem. Rev.* **2010**, *110*, 6891−6936.

(7) Beery, D.; Wheeler, J. P.; Arcidiacono, A.; Hanson, K. CdSe Quantum Dot Sensitized Molecular Photon Upconversion Solar Cells. *ACS Appl. Energy Mater.* **2019**, *3*, 29−37.

(8) Cheng, Y. Y.; Nattestad, A.; Schulze, T. F.; MacQueen, R. W.; Fuckel, B.; Lips, K.; Wallace, G. G.; Khoury, T.; Crossley, M. J.; Schmidt, T. W. Increased upconversion performance for thin film solar cells: a trimolecular composition. *Chem. Sci.* **2016**, *7*, 559−568.

(9) Simpson, C.; Clarke, T. M.; MacQueen, R. W.; Cheng, Y. Y.; Trevitt, A. J.; Mozer, A. J.; Wagner, P.; Schmidt, T. W.; Nattestad, A. An intermediate band dye-sensitised solar cell using triplet-triplet annihilation. *Phys. Chem. Chem. Phys.* **2015**, *17*, 24826−24830.

(10) Börjesson, K.; Dzebo, D.; Albinsson, B.; Moth-Poulsen, K. Photon upconversion facilitated molecular solar energy storage. *J. Mater. Chem. A* **2013**, *1*, 8521.

(11) Yang, Z. Y.; Mao, Z.; Xie, Z. L.; Zhang, Y.; Liu, S. W.; Zhao, J.; Xu, J. R.; Chi, Z. G.; Aldred, M. P. Recent advances in organic thermally activated delayed fluorescence materials. *Chem. Soc. Rev.* **2017**, *46*, 915−1016.

(12) Hill, S. P.; Dilbeck, T.; Baduell, E.; Hanson, K. Integrated Photon Upconversion Solar Cell via Molecular Self-Assembled Bilayers. *ACS Energy Lett.* **2016**, *1*, 3−8.

(13) Singh-Rachford, T. N.; Castellano, F. N. Photon upconversion based on sensitized triplet-triplet annihilation. *Coord. Chem. Rev.* **2010**, *254*, 2560−2573.

(14) Mongin, C.; Moroz, P.; Zamkov, M.; Castellano, F. N. Thermally activated delayed photoluminescence from pyrenyl-functionalized CdSe quantum dots. *Nat. Chem.* **2018**, *10*, 225−230.

(15) Wei, P.; Zhang, X.; Liu, J.; Shan, G. G.; Zhang, H.; Qi, J.; Zhao, W.; Sung, H. H.; Williams, I. D.; Lam, J. W. Y.; et al. New Wine in Old Bottles: Prolonging Room-Temperature Phosphorescence of Crown Ethers by Supramolecular Interactions. *Angew. Chem., Int. Ed.* **2020**, *59*, 9293−9298.

(16) Bock, H. G.-H.; Gharagozloo-Hubmann, K.; Sievert, M.; Prisner, T.; Havlas, Z.; Havlas, Z. Single crystals of an ionic anthracene aggregate with a triplet ground state. *Nature* **2000**, *404*, 267−269.

(17) Dexter, D. L.; Schulman, J. H. Theory of Concentration Quenching in Inorganic Phosphors. *J. Chem. Phys.* **1954**, *22*, 1063−1070.

(18) Chen, R. F.; Knutson, J. R. Mechanism of fluorescence concentration quenching of carboxyfluorescein in liposomes-Energy transfer to nonfluorescent dimers. *Anal. Biochem.* **1988**, *172*, 61−77.

(19) Kasha, M.; Rawls, H. R.; Ashraf El-Bayoumi, M. The exciton model in molecular spectroscopy. *Pure Appl. Chem.* **1965**, *11*, 371−392.

(20) Chaudhuri, K. D. Concentration quenching of fluorescence in solutions. *Z. Phys.* **1959**, *154*, 34−42.

(21) Zhang, X.; Chen, Z. J.; Wurthner, F. Morphology Control of Fluorescent Nanoaggregates by Co-Self-Assembly of Wedge- and Dumbbell-Shaped Amphiphilic Perylene Bisimides. *J. Am. Chem. Soc.* **2007**, *129*, 4886−4887.

(22) Bialas, D.; Zitzler-Kunkel, A.; Kirchner, E.; Schmidt, D.; Wurthner, F. Structural and quantum chemical analysis of exciton coupling in homo- and heteroaggregate stacks of merocyanines. *Nat. Commun.* **2016**, *7*, 12949.

(23) Benson, C. R.; Kacenauskaite, L.; VanDenburgh, K. L.; Zhao, W.; Qiao, B.; Sadhukhan, T.; Pink, M.; Chen, J.; Borgi, S.; Chen, C.-H.; et al. Plug-and-Play Optical Materials from Fluorescent Dyes and Macrocycles. *Chem* **2020**, *6*, 1978−1997.

(24) Chen, J.; Fateminia, S. M. A.; Kacenauskaite, L.; Baerentsen, N.; Gronfeldt Stenspil, S.; Bredehoeft, J.; Martinez, K. L.; Flood, A. H.; Laursen, B. W. Ultrabright Fluorescent Organic Nanoparticles Based on Small-Molecule Ionic Isolation Lattices. *Angew. Chem., Int. Ed. Engl.* **2021**, *60*, 9450−9458.

(25) Chen, J. S.; Stenspil, S. G.; Kaziannis, S.; Kacenauskaite, L.; Lenngren, N.; Kloz, M.; Flood, A. H.; Laursen, B. W. Quantitative Energy Transfer in Organic Nanoparticles Based on Small-Molecule Ionic Isolation Lattices for UV Light Harvesting. *ACS Appl. Nano Mater.* **2022**, *5*, 13887−13893.

(26) Kacenauskaite, L.; Stenspil, S. G.; Olsson, A. H.; Flood, A. H.; Laursen, B. W. Universal Concept for Bright, Organic, Solid-State Emitters-Doping of Small-Molecule Ionic Isolation Lattices with FRET Acceptors. *J. Am. Chem. Soc.* **2022**, *144*, 19981−19989.
(27) Haketa, Y.; Sasaki, S.; Ohta, N.; Masunaga, H.; Ogawa, H.; Mizuno, N.; Araoka, F.; Takezoe, H.; Maeda, H. Oriented salts: dimension-controlled charge-by-charge assemblies from planar receptor-anion complexes. *Angew. Chem., Int. Ed. Engl.* **2010**, *49*, 10079−10083.
(28) Lee, S.; Chen, C. H.; Flood, A. H. A pentagonal cyanostar macrocycle with cyanostilbene CH donors binds anions and forms dialkylphosphate [3]rotaxanes. *Nat. Chem.* **2013**, *5*, 704−710.
(29) Saltiel, J.; Charlton, J. L. Essay 14—Cis-Trans Isomerization of Olefins. *Org. Chem.* **1980**, *42*, 25−89.
(30) Zhang, Y.; Wang, K.; Zhuang, G.; Xie, Z.; Zhang, C.; Cao, F.; Pan, G.; Chen, H.; Zou, B.; Ma, Y. Multicolored-fluorescence switching of ICT-type organic solids with clear color difference: mechanically controlled excited state. *Chem.—Eur. J.* **2015**, *21*, 2474−2479.
(31) Grabowski, Z. R.; Rotkiewicz, K.; Rettig, W. Structural Changes Accompanying Intramolecular Electron Transfer- Focus on Twisted Intramolecular Charge-Transfer States and Structures. *Chem. Rev.* **2003**, *103*, 3899−4032.
(32) Goerner, H. Phosphorescence of trans-Stllbene, Stilbene Derivatives, and Stilbene-like Molecules at 77 K. *J. Phys. Chem.* **1989**, *93*, 1826−1832.
(33) Hirsch, B. E.; Lee, S.; Qiao, B.; Chen, C. H.; McDonald, K. P.; Tait, S. L.; Flood, A. H. Anion-induced dimerization of 5-fold symmetric cyanostars in 3D crystalline solids and 2D self-assembled crystals. *Chem. Commun.* **2014**, *50*, 9827−9830.
(34) Fatila, E. M.; Twum, E. B.; Sengupta, A.; Pink, M.; Karty, J. A.; Raghavachari, K.; Flood, A. H. Anions Stabilize Each Other inside Macrocyclic Hosts. *Angew. Chem., Int. Ed.* **2016**, *55*, 14057−14062.
(35) Fatila, E. M.; Twum, E. B.; Karty, J. A.; Flood, A. H. Ion Pairing and Co-facial Stacking Drive High-Fidelity Bisulfate Assembly with Cyanostar Macrocyclic Hosts. *Chem.—Eur. J.* **2017**, *23*, 10652−10662.
(36) Fatila, E. M.; Pink, M.; Twum, E. B.; Karty, J. A.; Flood, A. H. Phosphate-phosphate oligomerization drives higher order co-assemblies with stacks of cyanostar macrocycles. *Chem. Sci.* **2018**, *9*, 2863−2872.
(37) Liu, Y.; Singharoy, A.; Mayne, C. G.; Sengupta, A.; Raghavachari, K.; Schulten, K.; Flood, A. H. Flexibility Coexists with Shape-Persistence in Cyanostar Macrocycles. *J. Am. Chem. Soc.* **2016**, *138*, 4843−4851.
(38) An, B.-K.; Kwon, S. K.; Jung, S. D.; Park, S. Y. Enhanced Emission and Its Switing in Fluorescent Organic Nanoparticles. *J. Am. Chem. Soc.* **2002**, *124*, 14410−14415.
(39) Fadler, R. E.; Flood, A. H. Rigidity and Flexibility in Rotaxanes and Their Relatives: On Being Stubborn and Easy-going. *Front. Chem.* **2022**, *10*, 856173.
(40) Liu, Y.; Sengupta, A.; Raghavachari, K.; Flood, A. H. Anion Binding in Solution: Beyond the Electrostatic Regime. *Chem* **2017**, *3*, 411−427.
(41) Qiao, B.; Hirsch, B. E.; Lee, S.; Pink, M.; Chen, C. H.; Laursen, B. W.; Flood, A. H. Ion-Pair Oligomerization of Chromogenic Triangulenium Cations with Cyanostar-Modified Anions That Controls Emission in Hierarchical Materials. *J. Am. Chem. Soc.* **2017**, *139*, 6226−6233.
(42) Sandros, K.; Haglid, F.; Ryhage, R.; Ryhage, R.; Stevens, R. Transfer of Triplet State Energy in Fluid Systems III. Reversile Energy Transfer. *Acta Chem. Scand.* **1964**, *18*, 2355−2374.
(43) Saltiel, J.; Khalil, G.-E.; Schanze, K. Trans-stilbene Phosphorescence. *Chem. Phys. Lett.* **1980**, *70*, 233−235.
(44) Benson, C. R.; Maffeo, C.; Fatila, E. M.; Liu, Y.; Sheetz, E. G.; Aksimentiev, A.; Singharoy, A.; Flood, A. H. Inchworm movement of two rings switching onto a thread by biased Brownian diffusion represent a three-body problem. *Proc. Natl. Acad. Sci. U.S.A.* **2018**, *115*, 9391−9396.
(45) Giachino, G. G.; Kearns, D. R. Nature of the External Heavy-Atom Effect on Radiative and Nonradiative Singlet−Triplet Transitions. *J. Chem. Phys.* **1970**, *52*, 2964−2974.
(46) Merkel, P. B.; Dinnocenzo, J. P. Thermodynamic energies of donor and acceptor triplet states. *J. Photochem. Photobiol., A* **2008**, *193*, 110−121.
(47) Kovalenko, S. A.; Dobryakov, A. L.; Ioffe, I.; Ernsting, N. P. Evidence for the phantom state in photoinduced cis-trans isomerization of stilbene. *Chem. Phys. Lett.* **2010**, *493*, 255−258.

https://doi.org/10.1021/acs.jpca.3c02701
J. Phys. Chem. A 2023, 127, 5841−5850

Appendix 2-b: Publication SI – Triplet State of Cyanostar

Supporting Information

Triplet States of Cyanostar and its Anion Complexes

Fredrik Edhborg,[1] Axel Olesund,[1] Vikrant Tripathy,[2] Yang Wang,[3] Tumpa Sadhukhan,[2,4] Andrew H.Olsson,[2] Niels Bisballe,[3] Krishnan Raghavachari,[2] Bo W. Laursen,[3] Bo Albinsson,[1*] and Amar H. Flood[2*]

1. Chalmers University of Technology, Department of Chemistry and Chemical Engineering, 41296 Gothenburg, Sweden

Fredrik Edhborg (orcid.org/0000-0001-5168-2935),

Axel Olesund (orcid.org/0000-0003-1202-7844),

Bo Albinsson (orcid.org/0000-0002-5991-7863)

2. Department of Chemistry, Indiana University, 800 E. Kirkwood Ave, Bloomington, IN 47405, USA

Vikrant Tripathy (orcid 0000-0002-3246-0680),

Tumpa Sadhukhan (orcid 0000-0003-1995-7286),

Andrew H. Olsson (orcid 0000-0003-2000-7341),

Krishnan Raghavachari (orcid 0000-0003-3275- 1426),

Amar H. Flood (orcid: 0000-0002-2764-9155)

3. Nano-Science Center & Department of Chemistry, University of Copenhagen, Universitetsparken 5, 2100 Copenhagen, Denmark

Yang Wang (orcid: 0000-0003-0867-2752),

Niels Bisballe (orcid: 0000-0002-4476-5481),

Bo W. Laursen (orcid: 0000-0002-1120-3191)

4. Department of Chemistry, SRM Institute of Science and Technology, Kattankulathur Campus, Chennai 603203, India

*Email: balb@chalmers.se
*Email: aflood@iu.edu

Contents

- Synthetic Methods
- Phosphorescence quenching
- Cyanostar Phosphorescence
- Computational Chemistry

Synthetic methods

General remarks: ^{1}H-NMR spectra were acquired on 500 MHz instruments by Bruker. Chemical shifts for ^{1}H-NMR spectra are reported relative to TMS, referenced to the solvent residual peak for DMSO-d_6 (δ = 2.50 ppm). HRMS was recorded on an ESPMALDI-FT-ICR instrument equipped with a 7 T magnet (the instrument was calibrated using sodium trifluoroacetate cluster ions prior to acquiring the spectra) or a MicrOTOF-QII-system using ESP (calibrated using formic acid).

Methanol was dried over 3 Å mol. sieves for 48 h prior to use. 4'-(4-Tolyl)-2,2′:6′,2″-terpyridine (**S1**) and other reagents and solvents were obtained from commercial suppliers and used without further purification.

Synthesis of PtTA

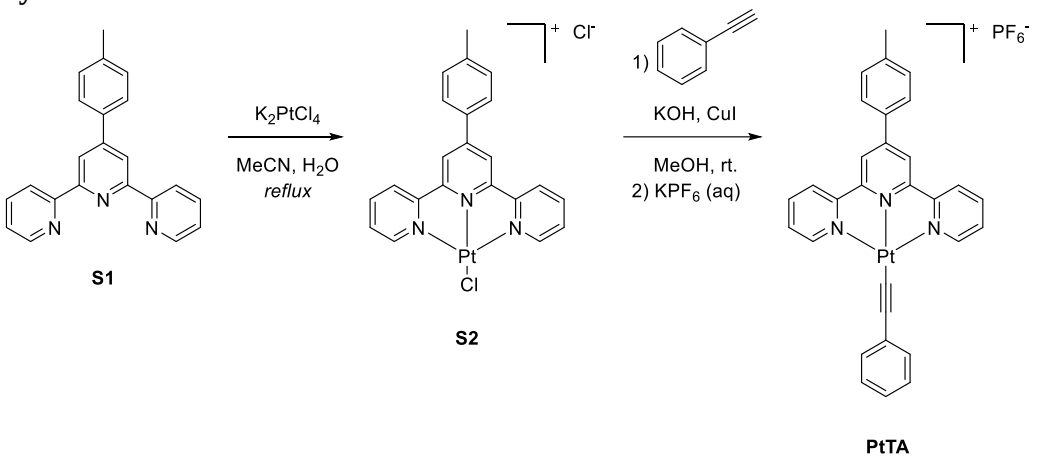

Scheme S1. Synthesis of PtTA.

S2 was synthesized from **S1** according to a previously reported literature procedure. [1] ^{1}H-NMR (500 MHz, DMSO-d_6): δ =8.98 (s, 2H), 8.93 (d, *J* = 5.6 Hz, 2H), 8.87 (d, *J* = 8.0 Hz, 2H), 8.54 (t, *J* = 7.9 Hz, 2H), 8.14 (d, *J* = 7.8 Hz, 2H), 7.96 (t, *J* = 6.7 Hz, 2H), 7.50 (d, *J* = 7.8 Hz, 2H), 2.45 (s, 3H). Signals are consistent with previous literature reports. [2]

Platinum(II) 4'-(4-tolyl)-2,2':6',2''-terpyridine phenylacetylide hexafluorophosphate (PtTA): Phenylacetylene (25 µL, 0.23 mmol) and KOH (14 mg, 0.25 mmol) were combined in dry MeOH (15 mL, 0.01 M) in a dry round-bottomed flask under moderate stirring at rt. After 1 h **S2** (101 mg, 0.172 mmol) and CuI (6.6 mg, 0.034 mmol) were added and the resulting yellow solution turned orange within 10 minutes. After 17.5 h the orange-brown reaction mixture was quenched by pouring into 0.2 M aqueous KPF_6 The resulting precipitate was isolated by filtration and washed with water (3 x 25 mL). The precipitate was then eluted off the filter with MeCN. The solution was reduced to 50 mL by evaporation of excess solvent, before the mixture was sonicated and poured into MeOH (150 mL) under vigorous stirring. Stirring was halted for the red precipitate to settle and was then isolated by filtration, followed by washing of the precipitate with MeOH (3 x 25 mL). This gave the title compound as a red solid (58 mg, 44 %). ^{1}H-NMR (500 MHz, DMSO-d_6): δ = 9.18 (d, *J* = 5.6 Hz, 2H), 9.03 (s, 2H), 8.88 (d, *J* = 8.0 Hz, 2H), 8.55 (t, *J* = 7.9 Hz, 2H),

8.13 (d, *J* = 7.9 Hz, 2H), 7.94 (t, *J* = 6.7 Hz, 2H), 7.53-7.48 (m, 4H), 7.36 (t, *J* = 7.5 Hz, 2H), 7.28 (t, *J* = 7.5 Hz, 1H), 2.45 (s). The signal at δ = 2,45 ppm for the tolyl methyl group could not be integrated due to overlap with the solvent residual. Signals are consistent with previous literature reports for the corresponding chloride salt. [2]

NMR spectra

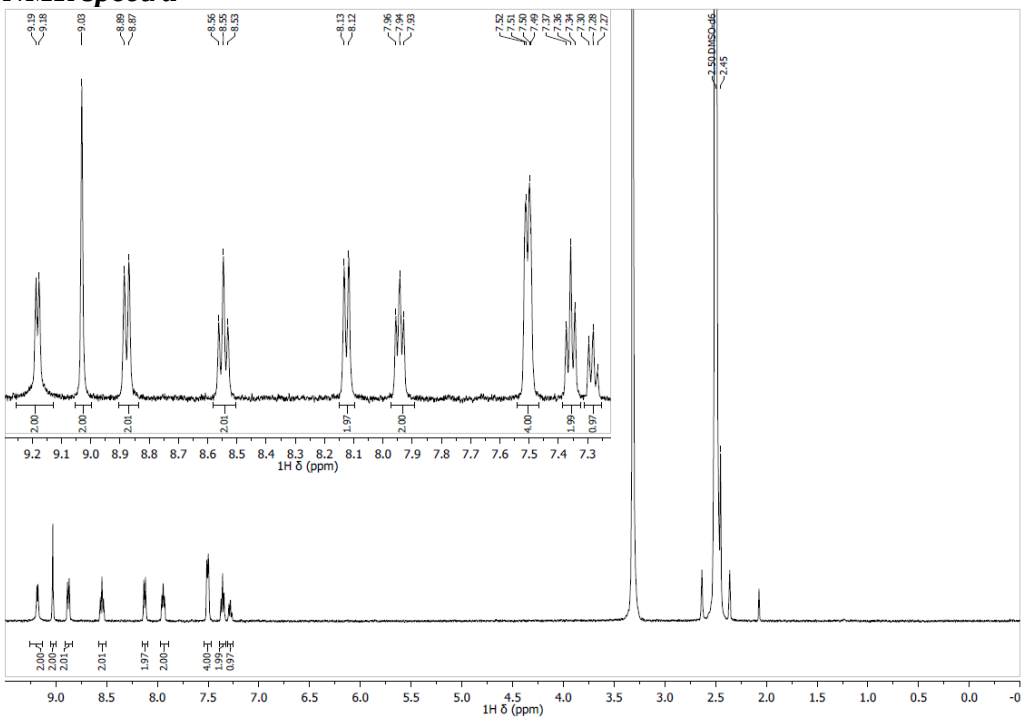

^{1}H-NMR spectrum (DMSO-d_6) of PtTA.

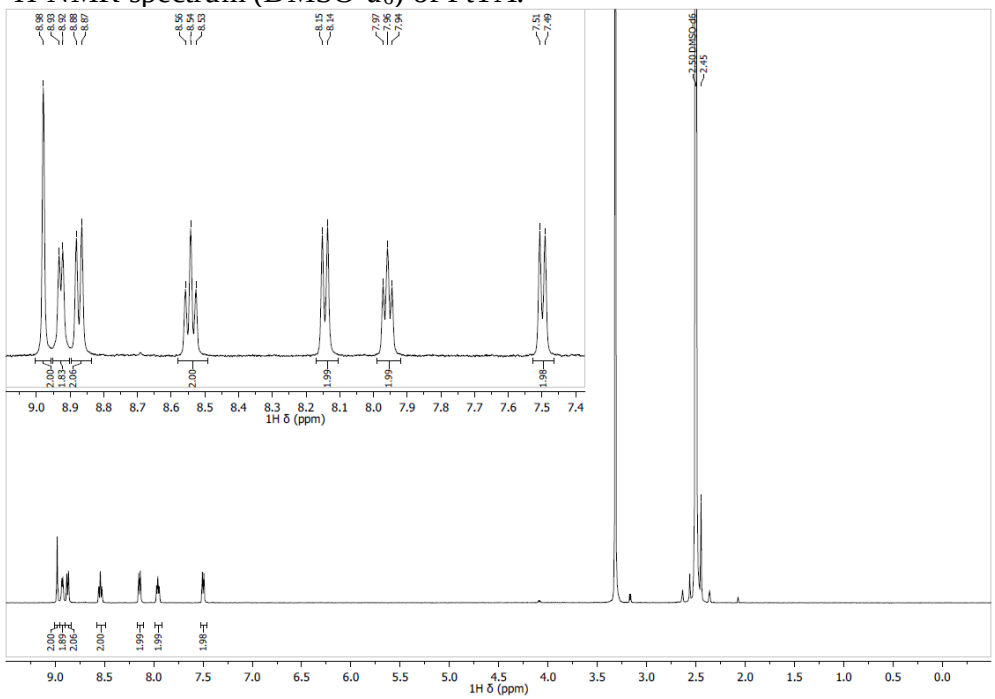

^{1}H-NMR spectrum (DMSO-d_6) of **S2**.

Phosphorescence quenching

The absorption and emission spectra of the phosphorescent donors used for determining the triplet energy of cyanostar (**CS**) and cyanostar anion complex (**CS**$_2$•X$^-$) using the Sandros method are shown in Figure S1. The triplet energies of the donors were determined from their phosphorescence spectra, see Table S1. The peak of the highest energy phosphorescence band was used as an estimate of the triplet energy for all donors except for PtTA, which has a broad and unstructured phosphorescence spectrum. Therefore, the triplet energy of PtTA was estimated from the phosphorescence onset wavelength, here set to be 570 nm. The rate constant of triplet energy transfer (k_{TET}) from the donors to CS and CS_2•PF_6•TBA was measured using the Stern-Volmer method, see Figure S1 and Table S1.

***Table S1**. Triplet energy of phosphorescent donors and rate constants of triplet energy transfer to **CS** and **CS**$_2$•PF_6•TBA.*

Donor	**Triplet energy (eV)**	**k_{TET} ($M^{-1}s^{-1}$)**	
		CS	**CS**$_2$•PF_6•TBA
Ir(p-CF_3-ppy)$_3$	2.45	1.96E+09	3.50E+09
Ir(ppy)$_3$	2.42	7.20E+09	6.57E+09
PtTA	2.17	-	8.91E+09
PtOEP	1.93	2.85E+08	6.95E+07
PtTPP	1.88	8.50E+07	2.00E+07
PdOEP	1.87	1.46E+08	3.57E+07
PdTPP	1.78	1.72E+07	3.15E+06

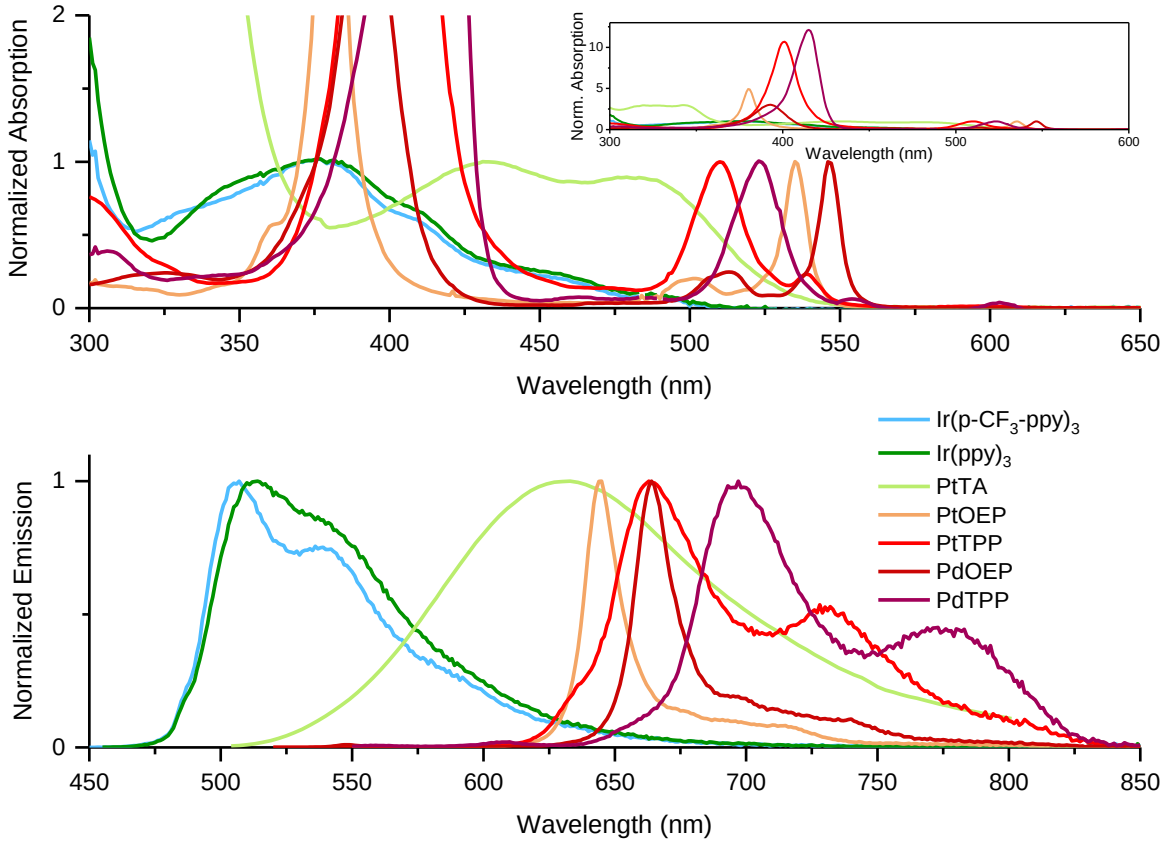

Figure S1. *Normalized absorption and emission spectra of phosphorescent donors. All compounds were dissolved in THF, except for PtTA which was dissolved in DCM.*

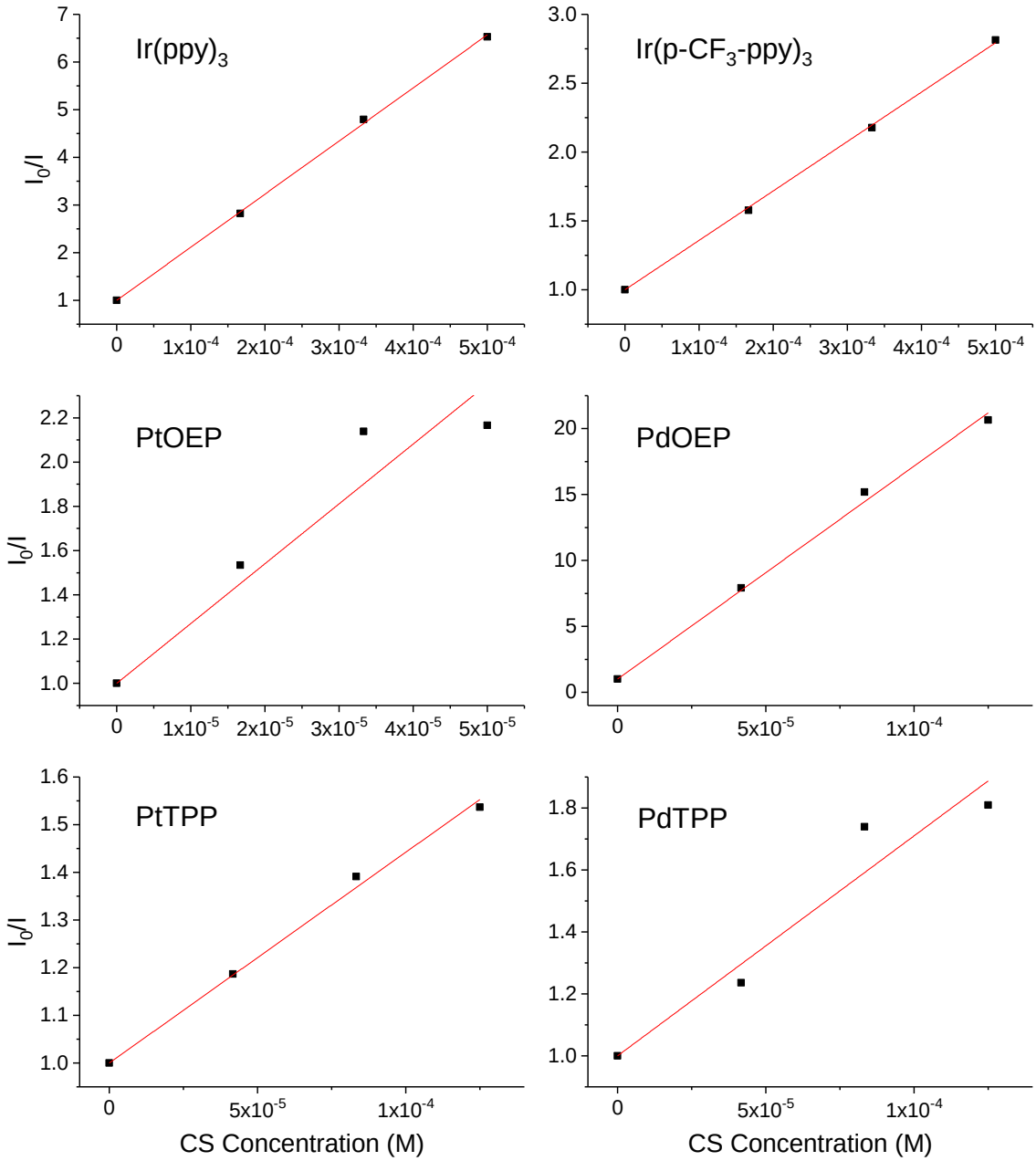

Figure S2. *Stern-Volmer plots with various phosphorescent triplet donors and* ***CS*** *as triplet quencher. Measured in THF at room temperature. Donor concentration approximately 5-10 μM.*

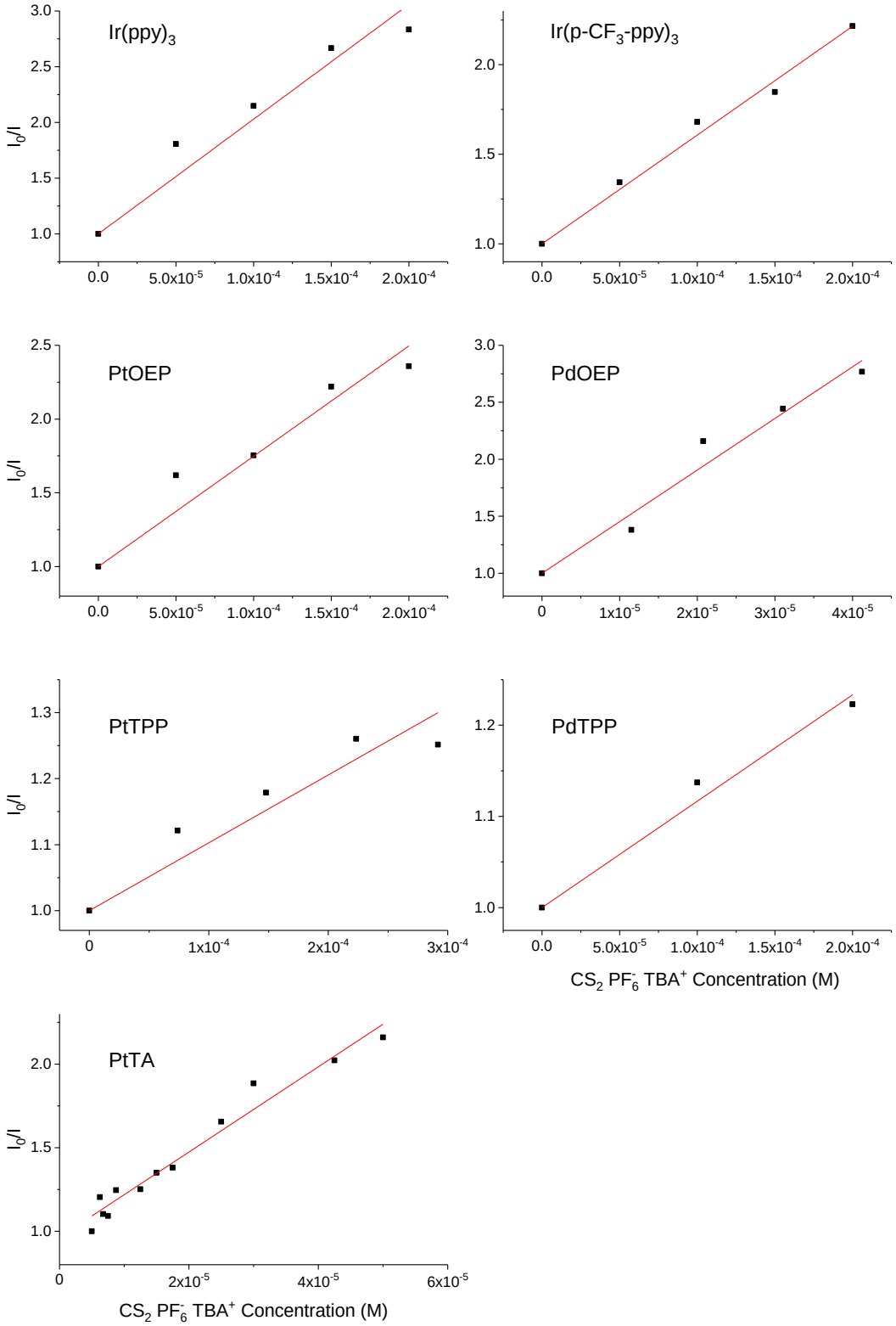

Figure S3. *Stern-Volmer plots with various phosphorescent triplet donors and* ***CS$_2$•PF$_6$•TBA*** *as triplet quencher. Measured in THF at room temperature. Donor concentration approximately 10 µM. (For PtTA, donor concentration 5 µM, dissolved in DCM).*

Cyanostar Phosphorescence

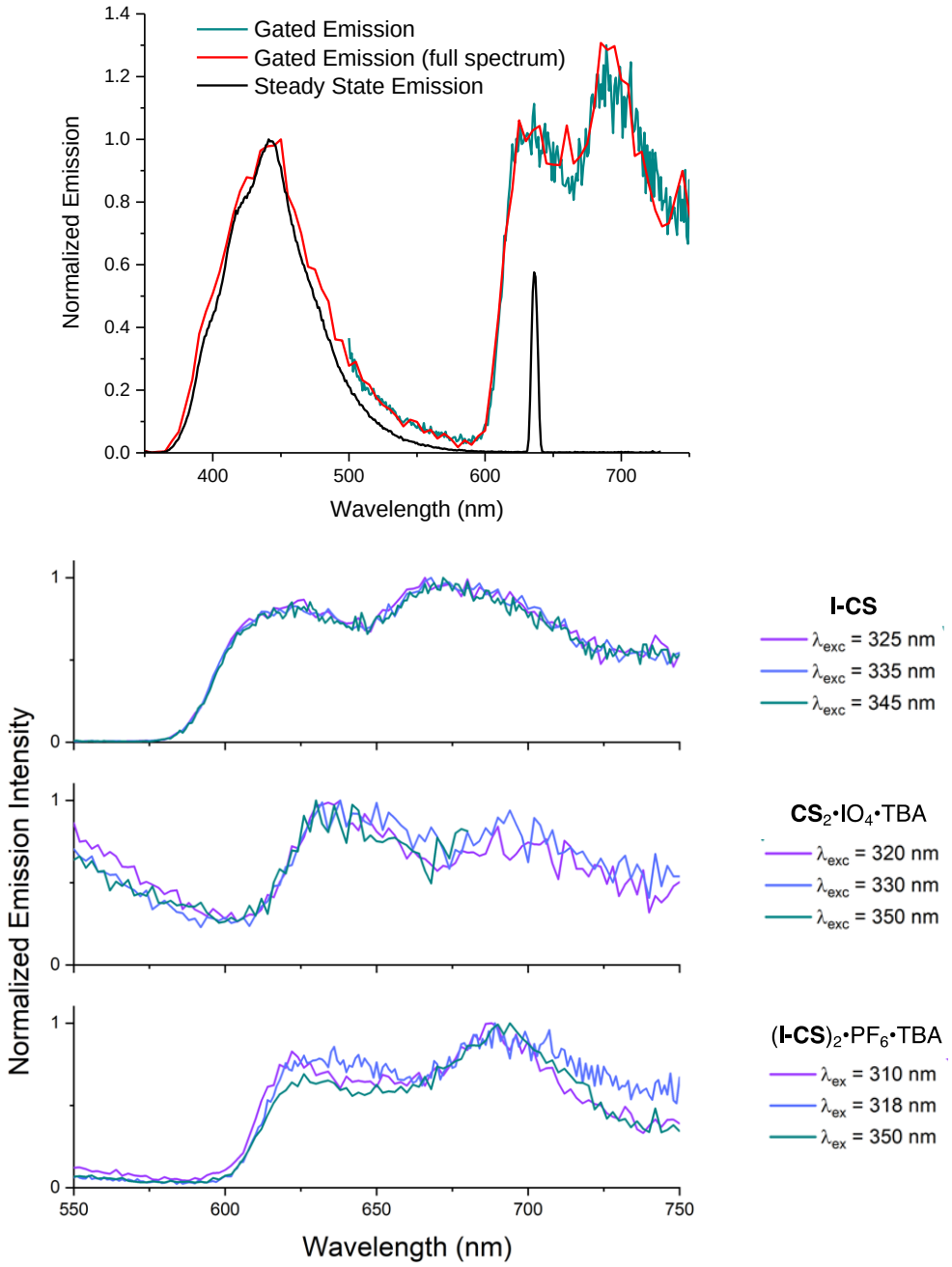

Figure S4. *(Top) Emission spectrum of* ***(I-CS)***$_2$*•PF*$_6$*•TBA in MeTHF at 85 K,* λ_{ex}*=318 nm. The teal line shows gated emission spectrum scanned over the cyanostar phosphorescence (same data as shown in the spectra below). Red line shows gated emission spectrum scanned over both the cyanostar fluorescence and phosphorescence. Black line shows steady state fluorescence spectrum. The peak at 636 nm for black line origins from scattering of second order diffracted excitation light. (Bottom) Phosphorescence spectra of* ***I-CS****,* ***CS***$_2$*•IO*$_4$*•TBA, and* ***(I-CS)***$_2$*•PF*$_6$*•TBA. Spectra measured in MeTHF (~20-40 μM) at 85 K at various excitation wavelengths.*

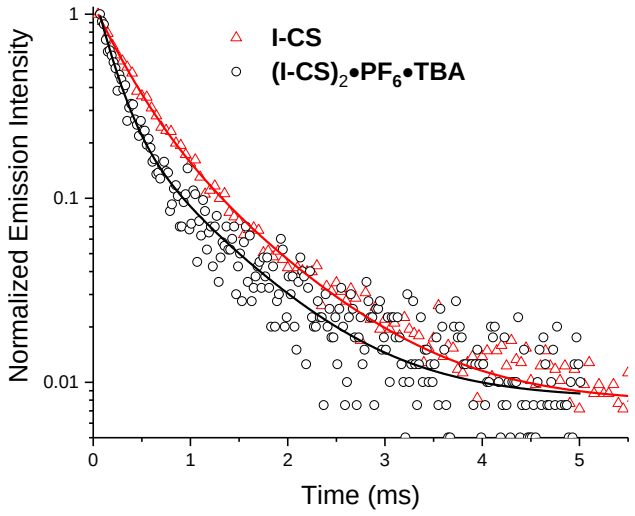

Figure S5. *Phosphorescence decay of* ***I-CS*** *and* ***(I-CS)***$_2$*•PF_6•TBA. Measured at 85 K in MeTHF.* λ_{ex}*= 325 nm,* λ_{em}*= 610 nm* ***(I-CS)*** *and* λ_{ex}*= 318 nm,* λ_{em}*= 625 nm* ***((I-CS)***$_2$*•PF_6•TBA).* *Solid lines show biexponential fit,* $I(t) = A_1 * e^{-t/\tau_1} + A_2 * e^{-t/\tau_2} + \gamma_0$ *. Fit parameters shown in Table S2.*

Table S2. *Fit parameters for emission decay shown in Figure S5.*

	I-CS	**(I-CS)**$_2$•PF_6•TBA
A_1	0.755	1.077
τ_1 (ms)	0.311	0.177
A_2	0.372	0.276
τ_2 (ms)	0.872	0.794
y_0	0.008	0.008

Computational Chemistry

Density functional theory (DFT) calculations have been performed to investigate the electronic states of the parent cyanostar as well as some of its relevant associated species. Time-dependent DFT (TDDFT) is employed to obtain excited singlet state properties including the excitation and emission energies along with the associated oscillator strengths. The *tert*-butyl groups of cyanostar (**CS**) are replaced by hydrogen atoms in the model compound **CSH** to reduce the computational cost at very little loss in accuracy. Structures were optimized at B3LYP-D3BJ/6-31G level of theory for the cyanostar, **CSH**, its dimer, $(\mathbf{CSH})_2$, and the 2:1 complex, $(\mathbf{CSH})_2 \bullet PF_6^-$. Polarization functions are added to the anion to accommodate the hypervalent phosphorous atom. Frequency calculations are performed, at same level of theory, to verify the structures being local minima. Single point calculations were performed on the optimized geometries using CAM-B3LYP-D3BJ/6-31+G(d). Dichloromethane (ε = 8.93) was used as the solvent implemented with a CPCM continuum solvation model. This model should be representative of medium polarity solvents. A modest change in the polarity of solvent, such as for THF (ε = 7.58), is expected to have insignificant impact on our results.

Coordinates

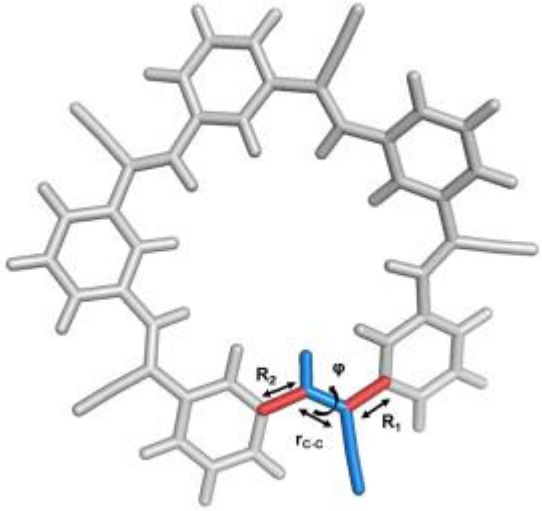

Figure S6. The bonds and dihedral angle next the C=C bond, in the stilbene unit undergoing rotation, also change. All the coordinates undergoing significant change are highlighted here.

Ground state singlet (S_0)

Lowest energy conformer, i.e., *m*-M_2P_3 or *m*-P_2M_3, of ground state **CSH**.[3] Only one of the 10 possible degenerate structures are used here.

Table S1: The values of the bonds and dihedral angle next the C=C bond highlighted in

Coordinate	Value
R1	1.49 Å
R2	1.46 Å
ϕ	24^0

H	1.29200	7.64400	1.86600	H	-6.69100	1.31200	-1.27700
C	1.22500	6.67500	1.38600	H	-2.77800	1.88100	0.43300
C	1.06400	4.18500	0.15800	C	-4.43900	-0.01300	-0.19600
C	2.39700	5.99100	1.04700	C	-5.20500	-1.12000	-0.41100
C	-0.02800	6.12300	1.12200	H	-3.45800	-0.20900	0.22700
C	-0.12700	4.86300	0.49000	C	-6.54800	-1.05200	-0.89300
C	2.32700	4.72300	0.44000	N	-7.65800	-1.05400	-1.28100
H	3.36100	6.43500	1.26500	H	-5.79900	-5.58800	0.79200
H	-0.91500	6.67200	1.40500	C	-5.10400	-4.80200	0.51900
H	0.98900	3.23400	-0.35700	C	-3.33100	-2.78900	-0.22100
C	3.56600	3.96800	0.10300	C	-5.58700	-3.52300	0.23100
C	3.58400	2.60500	0.06400	C	-3.73900	-5.08100	0.45900
H	2.65500	2.12600	0.35800	C	-2.82500	-4.06800	0.09100
C	4.72200	4.76700	-0.15300	C	-4.69900	-2.49300	-0.13200
N	5.64400	5.47000	-0.34400	H	-6.65100	-3.32300	0.29100
C	4.63200	1.65500	-0.29500	H	-3.39700	-6.08300	0.67300
C	6.49800	-0.35700	-0.93600	H	-2.63600	-2.02500	-0.55400
C	5.90300	1.99400	-0.81100	C	-1.37900	-4.24100	-0.02000
C	4.32300	0.29000	-0.11400	C	-0.55600	-5.23400	0.42500
C	5.23200	-0.72600	-0.44200	H	-0.88600	-3.42200	-0.53400
C	6.82000	0.99100	-1.11800	C	-1.04900	-6.38100	1.12200
H	6.17700	3.02700	-0.97400	N	-1.39900	-7.34000	1.70300
H	3.35900	0.03700	0.31100	H	3.61800	-7.27500	0.03200
H	7.79500	1.25800	-1.51000	C	3.05600	-6.34800	0.04600
H	7.22400	-1.12100	-1.18900	C	1.60000	-3.97800	0.06700
C	-1.37200	4.18600	0.14300	C	1.67200	-6.38500	0.23700
C	-2.67300	4.59100	0.19900	C	3.72200	-5.13700	-0.13300
H	-1.22000	3.18400	-0.24700	C	2.99800	-3.92400	-0.11700
C	-3.05800	5.90900	0.59100	C	0.92200	-5.19300	0.23900
N	-3.42900	6.98200	0.89600	H	1.17400	-7.33800	0.37200
H	-6.92900	3.74200	-1.51600	H	4.79100	-5.14200	-0.28900
C	-6.01600	3.33300	-1.09900	H	1.05300	-3.04300	0.10800
C	-3.67100	2.29400	-0.02300	C	3.57800	-2.59300	-0.27800
C	-4.98900	4.19800	-0.71000	C	4.87200	-2.16300	-0.28000
C	-5.88000	1.95200	-0.96300	H	2.83200	-1.81700	-0.41700
C	-4.69700	1.40800	-0.41200	C	5.97800	-3.05500	-0.12300
C	-3.79100	3.68200	-0.18000	N	6.92200	-3.74300	0.00500
H	-5.11100	5.26800	-0.82900				

Singlet Excited state (S_1)

Table S2: The values of the bonds and dihedral angle next the C=C bond highlighted in

Coordinate	Value
R1	1.44 Å
R2	1.41 Å
ϕ	-2.6^0

H	-2.06100	7.71600	-0.98800	H	6.62900	1.87900	1.01900
C	-1.89000	6.68400	-0.70400	H	2.57800	2.17900	-0.41600
C	-1.46000	4.03100	0.02100	C	4.45300	0.42600	-0.04500
C	-2.97800	5.82600	-0.53800	C	5.34300	-0.60700	0.00200
C	-0.58500	6.22900	-0.51800	H	3.45700	0.15700	-0.38300
C	-0.35000	4.88700	-0.14200	C	6.72100	-0.43000	0.32900
C	-2.77500	4.47600	-0.18600	N	7.86600	-0.33800	0.58100
H	-3.98400	6.19900	-0.69500	H	6.16200	-4.94900	-1.51400
H	0.23500	6.91800	-0.66000	C	5.44300	-4.24400	-1.11200
H	-1.27800	3.01100	0.33800	C	3.60900	-2.42000	-0.08900
C	-3.93800	3.55900	-0.05100	C	5.85300	-2.94200	-0.80600
C	-3.82400	2.20300	-0.19300	C	4.12200	-4.64400	-0.91500
H	-2.82300	1.84100	-0.40400	C	3.18000	-3.73100	-0.38700
C	-5.18300	4.19900	0.23600	C	4.93000	-2.00600	-0.30200
N	-6.17700	4.77700	0.48100	H	6.88500	-2.65000	-0.97000
C	-4.81700	1.14000	-0.12300	H	3.83100	-5.65200	-1.17300
C	-6.61800	-1.03700	-0.04600	H	2.89300	-1.73300	0.34600
C	-6.22200	1.35500	-0.10600	C	1.78000	-4.02300	-0.11900
C	-4.33600	-0.18000	-0.10900	C	1.08000	-5.19700	-0.10700
C	-5.21000	-1.30200	-0.07500	H	1.19900	-3.14500	0.14800
C	-7.10000	0.26300	-0.06200	C	1.69500	-6.46900	-0.31000
H	-6.63100	2.35400	-0.15100	N	2.16000	-7.53900	-0.46100
H	-3.26500	-0.33400	-0.09800	H	-2.75400	-7.13800	1.71000
H	-8.16900	0.44000	-0.05100	C	-2.32400	-6.29600	1.17900
H	-7.31100	-1.86900	-0.02300	C	-1.18300	-4.13400	-0.18700
C	0.96500	4.29900	0.09800	C	-0.96300	-6.32100	0.83800
C	2.21800	4.83900	0.07300	C	-3.12400	-5.20800	0.86100
H	0.92300	3.24400	0.35100	C	-2.57600	-4.08000	0.14600
C	2.45900	6.22700	-0.16400	C	-0.37900	-5.21300	0.17000
N	2.71700	7.36000	-0.34500	H	-0.35200	-7.17600	1.10500
H	6.63300	4.29100	1.48000	H	-4.16600	-5.21200	1.14900
C	5.74200	3.82600	1.07200	H	-0.76400	-3.31000	-0.75500
C	3.45100	2.64500	0.02700	C	-3.30600	-2.92900	-0.21600
C	4.60900	4.60600	0.82600	C	-4.71400	-2.65700	-0.06700
C	5.74000	2.45700	0.80900	H	-2.72600	-2.14600	-0.69400
C	4.58600	1.84300	0.27300	C	-5.65600	-3.70200	0.02600
C	3.43900	4.01800	0.31000	N	-6.45700	-4.57100	0.11100
H	4.63000	5.66800	1.04500				

CSH triplet

Table S3: The values of the bonds and dihedral angle next the C=C bond highlighted in

Coordinate	Value
R1	1.44 Å
R2	1.42 Å
ϕ	4.7^0

H	-0.65400	7.87600	0.40800	H	7.13000	0.66000	-0.13000
C	-0.64200	6.79200	0.38200	H	2.93300	1.53600	-0.51300
C	-0.62100	4.00700	0.35700	C	4.55200	-0.47300	-0.41000
C	-1.84600	6.08700	0.44800	C	5.19700	-1.64900	-0.16300
C	0.57400	6.11800	0.28600	H	3.51300	-0.57100	-0.70700
C	0.60100	4.70600	0.26600	C	6.57600	-1.70700	0.20200
C	-1.85100	4.67900	0.42500	N	7.70900	-1.80300	0.50100
H	-2.78100	6.63000	0.51400	H	5.03700	-6.29900	-0.62200
H	1.49100	6.68800	0.25700	C	4.48800	-5.37800	-0.46000
H	-0.59600	2.92300	0.38800	C	3.09200	-3.01000	-0.06500
C	-3.14700	3.94300	0.46000	C	5.18000	-4.16400	-0.40900
C	-3.30900	2.70000	-0.07500	C	3.10000	-5.42100	-0.31500
H	-2.41800	2.25100	-0.50500	C	2.38200	-4.22400	-0.10700
C	-4.21900	4.64500	1.09600	C	4.48400	-2.95500	-0.22000
N	-5.05700	5.26100	1.64500	H	6.25800	-4.15500	-0.52700
C	-4.50500	1.86500	-0.19300	H	2.58700	-6.37100	-0.37200
C	-6.72600	0.15300	-0.57900	H	2.53300	-2.10300	0.13000
C	-5.83000	2.34900	-0.06700	C	0.93700	-4.12300	0.07300
C	-4.31600	0.51000	-0.51800	C	-0.00100	-5.05300	0.40600
C	-5.41000	-0.36700	-0.71700	H	0.55500	-3.11200	-0.03900
C	-6.91900	1.49100	-0.25600	C	0.32500	-6.40600	0.72400
H	-6.01800	3.39100	0.14600	N	0.54700	-7.52500	1.00600
H	-3.30800	0.12600	-0.63100	H	-4.16700	-5.12700	2.51800
H	-7.92600	1.88100	-0.16200	C	-3.56000	-4.73300	1.71100
H	-7.57800	-0.50000	-0.73300	C	-1.97700	-3.73700	-0.37000
C	1.82000	3.90300	0.19200	C	-2.24300	-5.18900	1.55200
C	3.09000	4.23900	-0.17400	C	-4.09200	-3.77600	0.85400
H	1.67200	2.86500	0.47100	C	-3.31300	-3.26200	-0.22800
C	3.44800	5.56200	-0.58100	C	-1.43400	-4.66500	0.52000
N	3.79700	6.62800	-0.93200	H	-1.83700	-5.92600	2.23600
H	7.60000	3.06500	0.08400	H	-5.10800	-3.42800	0.99200
C	6.57600	2.72700	-0.02600	H	-1.38300	-3.37300	-1.20100
C	3.94700	1.87900	-0.34500	C	-3.82500	-2.32700	-1.16100
C	5.54000	3.66600	-0.04400	C	-5.18400	-1.74200	-1.08100
C	6.30900	1.36300	-0.14300	H	-3.20100	-2.03800	-2.00400
C	4.97800	0.91800	-0.30000	C	-6.26500	-2.58100	-1.40600
C	4.20300	3.24800	-0.19100	N	-7.15400	-3.31600	-1.67000
H	5.76900	4.72000	0.06300				

$(CSH)_2PF_6$ triplet

Table S4: The values of the bonds and dihedral angle next the C=C bond highlighted in

Coordinate	Value
R1	1.44 Å
R2	1.40 Å
ϕ	-3.9^0

N	-6.66700	-3.92500	2.40100	C	6.30700	2.24100	1.49600
C	-5.60500	-3.51600	2.10500	C	6.11600	3.61800	1.35500
C	-4.28900	-3.07900	1.75800	C	4.83700	4.17100	1.40200
C	-3.26000	-4.14900	1.66600	C	2.61000	6.16700	2.02900
C	-3.64600	-5.50000	1.57600	N	3.24200	7.13100	2.25700
C	-2.68300	-6.50600	1.46600	C	-0.15700	6.60500	1.64000
C	-1.32400	-6.19800	1.46100	C	-1.52700	6.85900	1.54100
C	-0.90800	-4.85200	1.55300	C	-2.44700	5.81300	1.53100
C	-1.88900	-3.84600	1.64300	H	1.62600	2.97800	1.42700
C	0.48000	-4.40200	1.51400	H	3.05300	1.32000	1.86300
C	1.63700	-5.08400	1.74700	H	4.71600	5.23500	1.25800
C	1.63500	-6.46900	2.10300	H	7.30900	1.83200	1.44500
N	1.69200	-7.60300	2.40400	H	-0.28100	3.20400	1.71000
C	-4.00200	-1.76600	1.54000	H	0.53900	7.43500	1.64100
C	-4.85400	-0.58300	1.59300	H	-3.50000	6.03200	1.42800
C	-6.26200	-0.59700	1.51000	H	-2.33200	2.39800	1.29700
C	-6.97000	0.60300	1.54200	H	3.41900	-0.55700	1.32900
C	-6.30200	1.82400	1.66600	H	4.06200	-6.32100	1.59700
C	-4.89700	1.86800	1.73600	H	6.52000	-2.82100	1.38000
C	-4.19200	0.65600	1.69100	H	2.25600	-2.41400	1.70800
C	-4.19100	3.17400	1.82500	H	0.58200	-3.35400	1.25300
C	-5.00000	4.28900	2.20400	H	-1.55100	-2.81900	1.70800
N	-5.70700	5.17100	2.52700	H	-4.69700	-5.76300	1.57500
C	-2.85800	3.30400	1.57300	H	-0.60200	-6.99300	1.35500
C	-1.99400	4.47900	1.61100	H	-2.97200	-1.53500	1.29300
C	-0.60800	4.23600	1.68000	H	-3.11000	0.64500	1.74200
C	0.32600	5.28400	1.70800	H	-6.79900	-1.52600	1.38700
C	1.79000	5.02500	1.76900	H	-6.87300	2.74500	1.68400
C	2.32700	3.78500	1.59800	H	6.97300	4.26100	1.19100
C	3.71600	3.33600	1.59300	H	6.28400	-5.26900	1.41400
C	3.92200	1.94800	1.72200	H	-1.87600	7.88200	1.46000
C	5.20500	1.38200	1.67400	H	-2.99900	-7.53900	1.37300
C	5.40300	-0.08900	1.76100	H	-8.05000	0.59100	1.45900
C	6.73400	-0.51200	2.06500	N	-1.72600	7.63200	-2.31900
N	7.84300	-0.80300	2.32300	C	-1.66300	6.48800	-2.05700
C	4.39300	-0.98000	1.55000	C	-1.65500	5.09200	-1.74900
C	4.38900	-2.44000	1.57200	C	-2.99400	4.45000	-1.65000
C	5.53700	-3.25700	1.48500	C	-4.14800	5.23300	-1.46400
C	5.40200	-4.64300	1.49700	C	-5.39800	4.62700	-1.31300
C	4.14200	-5.24000	1.59600	C	-5.53100	3.24000	-1.35800
C	2.98000	-4.44900	1.66900	C	-4.39200	2.43100	-1.55600
C	3.12500	-3.05400	1.65000	C	-3.13700	3.05500	-1.69600

C	-4.39400	0.97000	-1.56200
C	-5.41400	0.08400	-1.73900
C	-6.75100	0.51900	-1.99800
N	-7.86400	0.82200	-2.22300
C	-5.22200	-1.39100	-1.67600
C	-3.94000	-1.96000	-1.70300
C	-3.74000	-3.35000	-1.60300
C	-4.86600	-4.18900	-1.45900
C	-6.14300	-3.63200	-1.42800
C	-6.32800	-2.25100	-1.54100
C	-2.35200	-3.79900	-1.58900
C	-1.80300	-5.02900	-1.78900
C	-0.33400	-5.25300	-1.71000
C	0.17100	-6.55200	-1.44800
C	1.54900	-6.75100	-1.28200
C	2.44800	-5.70100	-1.39600
C	1.98200	-4.38000	-1.71400
C	0.56300	-4.20100	-1.85200
C	2.79500	-3.25300	-1.90600
C	4.27100	-3.15300	-1.84400
C	4.92800	-1.88500	-1.68700
C	6.35300	-1.80500	-1.62900
C	6.25600	0.61500	-1.50100
C	4.84400	0.57700	-1.54600
C	4.19700	-0.66800	-1.59800
C	3.98500	1.75700	-1.49800
C	4.26600	3.06100	-1.77300
C	5.56900	3.48900	-2.17800
N	6.61700	3.89500	-2.52100
C	3.24100	4.13600	-1.68500
C	3.63300	5.48300	-1.57900
C	2.67400	6.49200	-1.45600
C	1.31400	6.18900	-1.45800
C	0.89300	4.84700	-1.57900
C	1.87000	3.83700	-1.67900
C	-0.49600	4.40300	-1.55200
C	5.08300	-4.28600	-2.02200
N	5.79800	-5.21900	-2.16300
C	-2.59900	-6.18000	-2.07600
N	-3.21400	-7.15200	-2.31900
C	6.99000	-0.57900	-1.52400
H	-7.33000	-1.84200	-1.50100
H	-4.74700	-5.25600	-1.33900
H	-3.06500	-1.33400	-1.80500
H	-3.41100	0.54600	-1.38700
H	-2.27300	2.42200	-1.84200
H	-6.50400	2.79700	-1.20600
H	-4.06700	6.31200	-1.41200
H	-0.60000	3.34800	-1.32500
H	1.53200	2.81200	-1.76600
H	0.59500	6.98400	-1.33300
H	4.68500	5.74200	-1.57000
H	2.96400	1.53300	-1.21100
H	3.11700	-0.68000	-1.56600
H	6.93800	-2.71600	-1.66100
H	6.78000	1.55400	-1.41000
H	2.28100	-2.33800	-2.16300
H	0.21100	-3.20200	-2.07900
H	3.49900	-5.88600	-1.24000
H	-0.51100	-7.38800	-1.34700
H	-1.65200	-3.00100	-1.37300
H	8.07200	-0.54000	-1.45900
H	2.99400	7.52200	-1.34400
H	1.91600	-7.74400	-1.04500
H	-6.27300	5.24300	-1.14300
H	-7.00600	-4.27600	-1.29800
P	0.02600	-0.02600	-0.08700
F	0.89700	0.55400	-1.35000
F	1.03400	-1.31000	0.01900
F	0.97700	0.81100	0.95400
F	-0.98500	1.26500	-0.19500
F	-0.92600	-0.85400	-1.13200
F	-0.84900	-0.59900	1.17300

$(CSH)_2$ triplet

Table S5: The values of the bonds and dihedral angle next the C=C bond highlighted in

Coordinate	Value
R1	1.44 Å
R2	1.41 Å
ϕ	-4.7^0

N	-5.81500	-5.24600	2.21100	C	5.64800	3.51100	1.54400
C	-4.84700	-4.61500	1.99600	C	5.17500	4.82000	1.42200
C	-3.63500	-3.89900	1.75000	C	3.80900	5.09500	1.46700
C	-2.39900	-4.72800	1.69000	C	1.20900	6.59200	2.03600
C	-2.49200	-6.13000	1.60400	N	1.62300	7.67100	2.24800
C	-1.34000	-6.91500	1.52500	C	-1.57800	6.44400	1.58100
C	-0.07400	-6.33200	1.54200	C	-2.96900	6.40800	1.45600
C	0.05200	-4.92800	1.62600	C	-3.65900	5.19800	1.47800
C	-1.12000	-4.15000	1.69100	H	0.90900	3.25900	1.49400
C	1.31900	-4.20200	1.59700	H	2.65800	1.92800	1.89100
C	2.59500	-4.62500	1.81600	H	3.47200	6.11200	1.34200
C	2.88600	-5.97900	2.17000	H	6.71400	3.32200	1.49700
N	3.17900	-7.07700	2.47000	H	-1.01500	3.10100	1.85200
C	-3.62600	-2.54500	1.59500	H	-1.06600	7.39700	1.55000
C	-4.70700	-1.56600	1.60100	H	-4.73100	5.19800	1.35100
C	-6.07800	-1.87000	1.45300	H	-2.83000	1.86800	1.44700
C	-7.01700	-0.84100	1.42800	H	3.41200	0.17500	1.36300
C	-6.62300	0.49400	1.55200	H	5.22000	-5.33700	1.64400
C	-5.26300	0.83000	1.68900	H	6.90700	-1.41200	1.34500
C	-4.32500	-0.21400	1.71000	H	2.65600	-1.88000	1.76700
C	-4.84600	2.25700	1.77000	H	1.20200	-3.15100	1.35400
C	-5.89700	3.19200	2.02400	H	-1.00500	-3.07500	1.76000
N	-6.79300	3.91900	2.24400	H	-3.46400	-6.60800	1.58400
C	-3.55300	2.65800	1.61500	H	0.79900	-6.96100	1.46300
C	-2.94900	3.98700	1.62600	H	-2.65200	-2.09400	1.43800
C	-1.54500	4.03900	1.73700	H	-3.27000	0.00100	1.82800
C	-0.84000	5.25200	1.71800	H	-6.40800	-2.89000	1.32800
C	0.64700	5.30000	1.79600	H	-7.37300	1.27600	1.52000
C	1.43300	4.19700	1.64600	H	5.87900	5.63000	1.27400
C	2.88500	4.04200	1.63900	H	7.17500	-3.85700	1.40200
C	3.37700	2.72600	1.75000	H	-3.51600	7.33400	1.32300
C	4.75000	2.43800	1.70200	H	-1.43200	-7.99100	1.43900
C	5.25700	1.04000	1.77300	H	-8.06600	-1.07700	1.29700
C	6.65000	0.90200	2.06100	N	-3.22100	7.11500	-2.24200
N	7.79800	0.84200	2.30400	C	-2.92400	6.00100	-2.01700
C	4.45600	-0.04200	1.56500	C	-2.62500	4.62700	-1.75700
C	4.74700	-1.47100	1.57800	C	-3.80100	3.71700	-1.68600
C	6.03600	-2.03800	1.47100	C	-5.10000	4.24300	-1.55100
C	6.18600	-3.42400	1.49700	C	-6.20300	3.39300	-1.44200
C	5.07700	-4.26300	1.62900	C	-6.04700	2.00900	-1.47700
C	3.77800	-3.72600	1.71500	C	-4.75800	1.45100	-1.61900
C	3.63700	-2.33100	1.68200	C	-3.65500	2.32200	-1.71500

C	-4.45800	0.02300	-1.61700	C	-0.07500	4.91100	-1.59100
C	-5.25800	-1.06700	-1.78300	C	1.09100	4.12600	-1.69000
C	-6.65900	-0.93800	-2.03800	C	-1.34500	4.19200	-1.58800
N	-7.81200	-0.88400	-2.25900	C	5.96600	-3.15300	-2.17400
C	-4.74400	-2.46300	-1.71000	N	6.84400	-3.93300	-2.31400
C	-3.37000	-2.74500	-1.74300	C	-1.15300	-6.61100	-2.00400
C	-2.87300	-4.06000	-1.63900	N	-1.54000	-7.70500	-2.18900
C	-3.79300	-5.11900	-1.48700	C	7.02700	0.86300	-1.45700
C	-5.16000	-4.85000	-1.45200	H	-6.70400	-3.35900	-1.52700
C	-5.63700	-3.54200	-1.56700	H	-3.45000	-6.13600	-1.36800
C	-1.42100	-4.20700	-1.63700	H	-2.65000	-1.94500	-1.86700
C	-0.62400	-5.30200	-1.78800	H	-3.40700	-0.18500	-1.44600
C	0.86000	-5.20700	-1.70800	H	-2.67400	1.87800	-1.83100
C	1.62100	-6.33400	-1.30700	H	-6.91400	1.37600	-1.36400
C	3.00500	-6.21900	-1.12400	H	-5.24800	5.31600	-1.51300
C	3.66300	-5.01700	-1.34200	H	-1.22600	3.12800	-1.41600
C	2.94000	-3.86900	-1.81000	H	0.97200	3.05600	-1.80900
C	1.52300	-4.01400	-1.98200	H	-0.80500	6.94000	-1.33200
C	3.51700	-2.62600	-2.12500	H	3.45500	6.56100	-1.50500
C	4.93600	-2.21500	-1.98800	H	2.63200	2.06900	-1.29800
C	5.30200	-0.84400	-1.76000	H	3.27600	-0.06300	-1.73700
C	6.67200	-0.46700	-1.62500	H	7.43900	-1.23200	-1.64800
C	6.05400	1.87200	-1.44100	H	6.36200	2.89700	-1.30000
C	4.68500	1.54000	-1.56200	H	2.85600	-1.88200	-2.55600
C	4.32700	0.18700	-1.68400	H	0.97200	-3.15800	-2.35500
C	3.59500	2.51200	-1.52600	H	4.72600	-4.95600	-1.16900
C	3.60100	3.85700	-1.74500	H	1.12800	-7.27900	-1.11900
C	4.80100	4.55900	-2.07900	H	-0.89600	-3.27100	-1.47300
N	5.75500	5.18300	-2.36600	H	8.07000	1.12900	-1.33400
C	2.37400	4.69500	-1.66600	H	1.43300	7.95400	-1.29600
C	2.47800	6.09300	-1.53700	H	3.56800	-7.08100	-0.78600
C	1.33200	6.88300	-1.42200	H	-7.19200	3.81700	-1.31400
C	0.06200	6.30900	-1.44900	H	-5.86300	-5.66400	-1.31600

References

1. Zhao, T. C.; Liu, R.; Shi, H.; Shu, M. L.; Hu, J. Y.; Li, H.; Zhu, H. J., Synthesis, tunable photophysics and nonlinear absorption of terpyridyl Pt(II) complexes bearing different acetylide ligands. *Dyes and Pigments* **2016,** *126*, 165-172.

2. Kotturi, K.; Masson, E., Directional Self-Sorting with Cucurbit 8 uril Controlled by Allosteric pi-pi and Metal-Metal Interactions. *Chemistry-a European Journal* **2018,** *24*, 8670-8678.

3. Liu, Y.; Singharoy, A.; Mayne, C. G.; Sengupta, A.; Raghavachari, K.; Schulten, K.; Flood, A. H., Flexibility Coexists with Shape-Persistence in Cyanostar Macrocycles. *Journal of the American Chemical Society* **2016,** *138*, 4843-4851.

Appendix 3-a: Manuscript of PtTA-SMILES

Turning on Molecular Phosphorescence in Materials by Supramolecular Organization in Small-Molecule Ionic Isolation Lattices

Yang Wang[1], Marko H. Nowack[1], Niels Bisballe[1], Maria S. Thomsen[1], Maren Pink[2], Amar H. Flood[2], Bo W. Laursen[1*]

1. Nano-Science Center & Department of Chemistry, University of Copenhagen, Universitetsparken 5, 2100 Copenhagen, Denmark

2. Department of Chemistry, Indiana University, 800 E. Kirkwood Ave, Bloomington, IN 47405, USA.

ABSTRACT: Apart from the desirable long-lasting emission, it always requires stringent conditions to generate, measure and utilize phosphorescence. Therefore, upon the emergence of small-molecule ionic isolation lattices (SMILES) and the great success in transferring fluorophores' emission from solution to highly dense solids, we have been envisioning a smooth incorporation of phosphorescence and SMILES. For the first time, we investigated the underlying molecular interactions between phosphorescent dyes and cyanostar (CS), the key structure-directing unit for SMILES, and proved a discipline of selecting phosphorescent complexes to be applied into SMILES based on the comparison of triplet state energies ($E_{T\text{-}dye} < E_{T\text{-}CS}$). Then bright phosphorescent SMILES single crystals and solids were characterized, affirming the underlying compatibility of phosphorescence in SMILES strategy. Further analysis on the radiative and non-radiative processes in the solids provided a mechanistic and quantitative understanding of how steric effect exerted by SMILES influence the phosphorescent emissivity. Based on a selection of the most reproduced phosphorescence in Pt3-SMILES (λ_{em}=670 nm, Φ=0.05, τ=2 μs), we generated a brightly emissive phosphorescent Pt3-SMILES nanoparticle with decent emissivity and lifetime (1μs), and its optical properties highly mimics single crystal state emission. Therefore we confirm that SMILES can enable a reinstated and even strengthened phosphorescence in dense solids, which strikingly outcompetes solution-state emission.

1 Introduction

Luminescent materials, especially emissive molecular materials are of great interest for applications in materials and life science, including e.g.; lightning and displays, lasers, sensors, and probes and labels for bioimaging.[1-4] The usage of such materials in particular benefits from efficient synthesis protocols for the molecular building blocks and their tunability with respect to optoelectronic properties. Furthermore, an extensive empirical and theoretical understanding of photophysical structure

property relations have been developed for molecular dyes, aiding this process. Nevertheless, to reach the goal of functional materials, most researchers encountered barriers to translating molecular-level solution state photophysical properties to solid state materials. The aggregated/solid molecular materials are subjects to aggregation caused quenching (ACQ) and spectral shifts from the intrinsic molecular-level emission hereby induce difficulties in predicting and designing the emissive properties of molecular materials.[5]

Recently we developed the SMILES (*Small-Molecule Ionic Isolation Lattices*) strategy to reinstate molecular photophysical properties into solids[6-8]. By adding the anion binding macrocycle cyanostar (CS) to cationic fluorophores the associated counter anions are bound in large disc-shaped 2:1 anion complexes CS_2X^- that ensures alternating charge by charge stacking with the cationic dyes (Scheme 1a)[7]. This isolation of cationic dyes in SMILES materials prohibits strong dye-dye interactions and thus counteract ACQ and spectral shifts, endowing SMILES materials with bright solution-like fluorescence properties. Fluorescent SMILES have been demonstrated for a range of important fluorophore classes including rhodamines, cyanines, oxazines, and trianguleniums, as crystals, powders, thin films and in polymer matrices[9]. Ultra bright fluorescent SMILES nanoparticles for bioimaging have also been

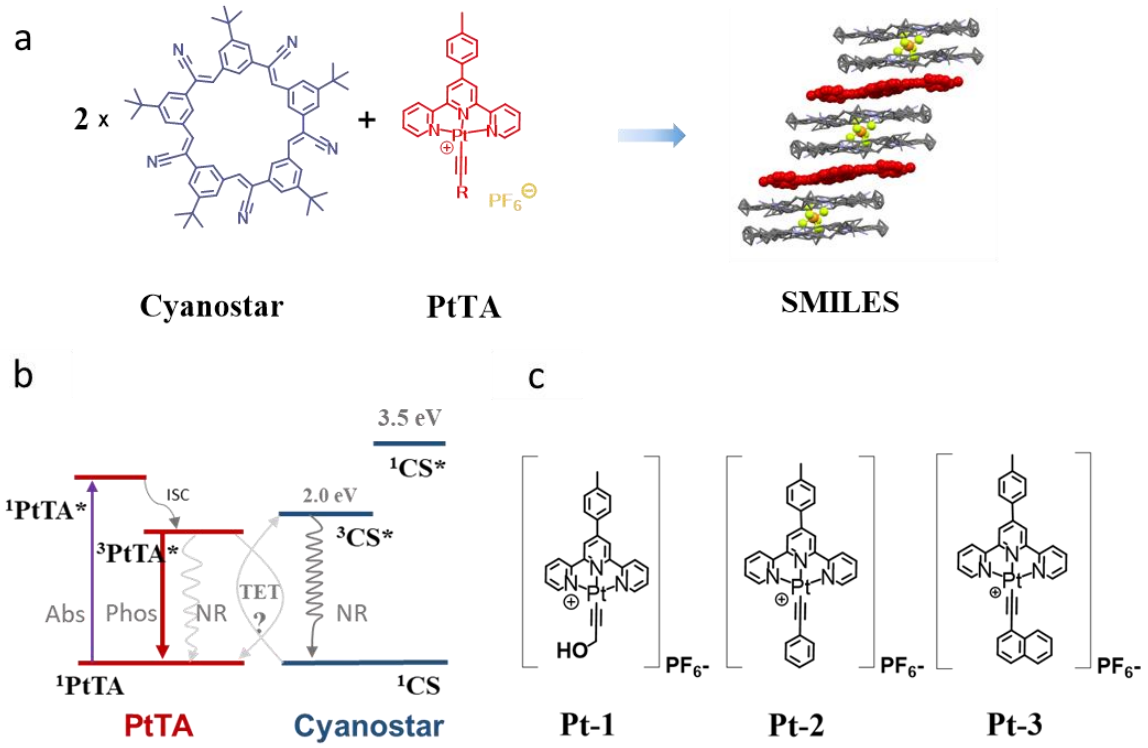

Scheme 1. (a) Illustration of the formation and structure of SMILES, 2:1 anion complexes are formed from CS and PF6- ions that in solids packs alternating with the planar PtTA dyes. (b) Relative state energy of cyanostar and sensitivation of the CS triplet state via triplet energy transfer (TET). (c) Molecular structures of three PtTA compounds: **Pt1**, **Pt2** and **Pt3**..

developed by nanoprecipitation in the presence of amphiphilic ligands[6,10]. However, thus far SMILES materials have been limited to fluorescent dyes and no examples of SMILES with phosphorescent dyes have been investigated.

Phosphorescent molecular materials are particular interesting with respect to sensing and imaging modalities exploring the μs to sec. long decay times[11,12]. Triplet excitons have also found important applications in light-emitting diodes (LED) [13], and for triplet–triplet annihilation photon upconversion (TTA-UC) technologies[14,15]. Thus, the scope of SMILES materials might be further expanded if triplet excitons of phosphorescent dyes can be generated and protected in SMILES materials.

A recent study showed, that in solution the CS_2X^- anion complex itself has a relative low T_1 state at 2.0 eV, which efficiently quench triplet excited dyes with higher energy via triplet energy transfer (TET) (Scheme 1b). Thus while SMILES materials can accommodate a broad range of excited singlets within its >3 eV HOMO-LUMO window[7], we may envision that if SMILES at all can accommodating triplet excited states they will have to have T_1 energies lower than ~2 eV[16]. The T_1 energy of CS_2X^- is suggested to be strongly modified by relaxation of the molecular conformation in solution but less so in solid state. Eventually these results raise the questions: can the SMILES strategy be applied to triplet excited dyes and reinstate intrinsic molecular phosphorescence in solid materials? And if so, what triplet energies are compatible with the CS_2X^- anion complex used in SMILES?

For this investigation, we selected a series of planar mono-cationic PtTA (Pt(II) Terpyridyl Acetylide) dyes[17,18] (Scheme 1c) with T_1 energies close to 2 eV : **Pt1** (2.3 eV), **Pt2** (2.07 eV), **Pt3** (1.92 eV) for the explorations of phosphorescent SMILES systems. Apart from the μs range emission lifetime, the PtTAs are known for distinct red-shifted emission bands in aggregates originating from formation of stacked dimers with Pt-Pt contacts, which are useful for distinguishing SMILES packing from non-SMILES PtTA aggregates[19-21]. Single crystal XRD characterization show that all three PtTAs form SMILES structures when crystallized with two equivalents of CS. Spectroscopic measurements show that **Pt1-SMILES** materials are non-emissive, while **Pt2-SMILES** and **Pt3-SMILES** show solution-like phosphorescence. **Pt2-SMILES** and **Pt3-SMILES** have quantum yields in the range of 4~5% and lifetime of 1~2 μs at ambient conditions. Especially, **Pt3-SMILES** show favorable emission properties and we were able transfer these properties to into 26 nm sized water-soluble nanoparticles stabilized by PEG amphiphiles. We find that the SMILES concept can be applied for phorphorescent emitters as long as the emissive triplet excited state has an energy below the triplet energy of CS_2X^-, which we envision to be 2.0 eV for CS triplet state.

2 Results and Discussion

2.1 Photophysical properties of PtTA in solution

The three PtTA complexes, hydroxylacetylide complexe (**Pt1**), phenylacetylide complexe (**Pt2**) and

naphthylacetylide complexe (**Pt3**) (Scheme 1c) were synthesized based on literature procedures. Detailed synthetic procedures and NMR characterization are provided in supporting information (SI§1). Figure 2 shows absorption, emission, and excitation spectra in DCM solution. As previously reported, solvent effects are of large importance for the photophysical properties of PtTAs,[18,20,22,23] and we find that emission is considerable quenched both in actionitrile (MeCN) and tetrahydrofurane (THF) solutions (Figure S1). In general, the three PtTA complexes have best photoluminescent behaviours in DCM attributed by stronger emission, longer emission lifetime with single-exponential decay features.

Apart from solvent effects, direct comparisons of intrinsic photophysical properties among three PtTA complexes can be achieved in Figure 2 and Figure S2. In agreement with the literature, absorption curves of three complexes display multiple absorption bands above 300 nm. The first intense band (300-350 nm) has been assigned to transitions in the terpyridine ligand. Furthermore, the visible region contains two transitions at 410-430 nm and 480-500 nm that has been classified as singlet state metal-to-ligand charge-transfer (^{1}MLCT) transitions, though emission are originated from the triplet ^{3}MLCT state involving the acetylide ligand.[17,18,24]. With the changes of ancillary substituent on the acetylide ligand, the emission of PtTA complexes is tuned from 560 nm (**Pt1**) to 620 nm (**Pt2**) and 690 nm (**Pt3**). Emission lifetimes (Figure S1) varies from 1.7 μs (**Pt1**) to 0.48 μs (**Pt2**) and 77ns (**Pt3**), accompanied by comparable decrease in emission yields. Based on the calculations on deactivation constants, the photophysical property differences among three PtTA complexes are mainly originated from different non-radiative decay constant (k_{nr}) though the radiative constant k_r are similar (3×10^4 s^{-1}), and the intrinsic exciton's lifetimes are $\tau\approx33$ μs for all three complexes, as summarized in Table 1. Microsecond time-gated emission spectra of three complexes (Figure S3) are identical to the steady-state spectra. This supports classifying PtTA's emission as phosphorescence, furthermore we estimate the triplet energy levels of three complexed from the emission spectra: 2.30eV (**Pt1**), 2.07eV (**Pt2**) and 1.92eV (**Pt3**) (SI§3.1).

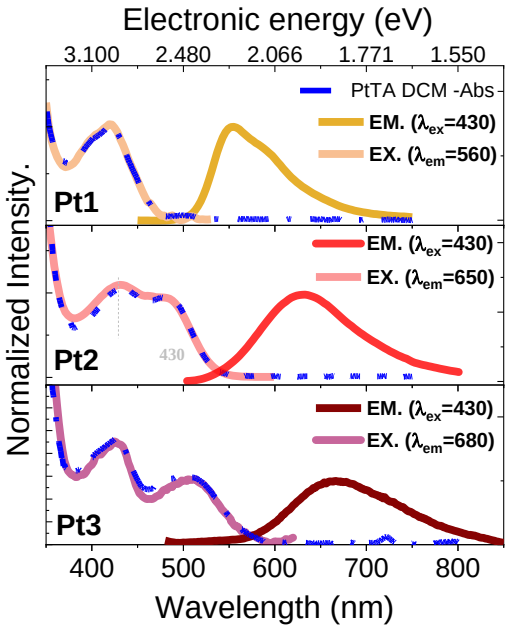

Figure 1. Steady state photophysical characterizations of PtTA (Pt1, Pt2, Pt3) complexes in DCM. All measurements were conducted with an optically diluted concentration (10 μM), at room temperature. Excitation curves were normalized in accordance with the shape of the absorption curves, emission curves were normalized for intensity.

2.2 Molecular Interactions and Triplets Energy Transfer in solution

To study the possible interactions between PtTA complexes and CS, Stern-Volmer titration experiments were conducted by adding increasing amounts of tetrabutylammonium (TBA) [CS_2PF_6] to PtTA[CS_2PF_6] solutions. Figure 2 shows Stern-Volmer quenching plots for lifetime and relative emission quantum yields (absorption normalized luminescence intensity) of each PtTA complex. For **Pt1** (Figure 2a) and **Pt2** (Figure 2b), a clear quenching phenomenon is observed for both PtTA complexes with the addition of $CS_2PF_6^-$, as both emission intensity and lifetime decreases for each PtTA (Figure S6, S7). In agreement with the Stern-Volmer equation for dynamic quenching (Equation 1), both plots of τ_0/τ and I_0/I for each PtTA display identical slopes. The bimolecular quenching constants (k_q) for quenching of **Pt1** and **Pt2** by $CS_2PF_6^-$ were calculated from the slopes.

$$\frac{\tau_0}{\tau} = \frac{I_0}{I} = 1 + k_q \tau_0 [Q] \qquad (1)$$

Where τ_0 and τ are luminescent lifetimes without and with the existence of quencher, I_0 and I are luminescent intensities without and with the existence of quencher, k_q is the diffusional quenching constant and [Q] is the concentration of quencher. In this report, I_0 and I were calibrated by the corresponding absorbance at the excitation wavelength.

The bimolecular quenching constant k_q for **Pt1**[CS_2PF_6]-TBA[CS_2PF_6] and **Pt2**[CS_2PF_6]-TBA[CS_2PF_6] are 9×10^9 $M^{-1}\bullet s^{-1}$ and 1×10^{10} $M^{-1}s^{-1}$, respectively. The k_q for τ_0/τ and I_0/I are almost identical for both **Pt1**[CS_2PF_6]-TBA[CS_2PF_6] and **Pt2**[CS_2PF_6]-TBA[CS_2PF_6] systems, indicating a dynamic quenching feature between CS and Pt1 (Pt2)[25].

Prior studies on CS by Edhborg and colleagues suggested that the bimolecular quenching constant k_q can be referred to triplet energy transfer constant k_{TET} [16], therefore the triplet energy transfer between PtTA complexes and CS were based on molecular collisions driven by diffusion limitation (1×10^{10} $M^{-1}\bullet s^{-1}$), and presumably in the format of Dexter-exchange. As proven beforehand, the triplet energy of the $[CS_2PF_6]^-$ complex is 2.0eV, thereby the

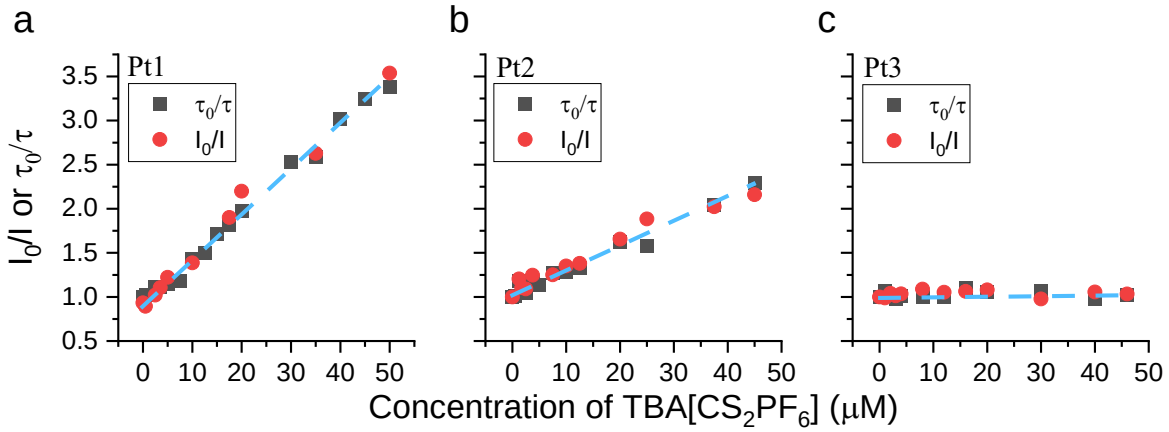

Figure 2. Stern-Volmer plots (lifetime and emission intensity) for PtTA (**Pt1**, **Pt2** and **Pt3**) (5 μM in DCM) as function of increasing concentration of TBA[CS_2PF_6] at 298K. Emission intensities were normalized with respect to the absorption at the excitation wavelength (Figure S6).

triplet energy of **Pt1** (2.21eV) and **Pt2** (2.07eV) both satisfy the exothermic requirement. **Pt3** display unchanged emission intensity and lifetime with the addition of $CS_2PF_6^-$, suggesting that CS cannot effectively quench **Pt3** within the concentration range.

2.3 Properties of the PtTA-SMILEs Solids

The phosphorescence emitted by the PtTA complexes has been well utilized in aggregated conditions[23], though the application requires a delicate manipulation on intermolecular intercalating and π-π stacking structures[26]. Nevertheless, the elongated triplet exciton migration pathway in such strong coupling conditions induce higher potential of quenching by traps in the vicinity or at the surfaces, thereby bulky polymer protections and careful fabrications are normally required[27,28]. Under such circumstance, the SMILES strategy was adopted to testify how the macromolecular spatial isolation will influence the phosphorescent properties of PtTA complexes in the solid condition.

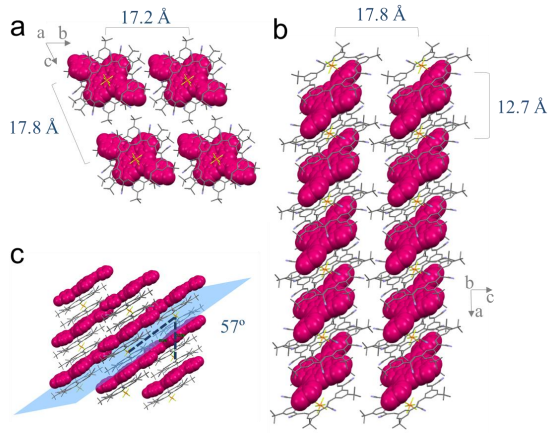

Figure 3. Molecular stacking of Pt2•CS_2PF_6 SMILES crystal based on single crystal XRD characterizations. The unit is Ångstrom for numbers in a and b, Pt2 cation shown in red space filling mode and CS_2PF_6 as stick mode.

Crystal structure of PtTA-SMILEs lattices. In order to inner structure of PtTA-SMILES solids, all three PtTA-SMILES single crystals were grown and characterized (§1.2, Figure S8-S9, Table S1). A characteristic SMILES packing structure was confirmed by single crystal XRD characterization, indicating an alternating packing of PtTA complex and CS. Figure 3 show the charge-by-charge packing of the planar cationic **Pt2** complex separated by $CS_2PF_6^-$, which is in good agreement with previous reported SMILES crystal structure[7]. The columns complexes are separated by 17-18 Å in the ab-plane (Figure 3a) while the separation between Pt2 cations is only 13 Å in the column (Figure 3b) where the molecular plans are tilted 57° with respect to the columnar axis (Figure 3c). For **Pt1** and **Pt3** SMILES, they show similar stacking structures in single crystals, which are different to the typical neat PtTA aggregate structure[23,28,29].

Luminescent properties of PtTA SMILEs Solids. One of the fundamental and essential application of SMILES materials is to reinstate the emissive performances of dyes even in densely packed aggregates as in the dilute solutions[7,9,10]. In order to testify how much phosphorescent emission can be reinstated in SMILES, an investigation on PtTA-SMILES solids photophysical properties is required for a final confirmation of the phosphorescent PtTA-SMILES strategy.

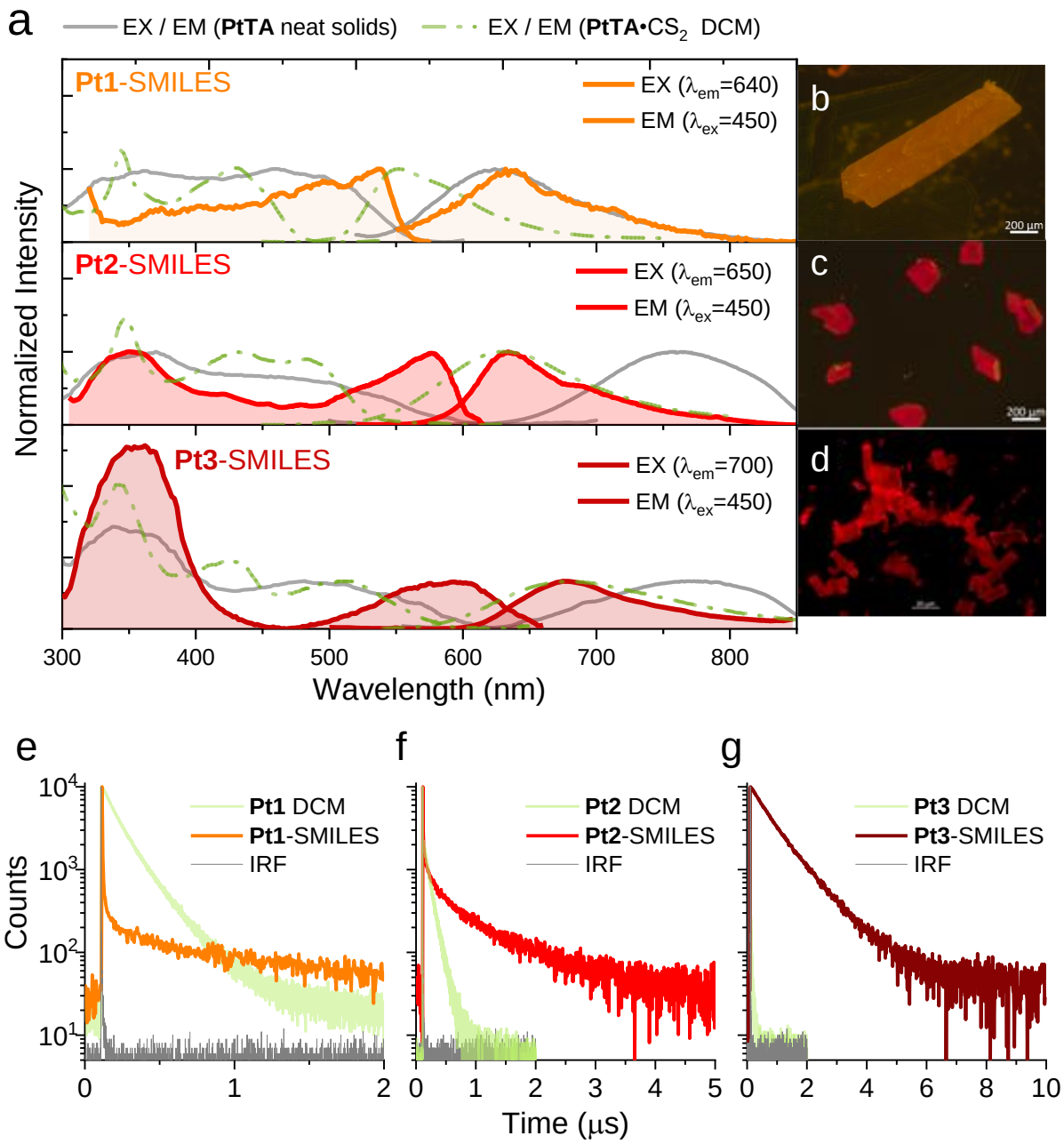

Figure 4. (a) Steady state optical properties of PtTA-SMILES crystals in comparison with PtTA in DCM solution and non-SMILES PtTA powders. Emission micrographs of crystals (b) **Pt1**-SMILES, (c) **Pt2**-SMILES and (c) **Pt3**-SMILES using 475/40 nm bandpass filter for excitation and 510 nm long pass filter in the emission path. Emission decay curves of crystal (e) **Pt1**-SMILES, (f) **Pt2**-SMILES and (g) **Pt3**-SMILES in comparison with corresponding decay curves of PtTA in DCM solution. 532nm long pass filter was used for decay curves characterizations in order to screen out scattering signals.

Figure 4 shows the steady-state and time-resolved measurements on PtTA-SMILES crushed crystallines. Pt1-SMILES is weakly luminescent, and the emission maximum locates close to the emission maximum of neat Pt1 aggregates, instead of resembling Pt1 solution state emission (Figure 4a). But for Pt2-SMILES and Pt3-SMILES, both crystalline materials are emissive under spectroscope or microscope (Figure 4c, 4d), reproducing emission curves similar to the corresponding solution state. Surprisingly, both SMILES crystal materials also show narrower band width (FWHM, the full width at half maximum) emission. The excitation spectra of all three SMILES crystals are apparently red-shifted when compared to the single molecular state, which may be classified as size-dependent spectral deformations (Figure S10) and strong attenuation in large size absorbers[5]. Compared to the pure Pt2 and Pt3 aggregates, embedding Pt2 and Pt3 into SMILES apparently rescue the intrinsic single molecular emission, improve QY and lifetime (Table 1 and Figure 4g, 4h). Especially for Pt3, whose QY and lifetime are 10 times more strengthened in SMILES solids compared to in solution state. Therefore, we eventually obtained two emissive phosphorescent SMILES crystalline materials: Pt2-SMILES (λ_{em}=635 nm, Φ=0.04, τ=1.5 μs) and Pt3-SMILES (λ_{em}=670 nm, Φ=0.05, τ=2 μs), whose photophysical properties outperform both single molecular state and their neat aggregates.

In general, the spectral measurements reinforce the two findings abovementioned: 1) efficient triplet energy transfer and 2) effective emission reinstatement. The benchmark for generating bright SMILES phosphorescence is determined by the differences between the complexes' triplet energy level ($E_{T\text{-}PtTA}$) and that of CS ($E_{T\text{-}CS}$). When $E_{T\text{-}PtTA} > E_{T\text{-}CS}$, such as Pt1, efficient triplet energy transfer underwent from Pt1 to CS in solid lattices. When $E_{T\text{-}PtTA} < E_{T\text{-}CS}$, such as Pt3, triplet energy transfer was not witnessed as a striking process in SMILES solids. When it comes to a situation that $E_{T\text{-}PtTA} \approx E_{T\text{-}CS}$, even if the TET process was proven diffusion-controlled efficient between Pt2 and CS in DCM solution, we still discover that Pt2-SMILES crystalline presents noticeable reproduction of bright Pt2 emission. This might be induced by the slight rise of $E_{T\text{-}CS}$ in constrained conformations within solid lattices and then alleviate the quenching of Pt2 triplets energy, further insights will be based on disentanglement of excitons' deactivation processes in the PtTA-SMILES solids.

2.4 Formation and properties of PtTA-SMILES Solids

While the single crystal samples provide valuable insight into the molecular spatial arrangements, many optical applications require thin films or powders. To confirm that SMILES structures can be reliably formed without slow crystal growing conditions we performed a 'titration' experiment for expedient synthesis of PtTA-SMILES solids. Solid samples with gradually increased molar ratios of CS/PtTA (from 0 to 3) where prepared by drop casting of DCM solution on glass slides to yield film-like solid samples. Figure 5a shows the emission spectra of such **PtTA•**CS_x solids, ranging from neat PtTA

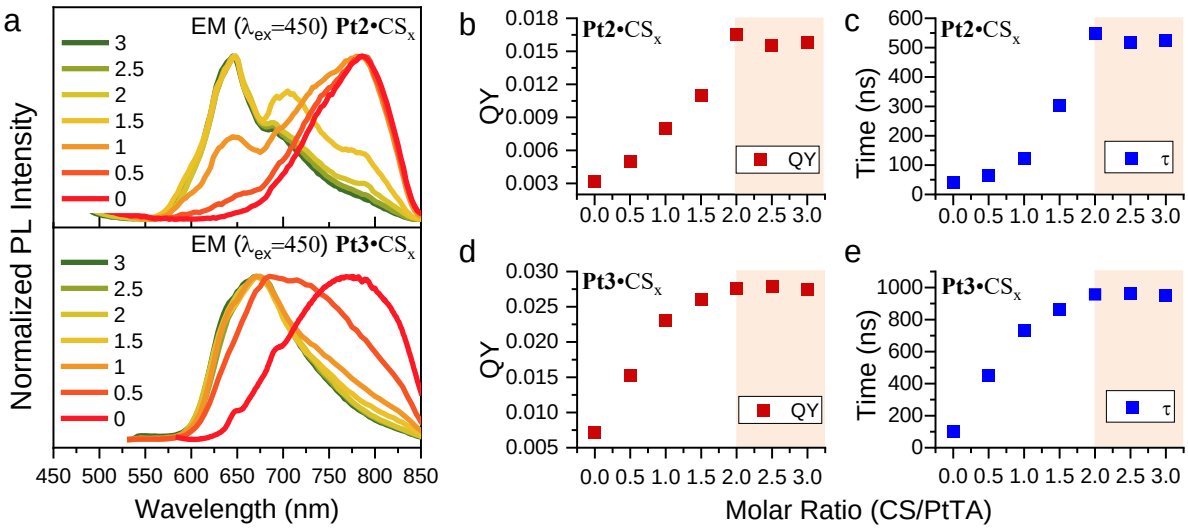

Figure 5. (a) Steady state emission spectra of drop cast PtTA solids with increasing molar ratio of CS. (b) emission quantum yields, and (c) emission lifetime of **Pt2** solids as function of molar ratio of CS. (d) emission quantum yields, and (e) lifetime of **Pt3** solids as function of different molar ratio of CS. Lifetime measurements were conducted at wavelengths of the emission maxima.

aggregates (PtTA•CS_0) without any CS, to **PtTA**•CS_3 solids with excess CS. For **Pt2**•CS_x and **Pt3**•CS_x. the addition of CS gradually changes the characteristic red-shifted emission of close contact stacked PtTA aggregates to the solution-like emission of SMILES. These spectral changes are accompanied by increase in Φ_{em} and τ (Figure 5b-5e). At 2.0 molar equivalents of CS, emission spectra changes have converged towards that of the SMILES crystals (see overlay in Figure S9). Φ_{em} and τ also reach constant values at 2.0 molar equivalents of CS, though somewhat lower than those found for single crystal samples as seen in Table 1. This observation is in good agreement with previous findings of general lower emission quantum yields for spin-coated and dropcast samples of fluorescent SMILES, where more structural defects lead to increased non-radiative deactivations.[7, 9, 29] This interpretation is supported by the calculated radiative rates (k_r) for the samples that are perfectly matching those found for Pt2 and Pt3 in solution and in SMILES crystals (Table 1),[32] as soon as the CS to PtTA molar ratio reaches 2.0, which complete the formation of the cyanostar anion complex ($CS_2PF_6^-$). Decay curves and photophysical data for all dropcast samples are found in Figure S10 and Table S4. The titration of CS into PtTA solids clearly demonstrates that effective decoupling of the PtTA complexes takes place at 2.0 equivalents and that the radiative properties at this point are similar to those of the SMILES structures found in single crystals.

2.5 Phosphorescent PtTA-SMILES Nanoparticles

With a purpose to validate the practical application of phosphorescent SMILES emitters, we adopted the well-established SMILES nanoparticle (NPs) methodology [6]. Especially, we focused on Pt3-SMILES which shows the largest improvement and its

long-decay NIR emission are better for applications in comparison to other two PtTA-SMILES solid materials.

Shown in Figure 7, we find that the Pt3-SMILES NPs shows similar optical properties to its solids state. Pt3-SMILES NPs emits at 670nm (Φ=0.03), and its excitation curve shows a red-shifted band compared to the Pt3 solution state, though the SMILES NPs by the less red-shifted excitation band (Figure S11). Within the core part of nanoparticles, the nanocrystalline structure is prone to generate more energetic traps at grain boundaries or inside the emitter when compared to single crystal, therefore we correspondingly observed a slight lifetime decrease in Pt3-SMILES NPs, but still being kept at a satisfying level (1~2 μs). For

Table 1. Photophysical properties of PtTA solutions, PtTA-SMILES crystals and solids.

Samples (Composition)		λ_{em} (nm)	τ (ns)	Φ (%)	k_r (s^{-1}) $\times 10^4$	k_{nr} (s^{-1}) $\times 10^4$	τ_0 (μs)
Solution (DCM, 5μM)	**Pt1**[PF_6]	555	1751	5.3	3.1	54	32.8
	Pt2[PF_6]	633	483	1.5	3.0	200	33.1
	Pt3[PF_6]	668	77	0.2	3.0	1300	33.3
Solution (DCM, 5μM)	**Pt1**[CS_2PF_6]	554	1138	3.4	3.0	85	33.2
	Pt2[CS_2PF_6]	633	462	1.4	3.0	210	33.2
	Pt3[CS_2PF_6]	672	80	0.3	2.9	1000	34.4
SMILES Single crystals	**Pt2**[CS_2PF_6]	635	1500	4.4	2.9	64	34.5
	Pt3[CS_2PF_6]	670	2200	5.4	2.9	47	35.1
Dropcast solids	**Pt2**[PF_6]	770	42	0.3	7.6	2370	13.1
	Pt3[PF_6]	780	95	0.7	7.8	1080	12.8
	Pt2[CS_2PF_6]	640	549	1.7	3.0	179	33.3
	Pt3[CS_2PF_6]	680	958	2.8	2.9	101	34.7
SMILES NPs	**Pt3**[$CS_{2.5}PF_6$]	675	990	3.1	3.1	98	31.9

*Rate constants calculated as $k_r = \Phi/\tau$, $k_{nr} = (1-\Phi)/\tau$), $\tau_0 = 1/k_r$

inner filter effect is less apparent in Pt3-

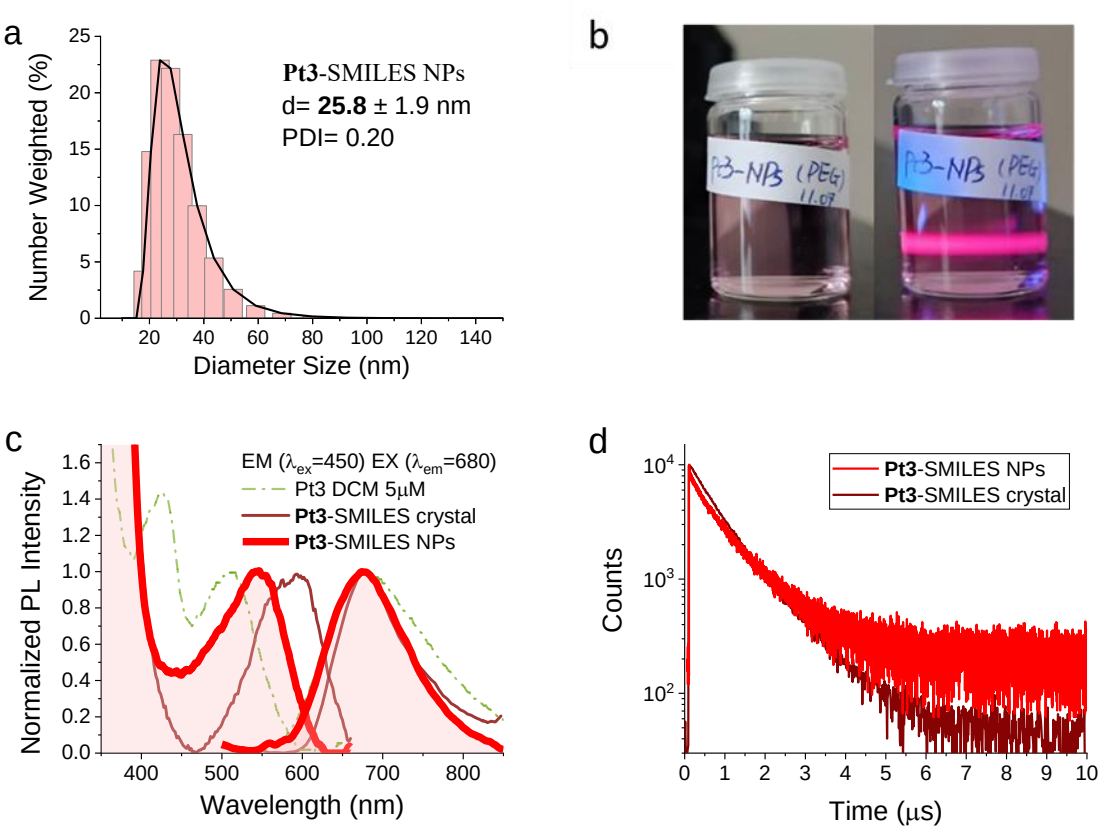

Figure 6. (a) Dynamic light scattering measurements on **Pt3**-SMILES nanoparticles size distribution. (b) Picture of **Pt3**-SMILES NPs aqueous solution illuminated by 405nm laser. (c) Steady state optical properties and (d) TCSPC decay curves of **Pt3**-SMILES nanoparticles in comparison to **Pt3** in DCM (10 μM) and **Pt3**-SMILES crystal. The decay curves were collected with a setup of λ_{ex}=450nm, λ_{em}=690nm.

morphological determinations, the Pt3-SMILES NPs shows unified size distribution with averaged size of 26 nm. In total, the fabrication of Pt3-SMILES NPs provides a longer decay phosphorescent probe for bio-imaging purposes.

3 Conclusions

In this research, for the first time we testify the SMILES strategy in reliably transferring the phosphorescent luminescence from solution state to highly densed solids, by combining CS with three PtTA chromophores whose triplet state energy level spanning across the CS triplet energy level ($E_{T\text{-}CS}$). Stern-Volmer titration experiments indicate that efficient triplet energy transfer from phosphorescent dyes to CS if $E_{T\text{-}dye} \geq E_{T\text{-}CS}$. It was experimentally proven that the $E_{T\text{-}CS} \approx 2.0$ eV.

A 'wane and wax' result was showcased for different PtTA-SMILES solids. The quenched emission in Pt1-SMILES and improved emission in Pt3-SMILES confirm the triplet energy transfer mechanism and firmly pinpoint a triplet energy boundary for choosing adaptable phosphorescent chromophores ($E_{T\text{-}dyes} < E_{T\text{-}CS} \approx 2$ eV). The role of CS in circumventing the nonradiative decay process was also explored to

quantitatively clarify the contributions of CS_2X^- spatial isolation to the phosphorescence improvement in the SMILES solids. Thereby we propose and validate a proof of concept for selectively harnessing phosphorescent chromophores' emission in high-density solids by utilizing SMILES method, and the generation of brightly emissive red-color Pt3-SMILES NPs paves a way for the application of SMILES in micro-second-range phosphorescent probes.

AUTHOR INFORMATION

Corresponding Author:

*Bo W. Laursen - Nano-Science Center & Department of Chemistry, University of Copenhagen, Universitetsparken 5, 2100 Copenhagen, Denmark. Orcid: 0000-0002-1120-3191. Email: bwl@chem.ku.dk

Conflicts of Interest:

No conflicts to declare.

Author Contributions

The PtTA complexes were synthesized by Niels Bisballe and Marko H Nowack. Maria S. Thomsen and Maren Pink contribute to the single crystal XRD structure analysis. Yang Wang conducted all other experiments including synthesis of SMILES crystals and titration experiments, spectroscopic measurements, data analysis, manuscript draft and editing. Bo W. Laursen contribute to conceptualization and correction, Amar H. Flood contribute to the manuscript correction. The manuscript was written through contributions of all authors. All authors have given approval to the final version of the manuscript.

ACKNOWLEDGMENT

YW appreciates the funding from the European Union's Horizon 2020 research and TALENT doctoral programme under the Marie Skłodowska-Curie grant agreement No 801199. AHF thanks the National Science Foundation for support (NSF-2118423). YW appreciates the characterization help technician Niels Vissing Holst.

REFERENCES

1 Zhao, Q., Li, F. & Huang, C. Phosphorescent chemosensors based on heavy-metal complexes. *Chem Soc Rev* **39**, 3007-3030 (2010). https://doi.org:10.1039/b915340c

2 Wang, X. D., Wolfbeis, O. S. & Meier, R. J. Luminescent probes and sensors for temperature. *Chem Soc Rev* **42**, 7834-7869 (2013). https://doi.org:10.1039/c3cs60102a

3 Wu, C. & Chiu, D. T. Highly fluorescent semiconducting polymer dots for biology and medicine. *Angew Chem Int Ed Engl* **52**, 3086-3109 (2013). https://doi.org:10.1002/anie.201205133

4 Gierschner, J., Varghese, S. & Park, S. Y. Organic Single Crystal Lasers: A Materials View. *Advanced Optical Materials* **4**, 348-364 (2015). https://doi.org:10.1002/adom.201500531

5 Gierschner, J. *et al.* Luminescence in Crystalline Organic Materials: From Molecules to Molecular Solids. *Advanced Optical Materials* **9**, 2002251 (2021). https://doi.org:10.1002/adom.202002251

6 Chen, J. *et al.* Ultrabright Fluorescent Organic Nanoparticles Based on Small-Molecule Ionic Isolation Lattices*. *Angew Chem Int Ed Engl* **60**, 9450-9458 (2021). https://doi.org:10.1002/anie.202100950

7 Benson, C. R. *et al.* Plug-and-Play Optical Materials from Fluorescent Dyes and Macrocycles. *Chem* **6**, 1978-1997 (2020). https://doi.org:10.1016/j.chempr.2020.06.029

8 Chen, Z. & Yam, V. W. W. Precise Size-Selective Sieving of Nanoparticles Using a Highly Oriented Two-Dimensional Supramolecular Polymer. *Angewandte Chemie* **132**, 4870-4875 (2020). https://doi.org:10.1002/ange.201913621

9 Kacenauskaite, L., Stenspil, S. G., Olsson, A. H., Flood, A. H. & Laursen, B. W. Universal Concept

for Bright, Organic, Solid-State Emitters horizontal line Doping of Small-Molecule Ionic Isolation Lattices with FRET Acceptors. *J Am Chem Soc* **144**, 19981-19989 (2022). https://doi.org:10.1021/jacs.2c08540

10 Chen, J. *et al*. Quantitative Energy Transfer in Organic Nanoparticles Based on Small-Molecule Ionic Isolation Lattices for UV Light Harvesting. *ACS Applied Nano Materials* **5**, 13887-13893 (2022). https://doi.org:10.1021/acsanm.2c01899

11 Yu, Y. *et al*. Room-Temperature-Phosphorescence-Based Dissolved Oxygen Detection by Core-Shell Polymer Nanoparticles Containing Metal-Free Organic Phosphors. *Angew Chem Int Ed Engl* **56**, 16207-16211 (2017). https://doi.org:10.1002/anie.201708606

12 Wang, S. *et al*. Biocompatible metal-free organic phosphorescent nanoparticles for efficiently multidrug-resistant bacteria eradication. *Science China Materials* **63**, 316-324 (2019). https://doi.org:10.1007/s40843-019-1191-9

13 Zhao, J., Wu, W., Sun, J. & Guo, S. Triplet photosensitizers: from molecular design to applications. *Chem Soc Rev* **42**, 5323-5351 (2013). https://doi.org:10.1039/c3cs35531d

14 Gray, V., Dzebo, D., Abrahamsson, M., Albinsson, B. & Moth-Poulsen, K. Triplet-triplet annihilation photon-upconversion: towards solar energy applications. *Phys Chem Chem Phys* **16**, 10345-10352 (2014). https://doi.org:10.1039/c4cp00744a

15 Edhborg, F., Bildirir, H., Bharmoria, P., Moth-Poulsen, K. & Albinsson, B. Intramolecular Triplet-Triplet Annihilation Photon Upconversion in Diffusionally Restricted Anthracene Polymer. *J Phys Chem B* **125**, 6255-6263 (2021). https://doi.org:10.1021/acs.jpcb.1c02856

16 Edhborg, F. *et al*. Triplet States of Cyanostar and Its Anion Complexes. *J Phys Chem A* **127**, 5841-5850 (2023). https://doi.org:10.1021/acs.jpca.3c02701

17 Yang, Q. Z., Wu, L. Z., Wu, Z. X., Zhang, L. P. & Tung, C. H. Long-lived emission from platinum(II) terpyridyl acetylide complexes. *Inorg Chem* **41**, 5653-5655 (2002). https://doi.org:10.1021/ic025580a

18 Guo, F., Sun, W., Liu, Y. & Schanze, K. Synthesis, photophysics, and optical limiting of platinum(II) 4'-tolylterpyridyl arylacetylide complexes. *Inorg Chem* **44**, 4055-4065 (2005). https://doi.org:10.1021/ic049266n

19 Yu, C., Wong, K. M., Chan, K. H. & Yam, V. W. Polymer-induced self-assembly of alkynylplatinum(II) terpyridyl complexes by metal...metal/pi...pi interactions. *Angew Chem Int Ed Engl* **44**, 791-794 (2005). https://doi.org:10.1002/anie.200461261

20 Yam, V. W., Chan, K. H., Wong, K. M. & Zhu, N. Luminescent platinum(II) terpyridyl complexes: effect of counter ions on solvent-induced aggregation and color changes. *Chemistry* **11**, 4535-4543 (2005). https://doi.org:10.1002/chem.200500106

21 Chan, A. K., Lam, W. H., Tanaka, Y., Wong, K. M. & Yam, V. W. Multiaddressable molecular rectangles with reversible host-guest interactions: modulation of pH-controlled guest release and capture. *Proc Natl Acad Sci U S A* **112**, 690-695 (2015). https://doi.org:10.1073/pnas.1423709112

22 Tam, A. Y., Lam, W. H., Wong, K. M., Zhu, N. & Yam, V. W. Luminescent alkynylplatinum(II) complexes of 2,6-bis(N-alkylbenzimidazol-2'-yl)pyridine-type ligands with ready tunability of the nature of the emissive states by solvent and electronic property modulation. *Chemistry* **14**, 4562-4576 (2008). https://doi.org:10.1002/chem.200701914

23 Wong, K. M., Tang, W. S., Lu, X. X., Zhu, N. & Yam, V. W. Functionalized platinum(II) terpyridyl alkynyl complexes as colorimetric and luminescence pH sensors. *Inorg Chem* **44**, 1492-1498 (2005). https://doi.org:10.1021/ic049079p

24 Shikhova, E. *et al*. Excited-state absorption properties of platinum(II) terpyridyl acetylides. *Inorg Chem* **46**, 3038-3048 (2007). https://doi.org:10.1021/ic0618652

25 Du, P. *et al*. Photoinduced electron transfer in platinum(II) terpyridyl acetylide chromophores: reductive and oxidative quenching and hydrogen production. *J Phys Chem B* **111**, 6887-6894 (2007). https://doi.org:10.1021/jp072187n

26 Law, A. S., Lee, L. C., Yeung, M. C., Lo, K. K. & Yam, V. W. Amyloid Protein-Induced Supramolecular Self-Assembly of Water-Soluble Platinum(II) Complexes: A Luminescence Assay for Amyloid Fibrillation Detection and Inhibitor Screening. *J Am Chem Soc* **141**, 18570-18577 (2019). https://doi.org:10.1021/jacs.9b09515

27 Po, C., Tam, A. Y., Wong, K. M. & Yam, V. W. Supramolecular self-assembly of amphiphilic anionic platinum(II) complexes: a correlation between spectroscopic and morphological properties. *J Am Chem Soc* **133**, 12136-12143 (2011). https://doi.org:10.1021/ja203920w

28 Zhang, K., Yeung, M. C., Leung, S. Y. & Yam, V. W. Living supramolecular polymerization achieved by collaborative assembly of platinum(II) complexes and block copolymers. *Proc Natl Acad Sci U S A* **114**, 11844-11849 (2017). https://doi.org:10.1073/pnas.1712827114

29 Leung, S. Y. *et al.* Luminescent cyclometalated alkynylplatinum(II) complexes with a tridentate pyridine-based N-heterocyclic carbene ligand: synthesis, characterization, electrochemistry, photophysics, and computational studies. *Chemistry* **19**, 10360-10369 (2013). https://doi.org:10.1002/chem.201300493

30 El-Sayed, M. A. Triplet state. Its radiative and nonradiative properties. *Accounts of Chemical Research* **1**, 8-16 (2002). https://doi.org:10.1021/ar50001a002

31 Wong, E. K., Chan, M. H., Tang, W. K., Leung, M. Y. & Yam, V. W. Molecular Alignment of Alkynylplatinum(II) 2,6-Bis(benzimidazol-2-yl)pyridine Double Complex Salts and the Formation of Well-Ordered Nanostructures Directed by Pt...Pt and Donor-Acceptor Interactions. *J Am Chem Soc* **144**, 5424-5434 (2022). https://doi.org:10.1021/jacs.1c12994

32 Yam, V. W., Wong, K. M. & Zhu, N. Solvent-induced aggregation through metal...metal/pi...pi interactions: large solvatochromism of luminescent organoplatinum(II) terpyridyl complexes. *J Am Chem Soc* **124**, 6506-6507 (2002). https://doi.org:10.1021/ja025811c

33 Tong, G. S. & Che, C. M. Emissive or nonemissive? A theoretical analysis of the phosphorescence efficiencies of cyclometalated platinum(II) complexes. *Chemistry* **15**, 7225-7237 (2009). https://doi.org:10.1002/chem.200802485

34 Lam, W. H., Lam, E. S. & Yam, V. W. Computational studies on the excited states of luminescent platinum(II) alkynyl systems of tridentate pincer ligands in radiative and nonradiative processes. *J Am Chem Soc* **135**, 15135-15143 (2013). https://doi.org:10.1021/ja406810a

35 Li, K. *et al.* Highly phosphorescent platinum(ii) emitters: photophysics, materials and biological applications. *Chem Sci* **7**, 1653-1673 (2016). https://doi.org:10.1039/c5sc03766b

36 Tang, W.-S., Lu, X.-X., Wong, K. M.-C. & Yam, V. W.-W. Synthesis, photophysics and binding studies of Pt(ii) alkynyl terpyridine complexes with crown ether pendant. Potential luminescent sensors for metal ions. *Journal of Materials Chemistry* **15** (2005). https://doi.org:10.1039/b501644d

Appendix 3-b: Manuscript SI of PtTA-SMILES

Supporting Information

Turing on Molecular Phosphorescence in Materials by Supramolecular Organization in *Small-Molecule Ionic Isolation Lattices*

Yang Wang[1], Marko H. Nowack[1], Niels Bisballe[1], Maria S. Thomsen[1], Maren Pink[2], Amar H. Flood[2], Bo W. Laursen[1]*

1. Nano-Science Center & Department of Chemistry, University of Copenhagen, Universitetsparken 5, 2100 Copenhagen, Denmark
2. Department of Chemistry, Indiana University, 800 E. Kirkwood Ave, Bloomington, IN 47405, USA

CONTENTS

§1 Synthetic procedures

§1.1 Synthesis of PtTA Complexes

General remarks: ^{1}H-NMR spectra were acquired on 500 MHz instruments by Bruker. Chemical shifts for ^{1}H-NMR spectra are reported relative to TMS, or referenced to the solvent residual peak for DMSO-d_6 (δ = 2.50 ppm). Methanol was dried over 3 Å mol. sieves for 48 h prior to use. 4'-(4-Tolyl)-2,2′:6′,2″-terpyridine (**S1**) and other reagents and solvents were obtained from commercial suppliers and used without further purification.

Synthesis of S2 : *Platinum(II) 4'-(4-tolyl)-2,2':6',2'' terpyridine chloride*

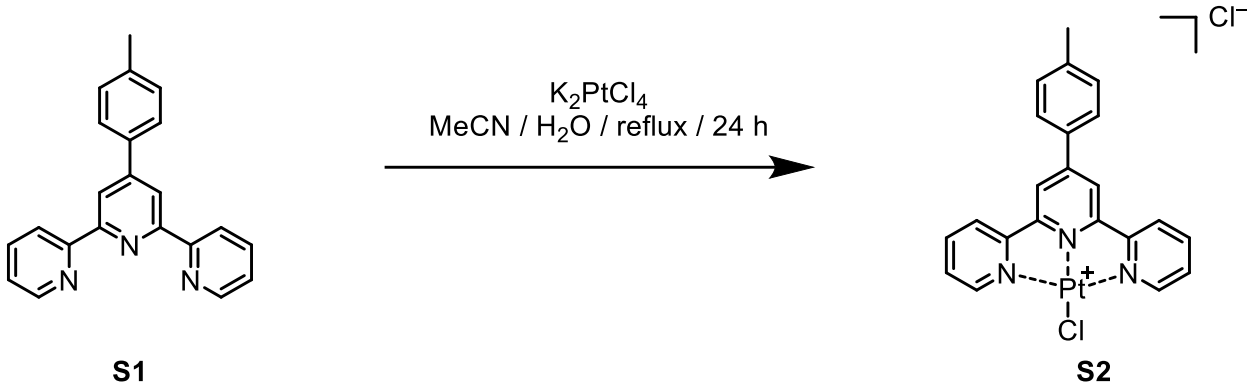

S1 **S2**

S2 was synthesized from **S1** according to a previously reported literature procedure[1].

^{1}H NMR (500 MHz, DMSO-*d6*): $\delta = \delta$ =8.98 (s, 2H), 8.93 (d, J = 5.6 Hz, 2H), 8.87 (d, J = 8.0 Hz, 2H), 8.54 (t, J = 7.9 Hz, 2H), 8.14 (d, J = 7.8 Hz, 2H), 7.96 (t, J = 6.7 Hz, 2H), 7.50 (d, J = 7.8 Hz, 2H), 2.45 (s, 3H).

Synthesis of Pt1: *Platinum(II) 4'-(4-tolyl)-2,2':6',2''-terpyridine methanolacetylide hexafluorophosphate*

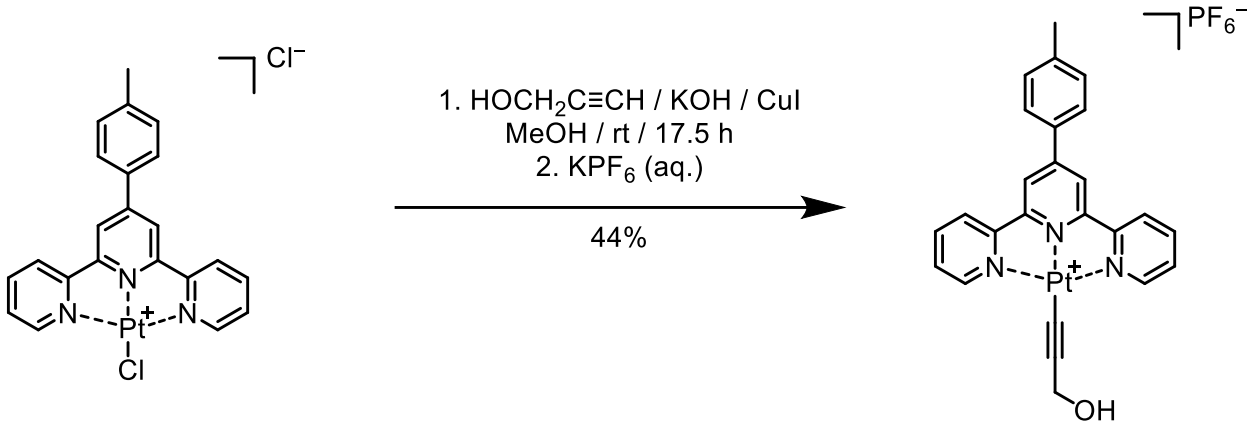

S2 **Pt1**

Pt1 was synthesized from **S2** according to a previously reported literature procedure[1]. The ^{1}H-NMR Signals are consistent with previous literature reports [1].

^{1}H-NMR (500 MHz, DMSO-*d6*)	δ =8.98 (s, 2H), 8.93 (d, J = 5.6 Hz, 2H), 8.87 (d, J = 8.0 Hz, 2H), 8.54 (t, J = 7.9 Hz, 2H), 8.14 (d, J = 7.8 Hz, 2H), 7.96 (t, J = 6.7 Hz, 2H), 7.50 (d, J = 7.8 Hz, 2H), 2.45 (s, 3H).

Synthesis of Pt2 : *Platinum(II) 4'-(4-tolyl)-2,2':6',2''-terpyridine phenylacetylide hexafluorophosphate*

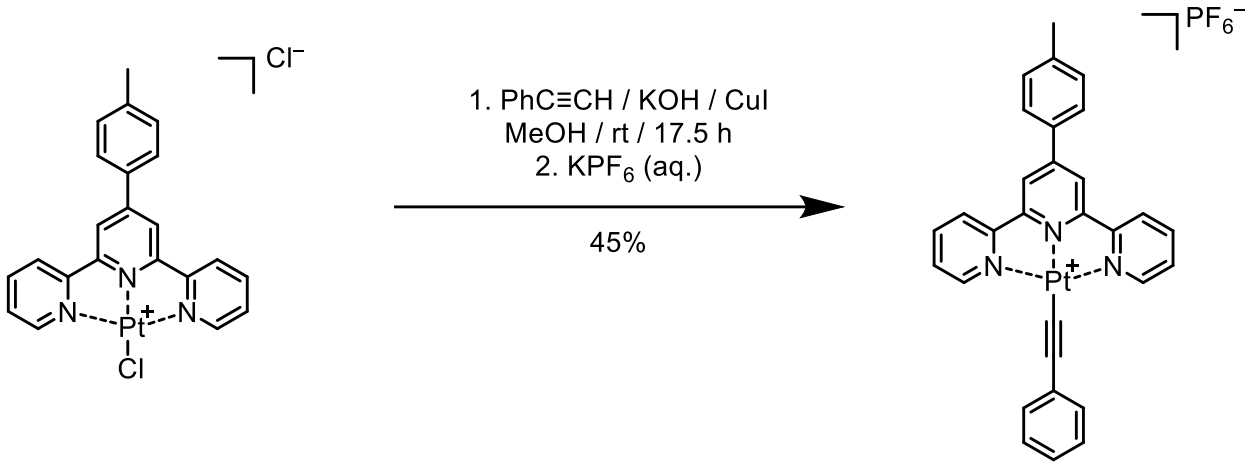

S2 **Pt2**

Pt2 was synthesized from **S2** according to modified literature procedure[2,3].

Synthetic processes: Phenylacetylene (25 µL, 0.23 mmol) and KOH (14 mg, 0.25 mmol) were combined in dry MeOH (15 mL, 0.01 M) in a dry round-bottomed flask under moderate stirring at room temperature. After 1 h, **S2** (101 mg, 0.159 mmol) and CuI (6.6 mg, 0.034 mmol) were added and the resulting yellow solution turned orange within 10 minutes. After 17.5 h the orange-brown reaction mixture was quenched by pouring KPF_6 (0.2 M). The resulting precipitate was isolated by filtration and washed with water (3 × 25 mL). The precipitate was then eluted off the filter with MeCN. The solution was reduced to 50 mL by evaporation of excess solvent, before the mixture was sonicated and poured into MeOH (150 mL) under vigorous stirring. Stirring was halted for the red precipitate to settle and was then isolated by filtration, followed by washing of the precipitate with MeOH (3 x 25 mL). This gave the titled compound **Pt2** as a red solid (58 mg, 0.072 mmol, 45 %).

^{1}H NMR (500 MHz, DMSO-*d6*): δ = 9.18 (d, *J* = 5.6 Hz, 2H), 9.03 (s, 2H), 8.88 (d, *J* = 8.0 Hz, 2H), 8.55 (t, *J* = 7.9 Hz, 2H), 8.13 (d, *J* = 7.9 Hz, 2H), 7.94 (t, *J* = 6.7 Hz, 2H), 7.53-7.48 (m, 4H), 7.36 (t, *J* = 7.5 Hz, 2H), 7.28 (t, *J* = 7.5 Hz, 1H), 2.45 (s).

Synthesis of Pt3: *Platinum(II) 4'-(4-tolyl)-2,2':6',2''-terpyridine naphthylacetylide hexafluorophosphate*

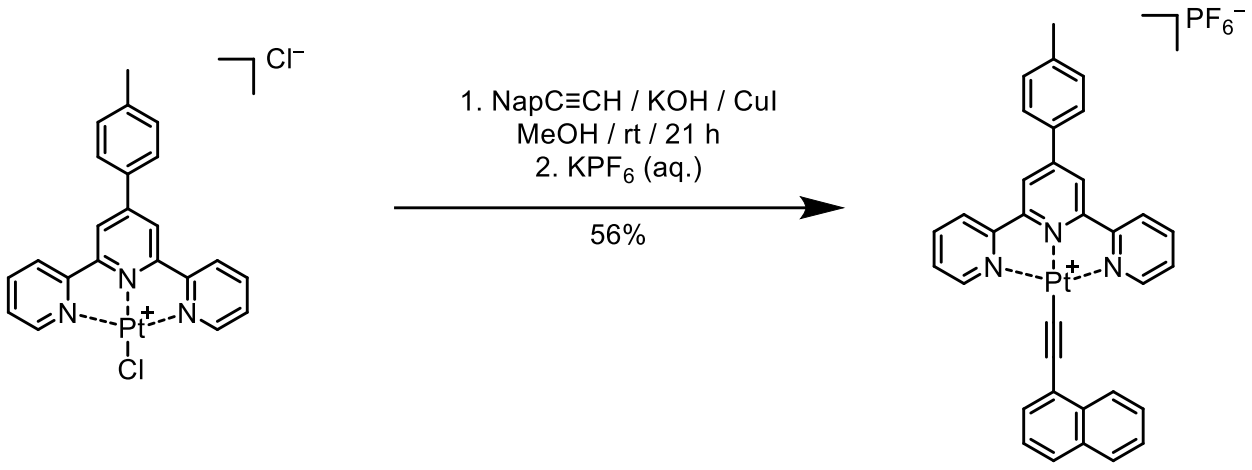

S2 **Pt3**

Pt3 was synthesized from **S2** according to modified literature procedure[3].

Synthetic processes: NapC≡CH (50 µL, 0.35 mmol) and KOH (17.5 mg, 0.35 mmol) were dissolved in MeOH (20 mL) and stirred at room temperature for 1 h. **S2** (106 mg, 0.167 mmol) and CuI (4.5 mg, 0.02 mmol) were added to the dark red solution, whereupon the solution turned dark orange over 10 min. The reaction mixture was stirred at room temperature for 21 h and poured into KPF_6 (0.2 M aq, 200 mL) under stirring. The dark red precipitate was filtered off, washed with H_2O (3 × 30 mL) and eluted off the filter with MeCN (200 mL). The solvent was concentrated in vacuo to 100 mL and sonicated for 5 min to redissolve the formed precipitate. The resulting solution was poured into Et_2O (300 mL) and stirred at rt for 2 h. The dark red precipitate was filtered off, washed with Et_2O (2 × 25 mL), eluted off the filter with MeCN, concentrated and dried in vacuo to yield **Pt3** as a dark red powder (81.2 mg, 0.094 mmol, 56%).

^{1}H NMR (500 MHz, DMSO-*d6*): δ (ppm) = 2.45 (s, 3H, $ArCH_3$), 7.47-7.52 (m, 3H, 3 × Ar*H*), 7.58 (t, 1H, *J* = 7.4 Hz, 1H), 7.63 (t, *J* = 7.5 Hz, 1H), 7.73 (d, *J* = 7.1 Hz, 1H), 7.86 (d, *J* = 8.3 Hz, 1H), 7.95 (q, *J* = 8.0 Hz, 2H), 8.12 (d, *J* = 7.8 Hz, 1H), 8.50 (d, *J* = 8.4 Hz, 1H), 8.53 (t, *J* = 8.0 Hz, 1H), 8.88 (d, *J* = 8.0 Hz, 1H), 9.03 (s, 1H), 9.22 (d, *J* = 5.6 Hz, 1H).

^{1}H-NMR (500 MHz, DMSO-*d*$_6$):.

S2

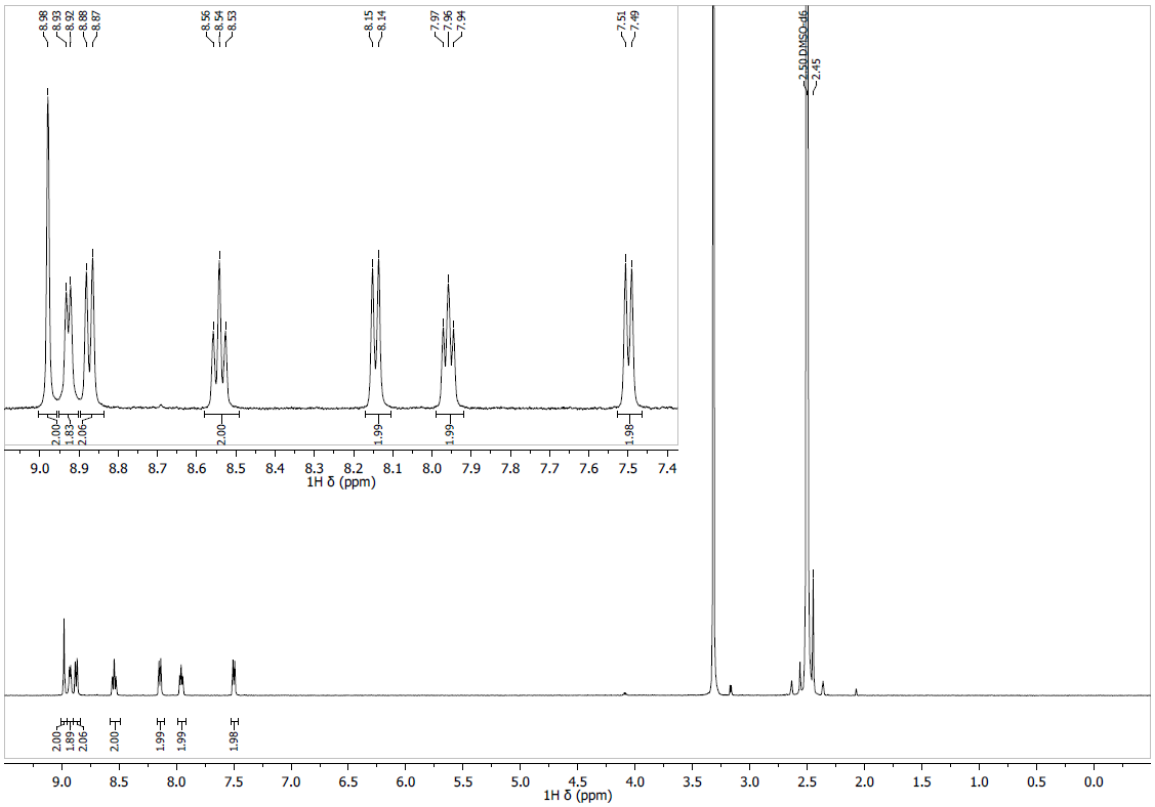

^{1}H-NMR spectra of **S2** (500 MHz, DMSO-*d6*)

Pt1

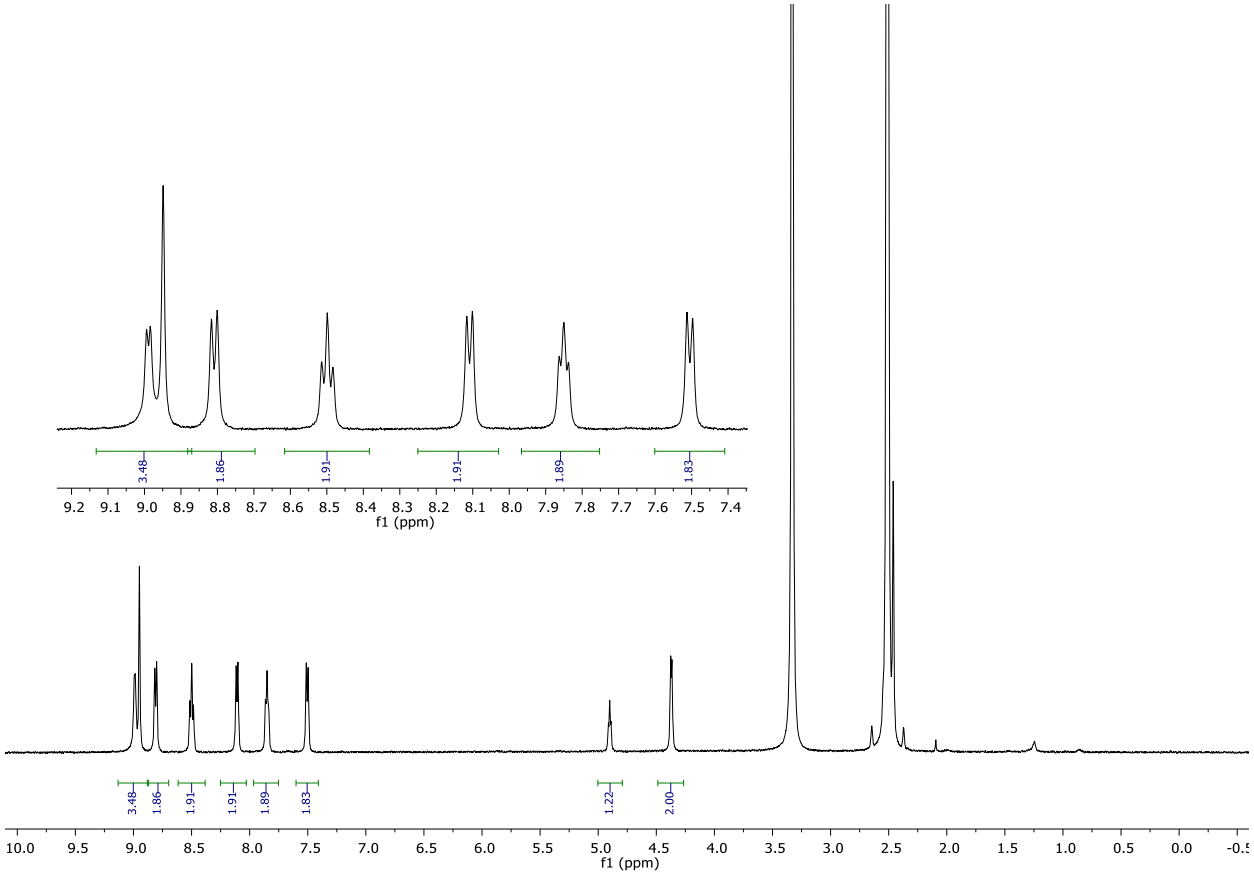

^{1}H-NMR spectra of **Pt1** (500 MHz, DMSO-*d6*)

Pt2

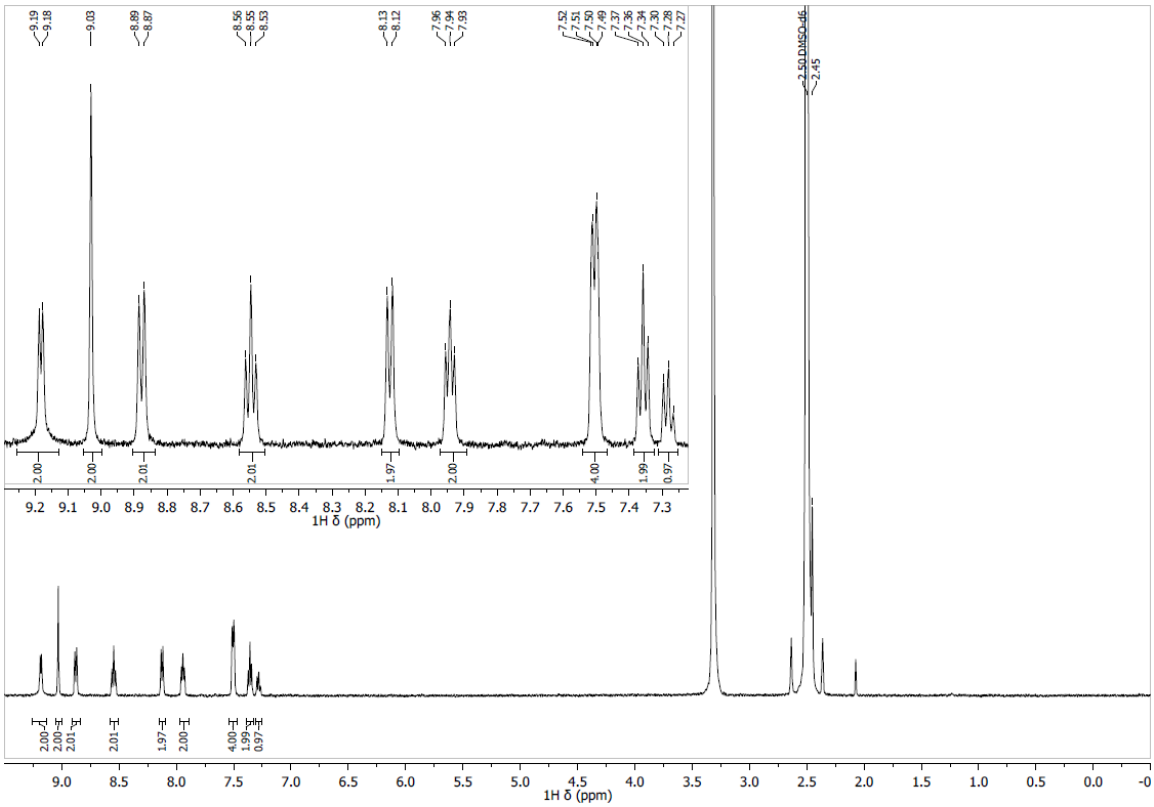

[1]H-NMR spectra of **Pt2** (500 MHz, DMSO-*d6*)

Pt3

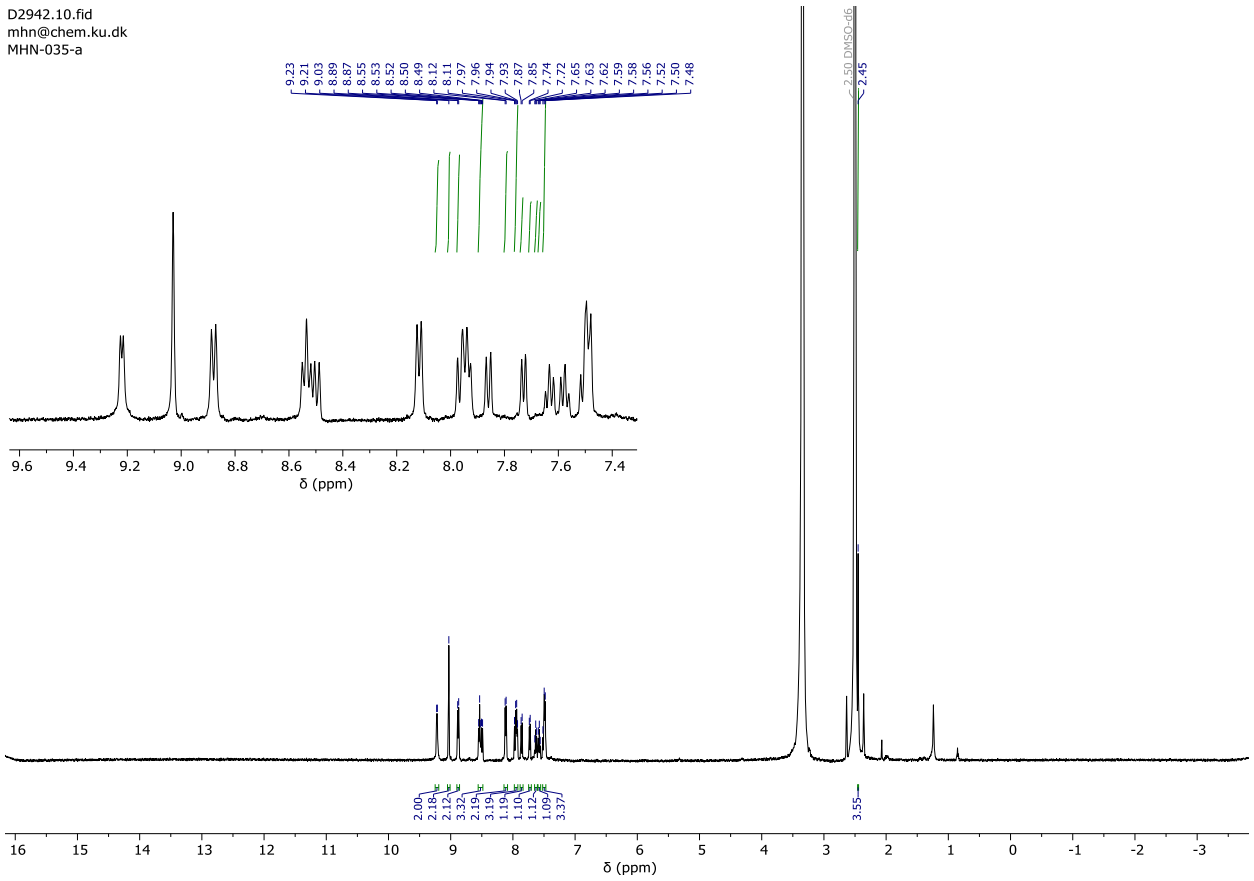

^{1}H-NMR spectra of **Pt3** (500 MHz, DMSO-*d6*)

§1.2 Synthetic method of PtTA-SMILEs crystals

Preparation of PtTA-SMILES single crystals:

5 mL of CS (1mM, DCM), and 4 mL of PtTA complex (0.5 mM, MeCN) were both filtered through hydrophobic PTFE filters (0.22μm), then mixed together in a 20 mL vial. After being ultrasonicated for 10 minutes, the vial was left still until crystals emerged.

§1.3 Synthetic method of Pt3-SMILEs nanoparticles

Procedures based on literature[4]:

1) **Pt3** (MeCN, 0.2 mM), CS (DCM, 1 mM) were mixed by following the molar ratio of CS/**Pt3**=2.5, with the addition of DCM, to reach a **Pt3**[$CS_{2.5}PF_6$] concentration of 50 μM.

2) 2mL **Pt3**[$CS_{2.5}PF_6$] (50 μM) and 0.7 mL DSPE-PEG (1 mg/mL, DCM) was mixed (DSPE-PEG accounts for 60% of total weight of the solids). All solvent was evaporate before 2mL THF was added to dissolve the solids with the assistance of ultrasonication.

3) Inject 1 mL of the prepared precursor solution in THF into a vial containing 10 mL distilled water, while ultrasonication and cooling on ice-bath. Then ultrasonication of the sample was continued for 15 minutes.

4) The sample was left in open vial overnight, in order to evaporate the THF.

§2 Instrumental setups and Measurements

§2.1 Spectroscopic Methods and Instrumentation

Steady-state: UV-Vis absorption spectra were measured with a Cary 300 spectrophotometer. Corrected photoluminescence spectra were obtained by a PTI Instruments spectrofluorimeter. All photophysical measurements were conducted at ambient temperature, 22 ± 2 ℃. All luminescent solution samples were measured in 1 cm2 anaerobic quartz cells.

TCSPC lifetime measurements were obtained by time-correlated single-photon counting on an PTI Instruments-FluoTime 300, the instrument response function was collected using a dilute solution of Ludox at the detection wavelength. Reconvolution of the fluorescence decay and instrumental response function (IRF) was performed on the Edinburgh software in conjunction with lifetime fitting. Finally, the data was exported and plotted by using Origin 2020.

Fluorescence microscopy: All micrographs of solid materials were taken using Zeiss fluorescence microscope, equipped with KL 2500 LCD halogen lamp as an excitation source, a LD EC Epiplan-NEOFLUAR 50x/0.55 HD DIC objective and an AxioCam MRc camera from Zeiss. Excitation (475 ± 20 nm) and emission (510 nm LP) filters were used in the excitation and detection path, respectively.

DLS measurements were obtained by Dynamic Light Scattering Zetasizer Pro Instrument (Malvern Panalytic).

§2.2 Stern-Volmer Quenching Experiments

Preparation of samples for Stern-Volmer quenching experiments is described as following:

1) Prepare PtTA (50 μM, DCM) solution, then filter with hydrophobic PTFE filters (0.22 μm).

2) 200 μL of PtTA (50 μM, DCM) was mixed with different volumes of TBA[CS_2PF_6] (50μM or 100 μM, DCM).

3) DCM was added to adjust all the solutions in order to reach a fixed volume of 2 mL.

The rate constant of triplet energy transfer (k_{TET}) from the donors to TBA[CS_2PF_6] was estimated using the bimolecular quenching constant k_q.

§2.3 Sample preparation and Measurements

Solid sample preparation:

Dropcast solids on glass cover: for measurements on solids, dropcast precursor solutions or suspension of solids (in heptane) on glass, then evaporate the solvents slowly.

Dissipated in viscous matrix: for measurements on neat aggregates and crystals optical properties (especially QY and τ), viscous matrix (propylene glycol, PG) was used to disperse crystallites for measurements.

QY: All solid samples collected with absolute method by using Integrating Sphere.

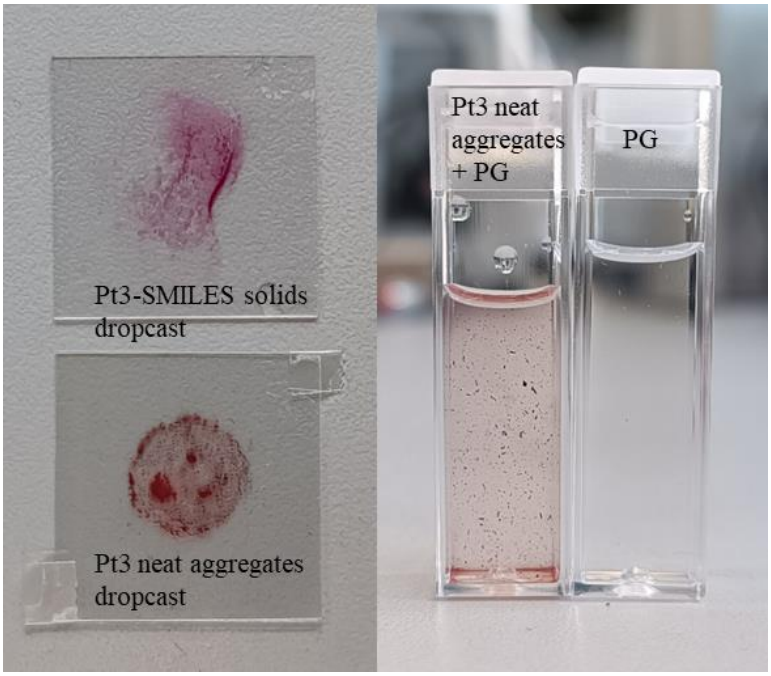

Comparison between solid samples on glass slids and in PG

§3 Supporting Graphs and Tables

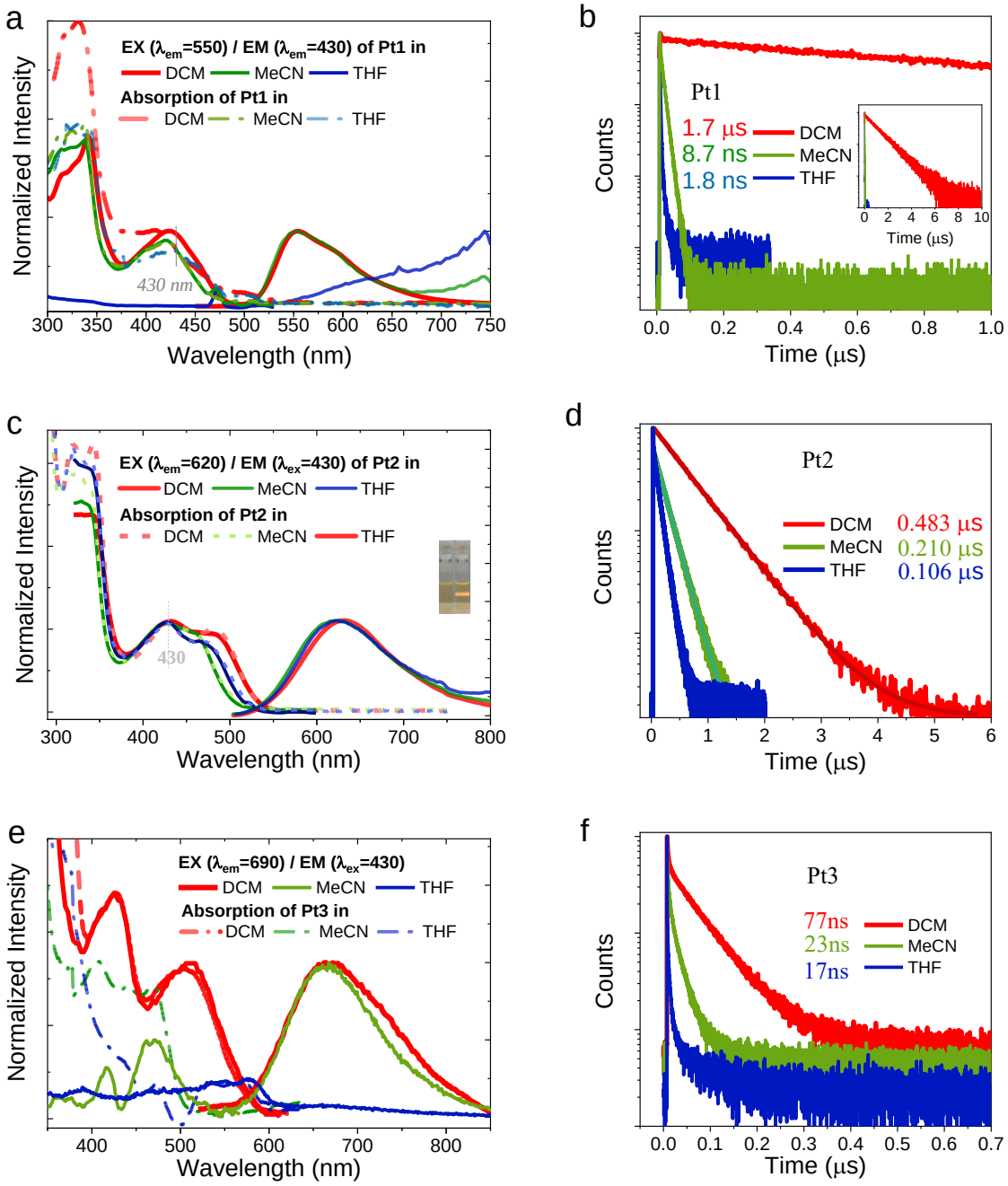

Figure S1. (a, c ,e) Steady state photophysical properties (absorption, emission and excitation) of **Pt1**, **Pt2** and **Pt3** in DCM, MeCN and THF (10 µM), respectively. Emission spectra were obtained at λ_{ex}=430 nm, excitation spectra were obtained at λ_{ex}=550 nm, 620 nm and 690 nm, respectively. (b, d, f) Time Correlated Single Photon Counting of **Pt1**, **Pt2** and **Pt3** in different optically diluted organic solutions (DCM, MeCN and THF, 10 µM). All PtTA complexes show displaying mono-exponential decay in DCM: **Pt1** (1.7 µs), **Pt2** (0.48 µs) and **Pt3** (0.077 µs).

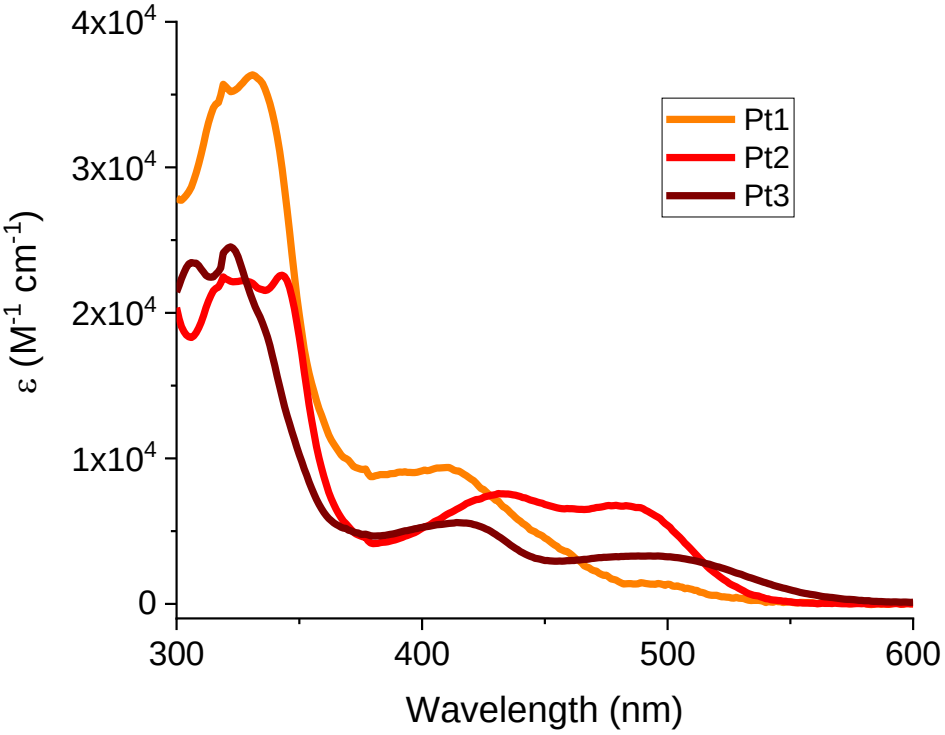

Figure S2. Absorption spectra of PtTA complexes showing the absorptivity of different bands. All samples were prepared in optically diluted DCM solutions.

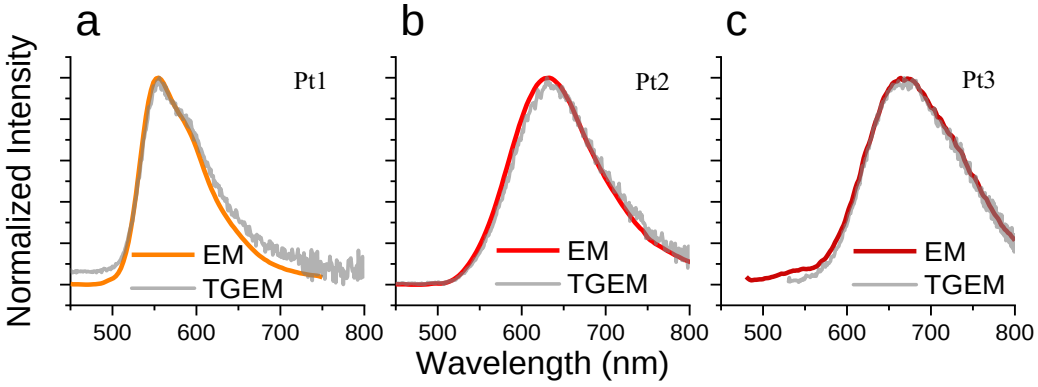

Figure S3. Steady-state emission spectra and time-gated (TG=5 μs) emission spectra of (a) **Pt1**, (b) **Pt2** and (c) **Pt3** in optically diluted DCM solution (10 μM, 298 K), though signals from Pt2 and Pt3 were very weak.

§3.1 PtTA triplet State Energy (ET).

The triplet energies of the PtTA complexes were estimated from their phosphorescence spectra in DCM, see Figure 1 and Figure S1. For PtTAs, which have broad and unstructured phosphorescence spectra, the triplet energy levels of PtTA were estimated from the phosphorescence onset at the wavelength where intensity reach 80% of maxima intensity. This match previous theoretical calculation and empirical tests on a **Pt2** analog system.[2,5,6] The following values were used: 540 nm for **Pt1**, 600 nm for **Pt2** and 646 nm for **Pt3**, yielding the following triplet energy level: $E_{T\text{-}Pt1}$ = 2.30 eV, $E_{T\text{-}Pt2}$ = 2.07 eV, $E_{T\text{-}Pt3}$ = 1.92 eV.[6, 7]

§3.2 Single molecular state of PtTA[CS_2PF_6]

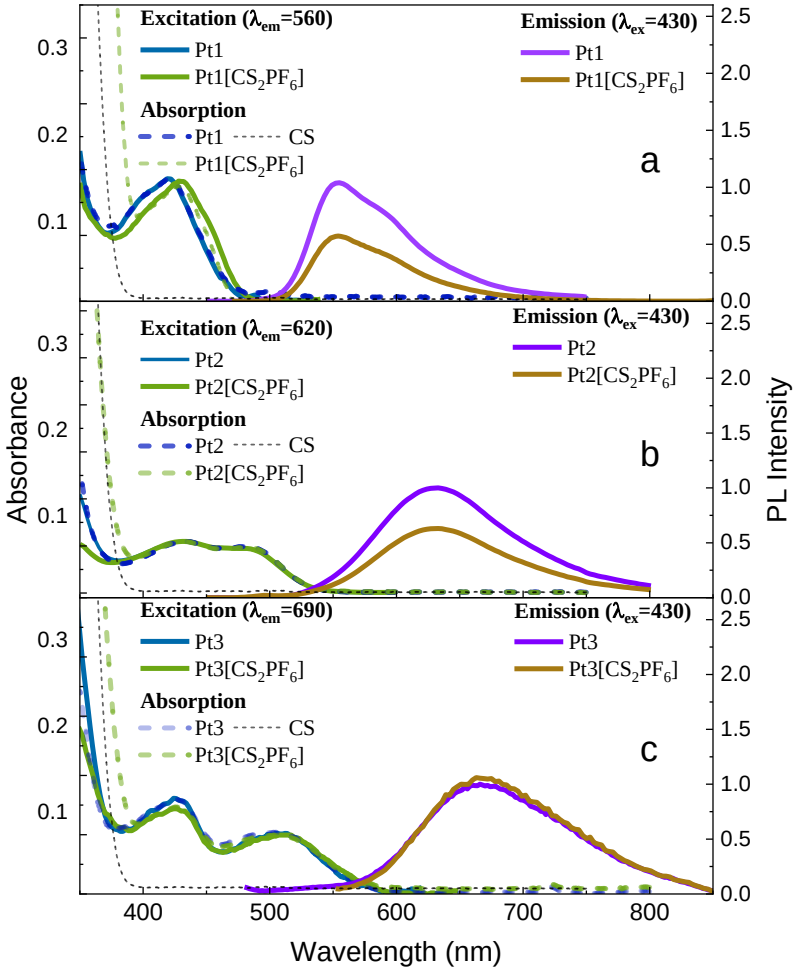

Figure S4. Steady state (emission, excitation and absorption) and time-gated emission (time gate=5μs) spectra of (a) **Pt1** and **Pt1**[CS_2PF_6], (b) **Pt2** and **Pt2**[CS_2PF_6] and (c) **Pt3** and **Pt3**[CS_2PF_6] (10 μM, DCM, 298 K). Absorption and excitation curves are normalized to compare the overlap. Steady state emission and time-gated emission are also normalized to show the overlap.

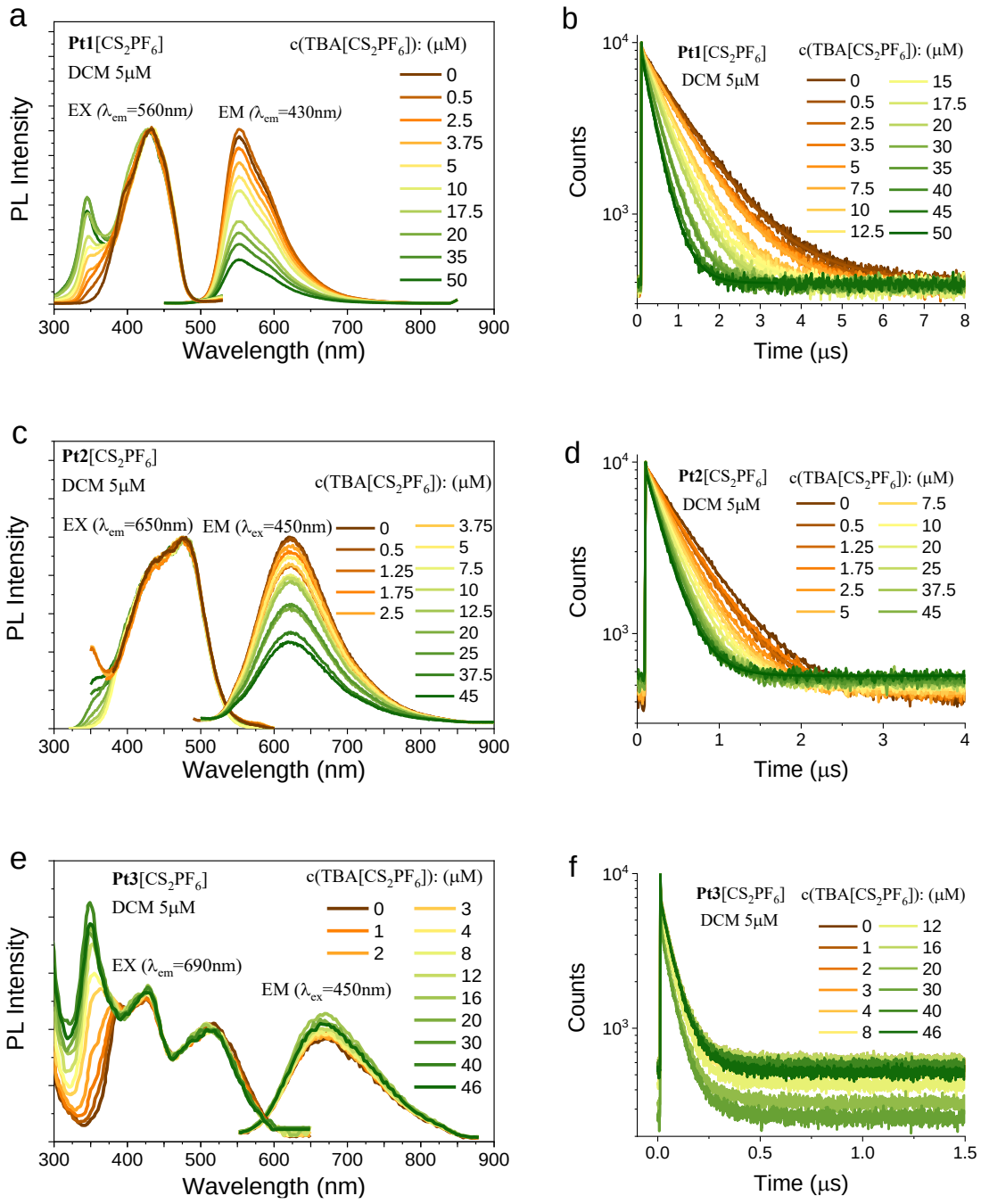

Figure S5 Steady state optical spectra and TCSPC decay curves for Stern-Volmer titration experiments of (a, b) **Pt1**[CS_2PF_6]-TBA[CS_2PF_6], (c, d) **Pt2**[CS_2PF_6]-TBA[CS_2PF_6] and (e, f) **Pt3**[CS_2PF_6]-TBA[CS_2PF_6]. The concentration of PtTA[CS_2PF_6] was fixed at 5 μM in DCM, different concentrations of TBA[CS_2PF_6] were added separately. Instrumental setup for decay curves were: λ_{ex}=450nm λ_{em}=560nm for **Pt1**[CS_2PF_6]-TBA[CS_2PF_6] in (b), λ_{ex}=450nm λ_{em}=620nm for **Pt2**[CS_2PF_6]-TBA[CS_2PF_6] in (d), λ_{ex}=450nm λ_{em}=690nm for **Pt3**[CS_2PF_6]-TBA[CS_2PF_6] in (f).

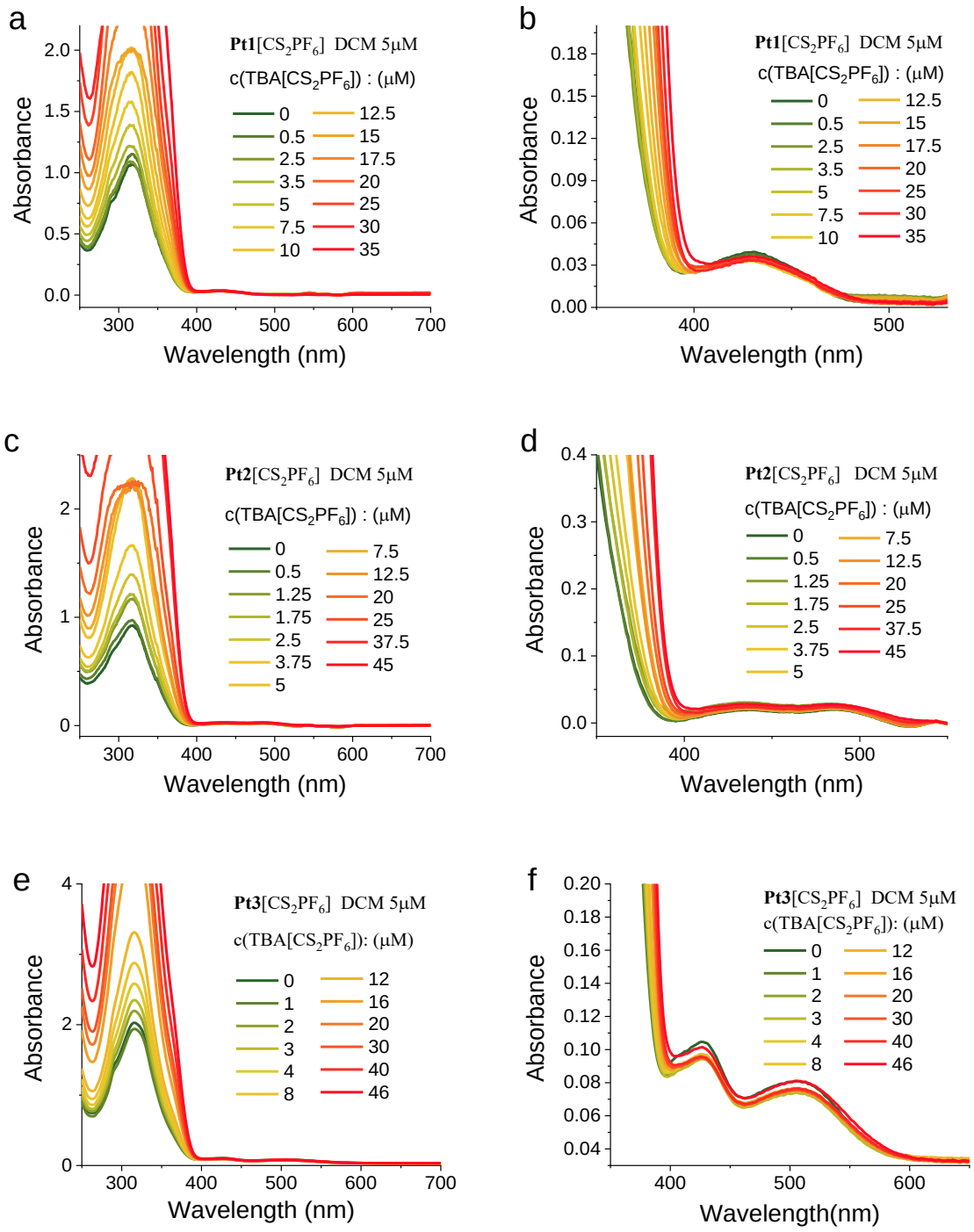

Figure S6. Absorption curves for Stern-Volmer titration experiments of (a, b) **Pt1**[CS_2PF_6]-TBA[CS_2PF_6], (c, d) **Pt2**[CS_2PF_6]-TBA[CS_2PF_6] and (e, f) **Pt3**[CS_2PF_6]-TBA[CS_2PF_6].

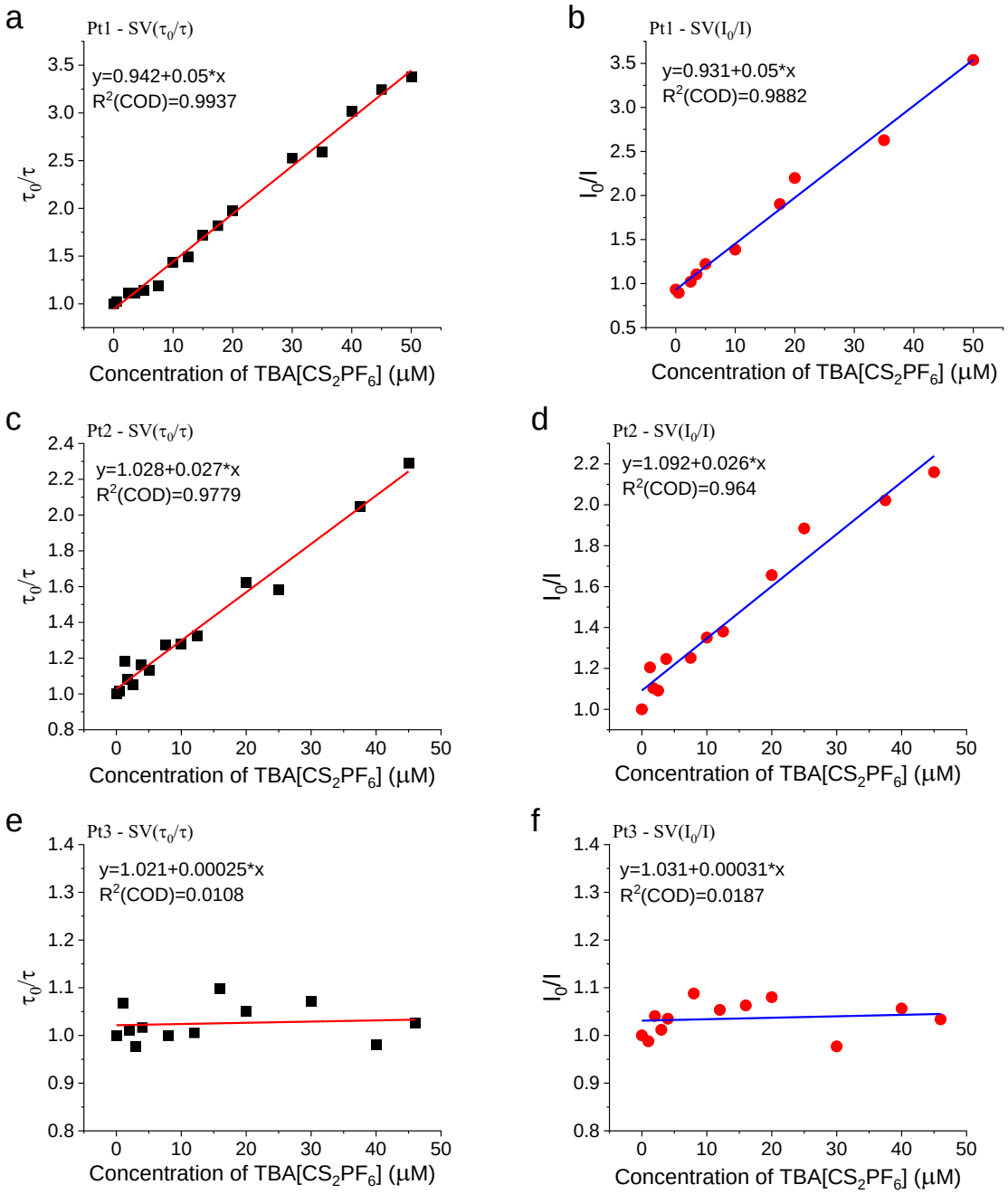

Figure S7. Fitted lines for Stern-Volmer quenching plots of PtTA[CS_2PF_6]-TBA[CS_2PF_6] systems.

Table S2. Fitted linear functions from Stern-Volmer plots of PtTA[CS_2PF_6]-TBA[CS_2PF_6]

Sample	Fitted Function		R-square (COD)	k_q ($M^{-1}s^{-1}$)
Pt1[CS_2PF_6]-TBA[CS_2PF_6]	τ_0/τ	y=0.942+0.050*x	0.9937	8.547E+09
	I_0/I	y=0.931+0.052*x	0.9882	8.889E+09
Pt2[CS_2PF_6]-TBA[CS_2PF_6]	τ_0/τ	y=1.028+0.027*x	0.9779	1.059E+10
	I_0/I	y=1.092+0.026*x	0.9644	1.020E+10
Pt3[CS_2PF_6]-TBA[CS_2PF_6]	τ_0/τ	y=1.021+0.00025*x	0.0108	---
	I_0/I	y=1.031+0.00031*x	0.0187	---

§3.3 PtTA-SMILES Crystal Solids

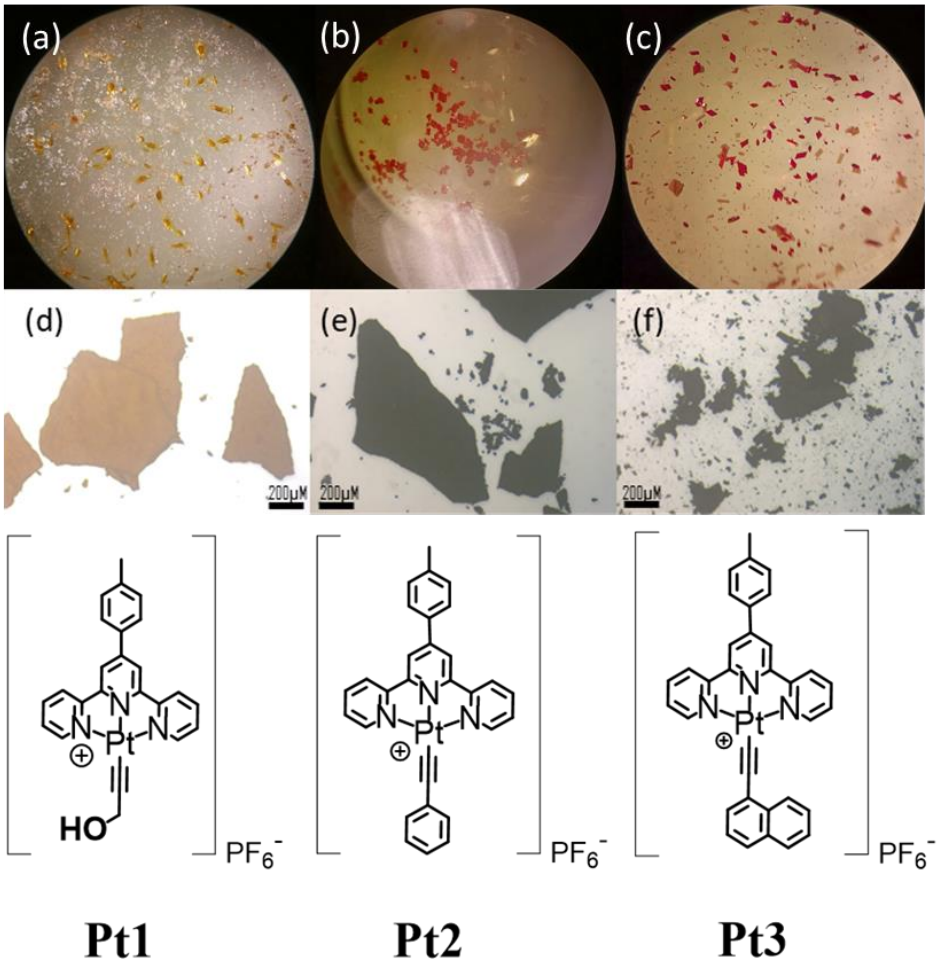

Figure S8. Crystal pictures under microscope for (a) **Pt1**-SMILES, (b) **Pt2**-SMILES and (c) **Pt3**-SMILES. Pictures of neat aggregates for (d) Pt1, (e) Pt2, (f) Pt3 under microscope.

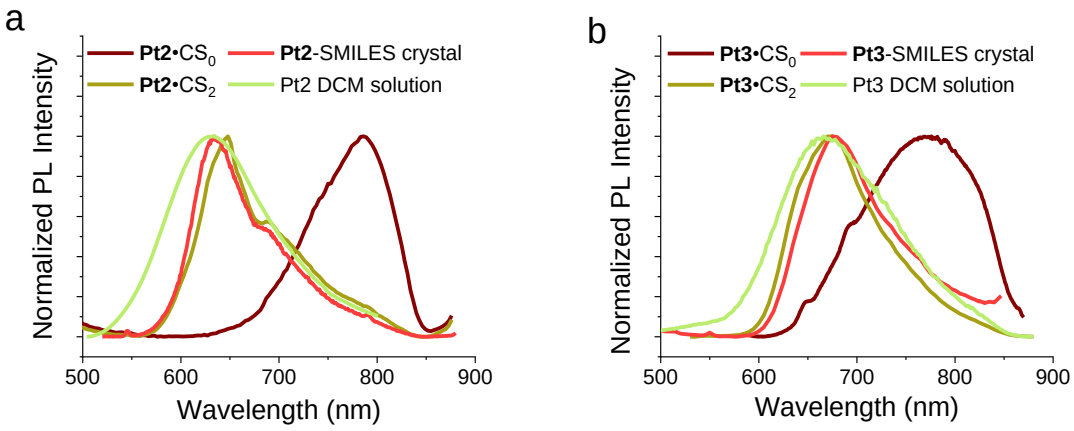

Figure S9. Emission spectra of (a) **Pt2**•CS_0, **Pt2**•CS_2 dropcast solids, **Pt2**-SMILES single crystal and **Pt2** in DCM solution; (b) **Pt3**•CS_0, **Pt3**•CS_2 dropcast solids, **Pt2**-SMILES single crystal and Pt3 in DCM solution. The excitation wavelength was λ_{ex}= 450 nm.

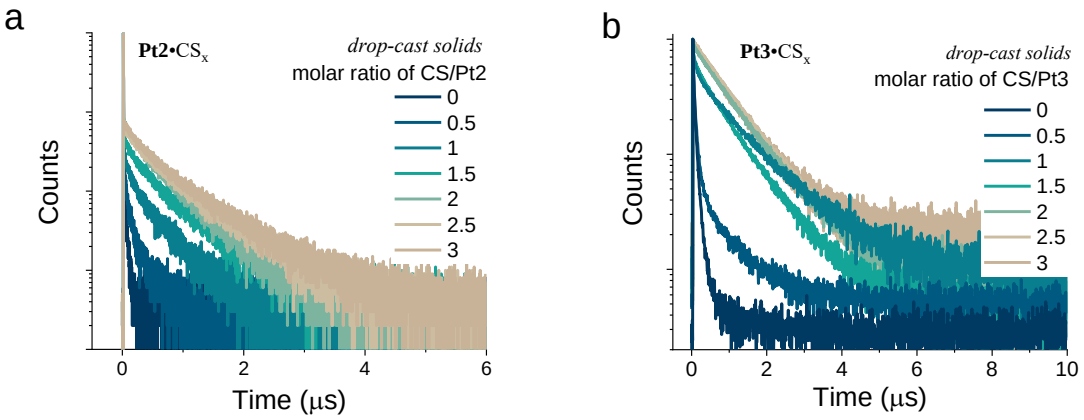

Figure S10. Decay curves of dropcast solids samples for (a) **Pt2** and (b) **Pt3** with different molar ratio of CS. Instrumental setup were λ_{ex}= 450 nm, with λ_{em} was set by each emission maximum in Figure 5(a).

Table S4. Photophysical properties of PtTA•CS_x solids[6,7].

PtTA•CS_x (Composition)		λ_{em} (nm)	τ (ns)	Φ_{em} (%)	k_r (s^{-1}) $\times 10^4$	k_{nr} (s^{-1}) $\times 10^4$	τ_0 (μs)
0	**Pt2**•CS_0	770	42	0.32	7.6	2373	13
0.5	**Pt2**•$CS_{0.5}$	770	66	0.5	7.6	1508	13
1.0	**Pt2**•$CS_{1.0}$	650, 750	122	0.8	6.6	813	15
1.5	**Pt2**•$CS_{1.5}$	650, 700	302	1.1	3.6	327	27
2.0	**Pt2**•$CS_{2.0}$	650	549	1.65	3.0	179	33
2.5	**Pt2**•$CS_{2.5}$	650	517	1.55	3.0	190	33
3.0	**Pt2**•$CS_{3.0}$	650	526	1.58	3.0	187	33
0	**Pt3**•CS_0	780	92	0.72	7.8	1079	13
0.5	**Pt3**•$CS_{0.5}$	700	451	1.53	3.4	218	29
1.0	**Pt3**•$CS_{1.0}$	680	735	2.3	3.1	133	32
1.5	**Pt3**•$CS_{1.5}$	680	861	2.6	3.0	113	33
2.0	**Pt3**•$CS_{2.0}$	680	958	2.76	2.9	102	35
2.5	**Pt3**•$CS_{2.5}$	680	961	2.79	2.9	101	34
3.0	**Pt3**•$CS_{3.0}$	680	953	2.74	2.9	102	35

*Rate constants calculated as $k_r = (\Phi/100)/\tau$, $k_{nr} = (1-\Phi/100)/\tau$, $\tau_0 = \tau/(\Phi/100)$

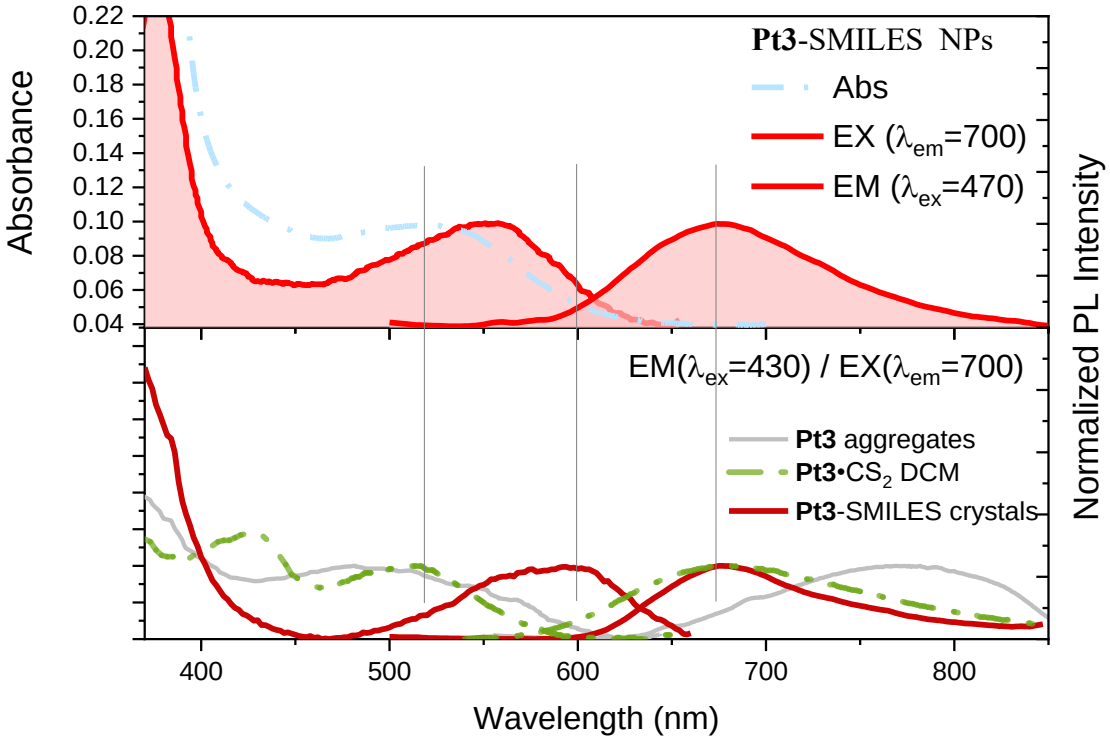

Figure S11. Steady state optical properties of **Pt3**-SMILES nanoparticles in comparison with emission and excitation curves of **Pt3**[CS_2PF_6] in DCM solution, **Pt3**-SMILES crystal and **Pt3** neat aggregates, all measured at room temperature.

§4 Reference

1 Zhao, T. C. *et al.* Synthesis, tunable photophysics and nonlinear absorption of terpyridyl Pt(II) complexes bearing different acetylide ligands. *Dyes and Pigments* **126**, 165-172 (2016). https://doi.org:10.1016/j.dyepig.2015.11.021

2 Yang, Q. Z., Wu, L. Z., Wu, Z. X., Zhang, L. P. & Tung, C. H. Long-lived emission from platinum(II) terpyridyl acetylide complexes. *Inorg Chem* **41**, 5653-5655 (2002). https://doi.org:10.1021/ic025580a

3 Guo, F., Sun, W., Liu, Y. & Schanze, K. Synthesis, photophysics, and optical limiting of platinum(II) 4'-tolylterpyridyl arylacetylide complexes. *Inorg Chem* **44**, 4055-4065 (2005). https://doi.org:10.1021/ic049266n

4 Chen, J. *et al.* Ultrabright Fluorescent Organic Nanoparticles Based on Small-Molecule Ionic Isolation Lattices*. *Angew Chem Int Ed Engl* **60**, 9450-9458 (2021). https://doi.org:10.1002/anie.202100950

5 Liu, X. J. *et al.* A Theoretical Investigation of Substituent Effects on the Absorption and Emission Properties of a Series of Terpyridylplatinum(II) Acetylide Complexes. *European Journal of Inorganic Chemistry* **2005**, 1856-1866 (2005). https://doi.org:10.1002/ejic.200400533

6 Lam, W. H., Lam, E. S. & Yam, V. W. Computational studies on the excited states of luminescent platinum(II) alkynyl systems of tridentate pincer ligands in radiative and nonradiative processes. *J Am Chem Soc* **135**, 15135-15143 (2013). https://doi.org:10.1021/ja406810a

7 Shikhova, E. *et al.* Excited-State Absorption Properties of Platinum(II) Terpyridyl Acetylides. *Inorganic Chemistry* **46**, 3038-3048 (2007). https://doi.org:10.1021/ic0618652

Appendix 4-a: Manuscript of Por4-SMILES

Boosting Triplet Emission in Porphyrin-Based Supramolecular Structures of Small-Molecule Ionic Isolation Lattices

Yang Wang[1], Marko H. Nowack[1], Amar H. Flood[2], Bo W. Laursen[1*]

1. Nano-Science Center & Department of Chemistry, University of Copenhagen, Universitetsparken 5, 2100 Copenhagen, Denmark

2. Department of Chemistry, Indiana University, 800 E. Kirkwood Ave, Bloomington, IN 47405, USA.

ABSTRACT: Combining red emission with extended lifetimes is crucial for improving chromophores used in bioimaging. We used a technique called Small-Molecule Ionic Isolation Lattices (SMILES) to create porphyrin-based emitters (Por4-SMILES) with better photophysical properties than those in solution. Por4-SMILES emits light at a new red-shifted wavelength of 690 nm, with quantum yields (1%) and the decay lifetime in the range of milliseconds.Comparing Por4-SMILES to the original Por4 under cryogenic conditions, the effectiveness of SMILES in restoring chromophores' light emission at room temperature is highlighted. This comparison also suggests a breakthrough with SMILES nanoparticles, offering longer-lasting phosphorescent emissions. These findings support our belief in SMILES' ability to enhance chromophores' phosphorescence properties, promising advancements in bioimaging applications.

1 Introduction

In the realm of bioimaging, biomarkers emitting light in the red to near-infrared (NIR) region hold promise due to their ability to minimize intrinsic luminescence from biological matrices. [1-4] Innovations like fluorescence lifetime imaging microscopy (FLIM) [5-7], which uses fluorescent lifetime as the sequencing channel instead of photon energy (wavelength), open new avenues for bioimaging by employing long-lived luminescent chromophores. The combination of red emission and long lifetime further enhances their practicality and desirability.

Building on preliminary success in reinstating/promoting phosphorescence in Pt3-SMILES (small-molecule ionic isolation lattices), [8-12] we aimed to explore phosphorescent SMILES systems capable of emitting in the red to NIR region with longer lifetimes reaching milliseconds. Our selection criteria for guest chromophores included compatibility with the SMILES

strategy, necessitating cationic and planar properties. Ultimately, we chose Palladium(III)–5,10,15,20–(Tetra-N-methyl-4-pyridyl) porphyrin, abbreviated as Por4.

Por4 has previously been investigated as a biosensor for detecting intermolecular interaction processes involving bio-based macromolecules such as DNA, peptides, and proteins. [13-16] While Por4 exhibits mixed fluorescence and phosphorescence, the triplet emission is typically weak. Encapsulation by macromolecules or oligomers has been shown to strengthen Por4's phosphorescence band, [17-19] but less attention has been paid to regulating its photophysical properties without chemical modification of its scaffold. Potential energy- and electron-transfer processes involving Por4 analogs bound to DNA suggest important impacts on Por4 emission from intermolecular interactions. [13] Based on these backgrounds, we propose that the strong cofacial stacking effect exerted by SMILES has the potential to enhance Por4's phosphorescence, facilitating the fabrication of long-lived red emissive chromophores, ultimately emerging as Por4-SMILES nanoparticles.

In contrast to Por4's weak phosphorescence with a short lifetime in solution state, Por4-SMILES solids and nanoparticles emit a new red-shifted band at 690 nm accompanied by millisecond lifetimes (1.36 ms for Por4-SMILES crystal and 0.3 ms for Por4-SMILES nanoparticles). This new phosphorescent band can also be observed by measuring Por4 at cryogenic conditions, indicating the effective impact of SMILES on reinstating Por4's intrinsic phosphorescence at room temperature. Detailed photophysical analysis suggests that the confinement of non-radiative pathways (T1-S0) is the main reason contributing to the boosted triplet emission in Por4-SMILES. Overall, this exploration of Por4-SMILES demonstrates the effective applicability of SMILES in generating phosphorescent materials.

2 Results and Discussions

2.1 Basic Photophysical Properties in Solution State

2.1.1 Photophysical Properties of Por4

The photophysical properties of Por4 are revealed by steady-state absorption, emission, excitation spectra, and time-correlated characterizations of its excited state. In Figure 1, the absorption spectra of Por4 in both organic solvent MeCN and aqueous solution exhibit typical porphyrin Soret band (417 nm) and Q band (521 nm). [17, 20] Notably, the emission spectra of Por4 differ between MeCN and H_2O environments. [21, 22] In MeCN, Por4 displays four distinct emission peaks (570 nm, 620 nm, 650 nm, and 720 nm), while in H_2O, emissions occur at 570 nm, 620 nm, and 700 nm, with discrepancies noted in the 650-750 nm range.

Decay curves reveal the coexistence of fluorescence and weak phosphorescence (Figure 1-b, c), with fluorescence lifetimes varying across emission wavelengths, ranging from <0.1 ns (approaching IRF) to 10 ns in MeCN and up to 5.2 ns in H_2O. Phosphorescence lifetimes are observed at 0.25 μs in MeCN and 1.51 μs in H_2O at λ_{em}=720 nm, as displayed in Figure S1. To confirm the origins of fluorescence and

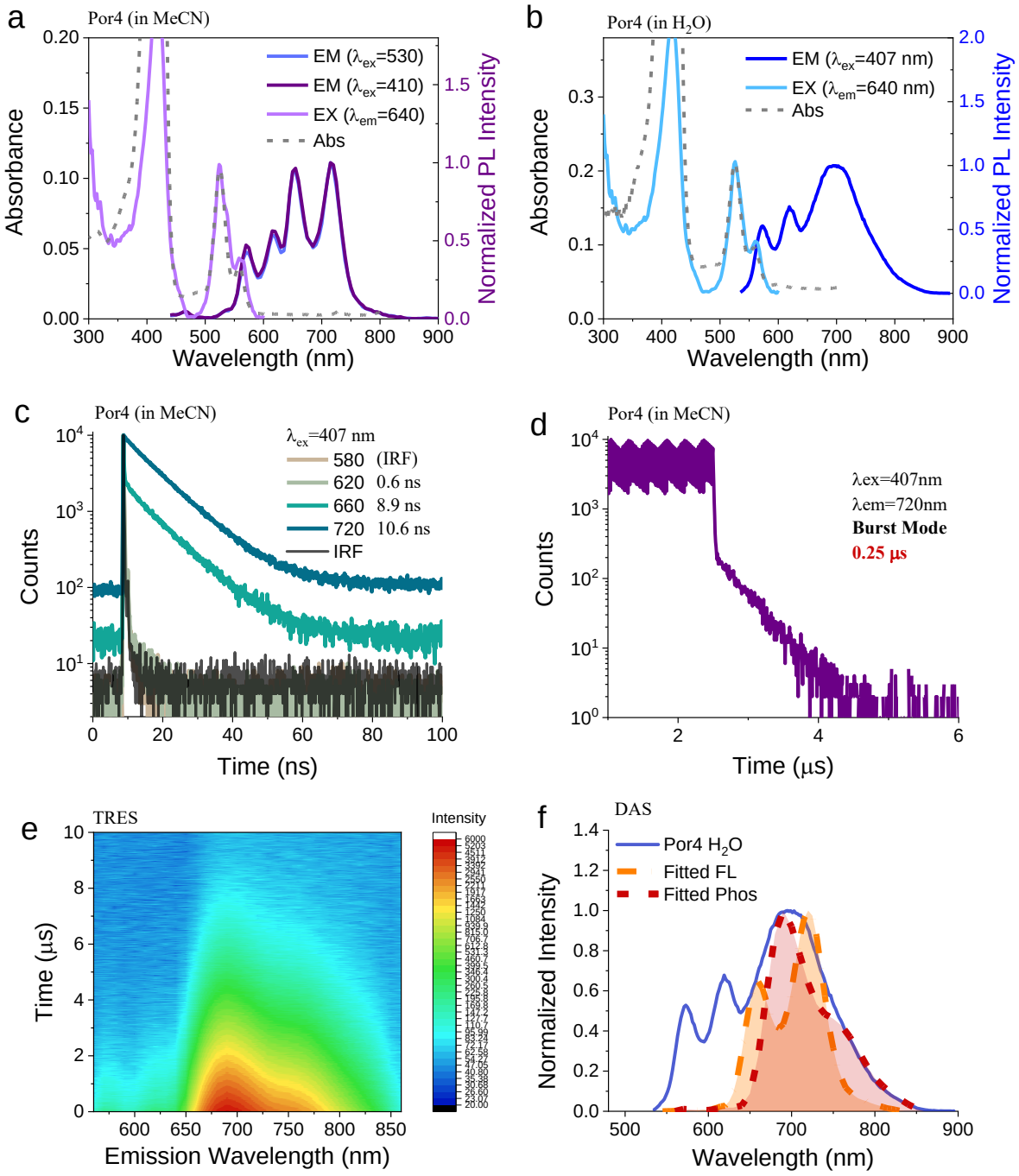

Figure 1. Photophysical properties of Por4 at an optically diluted concentration (5 μM), in MeCN and in H_2O. (a, b) Steady-state properties of absorption, emission, and excitation curves for Por4 in MeCN (a) and H_2O (b), the emission and excitation curves were normalized to the emission at 616nm. (c-d) Time-resolved decay curves for Por4 in MeCN, by using laser at λex=407nm, detections were at 570nm, 620nm, 655nm, and 720nm, separately. Burst mode was used to collect phosphorescence signals in (d). DAS (decay-associated spectra) measurements. (e) Plot of amplitudes for decay curves in the function of emission-TRES. (f) Emission curves of Por4 in H_2O (5 μM), and the fitted fluorescence and phosphorescence bands assigned to lifetime components of ~5 ns and ~1.5 μs. wavelength.

phosphorescence in Por4's emission, deoxygenation experiments were conducted for both MeCN and H_2O solutions.

As shown in Figure S2, removal of oxygen resulted in enhanced emission in the 650~800 nm range, while emission bands at 580 nm and 620 nm remained relatively unchanged. Additionally, the long decay components at λ_{em}=720 nm were prolonged, corresponding to the improved emission bands at 650-800 nm. In MeCN, Por4's long decay component extended from 0.25 μs to 2.24 μs after 30 minutes of degassing, while in H_2O, it increased from 1.5 μs to 19.8 μs within 10 minutes. The fast decay component at λ_{em}=720 nm remained constant despite degassing, indicating fluorescence, while the extended component represents phosphorescence, both with lifetimes in the microseconds range for MeCN and H_2O.

Heavy metal introduction into porphyrins enhances intersystem crossing efficiency, leading to room temperature phosphorescence. [17, 23, 24] Therein, the emission bands in the 650~850 nm range likely originate from triplet emission, with varying lifetimes in different solvents due to solvation effects and coordination forces between heavy metals and porphyrins. [15] To confirm this proposal, decay-associated spectra (DAS) were used [25] to differentiate fluorescence and phosphorescence contributions in Por4's emission, and the DAS suggest that emission bands at 570 nm and 620 nm likely have different origins than those in the 650~850 nm range.

In H_2O, DAS characterization showed overlapping emission components in the 620~850 nm range, attributed to fluorescence (~5 ns) and phosphorescence (~1.5 μs), as exhibited in Figure 1-c. However, comparing Por4's emission in MeCN to fitted fluorescence and phosphorescence bands, both emissions were present, as displayed in Figure S3. Therefore, it indicates that phosphorescence emission of Por4 is more pronounced in H_2O.

Above all, these findings provide insights into the intricate photophysical behavior of Por4 in different solvent matrices and underscore the interplay between its fluorescence and phosphorescence under different environmental conditions.

2.1.2 Bimolecular Interactions between Por4 and CS

The addition of macromolecules like CS has the potential to influence Por4's emission through alterations in the microenvironment or energy- and electron-transfer processes. [16, 26] Stern-Volmer titration experiments were conducted to investigate bimolecular interactions between CS and Por4. [27] Preliminary trials comparing Por4's photophysical properties before and after the addition of CS revealed minimal alteration in Por4's emission, with consistent absorption bands and coefficients (Figure 2-a, b). While Por4's phosphorescence lifetime slightly increased from 0.25 μs to 0.53 μs in mixed MeCN/DCM (50%/50%), as displayed in Figure S4, the fluorescence lifetime remained relatively unchanged. Addition of eight equivalents of CS did not significantly affect Por4's decay lifetime.

In Stern-Volmer experiments with low concentrations of Por4 chromophores, progressive increases in the absorption band

at 314 nm, attributed to CS, were observed, while Por4's absorption bands remained constant (Figure S5-a). The ratio of absorbance between the CS band at 314 nm and the Por4 bands exhibited a linear relationship up to a molar ratio of 10 for CS/Por4 (Figure S5-b). Despite changes in absorption spectra, Por4's emission and phosphorescent decay curves remained relatively unchanged in the presence of CS (Figure S5-c,d,e,f). These findings suggest that CS interacts dynamically with Por4, affecting its absorption properties, while leaving its emission characteristics largely unaffected.

Overall, as CS was gradually added into Por4 solutions, no significant alterations in Por4's emissivity or lifetime were observed, as evidenced by the flat Stern-Volmer plots for both intensity (I0/I) and lifetime (τ0/τ) in Figure 4.5-c and Figure 4.5-d. According to the Stern-Volmer equation:

$$I_0/I=\tau_0/\tau=1+k_q\,\tau_0\,[Q] \qquad (1)$$

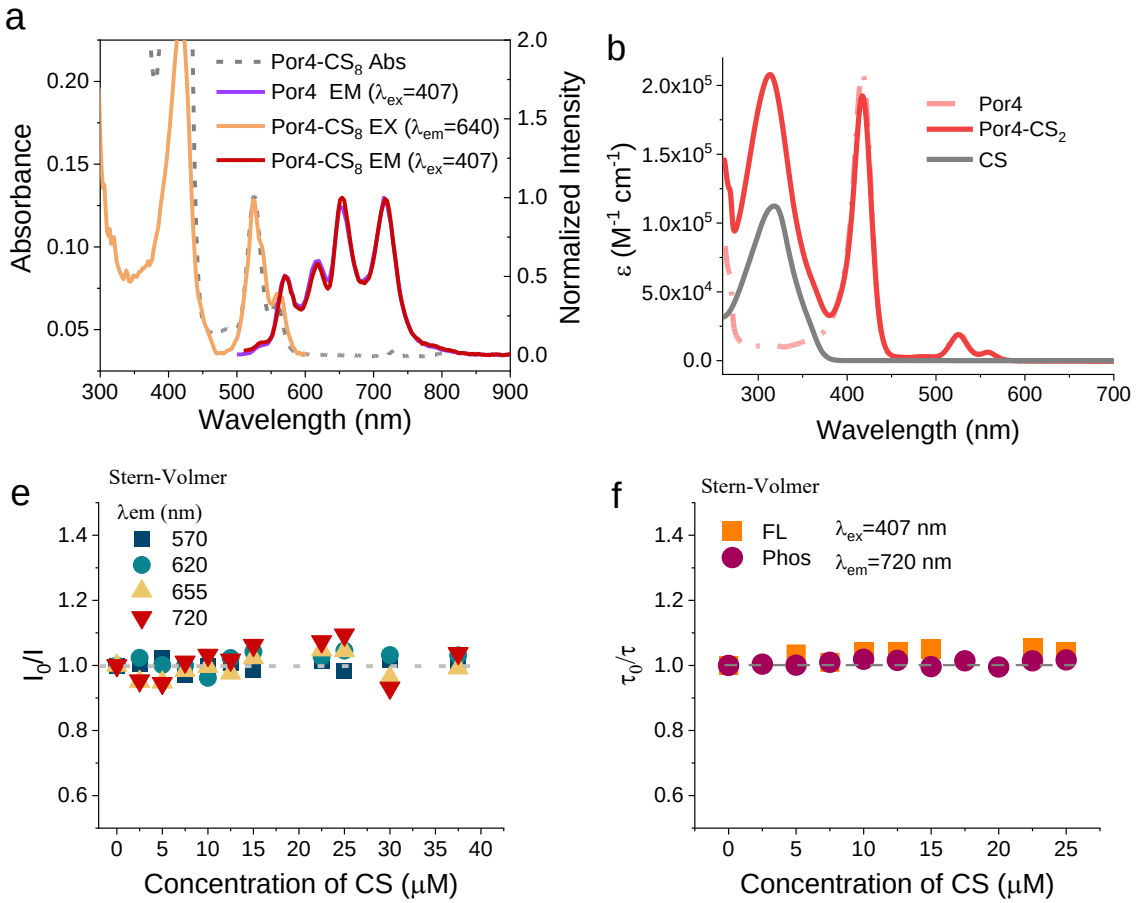

Figure 2. (a) Absorption spectra of Por4 and Por4-CS_8 in MeCN/DCM (5 μM). (b) Epsilon value of Por4, CS and Por4-CS_2. Por4-CS_2 is used to easily showcase the add-up of CS in the function of composition. (c) Decay curves of Por4-CS_8 in MeCN/DCM (5 μM), λ_{ex}=407 nm, λ_{em}=570 nm, 620 nm, 655 nm, and 720 nm, respectively. (d) Decay curves of Por4 and Por4-CS_8 in MeCN/DCM (5 μM), λ_{ex}=407 nm, λ_{em}=720 nm, burst mode was used. (e-f) Stern-Volmer plots for (f) luminescence intensity I_0/I and (f) lifetime τ_0/τ.

In which the I_0 and I refer to the luminescence intensity of chromophore (Por4) without and with the presence of quencher (CS), τ_0 and τ refer to the luminescence intensity of chromophore (Por4) without and with the presence of quencher (CS), k_q is the bimolecular quenching constant, [Q] is the concentration of quencher CS.

The flat Stern-Volmer plots in Figure 2-e and Figure 2-f indicate that $k_q = 0$, suggesting that no efficient energy transfer process occurred within the bimolecular interactions between Por4 and CS. [25]

2.2 Phosphorescence in Por4-SMILES

Following the established SMILES synthetic protocol, [10, 11] Por4-SMILES was synthesized with a molar ratio of CS/Por4=10 to ensure tetra-cationic charge balance. The process involved placing a concentrated mixture of CS and Por4 in MeCN/DCM (50%/50%) solvent in the dark until crystals formed and gradually grew in size. Por4-SMILES nanoparticles were then prepared by adding amphiphilic polymer DSPE-PEG2000, constituting 60wt% of the mixture. After thorough evaporation, the solution was

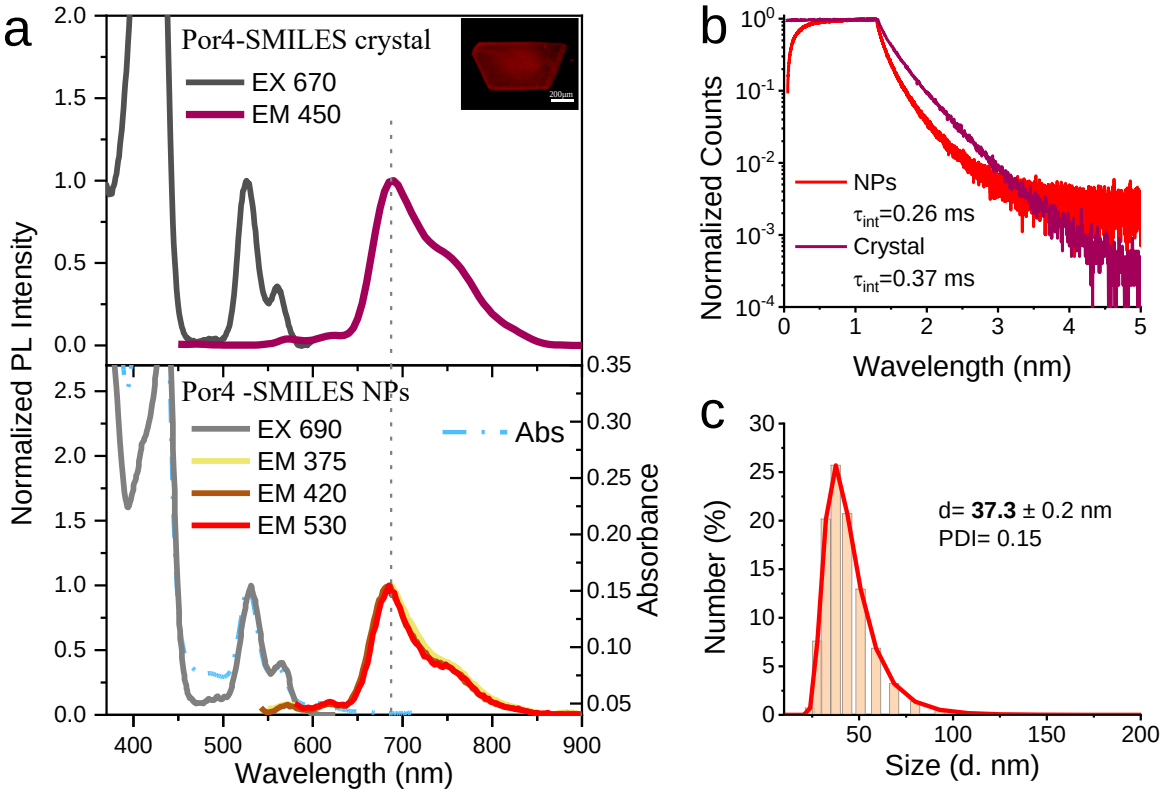

Figure 3. (a) Steady state photophysical properties of Por4-SMILES crystal and Por4-SMILES NPs. The number after EM is the wavelength used for illumination, and the number after EX is the wavelength being detected. Inserted picture is the fluorescence micrograph of Por4-SMILES crystal under microscope, scale bar is 200 μm. (b) Decay curves of Por4-SMILES crystal and Por4-SMILES NPs, excitation wavelength was 450nm, detector emission wavelength was 700nm. (c) Dynamic light scattering measurements of Por4-SMILES NPs, number-averaged size distribution is presented. PDI is the poly-distribution index.

re-dissolved in THF and injected into milli-Q water under ultrasonication.

Photophysical properties of Por4-SMILES crystals and nanoparticles were characterized in Figure 3. Unlike weak phosphorescence emission in MeCN or H_2O, both Por4-SMILES crystals and nanoparticles exhibited identical phosphorescence bands at 690 nm, resembling the phosphorescence component in DAS characterizations (Figure 1-f). The emission shapes remained constant regardless of the illumination wavelength, indicating consistent emission for Por4-SMILES (Figure 3-a).

Importantly, the phosphorescence lifetimes for Por4-SMILES crystal (0.37 ms) and Por4-SMILES nanoparticles (0.26 ms) were significantly prolonged compared to Por4's lifetimes in solution states (in MeCN: 0.25 μs, in H_2O: 1.51 μs), with quantum yields also enhanced (from 0.03% to 0.96% for nanoparticles and 1.20% for crystals). Such enhancements were not observed even with deoxygenation in Por4 solutions, attributing the improvement to the unique SMILES stacking structure, which confines Por4's rotational flexibility and prevents attacks from singlet oxygen.

Attempts to characterize the crystal structure were unsuccessful due to weak signals and lattice unit disorders. Stoichiometry between CS and Por4 within the Por4-SMILES crystal phase was elucidated by re-dissolving crystals into organic solvents and matching absorbance ratios against a standardized titration plot (Figure S6-a, b), revealing a molar composition with CS accounting for 88%. This corresponds to a molar ratio of CS/Por4=7.33, close to the expected ratio of 8, supporting the proposed structure of Por4$[CS_2PF_6]_4$. Comparatively, the emitted phosphorescence in Por4 aligns with the deconvoluted phosphorescent component observed in DAS characterization, consistent with the structure of Por4-SMILES.

In comparison to Por4 neat aggregates, Por4-SMILES crystals exhibit a remarkable enhancement in phosphorescence emission, with a quantum yield (QY) of 1.2% (compared to 0.03% for Por4 in MeCN), despite Por4 powders showing a longer lifetime component averaging 0.2 ms but with extremely weak emissivity (Figure S6-c, d). This enhancement in phosphorescence emission in Por4-SMILES crystals suggests a substantial improvement in Por4 triplet emission, rather than a dimerization effect. Moreover, Por4-SMILES nanoparticles, with a size distribution centered around 37 nm (Figure 3-c), demonstrate excellent stability during long-term storage, retaining their phosphorescence after two months (Figure S6-e,f), indicating the reliability and efficiency of the synthetic method employed. Given the distinct long-lived red emission observed in Por4-SMILES compared to Por4 in solution state or neat aggregates, further elucidation of the photophysical properties is essential to fully comprehend the origins of this desired emission for the potential utilization of Por4-SMILES in various applications, particularly in bio-imaging.

2.3 Explorations on the Enhanced Triplet Emission

2.3.1 Intrinsic Triplet Emission of Por4

To comprehend the mechanisms underlying the enhanced phosphorescence observed in Por4-SMILES, which contrasts with the weak phosphorescence exhibited by Por4 in solution, it is important to first establish a comprehensive understanding of Por4's intrinsic photophysical properties, particularly its triplet excited state. [25, 28, 29] Cryogenic conditions were employed to effectively depopulate Por4's triplet excited state, minimizing thermal decay and approximating the intrinsic triplet emission. Cryogenic cooling to 77K induced intense phosphorescence in Por4, characterized by emission bands at 670 nm and 742 nm (Figure 4-a, f), alongside a notably prolonged lifetime of 1.36 ms (Figure 4-b). The excitation curve closely resembled those observed in room temperature solutions and Por4-SMILES (Figure 4-d,e,f). This extended decay under cryogenic conditions, indicative of triplet excitons with lifetimes reaching up to 1.36 ms, contrasts sharply with previous reports on Por4, which lacked

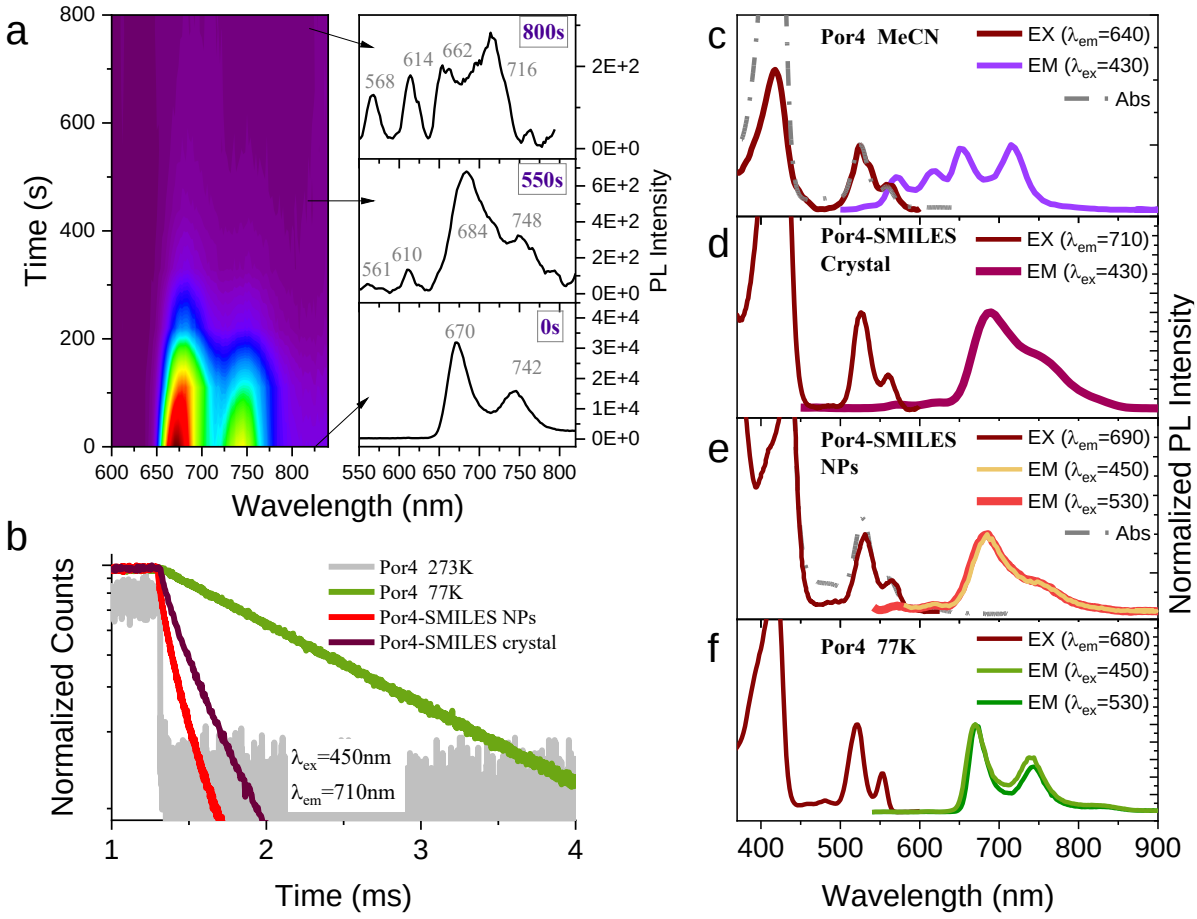

Figure 4. (a) Time correlated emission spectra of Por4 in MeCN/PG (10/90 vol%) in a freeze-thaw experiment transiting from 77K to 273K, and selected emission curves at specific moments (0s, 550s, 800s upon melting). (b) Decay curves of Por4 and Por4-SMILES at different conditions, the excitation wavelength was 450nm, detector was set at 710nm. Burst mode was used to collected the long-lived photons. (c-f) Comparisons of steady state photophysical properties of Por4 and Por4-SMILES in different conditions.

comprehensive investigations under such conditions.

Upon thawing the frozen matrix subsequent to cryogenic cooling, a rapid decline in phosphorescence intensity ensued, with emission bands at 670 nm and 742 nm gradually converging into a primary peak at approximately 690 nm. Eventually, phosphorescent emission diminished to levels comparable to the relatively stable fluorescence emission bands at 568 nm and 614 nm, unaffected by temperature alterations (Figure 4-a). This intensity decrease in phosphorescence emission coincided with a rapid decline in lifetime, decreasing from 1.39 ms at 77K to 1.79 μs at around 273K (Figure 4-b). Conversely, fluorescence decay remained consistently short and stable. The pronounced changes in phosphorescence emission from 77K to 273K suggest a high sensitivity of Por4's phosphorescence to environmental fluctuations, contrasting with the stability of fluorescence.

Interestingly, when correlating the freeze-thaw experiment with comparisons of Por4's optical performances under different conditions (MeCN solution, SMILES, and frozen PG), Por4-SMILES exhibited an intermediate phase resembling the freeze-thaw transition of Por4. This intermediate phase features strong phosphorescent emission with a maximum at 690 nm and lifetimes ranging from 1.79 μs to 1.39 ms. The similarity between the SMILES effect and cryogenic conditions in reinforcing Por4's triplet emission suggests that rigidified matrices resulting from densely stacked structures in SMILES and restricted molecular motion in the frozen state are key factors contributing to the enhanced Por4 phosphorescence. These observations elucidate the phenomenon of increased phosphorescence emission in previous studies, where encapsulation of Por4 by

Table 1. Photophysical properties of Por4 solutions and Por4-SMILES samples

Sample		λ_{em} (nm)	τ (λ_{em}=720 nm)	
			FL	Phos
Por4 (MeCN)	Before degass	570, 616, 652, 716	10.6 ns	0.25 μs
	After degass	568, 614, 715	10.4 ns	2.24 μs
Por4 (H_2O)	Before Degass	573, 621, 691	5.2 ns	1.51 μs
	After Degass	573, 621, 697	5.1 ns	19.80 μs
Por4 (PG/MeCN)	273K	570, 616, 652, 716	IRF	1.79 μs
	77K	670, 742	IRF	1.39 ms
Por4 SMILES Crystal		692	IRF	0.37 ms
Por4 SMILES NPs	Before Degass	694	IRF	0.30 ms
	After Degass	696	IRF	0.46 ms

*Absolute QY. Por4(MeCN): 0.03%, Por4 SMILES NPs before degass: 0.96%, Por4 SMILES crystal: 1.2%.

macromolecules such as DNA and peptides generated spatial confinement, restricting Por4's rotational freedom and solvent molecule access.

2.3.2 Analysis on Deactivation Pathways

The investigation into Por4-SMILES phosphorescence delved into the intricacies of its triplet excited state deactivation processes, as depicted in the Jablonski diagram (Figure 5-a). Upon photoexcitation, electrons can undergo various deactivation pathways, including fluorescence emission and intersystem crossing to the triplet excited state, followed by phosphorescence emission. Competitive non-radiative processes such as molecular vibration, quenching by oxygen, and bimolecular interactions with CS also affect the overall deactivation kinetics. While Por4 fluorescence arises from spontaneous emission, its phosphorescence involves a complex interplay of factors influenced by external conditions, with fluorescence proving less sensitive to environmental changes, as indicated in the following equations [25, 30]:

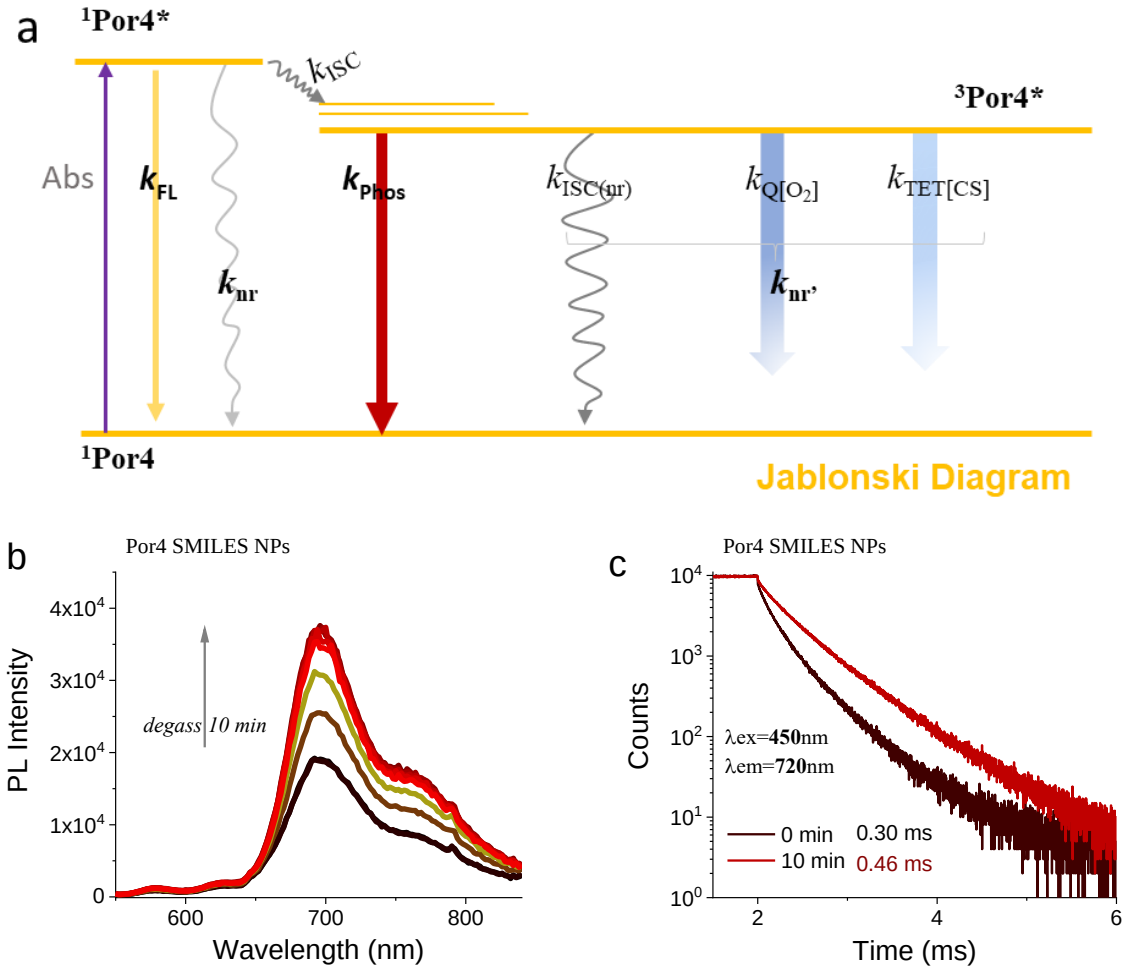

Figure 5. (a) Scheme of Jablonski energy diagram for Por4 photoexcitation processes. Degassing experiments for Por4-SMILES NPs for 10 minutes: (b) emission spectra, λ_{ex}=407nm. (c) Decay curves, λ_{ex}=450 nm, λ_{em}=720nm, burst mode was used.

$$\tau_{Fl} = \frac{1}{k_{Fl}+k_{nr}} \quad (2)$$

$$\tau_{Phos} = \frac{1}{k_{Phos}+k_{ISC(nr)}+k_{TET}+k_{Q(O_2)}} \quad (3)$$

where $k_{ISC(nr)}$ refers to the rate constant of intersystem crossing process from triplet excited state to ground state via Por4 molecular vibration, which dissipates exciton's energy. $k_{Q(O2)}$ refers to the rate constant of excitons quenched by O_2. And k_{TET} refers to triplet energy transfer rate constant induced by bimolecular interactions with CS.

Stern-Volmer titration experiments suggested that triplet energy transfer between Por4 and CS is unlikely, ruling out the factor of k_{TET}. Instead, the dominant non-radiative pathways influencing Por4 and Por4-SMILES phosphorescence are $k_{ISC(nr)}$ and $k_{Q(O2)}$. Deoxygenation experiments only marginally improved Por4 lifetime, as suggested by Figure 5-c,d and Table 1. Therefore, the impact of rigidified matrices in reducing $k_{ISC(nr)}$ with SMILES or cryogenic conditions is significantly highlighted, which leads to the two orders of magnitude enhancement of phosphorescence lifetime. Consequently, $k_{Q(O2)}$ is deemed less influential compared to $k_{ISC(nr)}$ in the overall non-radiative pathways. Ultimately, the effective enhancement of Por4 phosphorescence by SMILES is attributed to the spatial confinement of chromophores' rotational freedom and reduction of non-radiative pathways. The relocation of metalloporphyrin into a hydrophobic microenvironment near CS crucially restricts rotational and vibrational freedom, circumventing non-radiative decay pathways. Additionally, complexation with CS isolates the metalloporphyrin from external quenchers like solvent and oxygen, further enhancing its triplet emission.

3 Conclusion

This chapter showcases the successful assembly of tetracationic metalloporphyrin (Por4) into densely packed SMILES structures, resulting in a significant enhancement of Por4's phosphorescent emission, with lifetimes extending into the millisecond range. Specifically, we achieved Por4-SMILES crystal (λ_{em}=690 nm, τ=0.37 ms, Φ=1.2%) and Por4-SMILES nanoparticles (λ_{em}=690 nm, τ=0.30 ms, Φ=0.96%), marking a notable advancement in achieving long-lived red emission, albeit under cryogenic conditions.

Our investigations into Por4's intrinsic photophysical properties and its interactions with CS revealed valuable insights. We found that the enhanced phosphorescence in SMILES primarily stemmed from effective confinement of triplet exciton nonradiative deactivations, likely due to the reduction of Por4's conformational flexibilities within the SMILES stacking structures.

The discovery of Por4-SMILES represents an efficient method for enhancing phosphorescence without the need for complex chromophore modifications. Furthermore, it offers a practical avenue for incorporating ultralong decay luminescence into densely packed supramolecular systems, addressing the growing demand for longer lifetime detection in bioimaging applications.

AUTHOR INFORMATION

Corresponding Author

* Bo W. Laursen : bwl@chem.ku.dk

Conflicts of Interest

No conflicts to declare.

Author Contributions

The Por4 complex were synthesized by Marko H Nowack. Yang Wang conducted all other experiments including synthesis of SMILES crystals and titration experiments, spectroscopic measurements, data analysis, manuscript draft and editing. Bo W. Laursen contribute to conceptualization and supervision, Amar H. Flood contribute to the manuscript correction.

The manuscript was written through contributions of all authors. All authors have given approval to the final version of the manuscript.

ACKNOWLEDGMENT

YW appreciates the funding from the European Union's Horizon 2020 research and TALENT doctoral programme under the Marie Skłodowska-Curie grant agreement No 801199. AHF thanks the National Science Foundation for support (NSF-2118423). YW appreciates the characterization help technician Niels Vissing Holst.

REFERENCES

[1] K. Y. Zhang, Q. Yu, H. Wei, S. Liu, Q. Zhao, *Long-Lived Emissive Probes for Time-Resolved Photoluminescence Bioimaging and Biosensing*. *Chem Rev*. **2018**, 118, 1770-1839.

[2] L. Kacenauskaite, D. Gabrielaitis, N. Baerentsen, K. L. Martinez, T. Vosch, *Intrinsic anti-Stokes emission in living HeLa cells*. *PLoS One*. **2020**, 15, e0230441.

[3] C. Werner, M. Sauer, C. Geis, *Super-resolving Microscopy in Neuroscience*. *Chem Rev*. **2021**, 121, 11971-12015.

[4] A. Barbieri, E. Bandini, F. Monti, V. K. Praveen, N. Armaroli, *The Rise of Near-Infrared Emitters: Organic Dyes, Porphyrinoids, and Transition Metal Complexes*. *Top Curr Chem (Cham)*. **2016**, 374, 47.

[5] B. W. Laursen, S. A. Bogh, T. J. Sorensen, *Long fluorescence lifetime triangulenium dyes in imaging and fluorescence polarization assay*. *Methods Enzymol*. **2020**, 640, 249-265.

[6] R. Datta, T. M. Heaster, J. T. Sharick, A. A. Gillette, M. C. Skala, *Fluorescence lifetime imaging microscopy: fundamentals and advances in instrumentation, analysis, and applications*. *J Biomed Opt*. **2020**, 25, 1-43.

[7] M. Rosenberg, K. R. Rostgaard, Z. Liao, A. O. Madsen, K. L. Martinez, *Design, synthesis, and time-gated cell imaging of carbon-bridged triangulenium dyes with long fluorescence lifetime and red emission*. *Chem Sci*. **2018**, 9, 3122-3130.

[8] S. Lee, C. H. Chen, A. H. Flood, *A pentagonal cyanostar macrocycle with cyanostilbene CH donors binds anions and forms dialkylphosphate [3]rotaxanes*. *Nat Chem*. **2013**, 5, 704-710.

[9] C. R. Benson, L. Kacenauskaite, K. L. VanDenburgh, W. Zhao, B. Qiao, *Plug-and-Play Optical Materials from Fluorescent Dyes and Macrocycles*. *Chem*. **2020**, 6, 1978-1997.

[10] J. Chen, S. M. A. Fateminia, L. Kacenauskaite, N. Baerentsen, S. Gronfeldt Stenspil, *Ultrabright Fluorescent Organic Nanoparticles Based on Small-Molecule Ionic Isolation Lattices*. *Angew Chem Int Ed Engl*. **2021**, 60, 9450-9458.

[11] J. Chen, S. G. Stenspil, S. Kaziannis, L. Kacenauskaite, N. Lenngren, *Quantitative Energy Transfer in Organic Nanoparticles Based on Small-Molecule Ionic Isolation Lattices for UV Light Harvesting*. *ACS Applied Nano Materials*. **2022**, 5, 13887-13893.

[12] L. Kacenauskaite, S. G. Stenspil, A. H. Olsson, A. H. Flood, B. W. Laursen, *Universal Concept for Bright, Organic, Solid-State Emitters horizontal line Doping of Small-Molecule Ionic Isolation Lattices with FRET Acceptors*. *J Am Chem Soc*. **2022**, 144, 19981-19989.

[13] A. M. Brun, A. Harriman, *Energy- and Electron-Transfer Processes Involving Palladium Porphyrins Bound to DNA*. *Journal of the American Chemical Society*. **1994**, 116, 10383-10393.

[14] M. Aoudia, M. A. J. Rodgers, *Photoprocesses in Self-Assembled*

Complexes of Oligopeptides with Metalloporphyrins. *Journal of the American Chemical Society*. **1997**, 119, 12859-12868.

[15] E. Nyarko, N. Hanada, A. Habib, M. Tabata, *Fluorescence and phosphorescence spectra of Au(III), Pt(II) and Pd(II) porphyrins with DNA at room temperature*. *Inorganica Chimica Acta*. **2004**, 357, 739-745.

[16] P. M. Keane, J. M. Kelly, *Ground and excited state interactions of metalloporphyrin PtTMPyP4 with polynucleotides [poly(dG-dC)]2 and [poly(dA-dT)]2*. *Photochem Photobiol Sci*. **2016**, 15, 980-987.

[17] C. I. V. Ramos, A. R. Monteiro, N. M. M. Moura, M. A. F. Faustino, T. Trindade, *The Interactions of H(2)TMPyP, Analogues and Its Metal Complexes with DNA G-Quadruplexes-An Overview*. *Biomolecules*. **2021**, 11.

[18] N. C. Sabharwal, O. Mendoza, J. M. Nicoludis, T. Ruan, J. L. Mergny, *Investigation of the interactions between Pt(II) and Pd(II) derivatives of 5,10,15,20-tetrakis (N-methyl-4-pyridyl) porphyrin and G-quadruplex DNA*. *J Biol Inorg Chem*. **2016**, 21, 227-239.

[19] T. Biver, S. Aydinoglu, D. Greco, F. Macii, *Mechanistic details on Pd(II)/5,10,15,20-tetrakis(1-methyl-4-pyridyl)porphyrin complex formation and reactivity in the presence of DNA*. *Monatshefte für Chemie - Chemical Monthly*. **2017**, 149, 175-183.

[20] M. Taniguchi, J. S. Lindsey, D. F. Bocian, D. Holten, *Comprehensive review of photophysical parameters (ε, Φf, τs) of tetraphenylporphyrin (H2TPP) and zinc tetraphenylporphyrin (ZnTPP) – Critical benchmark molecules in photochemistry and photosynthesis*. *Journal of Photochemistry and Photobiology C: Photochemistry Reviews*. **2021**, 46.

[21] N. M. Barbosa Neto, D. S. Correa, L. De Boni, G. G. Parra, L. Misoguti, *Excited states absorption spectra of porphyrins – Solvent effects*. *Chemical Physics Letters*. **2013**, 587, 118-123.

[22] K. Kano, K. Fukuda, H. Wakami, R. Nishiyabu, R. F. Pasternack, *Factors Influencing Self-Aggregation Tendencies of Cationic Porphyrins in Aqueous Solution*. *Journal of the American Chemical Society*. **2000**, 122, 7494-7502.

[23] J. M. S. Lopes, R. N. Sampaio, A. S. Ito, A. A. Batista, A. E. H. Machado, *Evolution of electronic and vibronic transitions in metal(II) meso-tetra(4-pyridyl)porphyrins*. *Spectrochim Acta A Mol Biomol Spectrosc*. **2019**, 215, 327-333.

[24] D. B. Papkovsky, T. C. O'Riordan, *Emerging applications of phosphorescent metalloporphyrins*. *J Fluoresc*. **2005**, 15, 569-584.

[25] J. R. Lakowicz, *Principles of Fluorescence Spectroscopy*. (2006).

[26] H. M. Anula, E. Myshkin, A. Guliaev, C. Luman, E. O. Danilov, *Photo processes on self-associated cationic porphyrins and plastocyanin complexes 1. Ligation of plastocyanin tyrosine 83 onto metalloporphyrins and electron-transfer fluorescence quenching*. *J Phys Chem A*. **2006**, 110, 2545-2559.

[27] M. H. Gehlen, *The centenary of the Stern-Volmer equation of fluorescence quenching: From the single line plot to the SV quenching map*. *Journal of Photochemistry and Photobiology C: Photochemistry Reviews*. **2020**, 42.

[28] M. A. El-Sayed, *Triplet state. Its radiative and nonradiative properties*. *Accounts of Chemical Research*. **1967**, 1, 8-16.

[29] H. Zhao, L. Zang, Q. Liu, B. Ma, M. Kou, *Enhancement of the room temperature phosphorescence of metalloporphyrins using imidazole as a triplet state protector*. *Journal of Luminescence*. **2018**, 194, 29-32.

[30] B. Valeur, M. N. Berberan - Santos, *Molecular Fluorescence*. (2012).

Appendix 4-b: Manuscript SI of Por4-SMILES

Supporting Information

Boosting Triplet Emission in Porphyrin-Based Supramolecular Structures of *Small-Molecule Ionic Isolation Lattices*

Yang Wang[1], Marko H. Nowack[1], Amar H. Flood[2], Bo W. Laursen[1]*

1. Nano-Science Center & Department of Chemistry, University of Copenhagen, Universitetsparken 5, 2100 Copenhagen, Denmark

Yang Wang (orcid: 0000-0003-0867-2752)

Marko H. Nowack (orcid: 0000-0001-5118-1233)

Bo W. Laursen (orcid: 0000-0002-1120-3191)

2. Department of Chemistry, Indiana University, 800 E. Kirkwood Ave, Bloomington, IN 47405, USA

Amar H. Flood (orcid: 0000-0002-2764-9155)

CONTENTS

§1 Synthetic Parts

§1.1 Synthetic methods of Por4

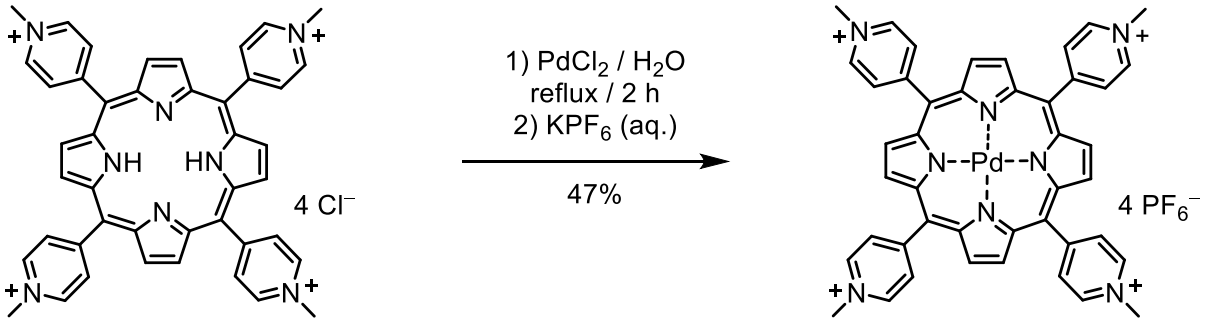

1 **2**

1 (204.0 mg, 0.248 mmol) and $PdCl_2$ (58.3 mg, 0.329 mmol) were suspended in H_2O (10 mL). The suspension was heated to reflux under N_2 for 2 h. The reaction progress was followed by UV-Vis absorption spectroscopy, as the change in the Soret band in characteristic (420 nm to 416 nm). The suspension was cooled to room temperature and filtered. The precipitate was washed with H_2O (3 × 5 mL). KPF_6 (0.2 M, 5 mL) was added to the filtrate under stirring, causing **2** to precipitate. The suspension was stirred at room temperature for 30 min and filtered. The precipitate was washed with H_2O (3 × 5 mL). The solid was eluted off the filter with MeCN and the solvent was evaporated in vacuo. The dark red solid was dried in vacuo overnight to yield **2** (158.1 mg, 0.116 mmol, 47%).

^{1}H-NMR (CD_3CN, 500 MHz): δ (ppm) = 9.07 (d, 8H, *J* = 6.2 Hz, Ar*H*), 8.97 (s, 8H, Por*H*), 8.76 (d, 8H, *J* = 6.2 Hz, 8H, Ar*H*), 4.68 (s, 12H, N^+CH_3).

^{19}F-NMR (CD_3CN, 470 MHz): δ (ppm) = −72.9 (d, J = 708 Hz, PF_6^-)

UV-Vis absorption of reaction mixture

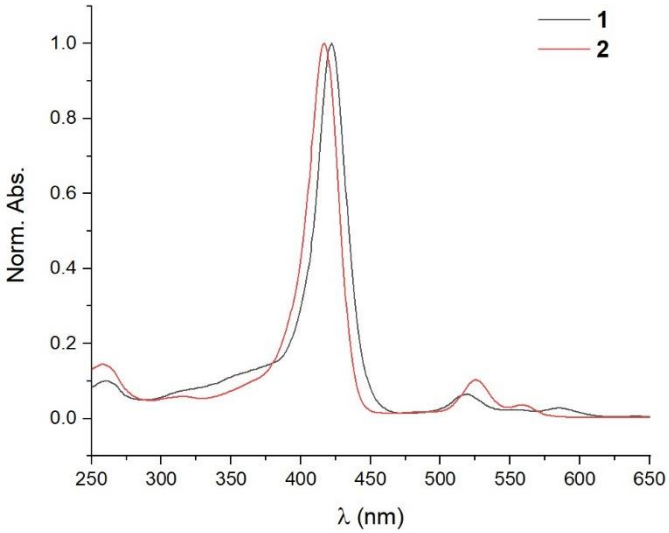

UV-Vis absorption spectra of porphyrin precursor-**1** and reactant **Por4-2**

^{1}H-NMR

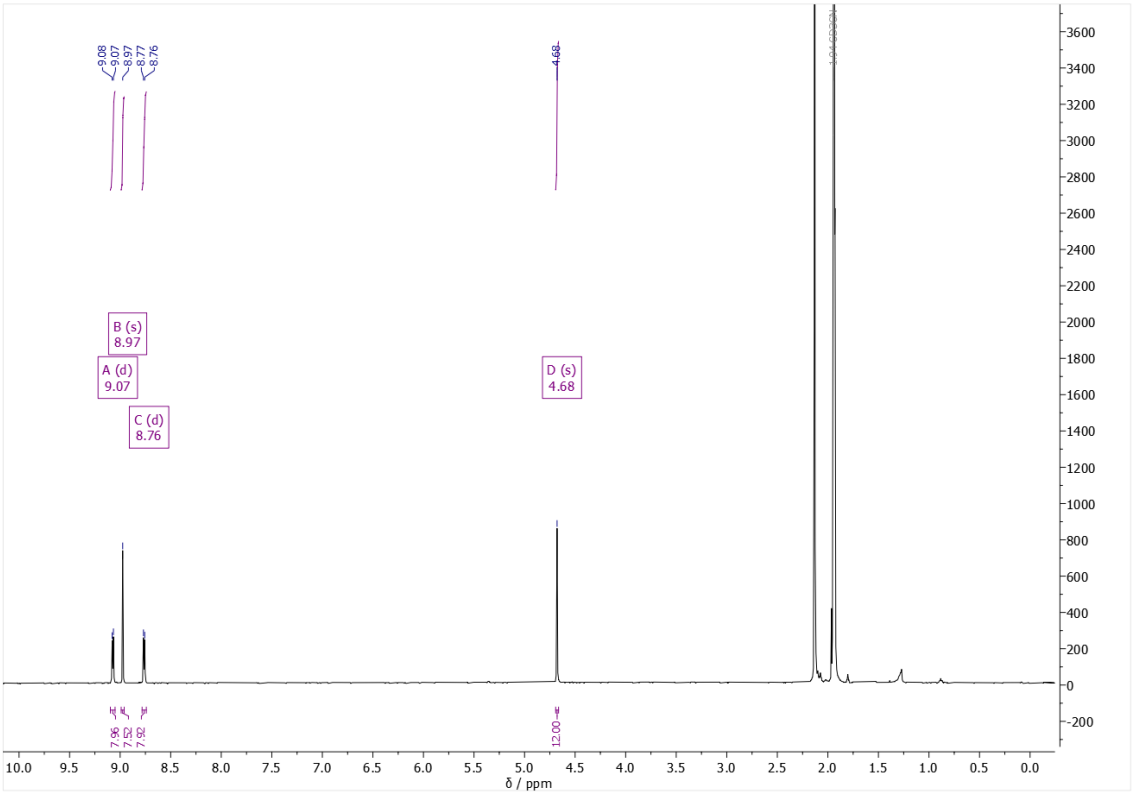

^{1}H-NMR spectra of **Por4** (500 MHz, CD_3CN-*d6*)

^{19}F-NMR

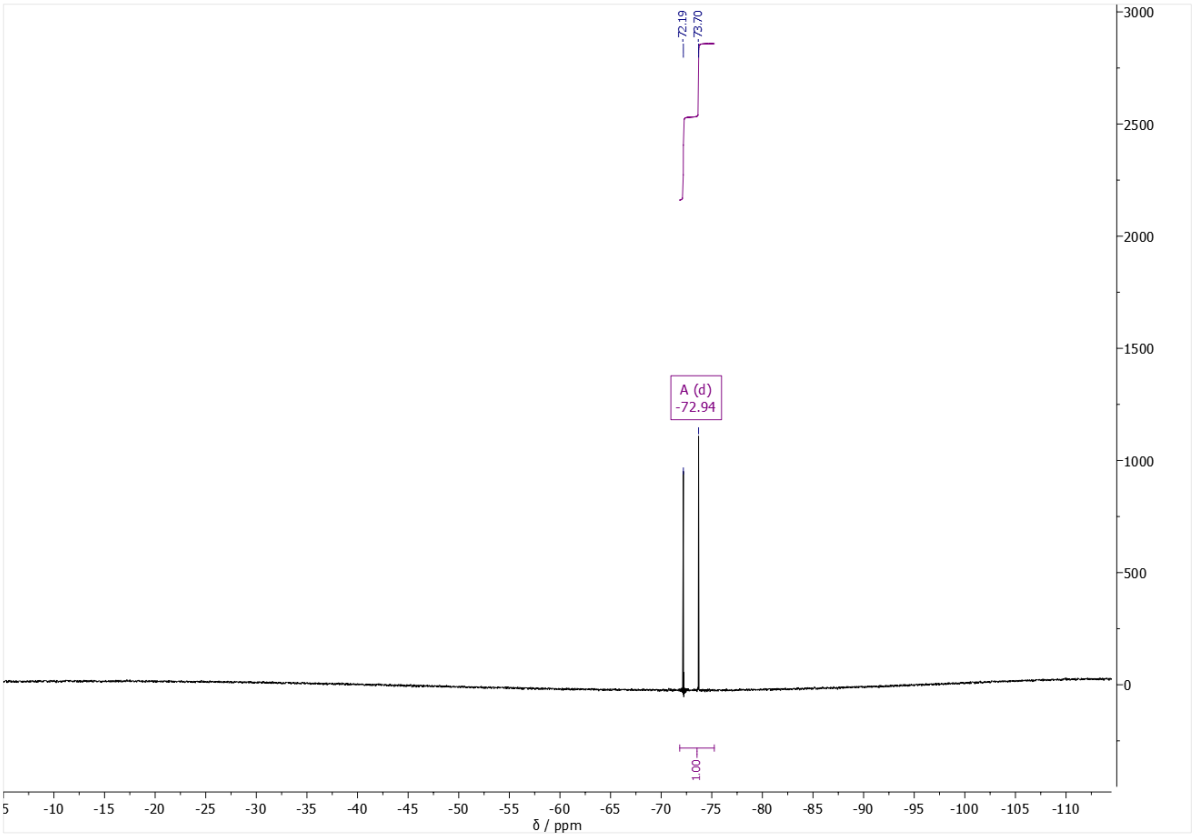

^{19}F-NMR spectra of **Por4** (500 MHz, CD_3CN-*d6*)

§1.2 Synthetic methods of SMILEs crystallines

4 mL of Por4 complex (0.5 mM, MeCN) and 10 molar equivalence of CS which is 10 mL of CS (1mM, DCM) were both filtered by hydrophobic PTFE filters (0.22μm), then mixed together in a 20 mL vial. After 10 minutes ultrasonication, the vial was placed in still until crystals emerged.

§1.3 Synthetic methods of SMILEs nanoparticles

Procedures:

1) Por4 (MeCN, 0.2 mM) and CS(THF, 1 mM) were prepared with the help of sonication and filtering (0.22 μM, hydrophobic filter). 2mL Por4 and 4 mL CS were mixed together, with the addition of 2 mL MeCN, in order to get Por4-CS_{10} precusor solution (50 μM).

2) Mixed 2 mL Por4-CS_{10} (50 μM) and 1.3 mL DSPE-PEG (1 mg/mL) together, then evaporate the solvent by using N_2 gas for slow consistent evaporation, which cost about 15 minutes, so that the temperature of solution cooled down, pinky reddish solids gradually emerged with observable red emission under 410 UV laser illumination.

3) 2 mL THF was added to dissolve the reddish solids, the solution was then injected into 10 mL distilled water, accompanied by ultrasonication for about 15 minutes.

§2 Instrumental Setups and Measurements

§2.1 Spectroscopic Methods and Instrumentation

Steady-state: UV-Vis absorption spectra were measured with a Cary 300 spectrophotometer. Corrected **photoluminescence** spectra were obtained by a PTI Instruments spectrofluorimeter. All photophysical measurements were conducted at ambient temperature, 22 ± 2 ℃. All luminescent solution samples were measured in 1 cm^2 anaerobic quartz cells.

TCSPC lifetime measurements were obtained by time-correlated single-photon counting on an PTI Instruments (FluoTime 300), the instrument response function (IRF) was collected using a dilute solution of Ludox at the detection wavelength. Reconvolution of the fluorescence decay and IRF was performed on the Edinburgh software in conjunction with lifetime fitting. Finally, the data was exported and plotted by using Origin 2020.

DLS measurements were obtained by Dynamic Light Scattering Zetasizer Pro Instrument (Malvern Panalytic).

§2.2 Stern-Volmer Quenching Experiments

*Preparation of samples for Stern-Volmer quenching experiments (Por4 at **low concentration**):*

1) Prepare Por4 (50 μM, MeCN) and CS (50 μM, DCM) solutions, then filter with hydrophobic PTFE filters (0.22 μm).

2) 200 μL of Por4 (50μM, MeCN) was mixed with different volumes of CS (50 μM, DCM), ranging from 0 μL to 3600 μL.

3) MeCN was added to adjust all the solutions in order to reach a fixed volume of 4 mL. The concentration of Por4 was set at **2.5 μM** for diluted samples, and CS concentration varied from 0 μM to 45 μM.

§2.3 Solid Sample Preparations

Solid sample preparation:

1) *Dropcast solids on glass cover*: for measurements on solids, dropcast precursor solutions or suspension of solids (in heptane) onto glass.
2) *Dissipated in viscous matrix*: for measurements on neat aggregates and crystals optical properties (especially QY and τ), viscous matrix (propylene glycol, PG) was used to disperse crystallites for measurements.

QY: All of the measured QY were collected with absolute method by using Integrating Sphere.

§3 Supporting Graphs and Tables

§3.1 Solution state

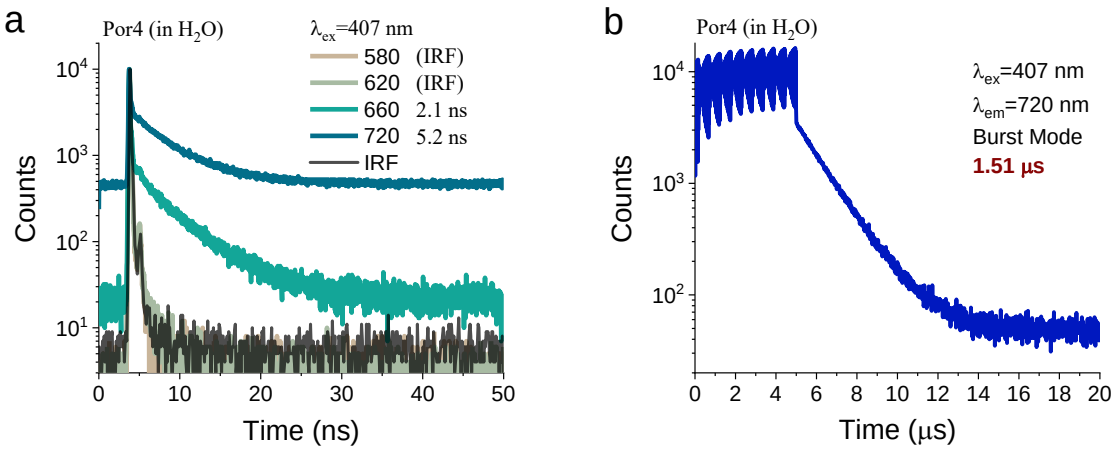

Figure S1. Photophysical properties of Por4 at an optically diluted concentration (5 µM) in H_2O. (a, b) Time-resolved decay curves for Por4 in H_2O, by using laser at λex=407nm, detectors were set at wavelengths of 570nm, 620nm, 655nm, and 720nm, separately. Burst mode was used to collect phosphorescence signals in (b).

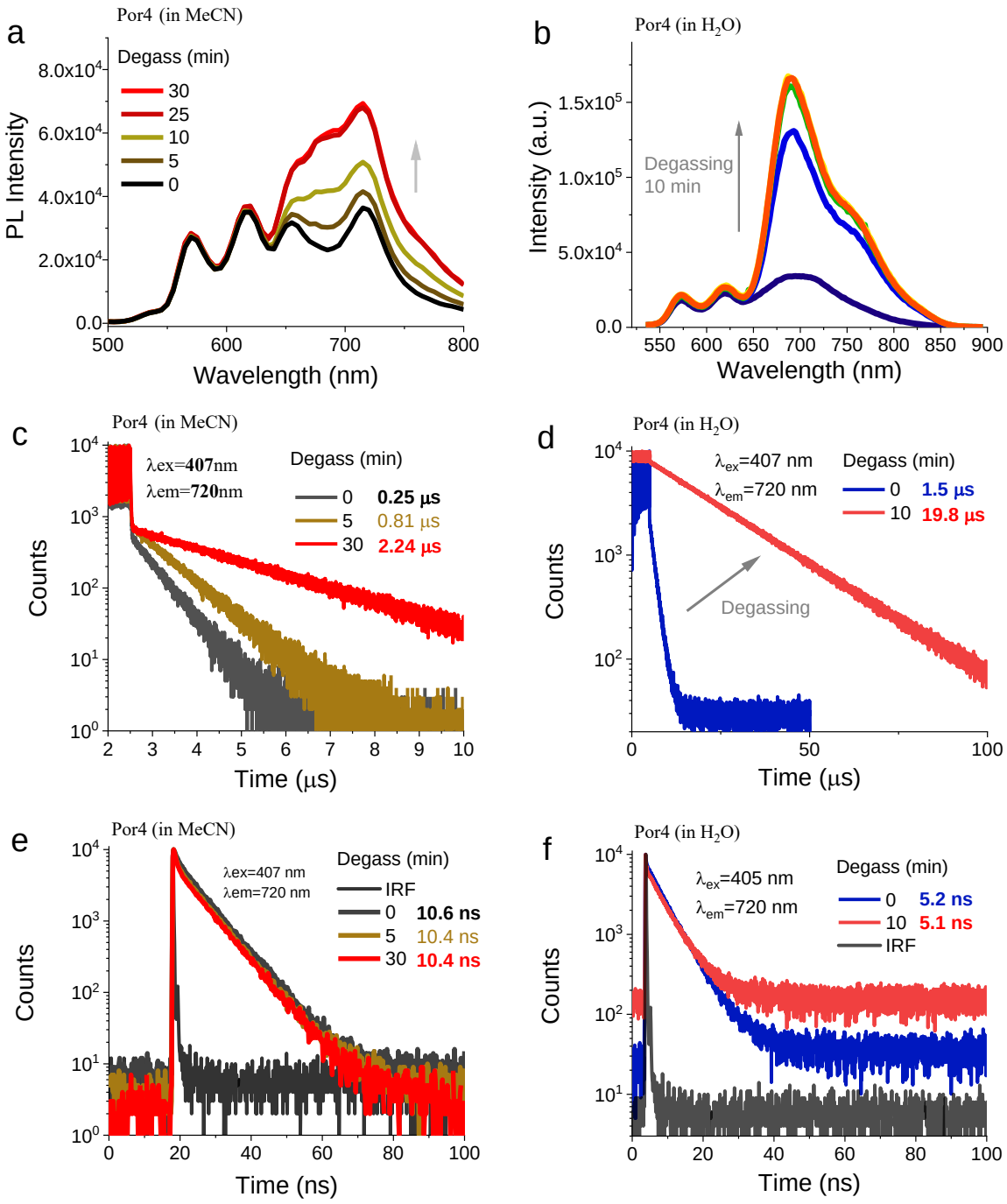

Figure S2. Deoxygenation experiments for Por4 in MeCN (5 µM) and H_2O (5 µM). (a) Emission curves for Por4 in MeCN degassed by N_2 for 30 minutes. (b) Emission curves for Por4 in H_2O were degassed by N_2 for 10 minutes. Decay curves for (c) phosphorescence and (e) fluorescence at λem=720 nm, for Por4 in MeCN degassed by N_2 for 30 minutes. Decay curves for (d) phosphorescence and (f) fluorescence at λem=720 nm, for Por4 in H_2O degassed by N_2 for 10 minutes. For all measurements, excitation was laser with λex=407 nm.

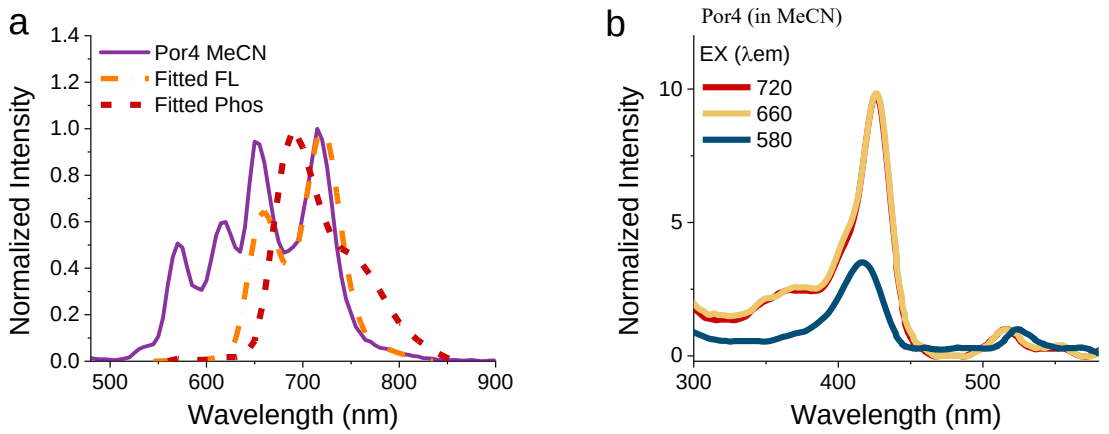

Figure S3. DAS (decay-associated spectra) measurements. (a) Comparison among the emission curve of Por4 in MeCN (5 μM), and the fitted fluorescence and phosphorescence bands. (b) Excitation curves of Por4 in MeCN, with dectors set at 580 nm, 660 nm and 720 nm.

Stern-Volmer Plot (Por4 low concentration)

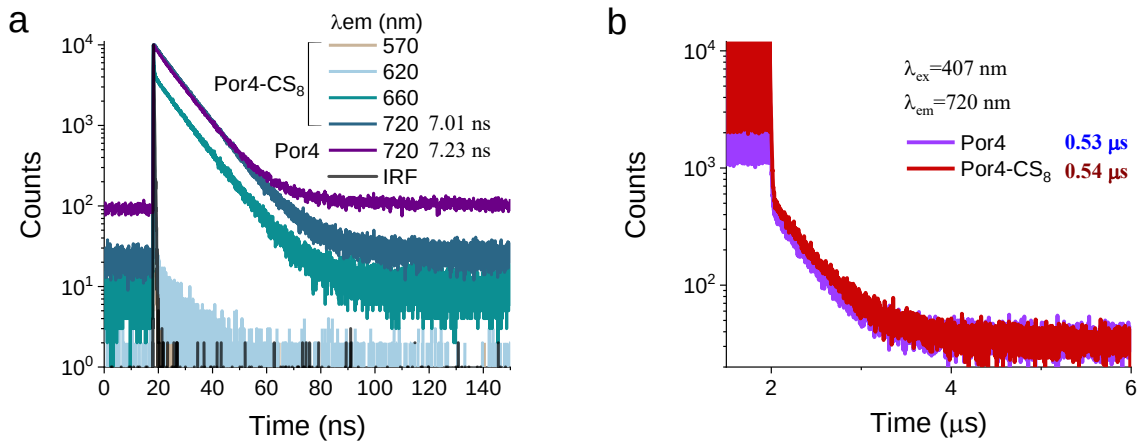

Figure S4. (a) Decay curves of Por4-CS_8 in MeCN/DCM (5 μM), λ_{ex}=407 nm, λ_{em}=570 nm, 620 nm, 655 nm, and 720 nm, respectively. (b) Decay curves of Por4 and Por4-CS_8 in MeCN/DCM (5 μM), λ_{ex}=407 nm, λ_{em}=720 nm, burst mode was used.

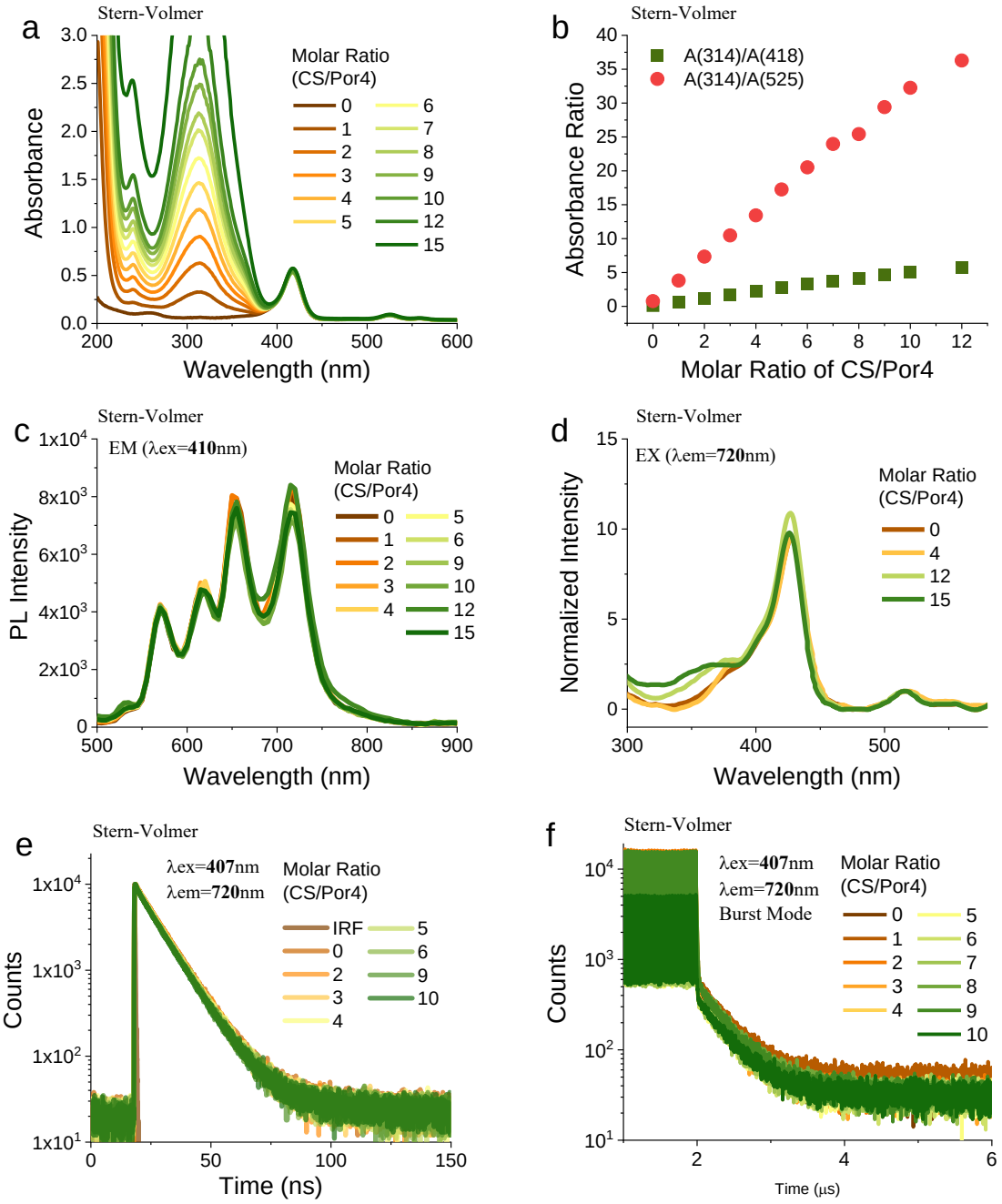

Figure S5. (a) Absorption spectra for Stern-Volmer titration between Por4 and CS. (b) Absorbance ratio between bands at 314nm and 418nm, 314nm and 525nm. (c) Emission spectra (λ_{ex}=410nm) and (a) Excitation curves (λ_{em}=720nm) for Stern-Volmer titration, all excitation curves were normalized to the band intensity at 525nm. (e,f) Decay curves for Stern-Volmer titration, λ_{ex}=450nm for both types of measurements, (e) for fluorescence and (d) for phosphorescence by using burst mode.

§3.2 Por4-SMILES crystalline and nanoparticles

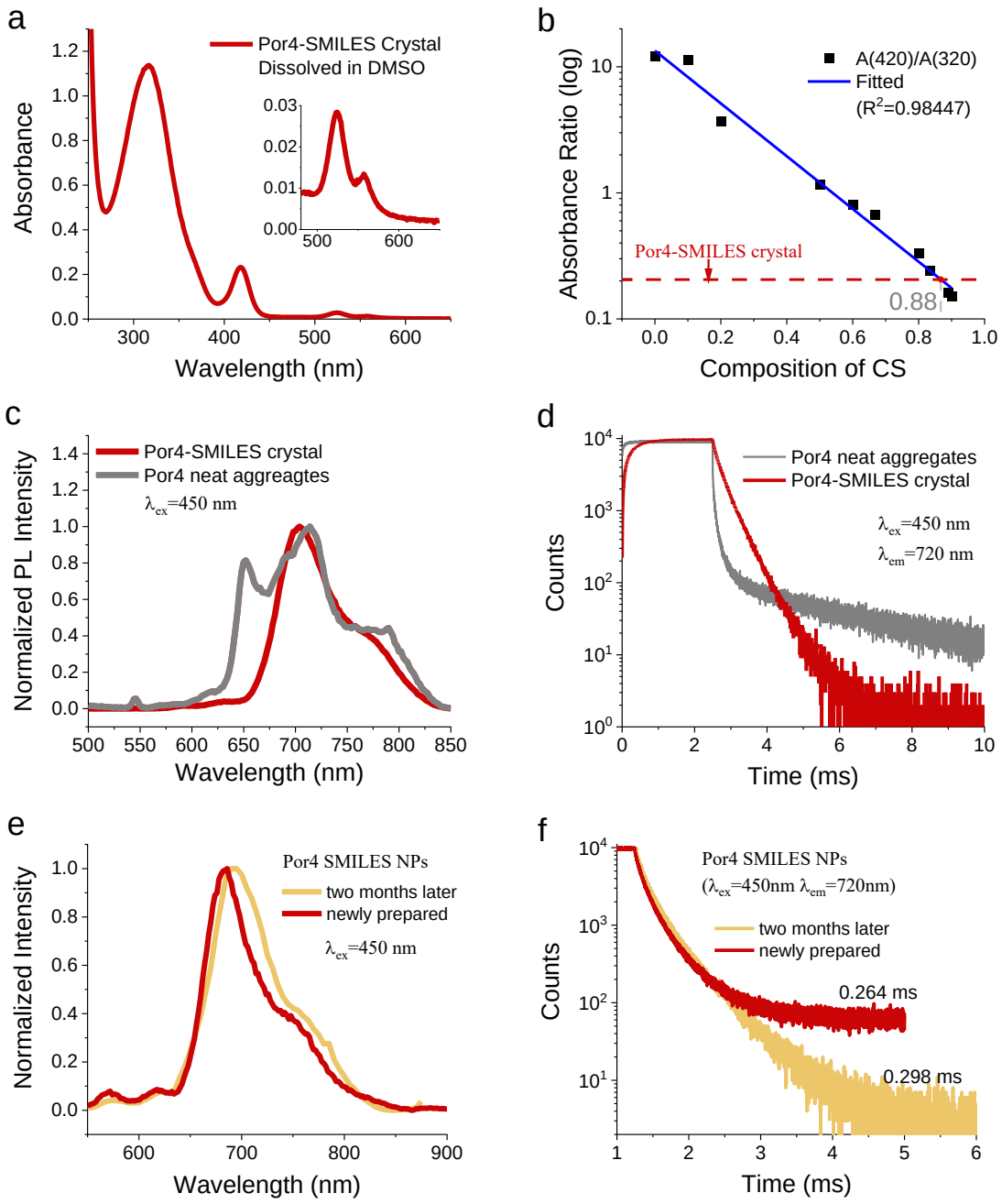

Figure S6. (a) Absorption curve of Por4-SMILES single crystal being re-dissolved. (b) Absorbance ratio between band 314nm (CS) and 420nm (Por4) in the function of CS composition. The solvent was MeCN/DCM (50/50 vol%). (c,d) Comparisons between Por4-SMILES single crystal and Por4 neat aggregates: (c) emission spectra, λ_{ex}=450 nm and (d) decay spectra, λ_{ex}=450 nm, λ_{em}=710 nm, burst mode was used for TCSPC measurements. (e,f) Photophysical stability comparison between freshly prepared Por4-SMILES NPs and sample being stored for two months: (e) steady state emission spectra λ_{ex}=450 nm. (f) decay spectra, λ_{ex}=450 nm, λ_{em}=710 nm, burst mode was used.

Appendix 5-a: Manuscript of TPT-SMILES

Long-Lived Excited State via Charge-Transfer Transition in Small-Molecule Ionic Isolation Lattices

Yang Wang[1], Sina Borgi[1], Amar H. Flood[2], Bo W. Laursen[1]*

1. Nano-Science Center & Department of Chemistry, University of Copenhagen, Universitetsparken 5, 2100 Copenhagen, Denmark
2. Department of Chemistry, Indiana University, 800 E. Kirkwood Ave, Bloomington, IN 47405, USA.

ABSTRACT: The development of the cation-anion-receptor strategy has generated significant interest in organic optical materials, providing customizable and predictable properties. Utilizing flexible non-covalent forces, macromolecule-based self-assembled systems offer versatility for various applications. Cyanostar (CS) and its self-assembly technique, Small-Molecule Ionic Isolation Lattices (SMILES), have emerged as effective methods for producing highly luminescent solid emitters. Our investigation into TPT-SMILES solids revealed a long-lived charge-transfer emissive state, facilitated by the favorable energetic configuration of TPT HOMO being lower than $CS_2 \bullet X^-$ HOMO. Through stepwise solids titration, we characterized the charge-transfer-induced emission, proposing different modes of emissive species based on previous TOTA-SMILES studies. The addition of CS into TPT effectively induces charge delocalization, extending the exciton's fate and resulting in long-lived (~80 ns) and red-shifted (620 nm) emission, with an intrinsic lifetime of 520 ns. This exploration expands our understanding of SMILES strategy application, offering a new avenue beyond the preceding energy matching requirements for fluorophores, but instead prolong the fate of excited state, thus shows potentials for optoelectrical materia

1 Introduction

The SMILES approach exploits charge-by-charge alternating lattices to spatially and electronically isolate cationic chromophores, [1-4] thereby enabling the faithful replication of optical properties observed in dilute solutions into solid emitters. X-ray characterizations have unequivocally confirmed the successful spatial isolation of these chromophores within SMILES crystals. With CS2•X^- anionic complexes offering a wide electronic window, the accommodation of various fluorophores is facilitated if their frontier molecular orbitals align within this range. [1] However, chromophores with frontier orbitals lying outside this electronic window may compromise the efficacy of the SMILES strategy in replicating solution-like properties in solid emitters. Nevertheless, for dyes with frontier orbitals deeper or higher than the CS2•X^- electronic window, efficient charge transfer-transition between dyes and CS2•X^- may give rise to new emission bands with desirable characteristics.

An illustrative exemplar is the co-assembly of the triangulenium cationic dye TOTA with CS, yielding an orange emission band distinct from TOTA's solution-state and crystal emissions. [5] This red-shifted emission band, coupled with a prolonged lifetime, is attributed to the hierarchical assembly structure of $(TOTA \bullet [CS_2BF_4])_n$

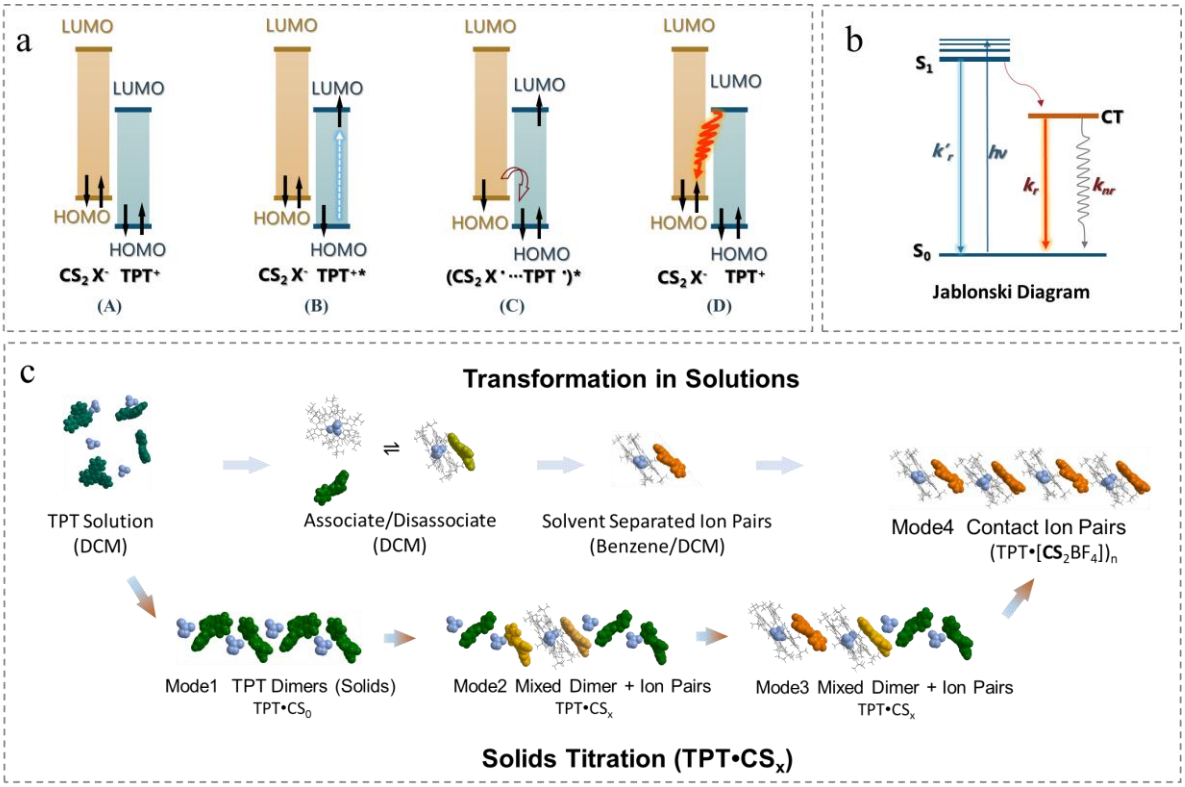

Figure 1. (a) Illustration of molecular orbital (MO) diagram for charge transfer transition. The scheme illustrates the steps involved in the charge-transfer mechanism: (**1**) Upon photoexcitation,an electron being photoexcited from TPT^+ HOMO to LUMO, labeled as TPT^+*. (**2**) Within close contacts between TPT^+* and $[CS_2BF_4]^-$, an electron migrated from adjacent $[CS_2BF_4]^-$ HOMO to the vacancy of TPT HOMO, therein induce forming into exciplex, an intermediate radical pair ($[CS_2BF_4]^{\bullet}\cdots TPT^{\bullet}$)*. (**3**) Excited TPT^+ relaxes back to ground state via photon emission, herein, electron from TPT^+ LUMO to $[CS_2BF_4]^-$ HOMO. (b) Jablonski diagram of charge transfer transition, k_r and k_r' refer to radiative rate constants for charge transfer induced radiation and the intrinsic TPT fluorescence. (c) Methods for transforming TPT solution to **TPT**-SMILES, which contains the hierarchical structure of contact ion pairs of (**TPT•**$[CS_2BF_4]$)$_n$, by either reducing the polarity of solvents or by using drop-cast solids. For the solids titration method, we propose various putative species of **TPT•**CS_x (x=0~3) solids composing different interaction modes between TPT dimers and **TPT•**$[CS_2BF_4]$ ion pairs. The green ones represent TPT dimers, the yellow ones represent TPT molecules approached by both dimers and $[CS_2BF_4]$ ion pairs, the orange ones represent TPT being stacked by $[CS_2BF_4]$ ion pairs.

and enhanced oligomerization through π-stacking. Density functional theory (DFT) calculations corroborate an energy mismatch between TOTA's HOMO and CS2•X^-, highlighting the predominant role of charge-transfer transitions in the mechanism underlying the new emission band. [1]

When delving into the topic of charge-transfer transition, electron donor-accepter systems will be the main focus. [6, 7] These systems consist of matched electron donors (D) and electron acceptors (A). Hereby the specification of charge-transfer transition within TPT-SMILES requires a fundamental understanding of electron donor-acceptor system in TPT-SMILES.

The pair of electron donor and accepter in a typical exciplex system undergo electrostatic interactions and electron migrations upon close contacts, which generate intermediate radical ion pairs. A new photon radiates along with the

intermediate species recombination process [8] (Figure 1-a,b).

$$A + D \xrightarrow{h\nu} A^* + D \xrightarrow{CT} \left(A^{\delta-} \cdots D^{\delta+}\right) \rightarrow A + D + h\nu \quad (1)$$

However, the formation of the TOTA•[CS_2BF_4] ion pair in a solvent mixture introduces uncertainty due to the photobleaching of emissive species. This strong quenching/photobleaching phenomenon is observed for TPT-SMILES as well. To investigate the formation of charge-transfer emission, it was proposed to utilize a higher ordered contact ion pair structure. To monitor the formation of charge-transfer emission in TPT-SMILES, we adopted the method of solid-state titration, where solutions containing different molar ratios of CS and TPT were drop-cast, and the changes in photophysical properties were measured in the solid samples. [9-11]

This method reduces the likelihood of emissive species being quenched and provides a different perspective to understand the transition from freely dissolved TPT to hierarchically assembled species (TPT•[CS_2BF_4])$_n$, as depicted in Figure 1-c. We proposed several modes to describe the differences in emissive species, ranging from TPT neat aggregates (TPT dimer, Mode 1), different mixed species of TPT dimers and TPT•[CS_2BF_4] ion pairs (Mode 2 and Mode 3), to eventually purely contact ion pairs (TPT•[CS_2BF_4])$_n$ (Mode 4).

In addition to the solid-state titration method, we also employed polystyrene film to embed and isolate the ion pairs of TPT•[CS_2BF_4]. Polystyrene mimics the low-polarity matrix of benzene and promotes close contact between TPT^+ and $[CS_2BF_4]^-$, thereby stabilizing and protecting the TPT•[CS_2BF_4] ion pair within polystyrene. Unlike in solutions, where intermediate radicals ($TPT^{\bullet}$ or $[CS_2BF_4]^{\bullet}$) may dissociate and have their charge-transfer emission quenched, embedding them in polystyrene prevents such disassociation and quenching. [9, 12-14]

Above all, in this study, we focus on three primary aspects:

(1) Detailed examination of the long-lived excited state induced by charge-transfer transitions in TPT-SMILES, with particular emphasis on tracking the formation of such states.

(2) Investigation of photophysical properties primarily in solid samples to mitigate uncertainties arising from quenching effects in solution states.

(3) Monitoring the transformation from monomer TPT to hierarchical (TPT•[CS_2BF_4])$_n$ structure by varying the molar ratio of CS/TPT in solids, thereby eliciting photophysical property changes stemming from different close contacts between TPT dimers and TPT•[CS_2BF_4] ion pairs. Proposed species representing different interaction modes are illustrated in Figure 1-c. Such a progressive probing approach facilitates our understanding of the intrinsic emissivity of variable hierarchical TPT•CSx structures in real fabrication scenarios.

2 Results and Discussion

2.1 Investigation on Charge-Transfer Ion Pair Formation

The investigations on the ion pair formation was first conducted by varying the solvent polarity. To examine how solvent composition affects cationic TPT fluorophores with the $CS_2BF_4^-$ anionic sandwich complex, we conducted titrations ranging from pure DCM solutions to a mixture of 95% benzene and 5% DCM. This aimed to favor contact ion pairs formation to induce the proposed charge-transfer transition. First of all, the basic photophysical properties of TPT in pure DCM was examined. The absorption spectra of TPT suggest a high absorption coefficient, which is 2.7×10^4 M^{-1} cm^{-1} at 418 nm (Figure S3), and can be sustained with the presence of CS in DCM solutions.

Exposed to different polarity of solvent mixtures, the absorption band of TPT (Figure S4-a) remains basically unchanged, except for the anticipated solvent polarity effects, which weaken the clear separation of absorption bands. Excitation spectra of TPT at 470 nm shows similar unchanging behavior (Figure S4-b). The emission spectrum of TPT exhibits a redshift of ~10 nm with decreasing solvent polarity (Figure S4-c).

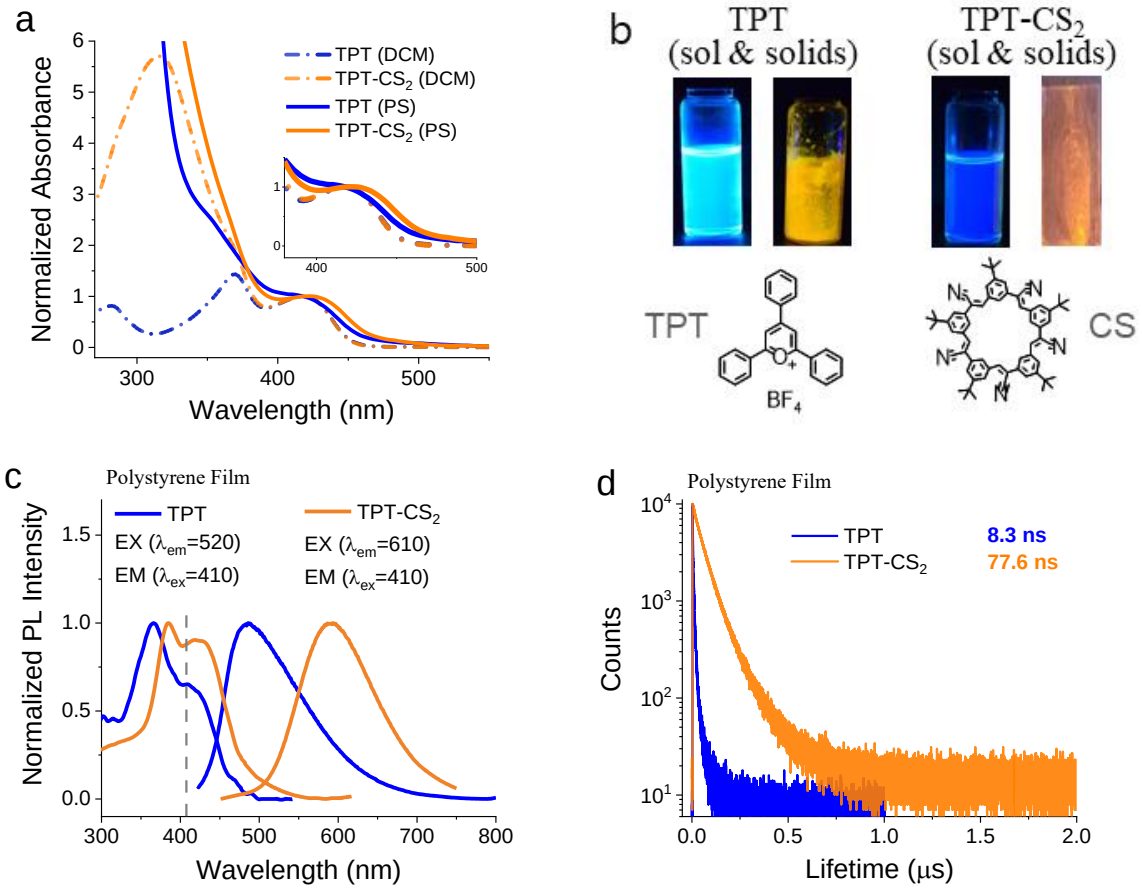

Figure 2. (a) Absorption spectra of TPT and TPT-CS_2 in DCM solutions. (b) Chemical structures of TPT and CS. Illustration of TPT and TPT-CS_2 in solution state and solid state under the illumination of 365nm ultraviolet light. (c) Emission and excitation curves of TPT and TPT-CS_2 in polystyrene thin films, λ_{ex}=410 nm for both emission curves, λ_{em}=520 nm for excitation curve of TPT, λ_{em}=610 nm for excitation curve of TPT-CS_2. (d) TCSPC decay curves for TPT (λ_{em}=520 nm) and TPT-CS_2 (λ_{em}=620 nm) in polystyrene thin films, laser light λ_{ex}=407 nm was used.

For the ion pair formation experiments, with the increase of benzene in the solvent mixture, the absorption spectra of TPT-CS_2 reveals a redshift (~10 nm) in the TPT absorption peak and increased CS absorption with higher benzene content (Figure S4-d). Once benzene content reaches 50%, a new emission band becomes evident in the emission spectrum at 620 nm (Figure S4-f). Excitation spectra (Figure S4-e) at 620 nm showes CS presence, suggesting excitability of CS in this exciplex system.

As mentioned above, the model of charge-transfer transition occurs in systems encompassing ionic donor and acceptor pairs can be described as follows [6, 12]:

$$A^+ + D^- \xrightarrow{h\nu} A^{+*} + D^- \xrightarrow{CT} (A^{\bullet} \cdots D^{\bullet})^* \rightarrow A^+ + D^- + h\nu \quad (2)$$

Eventually it can be theorized for electron donor-acceptor system in TPT-SMILES as following:

$$TPT^+ + CS_2X^- \xrightarrow{h\nu} TPT^{+*} + CS_2X^- \xrightarrow{CT} (TPT^{\bullet} \cdots CS_2X^{\bullet})^* \rightarrow A^+ + CS_2X^- + h\nu \quad (3)$$

With the fundamental information of charge-transfer transition in **TPT**-SMILES being well perceived from theoretical models in procedures (2). The formation of **TPT•**[CS_2BF_4] ion pair is the main reason for the unique charge-transfer emission band. The transformation from freely dissolved dyes to assembled species with CS are specified as following [5]:

$$\mathbf{TPT}^+[BF_4]^- \rightleftharpoons \mathbf{TPT}^+ + BF_4^- \quad \text{(in DCM, blue emission)} \quad (4)$$

$$2\mathbf{CS} + BF_4^- \rightleftharpoons [\mathbf{CS}_2\ BF_4]^- \quad \text{(in DCM)} \quad (5)$$

$$[\mathbf{CS}_2\ BF_4]^- + \mathbf{TPT}^+ \rightleftharpoons \mathbf{TPT}^+[\mathbf{CS}_2\ BF_4]^- \quad \text{(in B/D)} \quad (6)$$

$$n\ \mathbf{TPT}^+[\mathbf{CS}_2\ BF_4]^- \rightleftharpoons (\mathbf{TPT}\bullet[\mathbf{CS}_2\ BF_4])_n \quad \text{(in solids)} \quad (7)$$

However, the formation of the TPT•[CS_2BF_4] ion pair in a solvent mixture introduces photobleaching phenomenon. Therefore, to monitor the formation of charge-transfer emission in TPT-SMILES, we adopted the method of solid-state measurements.

2.2 Charge-Transfer Emission in SMILES

In Figure 2-a, TPT's absorption band remains unchanged In polystyrene film, while TPT-CS_2 exhibits a slight red-shift due to the formation of TPT•[CS_2BF_4] ion pairs. As in solution, both TPT and TPT-CS_2 emit blue light, while in solids, TPT emits yellow light and TPT-CS_2 emits orange light (Figure 2-b). The emission spectra in polystyrene film confirm these observations, with TPT emitting at 480 nm and TPT-CS_2 at 600 nm, similar the TPT•[CS_2BF_4] ion pairs emission at 620 nm (Figure 2-c).

The emission lifetime of TPT-CS_2 in polystyrene film (77.6 ns) is significantly longer than that of TPT (8.3 ns in film, 3.1 ns in solution) and even longer than TPT•[CS_2BF_4] ion pairs (13.1 ns in 95%:5%

Tolune:DCM solution), as shown in Figure 2-c, indicating sustained excited states induced by charge-transfer transitions within closely contacted ion pairs.

Under cryogenic conditions, TPT emits at 450 nm with a diffuse band at 520 nm, while TPT-SMILES emits charge-transfer emission at 620 nm (Figure S5). Excitation curves for these emissions differ, suggesting distinct origins. TPT-SMILES exhibits a long-lived emission lifetime (100 ns) compared to TPT (3 ns), indicating a significant prolongation of the excited state lifetime. However, this lifetime is still in the nanosecond range, shorter than typical phosphorescence lifetimes, suggesting the involvement of singlet states in the charge-transfer emission of TPT-SMILES.

2.3 Formation of the Long-Lived Excited State

Figure 3 displays fluorescent emission spectra of drop-cast solid samples containing varying molar ratios of TPT and CS (denoted as TPT•CS_x, x=0~3), and also absorption spectra of corresponding stock solutions (in DCM) before drop-casting onto glass (Figure S6-a). The linear absorbance ratio between typical TPT (418 nm) and CS (317 nm) bands ensures accurate CS addition. A systematic red-shift in emission maximum is observed in Figure S6-b, from TPT•CS_0-TPT neat aggregates (565 nm) to TPT•CS_3 solids (620 nm), with emission maxima stabilizing at CS/TPT molar ratio = 2, evident in TPT•CS_2, TPT•$CS_{2.5}$, and TPT•CS_3 solids all emitting at 620 nm.

To track emission changes from single molecular TPT to assembled TPT•[CS_2BF_4] ion pairs and higher-order oligomerization (TPT•[CS_2BF_4])$_n$, emission spectra of TPT (polystyrene film) and samples containing TPT•[CS_2BF_4] ion pairs (polystyrene film and solution) were recorded. Monomeric TPT and TPT-CS_2 polystyrene film samples emit at 490 nm and 600 nm, respectively, while TPT•[CS_2BF_4] ion pair in solution emits at 620 nm.

Compared to TPT monomer emission (490 nm), TPT neat aggregated solids (*Mode 1*, TPT dimers) exhibit a red-shifted emission maximum at 565 nm. As CS/TPT molar ratio increases, emission gradually shifts to 620 nm, reflecting increased proportions of TPT•[CS_2BF_4] ion pairs. Once CS/TPT ratio surpasses 2, TPT•[CS_2BF_4] ion pairs become the dominant emissive species.

Luminescence lifetime measurements on TPT•CS_x solids (Figure 3-b,c) reveal a gradually prolonged lifetime with increasing CS/TPT molar ratio, from 7 ns (TPT•CS_0, TPT neat aggregates) to 56 ns (TPT•CS_2 solids), plateauing when CS/TPT $\geq$ 2. Monitoring lifetime changes at different emission wavelengths confirms this trend, reaching a plateau when CS/TPT $\geq$ 2. The long-lived emission state arises from the addition of CS into TPT, leading to a much longer lifetime (65 ns in solids) than the parental components. As CS is added, TPT dimers' lifetime (7 ns) is gradually replaced by a much longer lifetime (~53 ns) due to charge-transfer transition in contact ion pairs (TPT•[CS_2BF_4])$_n$, which is defined as *Mode 4*.

2.4 Analysis on the Deactivation Pathways

Understanding the charge transfer mechanism in the TPT-SMILES system is complex, particularly based solely on steady-state measurements and lifetime data. [15] To

delve deeper into the excited state of charge-transfer emission, we evaluated radiative and non-radiative rates [16, 17] for samples including TPT•CS_x dropcast solids, TPT, and TPT-CS_2 in polystyrene film and solution (Table 1, Figure 4).

Figure 4 illustrates the quantum yield (QY) and lifetime of TPT•CS_x dropcast solids relative to CS/TPT molar ratio. A sharp decrease in QY occurs during TPT•[CS_2BF_4] formation, dropping from 18.6% (TPT dimer, TPT•CS_0) to 12.2% (TPT•CS_1), stabilizing at 10% for TPT•CS_3. Similarly, the lifetime of TPT•CS_x drop-cast solids sharply increases from 8 ns (TPT•CS_0) to 53 ns (TPT•CS_2), plateauing at CS/TPT ≥ 2.

Based on QY and lifetime data, we calculated corresponding rate constants for

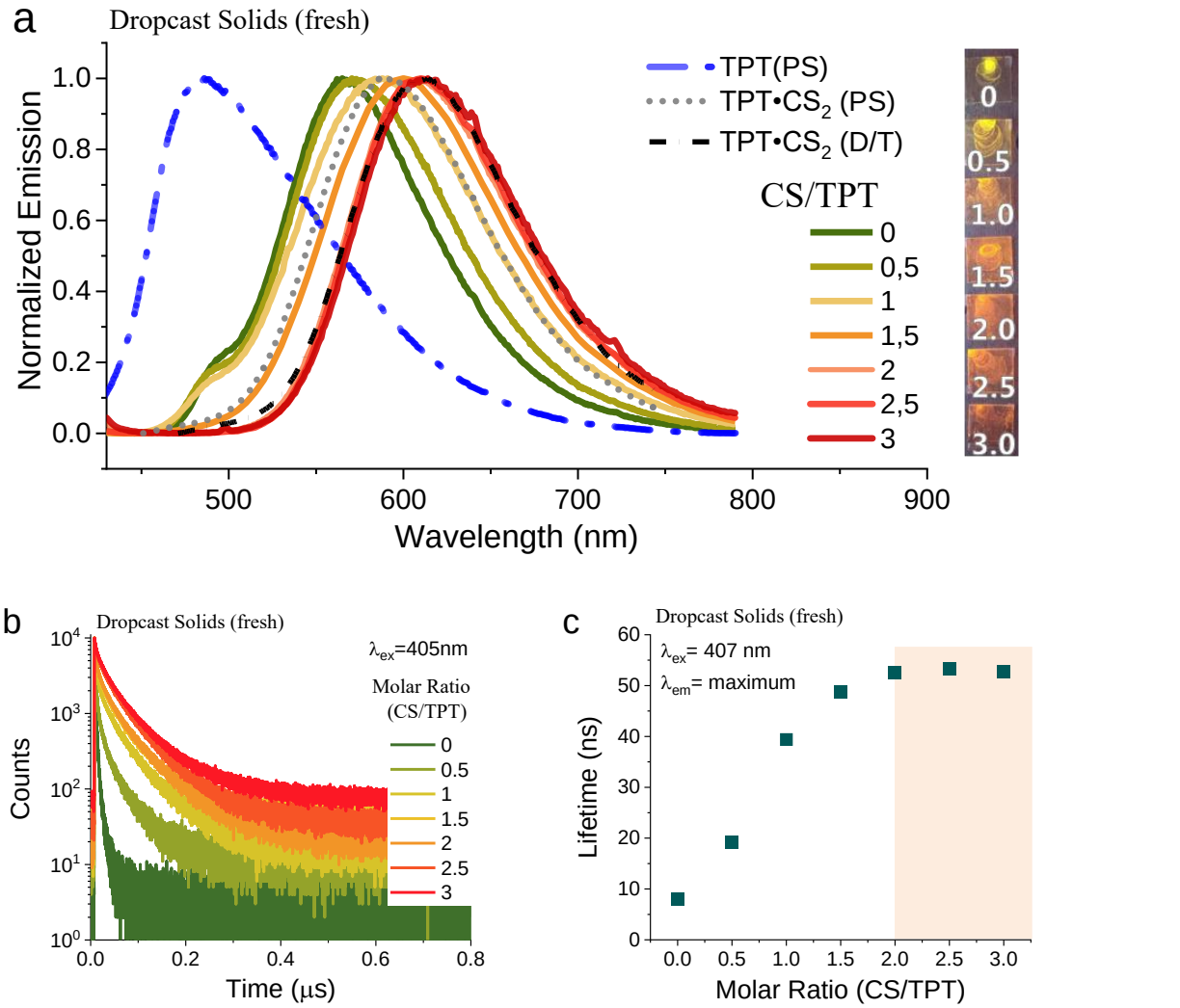

Figure 3. (a) Emission spectra (λ_{ex}=405 nm) of dropcast solids with different molar ratio of TPT and CS, and corresponding pictures under illumination of 365 nm ultraviolet light. Long dashed (— -) and dotted (•••••) curves refer to TPT and TPT-CS_2 drop-cast polystyrene thin films, short dashed (– • –) curve refers to **TPT**[CS_2BF_4] in solvent mixture of dichloromethane(D) and toluene(T) (D/T-10/90 vol%). (b) TCSPC decay curves of **TPT**•CS_x solids (x=0, 0.5, 1, 1.5, 2, 2.5, 3), and corresponding intensity averaged lifetime plot (c), with the detector set at the maximum of each emission curve.

radiative (k_r) and non-radiative (k_{nr}) deactivation pathways (Figure 4-b), along with intrinsic lifetime (τ_0) in Table 1. Comparing samples in solution and polystyrene film, we gain a comprehensive understanding of photophysical property changes from TPT to TPT•[CS_2BF_4] ion pairs.

Mode 1: Comparison between TPT monomer in DCM solution and TPT dimers in polystyrene film reveals a 6-fold increase in the radiative rate constant (k_r), attributed to strong coupling of molecular frontier orbitals. Additionally, dimer formation reduces the non-radiative constant (k_{nr}). Similar trends are observed when comparing TPT•[CS_2BF_4] in solution and in polystyrene film, indicating

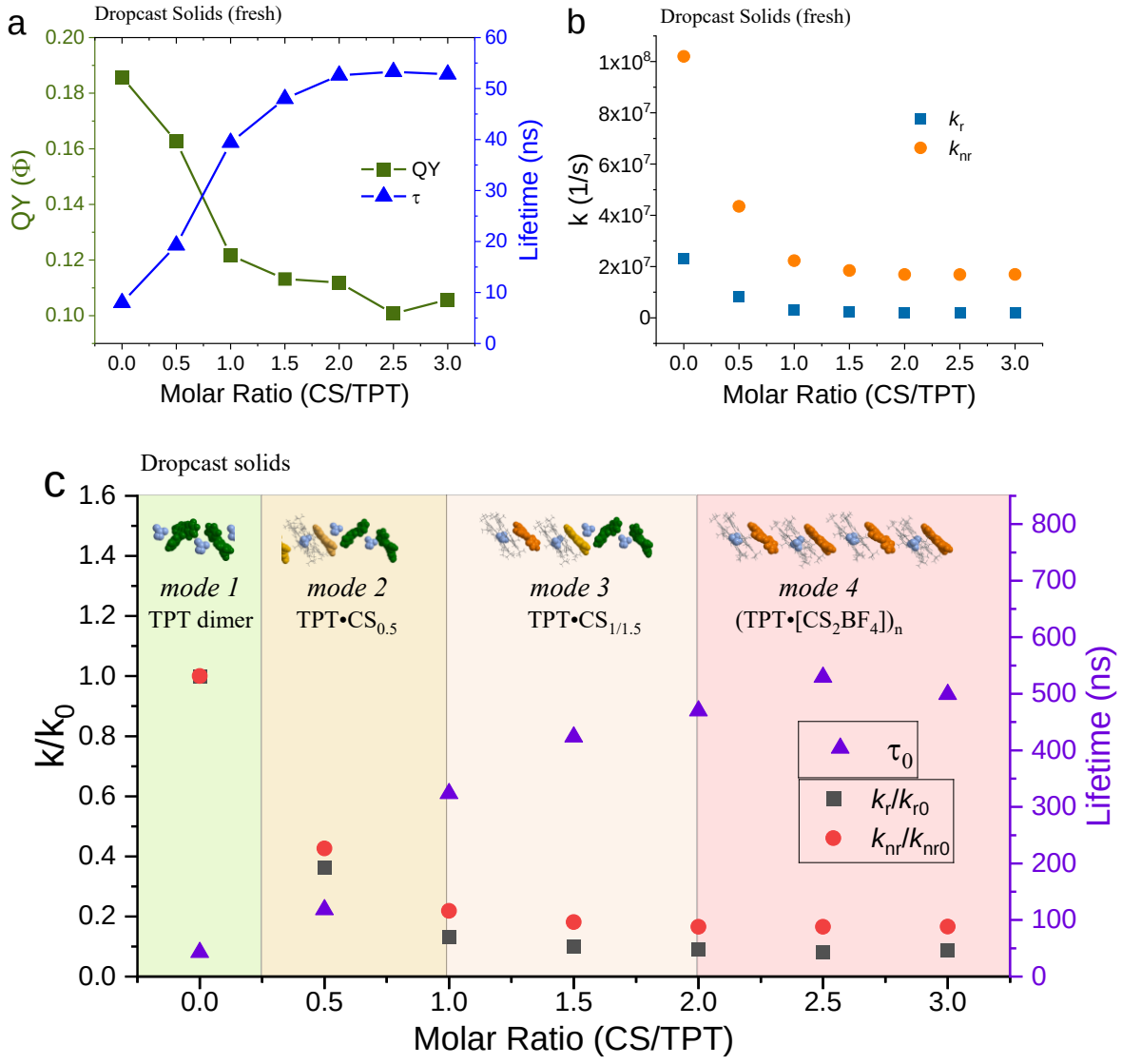

Figure 4. (a) Lifetime (detector set at emission maxima) and QYs of TPT•CS_x solids (x=0, 0.5, 1.0, 1.5, 2.0, 2.5, 3.0). (b) Radiative and non-radiative constants calculated from lifetime and QYs. (c) Illustration of the putative species within the dropcast TPT•CS_x solids and being classified into four modes. Deactivation rate constants ratio (k/k_0) and intrinsic lifetime (τ_0) as a the function of molar ratio CS/TPT, k_0 refers to k_r or k_{nr} for TPT•CS_0, k refers to k_r or k_{nr} for TPT•CS_x (x=0.5, 1, 1.5, 2, 2.5, 3).

similar k_r values and reduced k_{nr} in the polymer matrix. The intrinsic lifetime (τ_0) for TPT•[CS_2BF_4] in solution is larger but comparable to that in polystyrene. These findings provide insights into the photophysical properties of TPT dimers and ion pairs TPT•[CS_2BF_4], representing the initial and final stages of structure transformation.

Mode 2: In this mode, a minor fraction of $[CS_2BF_4]^-$ ion pairs coexists with predominantly TPT dimers. Certain TPT molecules adjacent to the ion pairs undergo charge delocalization with CS, resulting in changes in radiative and non-radiative processes. The k_r and k_{nr} values are 30% and 40% of TPT dimer's values, respectively, with a τ_0 of 118 ns, indicating prolonged excited state lifetimes compared to TPT dimers.

Mode 3: Coexistence of $[CS_2BF_4]^-$ ion pairs and TPT dimers characterizes this mode. TPT closely interacts with ion pairs, enhancing charge delocalization and promoting charge-transfer-induced emission. The k_r and k_{nr} values are 10% and 20% of TPT dimer's values, respectively, with τ_0 ranging from 324 to 424 ns, indicative of extended excited state lifetimes.

Mode 4: This mode represents the formation of hierarchical contact ion pairs (TPT•[CS_2BF_4])$_n$. The radiative and non-radiative rate constants reach a plateau, with values representing 8.5% and 17% of TPT dimer's values, respectively. The τ0 value is 520 ns, indicating significantly prolonged excited state lifetimes compared to TPT dimers.

Table 1. Photophysical properties of samples.

Sample (composition)		λ_{em} (nm)	Φ(%)[c]	τ (ns)	k_r (s^{-1})[d] ($\times 10^5$)	k_{nr} (s^{-1})[d] ($\times 10^5$)	τ_0 (ns)[d]
Solution[a]	TPT (DCM)	480	58.0	3.1	1883	1364	5
	TPT[CS_2BF_4] (95:5 B:D) [b]	620	2.0	13.1	15	746	657
Polystyrene film	TPT	490	24.7	8.3	298	907	34
	TPT•CS_2	600	14.2	77.6	18	111	546
Dropcast solids	TPT•CS_0	565	18.6	8.0	233	1020	43
	TPT•$CS_{0.5}$	572	16.3	19.3	84	435	118
	TPT•CS_1	588	12.2	39.4	31	223	324
	TPT•$CS_{1.5}$	600	11.3	48.0	24	185	424
	TPT•CS_2	610	11.2	52.6	21	169	470
	TPT•$CS_{2.5}$	615	10.1	53.3	19	168	529
	TPT•CS_3	618	10.3	52.8	20	169	514

a): cited from preliminary research done by Sina Borgi, *Thesis- Ionpair and Solid-state Emitters Based on Bimolecular Charge-Transfer Systems*, 2020, 09.
b): 95:5 B:D refers to 95%:5% Benzene:DCM solvent mixture.
c): The quantum yields were obtained by absolute method, using integrating sphere.
d): calculations for k_r, k_{nr}, τ_0. $k_r=\Phi/\tau$, $k_{nr}=(1-\Phi)/\tau$, $\tau_0=\tau/\Phi$

By tracking the formation of hierarchical $(TPT•[CS_2BF_4])_n$ structures in drop-cast solid samples, we confirm drastically changed optical performance compared to TPT monomers or dimers, owing to different radiative and non-radiative processes. Cofacial stacking with $[CS_2BF_4]^-$ ion pairs and charge delocalization with CS yield a long-lived emissive state via charge-transfer transition, with a distinct τ_0=520 ns.

In the model of charge-transfer transition for TPT-SMILES, the formation of ionic donor and acceptor pairs can lead to the generation of radicals ($TPT^•$ and $CS_2^•$) after electron transition. These radicals, lacking Coulombic attraction, may disassociate without external forces, rendering them susceptible to environmental quenchers, particularly $CS_2^•$. Absorption spectra of solution samples subjected to light exposure for seven days reveal a decrease in the CS absorption band, while the TPT absorption band remains stable (Figure S7-a). Interestingly, drop-casting these 'aged' solutions into solids results in emissions similar to TPT dimers (Figure S7-b), contrasting with the red-shifted emissions observed in fresh $TPT•CS_x$ solids. Additionally, Figure S7-c and Figure S7-d suggest that the lifetime of these aged samples is notably shorter compared to freshly prepared $TPT•CS_x$ solids. Monitoring photo-degradation in undried matrices containing polystyrene and DCM demonstrates a gradual reduction in charge-transfer emission, aligning with the decay towards TPT dimer emission (Figure S7-e,f). This suggests that the quenching of $TPT^+[CS_2BF_4]^-$ charge-transfer emission primarily results from attacks on $CS_2^•$ and CS structure decomposition. Consequently, once transformed into solids, TPT-SMILES can emit a stable, long-lived charge-transfer emission, corroborating observations made with $TOTA^+[CS_2BF_4]^-$ ion pairs.

3 Conclusion

With the experiments conducted for both solution samples and solid samples, we investigated the long-lived charge-transfer emissive state in TPT-SMILES solids, where the energetically favorable configuration of TPT HOMO being lower than $CS_2•X^-$ HOMO, thus facilitates prolonged lifetime and red-shifted emission. Through stepwise solids titration of $TPT•CS_x$, we characterized the charge-transfer-induced emission. Adapting information from previous studies on analogous TOTA-SMILES, we proposed different modes of emissive species, reflecting varied interactions between TPT dimers and $TPT•[CS_2BF_4]$ ion pairs. Our findings confirm that the addition of CS into TPT effectively induces charge delocalization, extending the exciton's fate and resulting in long-lived (~80 ns) and red-shifted (620 nm) emission, with an intrinsic lifetime reaching 520 ns. This exploration expands the understanding of utilizing the SMILES strategy, offering a novel pathway beyond the conventional 'HOMO-LUMO window' rule, yet yielding long-lived emission suitable for applications in photocatalysis and optoelectrical materials.

AUTHOR INFORMATION

Corresponding Author

* Bo W. Laursen : bwl@chem.ku.dk

Conflicts of Interest

No conflicts to declare.

Author Contributions

Sina Borgi conducted experiments for solution state research. Yang Wang conducted all other experiments including synthesis of solid TPT-SMILES samples, spectroscopic measurements, data analysis, manuscript draft and editing. Bo W. Laursen contribute to conceptualization and supervision, Amar H. Flood contribute to the manuscript correction.

The manuscript was written through contributions of all authors. All authors have given approval to the final version of the manuscript.

ACKNOWLEDGMENT

YW appreciates the funding from the European Union's Horizon 2020 research and TALENT doctoral programme under the Marie Skłodowska-Curie grant agreement No 801199. AHF thanks the National Science Foundation for support (NSF-2118423).

REFERENCES

[1] C. R. Benson, L. Kacenauskaite, K. L. VanDenburgh, W. Zhao, B. Qiao, *Plug-and-Play Optical Materials from Fluorescent Dyes and Macrocycles*. *Chem*. **2020**, 6, 1978-1997.

[2] L. Kacenauskaite, S. G. Stenspil, A. H. Olsson, A. H. Flood, B. W. Laursen, *Universal Concept for Bright, Organic, Solid-State Emitters horizontal line Doping of Small-Molecule Ionic Isolation Lattices with FRET Acceptors*. *J Am Chem Soc*. **2022**, 144, 19981-19989.

[3] J. Chen, S. G. Stenspil, S. Kaziannis, L. Kacenauskaite, N. Lenngren, *Quantitative Energy Transfer in Organic Nanoparticles Based on Small-Molecule Ionic Isolation Lattices for UV Light Harvesting*. *ACS Applied Nano Materials*. **2022**, 5, 13887-13893.

[4] P. Deshmukh, S. Satapathy, E. Michail, A. H. Olsson, R. Bushati, *Plug-and-Play Molecular Approach for Room Temperature Polariton Condensation*. *ACS Photonics*. **2024**.

[5] B. Qiao, B. E. Hirsch, S. Lee, M. Pink, C. H. Chen, *Ion-Pair Oligomerization of Chromogenic Triangulenium Cations with Cyanostar-Modified Anions That Controls Emission in Hierarchical Materials*. *J Am Chem Soc*. **2017**, 139, 6226-6233.

[6] C. J. Bender, *Theoretical models of charge-transfer complexes*. *Chemical Society Reviews*. **1986**, 15.

[7] R. S. Mulliken, W. B. Person, *Molecular complexes*. *(No Title)*. **1969**.

[8] S. L. Logunov, M. A. J. Rodgers, *Charge recombination reactions in self-assembled porphyrin-based ion-pair complexes*. *Journal of Photochemistry and Photobiology A: Chemistry*. **1997**, 105, 55-63.

[9] S. Garain, S. N. Ansari, A. A. Kongasseri, B. Chandra Garain, S. K. Pati, *Room temperature charge-transfer phosphorescence from organic donor-acceptor co-crystals*. *Chem Sci*. **2022**, 13, 10011-10019.

[10] H. L. Lee, J. Kang, J. Lim, S. C. Kim, S. O. Jeon, *Hybridization of short-range and long-range charge transfer excited states in multiple resonance emitter*. *Nat Commun*. **2023**, 14, 4818.

[11] G. Meng, H. Dai, Q. Wang, J. Zhou, T. Fan, *High-efficiency and stable short-delayed fluorescence emitters with hybrid long- and short-range charge-transfer excitations*. *Nat Commun*. **2023**, 14, 2394.

[12] H. J. Worner, C. A. Arrell, N. Banerji, A. Cannizzo, M. Chergui, *Charge migration and charge transfer in molecular systems*. *Struct Dyn*. **2017**, 4, 061508.

[13] K. Jinnai, R. Kabe, Z. Lin, C. Adachi, *Organic long-persistent luminescence stimulated by visible light in p-type systems based on organic photoredox catalyst dopants*. *Nat Mater*. **2022**, 21, 338-344.

[14] S. Feng, L. Wang, B. Milian-Medina, A. J. Meixner, M. S. Kwon, *Donor-Acceptor-Donor Triads with Flexible Spacers: Deciphering Complex Photophysics for Targeted Materials Design*. *Adv Mater*. **2023**, e2306678.

[15] J. Gierschner, J. Shi, B. Milián‐Medina, D. Roca‐Sanjuán, S. Varghese, *Luminescence in Crystalline Organic Materials: From Molecules to Molecular Solids*. *Advanced Optical Materials*. **2021**, 9, 2002251.

[16] J. R. Lakowicz, *Principles of Fluorescence Spectroscopy*. (2006).

[17] B. Valeur, M. N. Berberan‐Santos, *Molecular Fluorescence*. (2012).

Appendix 5-b: Manuscript SI of TPT-SMILES

Supporting Information

Long-Lived Excited State via Charge-Transfer Transition in *Small-Molecule Ionic Isolation Lattices*

Yang Wang[1], Sina Borgi[1], Amar H. Flood[2], Bo W. Laursen[1]*

1. Nano-Science Center & Department of Chemistry, University of Copenhagen, Universitetsparken 5, 2100 Copenhagen, Denmark
2. Department of Chemistry, Indiana University, 800 E. Kirkwood Ave, Bloomington, IN 47405, USA.

CONTENTS

§1 Synthetic Methods and Instrumental Measurements

§1.1 Materials Synthesis

Solution Samples:

Solution measurements were conducted using a 1 cm cuvette for all samples. Each sample's stock solution was diluted to ensure an absorbance below 0.1 at the desired excitation wavelength and towards the red end of the absorption spectrum. Dichloromethane (DCM) served as the solvent mixture for all experiments.

The TPT-BF4 stock solution, with a concentration of 0.63 mM, was diluted by taking 14 μL from the stock solution and diluting it to 2.5 mL in the cuvette to achieve the target absorbance. Similarly, the TPT-CS2BF4 stock solution, with a concentration of 0.45 mM, underwent a similar dilution process with 20 μL from the stock solution.

To create a solvent ratio of 95% benzene and 5% DCM, the cuvette was filled with a total of 0.125 mL DCM and 2.375 mL benzene. DCM was added first to prevent precipitation due to excess benzene. This solvent mixture was also employed in drop-casting experiments. Subsequently, the cuvette underwent N_2 purging for 4 minutes before fluorescence decay measurements were taken once more.

Solid Samples:

Drop-cast solids were fabricated through spin coating, wherein 20-40 μL of a concentrated sample was deposited onto a glass slide and spun at 1200 rpm for 60 seconds, resulting in the formation of a uniform and tidy thin film containing drop-cast solids. The solids of TPT-SMILES was also carefully grinded and dispensed in viscous propylene glycol (PG), then frozen the PG sample with liquid nitrogen for the cryogenic measurements.

To create polystyrene (PS) thin films doped with the proposed TPT-SMILES materials, a solution containing 25 mg/mL PS dissolved in DCM and another solution containing 1 mg/mL fluorophore dissolved in DCM were prepared. These two solutions were then mixed together, and 20-40 μL of the resulting PS-fluorophore mixture was spin coated onto the glass slide

§1.2 Instrumental Measurements

Steady-state: UV-Vis absorption spectra were measured with a Cary 300 spectrophotometer. Corrected photoluminescence spectra were obtained by a PTI Instruments spectrofluorimeter. All photophysical measurements were conducted at ambient temperature, 22 ± 2 ℃. All luminescent solution samples were measured in 1 cm2 anaerobic quartz cells.

TCSPC lifetime measurements were obtained by time-correlated single-photon counting on an PTI Instruments-FluoTime 300, the instrument response function was collected using a dilute solution of Ludox at the detection wavelength. Reconvolution of the fluorescence decay and instrumental response function (IRF) was performed on the Edinburgh software in conjunction with lifetime fitting. Finally, the data was exported and plotted by using Origin 2020.

Fluorescence microscopy: All micrographs of solid materials were taken using Zeiss fluorescence microscope, equipped with KL 2500 LCD halogen lamp as an excitation source, a LD EC Epiplan-NEOFLUAR 50x/0.55 HD DIC objective and an AxioCam MRc camera from Zeiss. Excitation (475 ± 20 nm) and emission (510 nm LP) filters were used in the excitation and detection path, respectively.

All thin film and crushed powders were measured using the FluoTime 300 from PicoQuant. Steady-state measurements utilized a xenon lamp as the excitation source, while time-resolved measurements employed lasers. To facilitate front-face excitation, the traditional cuvette holder was replaced with a slide holder, and mirrors were positioned accordingly, as depicted in Figure S1.

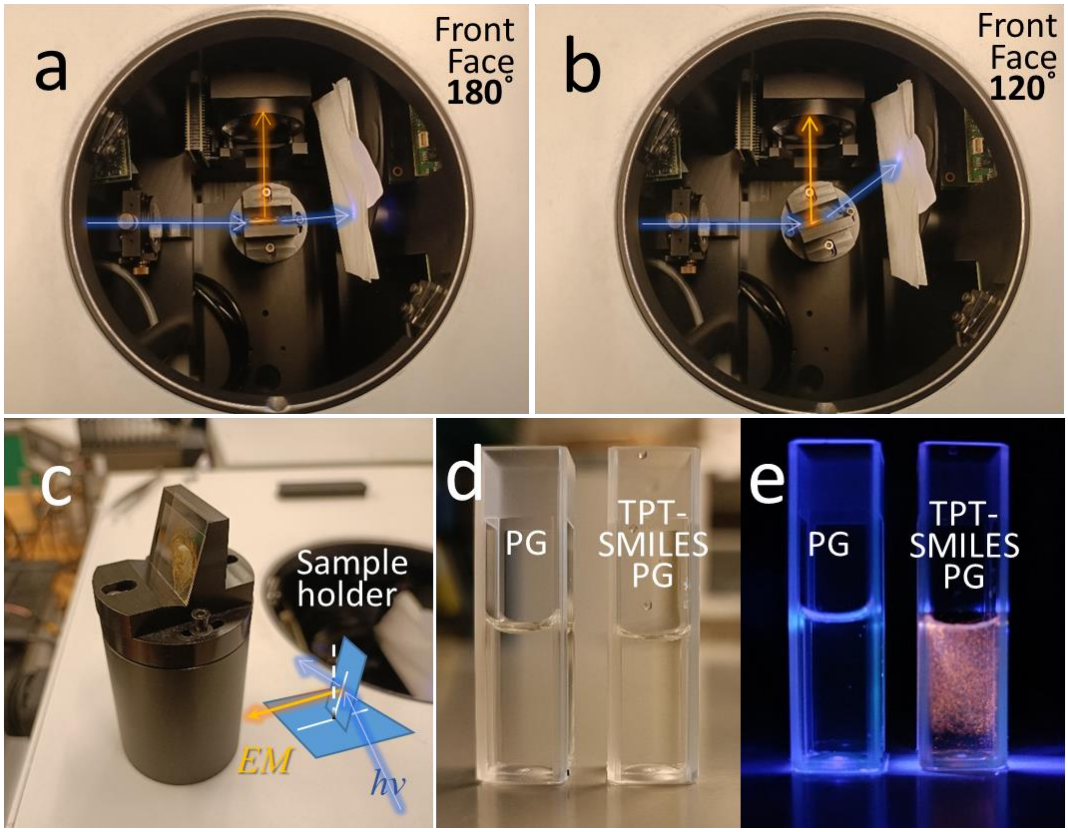

Figure S1. Experimental setup for the measurements of solid samples (**TPT**-SMILES) on glass slides or in viscous solvent (PG, propylene glycol). (a,b,c) Typical operations of front-face (FF) measurements on solid samples and the angle mentioned is the alignment angle between the incited illumination beam and scattered beam, the collection pathway of the sample's emission is always perpendicular to the incited illumination. (d,e) Solid powder samples were suspended into viscous PG, (d) under white light and (e) illuminated by ultraviolet light λ_{em}= 365 nm.

§2 Supporting Graphs

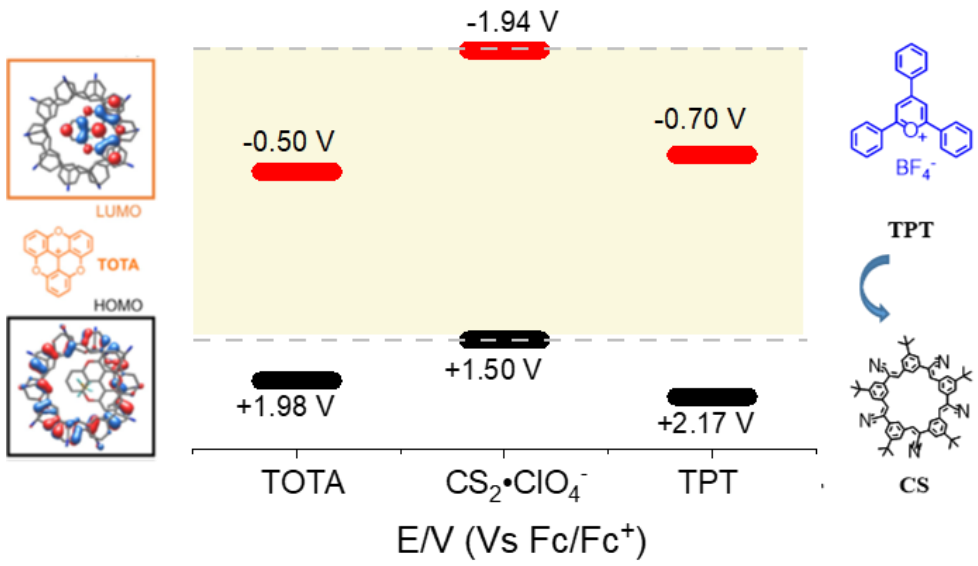

Figure S2. Energy level diagram showing positions of frontier orbitals mapped using electrochemistry, which suggests both TOTA's and TPT's frontier orbitals located outside of the CS2•X^- complex's electronic window.

Table S1. Orbital levels with their energy gap.[a]

Sample	LUMO [b] (V)	HOMO[b] (V)	HOMO-LUMO gap [c] (V)	$E_{0,0}$ (HOMO-LUMO gap)	$E_{0,0}$ (optical)	$\lambda_{em\text{-}max}$	$\lambda_{em\text{-}10\%}$
$CS_2{\bullet}X^-$ [d]	-1.94	1.50	3.44	360 nm			
TOTA[BF_4][d]	-0.50	1.98	2.48	500 nm (20 000 cm^{-1})	498 nm (20 080 cm^{-1})	520 nm (19 230 cm^{-1})	490 nm (20 408 cm^{-1})
TOTA[CS_2BF_4]	-0.50	1.50	2.00	620 nm (16 129 cm^{-1})	-	642 nm (15 576 cm^{-1})	-
TPT[BF_4] [e]	-0.70	2.17	2.87	432 nm (23 697 cm^{-1})	442 nm (22 624 cm^{-1})	480 nm (20 833 cm^{-1})	440 nm (22 727 cm^{-1})
TPT[CS_2BF_4]	-0.70	1.50	2.20	563 nm (17 762 cm^{-1})	-	620 nm (16 129 cm^{-1})	542 nm (18 450 cm^{-1})

a) the methods of obtaining the energy for 0-0 transition $E_{0,0}$: (1) calculated from the energy gap of the HOMO and LUMO; (2) calculated from the optical spectra, especially with the resources to the uprise higher energy side, where positions a 10% emission intensity to the emission maxima

b) reported values have been for different reference standards, e.g. E/V vs SCE or E/V vs Fc+/Fc in cyclic voltammetry. Therefore the data from Pavlishchuk and Addison[1] was used to convert all the values to E/V vs Fc+/Fc.

c) from cyclic voltammetry.

d) HOMO and LUMO level reported by Flood and Laursen.[2]

e) HOMO and LUMO level reported by Romero and coworkers.[3]

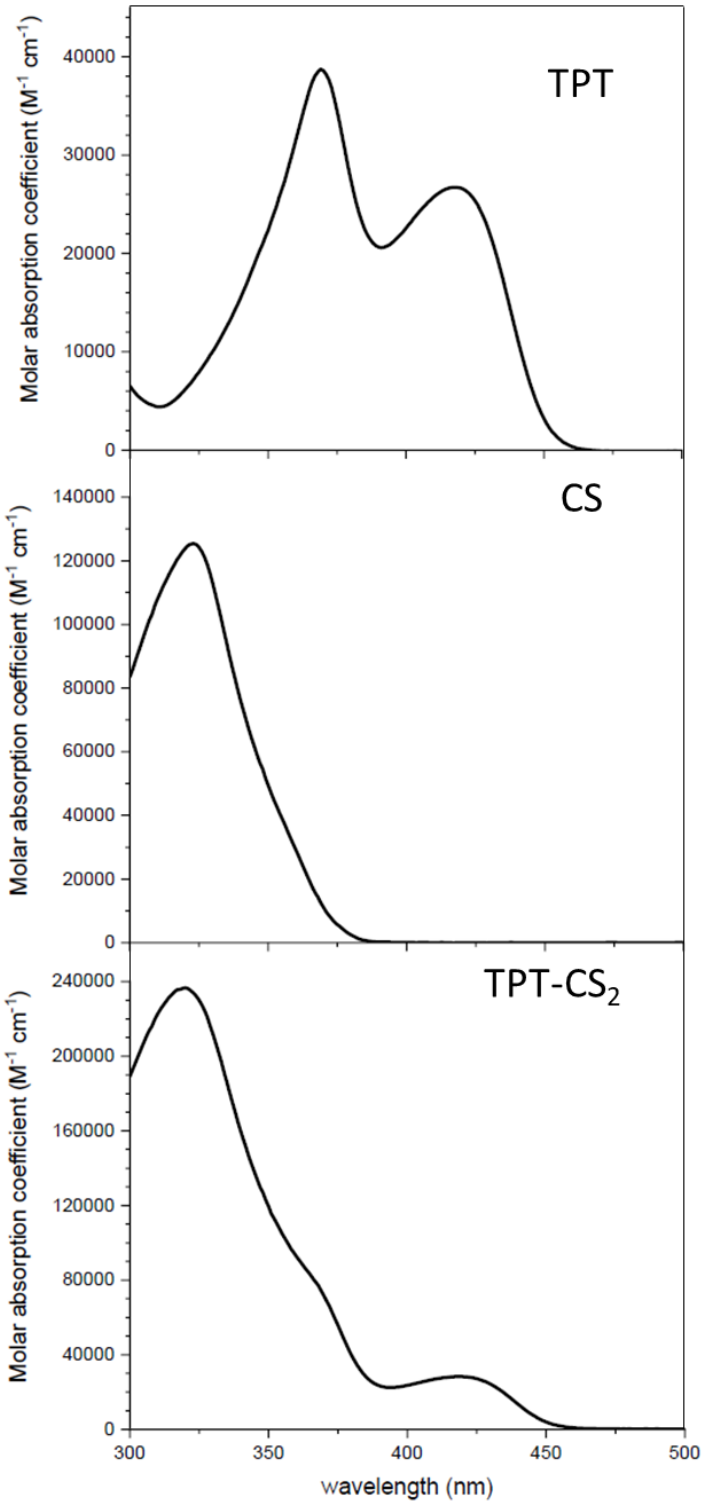

Figure S3. Molar absorption coefficient spectrum of TPT, CS and TPT-CS_2 in DCM.

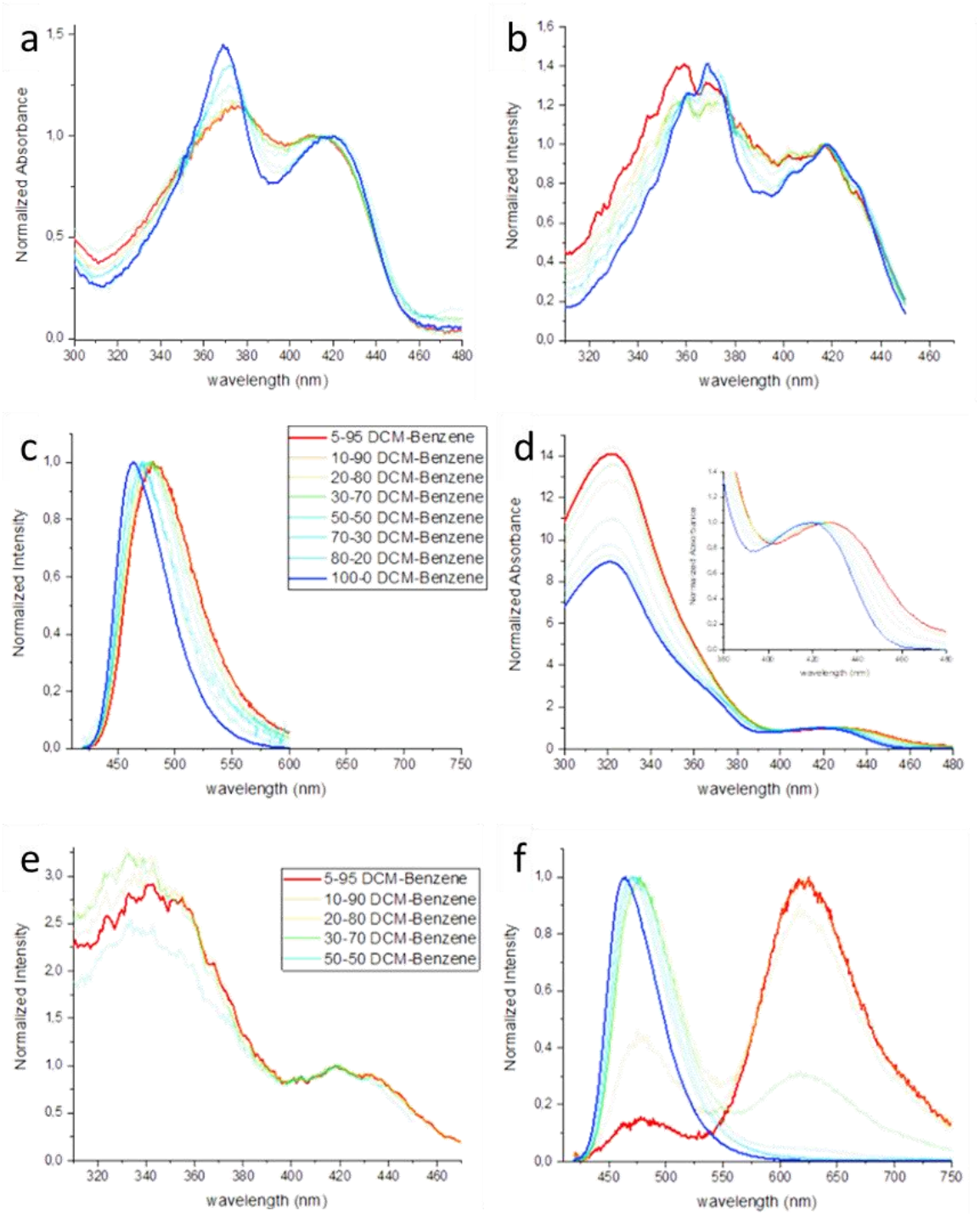

Figure S4. (a) Normalized absorption spectra and (b) normalized excitation spectra collected at 470 nm and (c) normalized emission spectra of TPT solutions, with λ_{ex}= 407 nm. (d) Normalized absorption spectra with an inset zoom in of the region 380 ~ 480 n. (e) Normalized excitation spectra collected at λ_{em}=600 nm and (f) normalized emission spectra of TPT-CS_2 solutions with λ_{ex}= 407 nm. All spectra varying from 100% DCM to 5% DCM and 95% benzene, except (f) which is only from 50% DCM and 50% benzene to 5% DCM and 95% benzene. All concentrations were made so that the absorption at λ_{ex} was kept below 0.1.

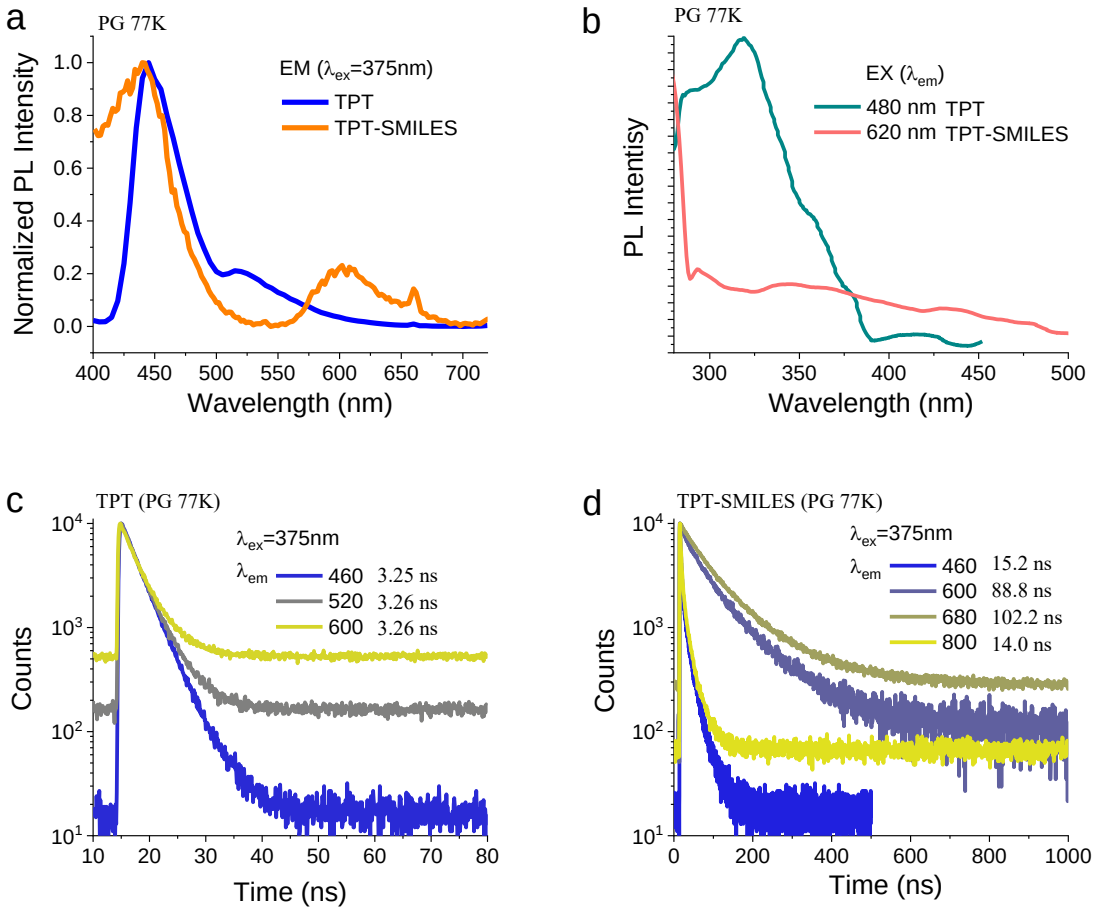

Figure S5. (a) Emission spectra of TPT chromophore and **TPT**-SMILES (TPT-CS_2) powders in frozen propylene glycol (PG) at 77K (by using liquid nitrogen), excitation wavelengh was 375 nm. TPT was dissolved in DCM then dissolved into PG, **TPT**-SMILES powders were made from dropcast solids and suspended into PG with good stability. (b) Excitation spectra of TPT and **TPT**-SMILES powders in frozen propylene glycol at 77K (liquid nitrogen), with detector set at 480 nm for TPT and 620 nm for **TPT**-SMILES. (c) TCSPC decay curves for TPT in frozen PG, with detector set at 460 nm, 520 nm and 600 nm, respectively. (d) TCSPC decay curves for **TPT**-SMILES powders in frozen PG, with detector set at 460 nm, 600 nm, 680 nm and 800 nm, respectively.

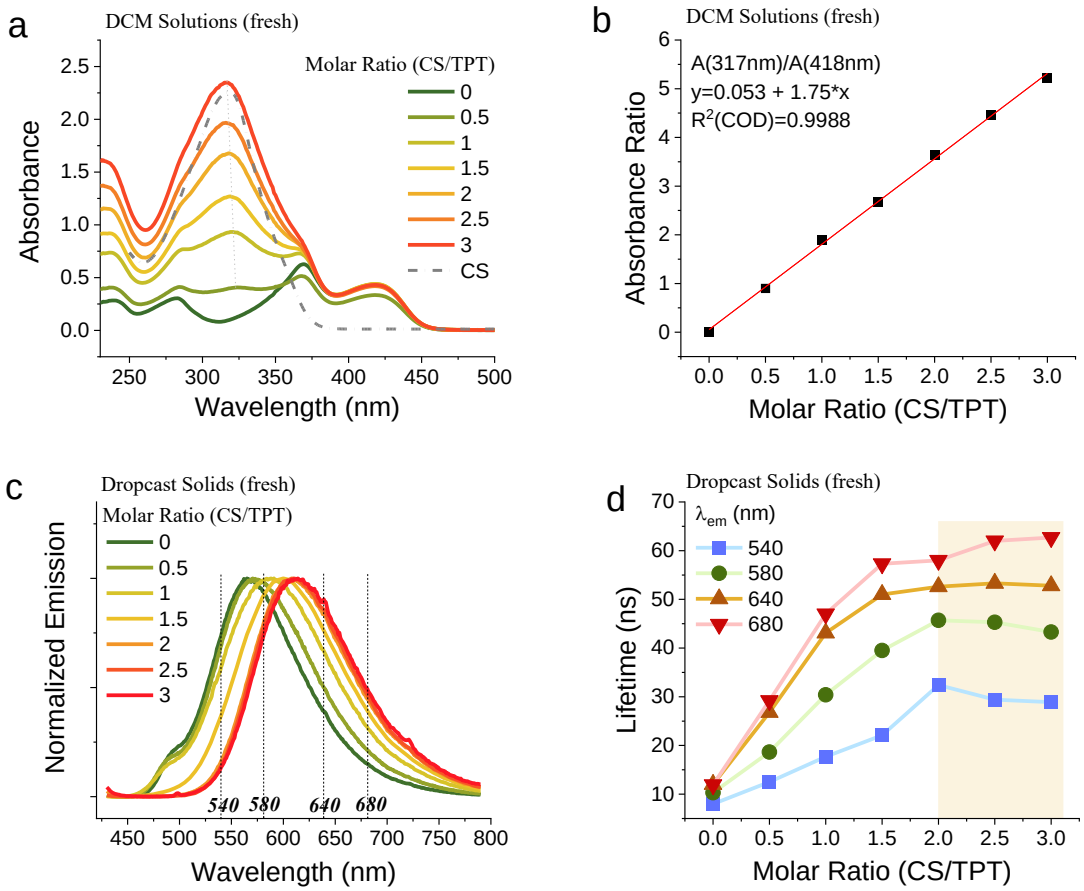

Figure S6. (a) Absorption spectra of solutions with different molar ratio of **TPT**[BF_4] and CS, in dichloromethane at the concentration of 10 μM of **TPT**[BF_4] and (b) Plot of absorbance at 317 nm in the function of CS/TPT molar ratio. (d) Intensity averaged lifetime plots for **TPT**•CS_x solids, with detector set at wavelength of 540 nm, 580 nm, 640 nm, and 680 nm, as shown in emission curves (c) to indicate the general tendency of lifetime changes with whole emission range covered.

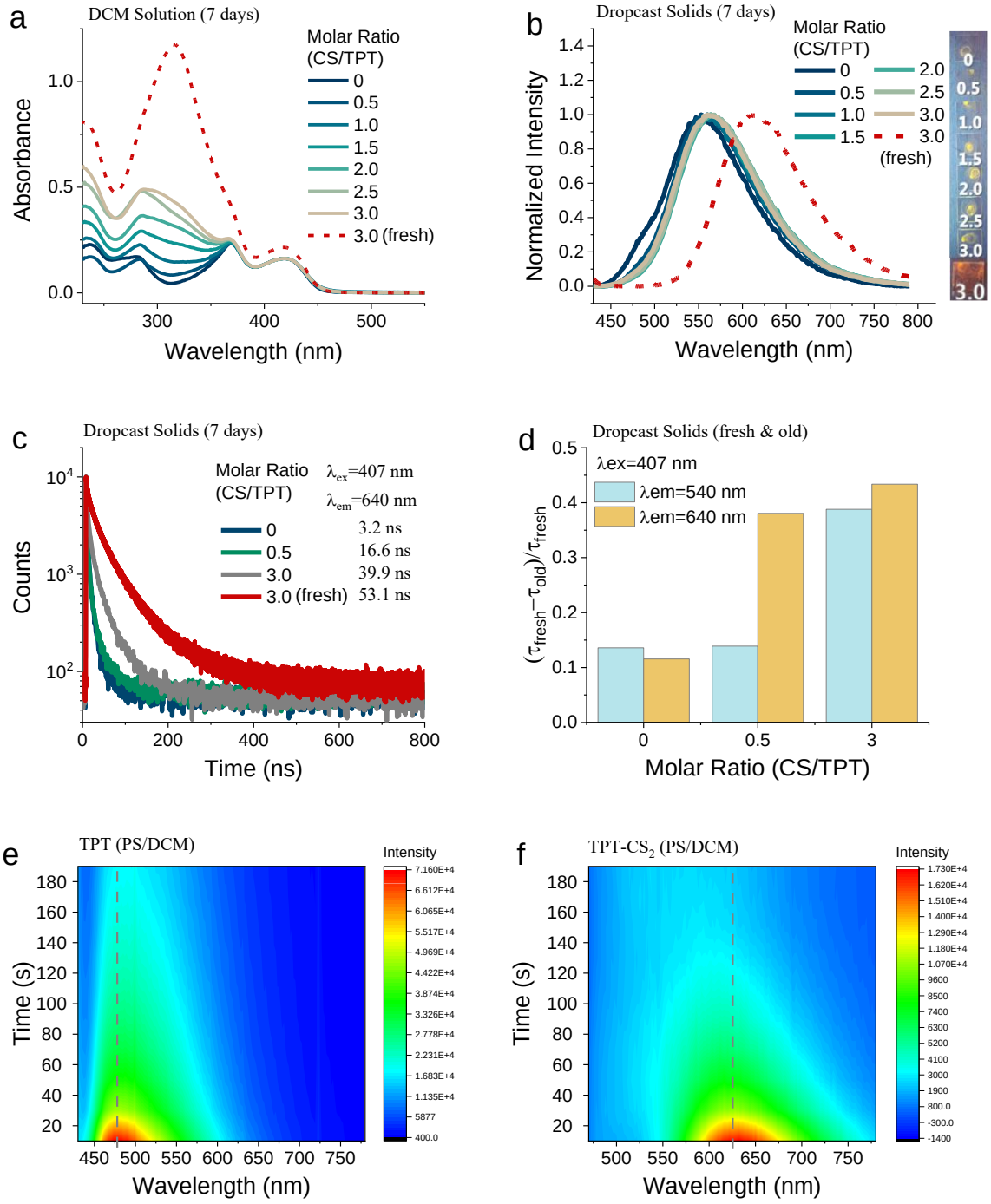

Figure S7. (a) Absorption spectra of TPT•CSx solutions (DCM 5 mM) and stored for 7 days with exposure to natural lights. (b) Emission curves of corresponding drop-cast solid samples. (c) Decay curves of old solid samples TPT•CS_x (x=0, 0.5, 3.0) in comparison to freshly prepared TPT•CS_3. (d) The decrease of lifetime in old solid samples (solution samples placed for 7 days) compared to freshly prepared samples (τ_{fresh} for fresh samples of TPT•CS_0 TPT•$CS_{0.5}$ TPT•CS_3, separately), lifetime were measured at λ_{em}=540 nm and 640 nm. (e-f) Time correlated emission spectra of (e) TPT and (f) TPT-CS_2 in undried polystyrene film (PS/DCM: 2/98 vol%), illuminated by laser light (λ_{ex}=407 nm).

§3 References

[1] V. V. Pavlishchuk, A. W. Addison, *Conversion constants for redox potentials measured versus different reference electrodes in acetonitrile solutions at 25°C*, *Inorganica Chim. Acta*, 2000, 298, 97–102.

[2] C. R. Benson, L. Kacenauskaite, K. L. Vandenburgh, W. Zhao, B. Qiao, T. Sadhukhan, M. Pink, *Plug-and-Play Optical Materials from Fluorescent Dyes and Macrocycles Plug-and-Play Optical Materials from Fluorescent Dyes and Macrocycles*, *CHEM*, 2020, 6, 1978–1997.

[3] N. A. Romero, D. A. Nicewicz, *Organic Photoredox Catalysis*, *Chem. Rev.*, 2016, 116, 10075–10166.

[4] M. Rosenberg, M. Santella, S. A. Bogh, A. V. Muñoz, H. O. B. Andersen, *Extended Triangulenium Ions: Syntheses and Characterization of Benzo-Bridged Dioxa- and Diazatriangulenium Dyes*, *J. Org. Chem.*, 2018, 84, 2556–2567.

海纳百川，有容乃大

壁立千仞，无欲则刚

Embrace diversities to elaborate the virtue of inclusiveness

Eliminate desires to silhouette the heart of persistency